UNIVERSITY OF CALIFORNIA, SAN DIEGO

Isolation of Four-Coordinate Iridium(I) Monohydrides and the X-ray Crystal Structure of a Cobalt Tris-Isocyanide Alkane sigma-Complex

A dissertation submitted in partial satisfaction of the requirements for the degree of Doctor of Philosophy

in

Chemistry

by

Matthew David Millard

Committee in charge:

Professor Joshua S. Figueroa, Chair
Professor Joseph M. O'Connor
Professor Nicholas C. Spitzer
Professor F. Akif Tezcan
Professor William C. Trogler

2013

The dissertation of Matthew David Millard is approved, and it is acceptable in quality and form for publication on microfilm and electronically.

Chair

University of California, San Diego

2013

DEDICATION

To my mother: for marrying the guy being chased by the cops while doing a wheelie on an orange motorbike up the street.

EPIGRAPH

NEVER SAY NO TO A CHALLENGE

Professor Karl O. Christe

TABLE OF CONTENTS

LIST OF FIGURES

LIST OF SCHEMES

LIST OF TABLES

LIST OF EQUATIONS

ACKNOWLEDGEMENTS

This is where I acknowledge the individuals who helped me along the way and who sacrificed, in one way or another, for my well–being. It should be obvious why I start with my parents Mrs. Roberta Anne Millard, the legendary Mr. Richard James Millard, and close friend Jon Garvens. These are the brave souls who saved me from my injudicious youth. If it were not for your patience, love, tolerance, and direction so generously and freely given to me, surely none of this would have been possible. It is essential to emphasize that my parental units have gone above and beyond the requirements for what parents should normally put up with and I aspire to give the unconditional love and wisdom they gave to me. What would a family be without a brother like Stephan Sean Millard? You taught me how to fix things that I broke and more importantly, you have stood by me through the worst of it.

I am honored to have been a part of the tenure process for Professor Joshua Salustiano Figueroa. It was obvious from the beginning that you were to conquer the inorganic chemistry world, with or without me, but to be at the epicenter with you on the path to victory was exhilarating and probably similar to training in the special forces. I have learned from you lessons on professionalism, specifically how to give a stellar presentation, and how to push myself beyond what I thought possible, then take pride in the extra investment, because that is what it took to get the job done correctly. My first, and likely most important, lesson from you was on "inflammable reflux condensers", sparked by none other than T. Ditri. This is when, and how, I learned to "get it done". Your zeal for uncovering Mother Nature's secrets, insatiable appetite for X–ray crystal structures, and scrupulous attention to detail has made my journey through graduate school both an enlightening and unique educational experience, and an impressive feat of heroics on my part. Overall, this process has been a "good sesh" and these words cannot convey my appreciation for the guidance and the lessons you have instilled into all of us "Figueroa's".

I would surely not have made it through graduate school without the support and guidance of Arnold L. Rheingold. You are more than just the crystallographer everyone wishes they had: you are a true individual, and underneath your brutally honest hard external shell is a caring, genuine human being (I will never forget you visiting me at the hospital!).

Liezel Labios, because of your help with editing this and other works, I forgive you for eating all my food. You have been a motivating and inspiring colleague the past five years, and it was always reassuring during the late nights to look over at your fume hood and see you diligently working. “Forearms” Treffly Brian Ditri, a big brother of sorts, you have been unbelievably helpful with your expertise in computers, Molecular Orbital Theory, and the ability to crush anything fragile with your incredibly strong hands. Our time together was definitely more exciting than it should have been. Alex Carpenter, you are certainly an interesting character and it has, in the end, been an absolute blast to work together. Despite all the torture we went through, I think the world of you. Brandon Barnett, I am glad we are still friends. Steven Philip George, most people think your inappropriateness is your biggest weakness: I think it is your greatest strength. You did not make long days any shorter but you did fill them with laughter. Charley, thanks for keeping the lab safe and the stories long. Doug you're a cool guy, hold down the fort for me. To the undergrads…good luck, you’re going to need it!

To the Olin family empire, Oskar, Eric, and Jess, thanks for the unwavering support, and our adventures to find ”The Endless Summer”. Doctors Ryan M. F. Howard “Yo” and Imran Jawaid, my two brothers from another mothers, because of ya’ll, I actually made it to graduate school, true story.

Drs. Curtis, Amy and Annabeth Moore, thanks for the countless hours of help, collaborating on the N_2 intercalation project, and allowing me to simultaneously use all four X–ray machines at once. Dr. Anthony Mrse, you are an NMR guru and an incredible human. I

will miss bothering you in the middle of the night and apologizing for whatever I broke, and in some cases fixed. We are not supposed to say this but everyone knows you are responsible for keeping the NMR facility functioning at UCSD. Prof. Charley Perrin, you are the Albert Einstein of organic chemistry, a brilliant duality of humility and intelligence: thanks for the guidance. Kyle Grice, you are a writing and editing BEAST. Thanks for all the help, direction, and fruitful discussion. A special thanks goes out to Eric Benson for help editing this work and the patience to answer an unremitting amount of questions from us first year graduate students. Dr. Su, I got you to smile and it was infectious. Your mass spec skills are inspiring and equally infectious. Skip Pomeroy, my first exposure to UCSD was you teaching me about the "green flash" at sunset. You have both figuratively and literally the biggest heart in the department. The essential German post-doc Nils Weidemann, your assistance was crucial to the lab, especially your talented vacuum distillation techniques, uncanny ability to stockpile an abundance of fluorinating reagents (never can have too much of these), and most importantly, your companionship. To the Kubiak laboratory, including but not limited to: Starla, Candace Sue, Gabe, Jane, and Kobe (I still don't know your real name), you lent me an unknown amount of items and I did not return them all, yet you continued to help me. Thanks…but whose fault is that?!!

A shout out goes to the undergraduate professors at University of North Florida who inspired me to enter into the world of chemistry: Dr. Lufaso (Inorganic!!), Dr. Stuart Chalk (I still respect the fanny-pack), Dr. Phil Davis ("Matt, you should go to grad school"), Dr. Ray Bowman (The go to fact guy on anything related to DNA and surviving in the wild), Melissa Bush, and John Pechonick. I switched into chemistry because of Dr. Chalk's nerdy jokes and fascinating lectures. Under Melissa Bush's tutelage, my lab skills were honed to perfection.

Outside of the lab is Professor Alfredo Barum, Ai Miuuu! Our training together is an island of serenity in a sea of madness. Also included on this island are Professors Clark

Gracie, Joel Tudor, and Harlen Berk. You have all kept me motivated and healthy. Mike Ragle, a master of working hard and generosity, you taught me by example. White backgrounds “732”, Davey Gonzales, you are a freak on a motorcycle and a determined human being. Thankfully, I think a little rubbed off on me. Josh “Good Time Haygood”, you showed me first-class morals, friendship, and confidence, much appreciated. Stephen Howell, you made it into the acknowledgments! Thanks for the edits and laughter. Clifford Mettier, “I’m fine, thanks for asking“.

I also wish to thank the SD riding crew for their camaraderie and friendship: Danny Daffer, Leslie Slagle, Jon Faure, Brian Shaw, XJakeKinneyX, and James Visser. Our crazy antics, after the injuries healed, made excellent memories.

The Emrhien kingdom “may Lloyd and Howard Powers always be watching over Scape”. Patrick Foley, thanks for the brotherhood “XForeverX”. Jack Shapiro, your love for mathematics was useful but your ability to match my number of push-ups was impressive: “xVx”. I will describe Gary Peters with two words, Spiritual Pillar. Jeff Finlay, you have always been there for me, thank you. Neck Beard, thanks for the memories. Aaron Hill, Derek Balmer, Cory Edmanstun, you have all been role models and GOD SPEED KEVIN HALL Jr., Never Let up…

SPECIFIC CHAPTER ACKNOWLEDGMENTS

Chapter 1: Much of the material for this chapter comes directly from a manuscript entitled "Four–Coordinate Iridium(I) Monohydrides: Reversible Dinitrogen Binding, Bond Activations, and Deprotonations" by Matthew D. Millard, Joshua S. Figueroa, Curtis E. Moore, and Arnold L. Rheingold, which has been published in *Journal of the American Chemical Society,* **2010**, 132 (16), pp 8921-8923.

Chapter 3: Much of the material for this chapter comes directly from a manuscript entitled "Crystallographic Characterization of a Cobalt sigma-Alkane Complex Formed in Solution" by Matthew D. Millard, Alex E. Carpenter, and Stephen P. George, Arnold L. Rheingold, and Joshua S. Figueroa, which has been submitted to *Science,* **2013-** in review.

VITA

2013	Doctor of Philosophy, University of California, San Diego
2009	Master of Science, University of California, San Diego
2007	Bachelor of Science, University of North Florida

PUBLICATIONS

"Crystallographic Characterization of a Cobalt sigma-Alkane Complex Formed in Solution" Millard, M. D.; Carpenter, A. E.; George S. P.; Moore, C. E.; Rheingold, A. L.; Figueroa, J. S. Science **2013-** in review.

*"Zwitterionic Stabilization of a Reactive Cobalt Tris-Isocyanide Monoanion by Cation Coordination"*Carpenter, A. E.; Margulieux, G. W.; Millard, M. D.; Moore, C. E.; Weidemann, N.; Rheingold, A. L.; Figueroa, J. S. Angew. Chem. Int. Ed. **2012,** 51, 9412-9416.

"Four-Coordinate Iridium(I) Monohydrides: Reversible Dinitrogen Binding, Bond Activations, and Deprotonations" Millard, M. D.; Moore, C.E.; Rheingold, A. L.; Figueroa, J. S. J. Am. Chem. Soc. **2010**, 132, 8921-8923.

"Bond Activation, Substrate Addition and Catalysis by an Isolable Two-Coordinate Pd(0 Bis-Isocyanide Monomer." Labios, L. A.; Millard, M. D.; Rheingold, A. L.; Figueroa, J. S. J. Am. Chem. Soc. **2009**, 131, 11318-11319.

"Thallium(I) as a Coordination Site Protection Agent: Preparation of an Isolable Zero-Valent Nickel Tris-Isocyanide" Fox, B. J.; Millard, M. D.; DiPasquale, A. G.; Rheingold, A. L.; Figueroa, J. S. Angew. Chem. Int. Ed. **2009**, 48, 3473-3477.

ABSTRACTS OF THE DISSERTATION

Isolation of Four-Coordinate Iridium(I) Monohydrides and the X-ray Crystal Structure of a Cobalt Tris-Isocyanide Alkane sigma-Complex

by

Matthew David Millard

Doctor of Philosophy in Chemistry

University of California, San Diego, 2013

Professor Joshua S. Figueroa, Chair

Detailed herein are the synthesis, characterization, and reactivity of three isolable four-coordinate iridium(I) monohydride complexes. Iridium(I) monohydrides containing the simple formula $HIrL_3$ have been postulated as reactive intermediates for over four decades escaping definitive evidence. The judicious use of the C–H activation resistant methyleneadamantyl phosphine $P(CH_2{}^1Ad)(i\text{-}Pr)_2$ (abbreviated L^{mAd}) and phosphinite $P(O^1Ad)(i\text{-}Pr)_2$ (abbreviated L^{oAd}) ligands allowed for the successful isolation and characterization of four-coordinate iridium(I) monohydride complexes $HIr(N_2)(L^{mAd})$, $[Li(12\text{-}c\text{-}4)][HIr(\kappa^2\text{-}P,C\text{–}L^{mAd})(L^{mAd})]$, and $[Li(12\text{-}c\text{-}4)_2][H_3Ir(\kappa^2\text{-}P,C\text{–}L^{oAd})(L^{oAd})]$.

These electron-rich monohydride complexes rapidly deprotonate protic reagents, such as $H_2N(2,6\text{-}(i\text{-}Pr)_2C_6H_3)$ and C_6F_5OH, and activate N-H, O-H, and H-H bonds. The sequential addition of 12-crown-4 with 1.0 equ. of a strong lewis base, i.e. $Li(CH_3)_3CLi$ to

cyclometallated complexes $H_2Ir(\kappa^2\text{-}P,C\text{-}L^{oAd})(L^{oAd})$ and $H_2Ir(\kappa^2\text{-}P,C\text{-}L^{mAd})(L^{mAd})$ produces four-coordinate anionic complexes $[Li(12\text{-}c\text{-}4)][HIr(\kappa^2\text{-}P,C\text{–}L^{mAd})(L^{mAd})]$ and $Li[12\text{-}c\text{-}4)_2][H_3Ir(\kappa^2\text{-}P,C\text{–}L^{oAd})(L^{oAd})]$, respectively.

Herein we also report the X–ray characterization of coordinated alkanes, *n*–hexane and *n*–heptane, forming cobalt metal complexes $(\mu^2\text{–}(\eta^2\text{-}H,C\text{–}(CH_3(CH_2)_4CH_3)[Co(SiMe_3)(CNAr^{Mes2})_3]_2\cdot(n\text{–}C_6H_{14})\cdot 2(C_6H_6)$ and $\mu^2\text{–}(\eta^2\text{-}H,C\text{–}(CH_3(CH_2)_5CH_3)[Co(SiMe_3)(CNAr^{Mes2})_3]_2\cdot(n\text{–}C_7H_{16})$ (Ar = Aryl, Mes = mesityl = 2,4,6–$Me_3C_6H_2$ and Me = methyl, CH_3). A continued effort to isolate and characterize alkane σ–complexes stems from the desire to control alkane C–H bond transformations, a significant synthetic challenge with high economic benefit.

Support for a distinct η^2-H,C σ–type interaction with *n*–hexane or *n*–heptane was provided by DFT and AIM analysis computations as well as r_{bp} parameter calculations. The diamagnetic complex, $Co(SiMe_3)(CNAr^{Mes2})_3$ forms from the addition of $(CH_3)_3SiCl$ to the zwitterionic complex $(\eta^2\text{–PPN})(Co(CNAr^{Mes2})_3$ (PPN = $(C_6H_5)_3P{=}N{=}P(C_6H_5)_3$). Crystallization of $Co(SiMe_3)(CNAr^{Mes2})_3$ with 5% v/v of C_6H_6 in *n*–hexane or *n*–heptane at -35 ˚C under an argon atmosphere produces single crystals of the respective alkane σ–complexes. When *n*-nonane (C_9H_{20}) is employed as the crystallization solvent, the unsaturated $Co(SiMe_3)(CNAr^{Mes2})_3$ forms single crystals of $Ar_{1/7}Co((SiCH_3)_3)(CNAr^{Mes2})_3$ which were manipulated in single crystal to single crystal (SC–SC) dinitrogen intercalation experiments, resulting in full occupancy and binding of dinitrogen to the cobalt metal center. Persistent in the solid-state are weak Van der Waals interactions from the $CNAr^{Mes2}$ ligands to the bound alkanes, *n*-hexane and *n*-heptane, possibly mimicking a clathrate-type entrapment mechanism. Distinct from clathrate networks is the strategic placement of a highly Lewis acidic cobalt center of proper electronic structure to engage in bonding.

Chapter 1

Isolation, Characterization, and Reactivity of a Vaska–Type Iridium(I) Monohydride

1.1 Introduction

Interest in transition metal monohydrides stems from the pivotal role they play in important transformations including: water gas shift reactions,[1,2] the Wacker process,[3] hydroformylation,[4,5] nitrile hydration,[6] carbonylation,[7-9] hydrogenation,[10] dehydrogenation,[11-14] and bond activations.[15-20] The common modality of these transformations is the intermediacy of a transition metal monohydride.

Metal hydrides were tolerated as exceptions to chemical bonding theories and remained controversial for quite some time. Speculated as early as 1807 by Humphry Davy, Gay Lussac and Thenard, the interaction of hydrogen with a metal atom would remain speculative for over 100 years until the mid 20th century. [21] Realization that metals actually form compounds with hydrogen was first shown by Wurtz in 1845, where he prepared a hydride of copper from hypophosphoric acid. [22] The metal hydrogen interaction was further substantiated by Graham's discovery in 1866 of palladium hydride. [23] The synthesis of the majority of all metals (and non–metals) with hydrogen as a ligand had been accomplished by the early 1920's. Most metal hydrides displayed a high propensity to lose hydrogen or undergo reactivity with other substrates but remained mere mysterious reactive inorganic materials. In particular, nickel hydrides played a critical role in support for high M–H reactivity. This was highlighted by Sabatier in 1926 with the use of nickel as a hydrogenating catalyst.[24] The first reasonably well defined hydride complex, although still considerably unstable, was $H_2Fe(CO)_4$ and $HCo(CO_4)$ by Walter Hieber, "the father of metal carbony

chemistry", in 1931.[25] The commercial availability of nuclear magnetic resonance spectrometers allowed for the accidental discovery of bis(cyclopentadienyl)hydridorhenium in 1955 by Wilkinson, which deepened the then limited understanding of the metal hydrogen interaction.[26] NMR spectroscopy became a benchmark technique to characterize the metal hydride moiety, as the proton attached to the metal shifts upfield in the NMR spectrum, as compared with hydrogens attached to main group elements. The next big breakthrough was lead by Chatt (to whom Wilkinson was not a fan) and Shaw with the discovery in 1957 of the surprisingly stable *trans*-$PtHCl(PEt_3)_2$ and eventual X–ray crystal structure. [27] This would be the first complex to contain observable IR spectroscopic features for the metal–hydrogen and metal–deuterium bond with accompanying X–ray crystallographic support. [28] These discoveries laid a solid foundation for the current electronic bonding picture of metal hydrides and why there is such an abundance of research on metal hydrides in academia and industry.

Transition metal hydrides quickly became popular as reactive intermediates and relevant catalysts. Schwartz's reagent (Cp_2ZrHCl), discovered in the early 1970's, facilitates the acylation of unsaturated hydrocarbons by hyrdozirconation, the *syn* addition of the Zr–H unit to alkynes and alkenes.[29] Otto Roelen, working closely with industrial scale Fisher–Tropsch products, uncovered the "Roelen synthesis", also known as hydroformylation, finding large scale industrial use with the cobalt catalyst $HCo(CO)_4$ or, currently, the rhodium complex $HRh(CO)(PPh_3)_3$.[30] Metal hydrides also mediate important biological processes, such as that of the diiron subcluster [FeFe]-hydrogenase, a metalloprotein complex that catalyzes the reversible reduction of protons to molecular hydrogen.[31]

These metal hydride complexes, along with hundreds of others, [32] comprise an area of active research. We took notice to late–metal hydride complexes and found that there is a complete lack of information pertaining to both structural and kinetic features of iridium (I) monohydride complexes containing the generalized molecular formula $XIrL_3$ (where X=

hydride). This was interesting because the well known and thoroughly studied Vaska's complex, an iridium (I) monochloride (Cl)IrCO(PPh_3), was stable and contains the general formula XML_3, where X = chloride and L = 2 electron donor. Mechanistic studies have shown that Vaska-type iridium complexes of the formula $XIrL_3$ (where X = halogen) adopt the square planar geometry and possess a high aptitude towards substrate oxidative addition, especially with respect to H_2 gas. Early support for the existence of Vaska–type iridium(I) monohydrides, of the formula $HIrL_3$, was found through formal trapping processes, computations, or inferred via IR spectroscopy which left many chemists questioning their reactivity profiles.[33-41] It was realized that these complexes have a high propensity towards activating an assortment of functional groups and small molecules but throughout the years these Vaska–type iridium(I) monohydrides have escaped isolation, thereby preventing detailed elucidation of their reactivity. Therefore, our group has focused upon synthetically accessing an isolable Vaska–type iridium(I) monohydride of the formula $HIrL_3$, allowing for the elucidation of its reactivity, as well as providing an avenue to study both its structural and electronic properties.

1.2 The Annals of Reactive Intermediates Comprising the Formula $HIrL_3$.

Proposed over 40 years ago, it was not until recently that a Vaska–type iridium(I) monohydride complex of the formula $HIrL_3$ (where L = a neutral 2–electron donor) was successfully isolated and fully characterized by our laboratory. [42] These reactive complexes have escaped previous isolation attempts as a result of intramolecular ligand activations, subsequent reactions with solvents/substrates, or other decomposition pathways. Square planar iridium(I) complexes and their accompanying reactivity patterns were first uncovered in the early 1960's by Lauri Vaska. These studies were instrumental in portraying the ability of these 16–electron species to undergo oxidative addition/reductive elimination reactions upon substrate addition (shown in Scheme 1.1).[43-46] Following Vaska's seminal investigations, Dolcetti in 1969 demonstrated the hydrogenation of α–olefins from the iridium complex

$Ir(PPh_3)_2H_3$. During the course of these reactions a "green color" appeared which they assigned as a reactive iridium(I) monohydride species. This proposed monohydride intermediate, inferred by IR spectroscopy and the green luster, is claimed to be the active catalyst in the hydrogenation of non– activated olefins. Employing a formal trapping process with the addition of H_2 gas, the green iridium(I) intermediate elicited reactivity that mirrored Vaska's complex, yielding an isolable 18–electron iridium(III) tri–hydride product (Scheme 1.2).[37]

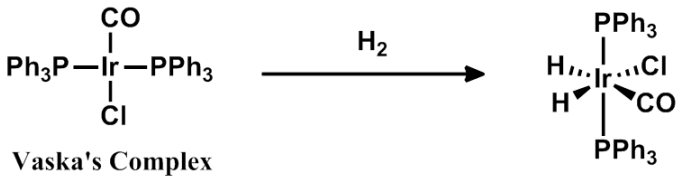

Scheme 1. 1. Vaska's Complex rapidly undergoes oxidative addition with H_2 gas.

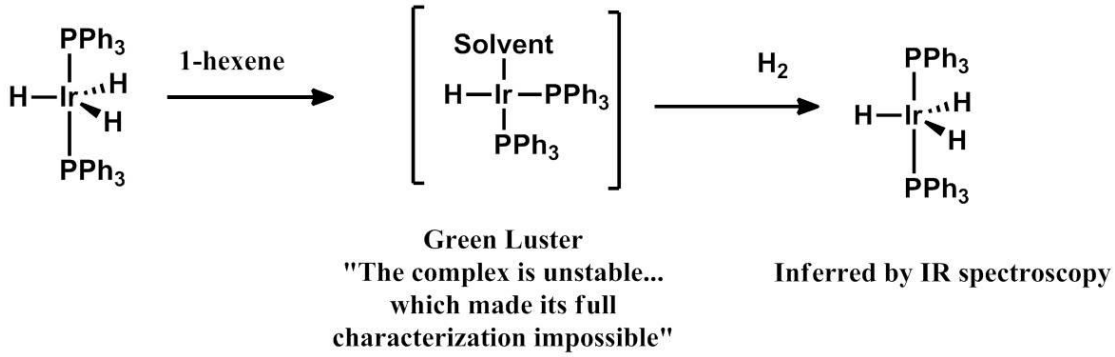

Scheme 1. 2. The first proposed Vaska type iridium(I) monohydride complex, where solvent is CH_2Cl_2.

Another crucial example of a proposed monohydride intermediate was by G. Geoffroy in 1976, where the photo–elimination of molecular hydrogen from a tri–hydride iridium(III) complex ($H_3Ir(PPh_3)_3$) formed the purported iridium(I) monohydride $HIr(PPh)_3$, that rapidly underwent intramolecular ortho C–H activation of the phenyl ring. This produced a coordinatively saturated Ir(III) complex of the formula ($H_2Ir(H_2Ir(\kappa^2$-*P*(Ph_2),*C*-Ph$)(PPh_3)_2$) (Scheme 1.3).

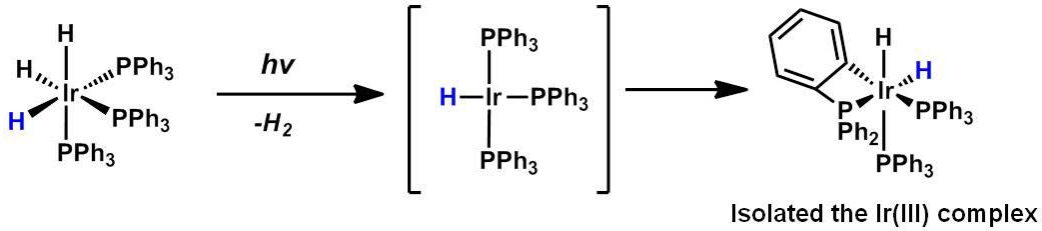

Scheme 1. 3. Photolytic elimination of H_2 gas with concomitant C–H ligand oxidative addition.

These studies revealed the coordinatively saturated iridium(III) tri–hydride ($Ir(PPh_3)H_3$) isomer to be actively participating in geometric interconversions under photolytic conditions. For a saturated metal complex to undergo geometric interconversion, it must undergo ligand dissociation forming an unsaturated intermediate species for which the authors postulate is an Iridium(I) monohydride complex $HIr(PPh_3)_3$. In attempting to deduce reactivity patterns of iridium(I) monohydrides, Harrod and Fawcet employed a formal trapping process where they added Si–D substrates (Ph_3SiD) and noted deuterium incorporation within the isolated iridium(III) products, suggesting Si–D bond activation. [16]

Notably, Eisenberg published several articles on iridium and rhodium complexes that, under photolytic conditions, were capable of catalyzing intramolecular aryl C–H bond activation. The authors were able to isolate/characterize several stable iridium(III) complexes and proposed that the active intermediate was likely an iridium(I) monohydride (Ir–H) which would be capable of arene C–H functionalization, in particular, the carbonylation of benzene to benzaldehyde.[7-9] During these initial iridium(I) hydride reactivity studies, it was also discovered that iridium(I) alkyl and alkoxide complexes ($XIrL_3$ where X = alkyl or alkoxide and L = CO or PPh_3) prepared *in situ* from a Vaska–type monochloride rapidly undergoes thermal decomposition to the more stable iridium(III) complex formula $HIrL_4$.[11-13]

With respect to electronic structure, Vaska–type iridium(I) monohydride complexes have been proposed to adopt a square planar geometry[47] (similar to Vaska's complex) involving double occupation of the four low–energy nonbonding metal d–orbitals Ir(d_{xy}, d_{xz},

d_{yz}, and d_z^2).[48,49] An investigation into the qualitative molecular orbital diagram reveals several inconsistencies with respect to why these complexes are unstable as compared to other square planar complexes (Vaska's complex) and the lighter congener rhodium. Interestingly, depicted in Figure 1.1 (left side), a qualitative D_{4h} molecular orbital splitting diagram illustrates a nonbonding p_z orbital of A_{2u} symmetry that is located lower in energy relative to the A_1g anti–bonding 6s orbital. Classic d^8 square planar complexes are, for electronic purposes, considered to be stable even though they are 16–electron. The stability in 16–electron complexes is from the high lying nonbonding Ir(p_z) orbital that possesses the same symmetry as the filled d_{z2} orbital. In contrast, the Vaska–type iridium(I) hydride complexes are not stable, even though they have been compared to stable square planar complexes. Furthermore, Vaska–type iridium(I) hydride complexes possess a high propensity towards substrate oxidative addition which supposedly involves the high lying nonbonding, empty Ir(P_z) orbital. The stability engendered with square planar platinum (II) and palladium (II) D_{4h} complexes can be speculated from charge arguments as Pt(II) oxidized to Pt(IV) is less favorable than the oxidation of Ir(I) to Ir(III).

A qualitative molecular orbital diagram was constructed to gain further insight into the instability of Vaska–type iridium (I) monohydrides (Figure 1.1). To determine if the geometry influences reactivity (D_{4h} vs.C_{2V}), w used the classic 16–valence electron, square planar, d^8, D_{4h}, molecular orbital diagram. Generic Vaska–type monohydrides of the formula $XIrL_3$ are C_2v symmetric and differ from D_{4h} in that there is allowed mixing of the A_1 symmetric orbitals. This mixing would mainly affect the 6s anti–bonding with d_{x2-y2} and the non–bonding p_z orbital. We speculate that classic D_{4h} complexes have discrete orbitals but once the symmetry is broken to C_{2v} it allows for mixing of the Ir A_1(6s*), Ir A_1(pz), and the Ir $A_1(d_{x2-y2})$. Furthermore, iridium belongs to the 5d transition metals and is well known to entertain relativistic effects which would lower the Ir A_1 (6s*) orbital, thereby increasing the

reactivity of iridium as compared to the lighter congener rhodium. There are several examples of isolable Vaska–type rhodium(I) monohydrides.[50-55] The mixing of orbitals due to broken symmetry does not lend support for the difference in reactivity between Vaska's complex and Vaska–type monohydrides.

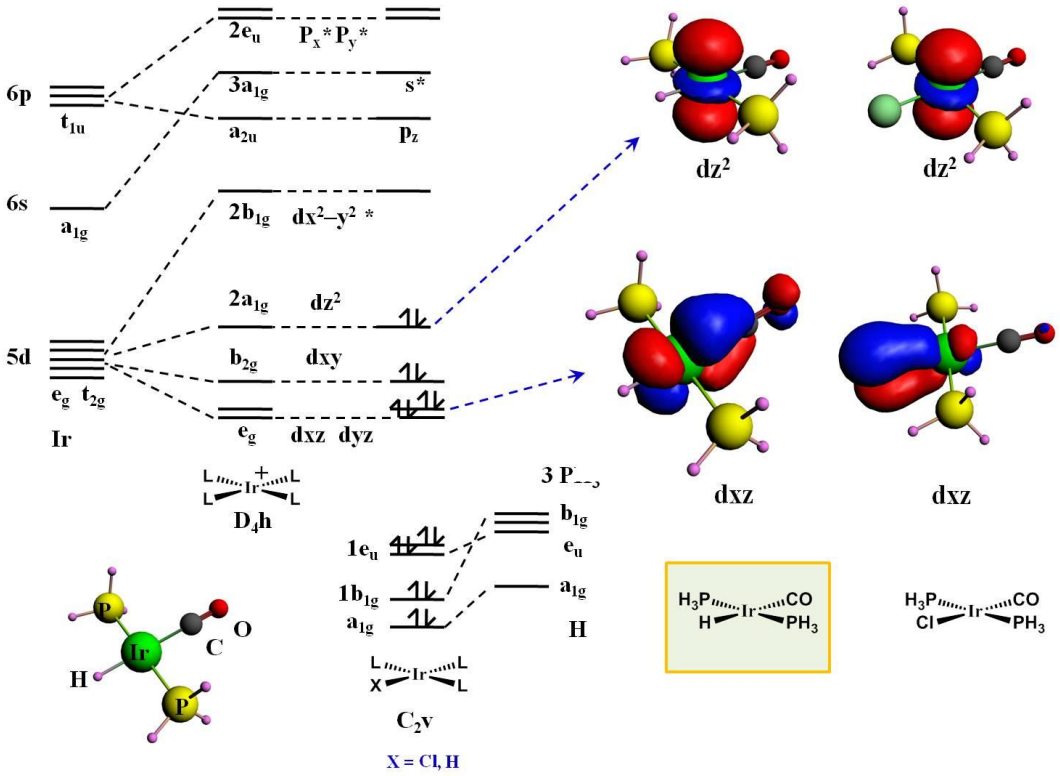

Figure 1. 1. Density Functional Theory molecular orbital diagrams highlighting the difference in bonding between $ClIr(CO)(PH_3)_2$ and $HIr(CO)(PH_3)_2$.

Hydride ligands have a long standing reputation for being involved in the reactive species during catalysis. There are several isolobal complexes mirroring Vaska–type iridium monohydrides. Building upon the isolobal analogy,[56] an unhindered square planar hydrido/hydroxo bis(phosphine) platinum(II) catalyst, $HPtOH(PR_3)_2$ (Scheme 1.4), that furnishes nitrile hydration consists of the formula X_2ML_2 (where M = Group 10 transition metal, L = 2–electron donor, and X = 1–electron donor), and is isolobal to $HIr(CO)(dppe)_2$ (Scheme 1.4), an iridium catalyst responsible for the carbonylation of benzene to benzaldehyde.[7-9] These metal complexes are also isolobal to the well known rhodium

hydroformylation catalysts of the formula $HRhL_3$,[5] (Scheme 1.4) and the platinum catalyst $HPtL_2X$, which has been exploited in the water gas shift reaction (Scheme 1.4). These complexes are linked by the isolobal analogy and the possession of a monohydride moiety as one of the X–type ligands. Therefore, with the utilization of Density Functional Theory (DFT), we were able to model several complexes in attempts to understand the electronic structure and stability differences between Vaska's complex and Vaska-type monohydrides.

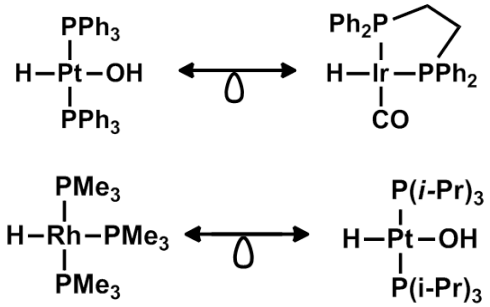

Scheme 1. 4. Isolobal analogy for several late metal catalysts.

We used model complexes $HIr(PH_3)_2(CO)$ and $ClIr(PH_3)_2(CO)$ with DFT methods at the CGA:BP level of theory to compare bonding differences between "X–type" ligands chloride and hydride. As portrayed in Figure 1.1 (right side), the chloride engages in $Cl_{(lone\ pair)} \rightarrow Ir_{(dxz)}$ ligand to metal π–back donation.[57] This bonding interaction likely stabilizes the electron deficient iridium metal center. The hydride ligand lacks any π–type bonding interaction. This lack of electron donation from the chloride ligand causes the metal center to be highly Lewis acidic and reactive towards Lewis bases. To achieve stability, Vaska–type monohydrides rapidly undergo oxidative addition or intramolecular C–H bond activation reactions.

1.3 Rational Ligand Design: Synthesis of a C–H Activation Resistant Tri–Alkyl Phosphine

Historically, all attempts to isolate low valent, low coordinate iridium(I) monohydrides resulted in the characterization of an iridium(III) product, leading to the

proposal that the fleeting iridium(I) intermediate had activated a substrate/ligand or was coordinated by an additional L–type ligand.[58-63] We reasoned that an Iridium(I) complex could be stabilized if a ligand platform was effective at discouraging intra–molecular C–H activation. Wilkinson, in 1980, published a thorough study on methods to thwart intramolecular cyclometallation using a new class of ligands, consisting of a methylene adamantyl unit.[64] This new class of methylene alkyls showed unprecedented resistance towards intramolecular C–H activation (Scheme 1. 5) and, in fact, allowed for the isolation of the first thermodynamically favored *trans*–dialkylplatinum(II) complex.[64] The methylene group serves as an added linker which places the β-position on a quaternary carbon within the adamantyl cage. This placement shuts down β–hydrogen C–H activation mechanisms, a troublesome decomposition pathway for iridium(I) monohydrides. Furthermore, the γ-proton is located on the adamantyl moiety causing it to be less susceptible to attack, as it is anchored away from the metal center by means of the interlocked adamantyl cage. In contrast to a neopentyl group, the rigidity of the adamantyl cage discourages the γ-proton from approaching the metal center. For these reasons the methylene adamantyl unit was installed into a phosphine ligand by G. Whitesides in 1987, yielding a dimethyl(methyleneadamantyl)phosphine ($P(CH_3)_3(CH_2{}^1Ad)$).[65] Although not inert, these methylene adamantyl phosphine ligands were less susceptible towards intra–molecular C–H

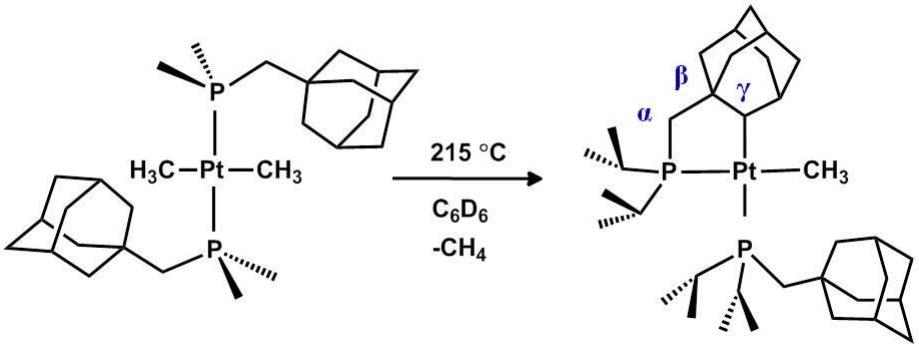

Scheme 1. 5. Original C–H activation–resistant methyleneadamantyl ligand.

bond activation. They further demonstrated that the adamantyl moiety undergo C–H bond activation at the γ–position but only under increased thermal conditions (above 215 ˚C). They speculate that the resultant five–membered metallacycle contains a significant amount of angle strain due to the interlocked adamantyl cage. Although seemingly valid, the ring strain argument was merely speculative as they did not report any X–ray crystal structures.

In 1985 Dahlenburg employed a sterically demanding di–*t*–butyl(neopentyl)phosphine wherein the iridium(I) intermediate was obviated and the inevitable intramolecular C–H activated iridium(III) product was isolated (Scheme 1.6, Figure 1.2).[58] Cyclometallation is more common with ligands that are able to direct the C–H bond in close proximity to the metal center, i.e. with neopentyl groups, as they enforce the proper geometry for the formation of a stable five–membered metalacycle.[65] With the success of the methylene adamantyl phophine ligand platform by Whitsides and the crystallographic evidence from Dahlenberg pertaining to the importance of C–H bond proximity, we endeavored to synthesize a phosphine that contained the useful topologies from the studies by Whitesides but avoid the pitfalls in Dahlenburg's iridium complexes.

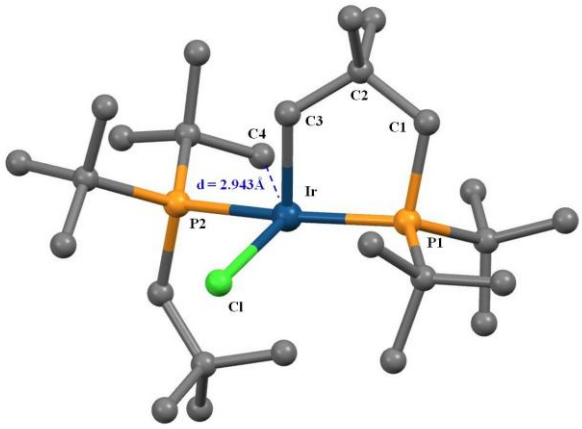

Figure 1. 2. X–ray crystal structure of a neopentyl phosphine iridium(III) complex from ref 51, no hydrogen atoms were included in the CIF file.

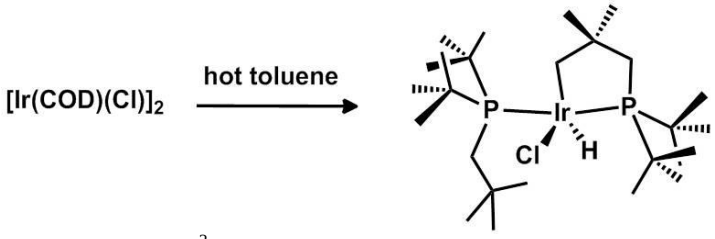

Scheme 1. 6. Synthesis of HIr(Cl)(κ^2-*P*,*C*-$CH_2(CH_3)_3$)(*t*-butyl)$_2$)(P($CH_2(CH_3)_3$)(*t*-butyl)$_2$. Structure shown in Figure 1.2

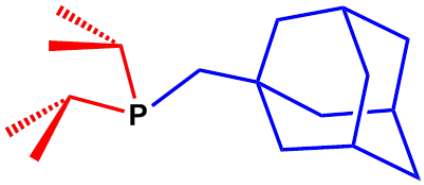

Figure 1. 3. Tri–alkyl phosphine P($CH_2{}^1$Ad)(*i*-Pr)$_2$ (L^{mAd}; mAd = methylene-1-adamantyl).

We utilized the tri–alkyl phosphine P($CH_2{}^1$Ad)(*i*-Pr)$_2$ (L^{mAd}; mAd = methylene-1-adamantyl); a phosphine ligand that resists intramolecular C–H activation (shown in blue, Figure 1.3), as well as possessing increased steric encumbrance (Figure 1.3, shown in red). It was soon discovered that published preparations were unreliable and the Grignard reagent ($AdCH_2MgBr$) was sluggish towards magnesium activation (under standard Grignard conditions) and decomposed by means of a Wurtz–type coupling with heat, producing 1,2–diadmantylethane.[66] We developed a reliable synthesis for the Grignard reagent with the use of Rieke magnesium.[67] Although THF (Tetrahydrofuran) is a favorable solvent due to its higher boiling point as compared to Et_2O (66 ˚C vs 35 ˚C), the effect on Schlenk equilibria, and increased solubility for reagents, it was avoided due to the intractable mixtures of products formed upon addition of the Grignard reagent to ClP(*i*-Pr)$_2$ in THF. The solvent Et_2O was successfully employed as the reaction medium even though it has a lower boiling point (bp = 34°C) than the temperature necessary for melting potassium (mp = 68°C) (Figure 1.4). The addition of an Et_2O solution of $AdCH_2MgBr$ to a -78 ˚C Et_2O solution of Chlorodiisopropylphosphine $[(CH_3)_2CH]_2PCl$ afforded the trialkly phosphine P($CH_2{}^1$Ad)(*i*-Pr)$_2$ with spectroscopic features ^{31}P NMR δ = –12.5 ppm (Scheme 1.7, Figure 1.4 and Figure

1.5). This phosphine ligand is highly O_2 sensitive and rapidly forms the phosphine oxide when exposed to air or 1.0 equivalent of O_2 gas (^{31}P NMR δ = 50 ppm).

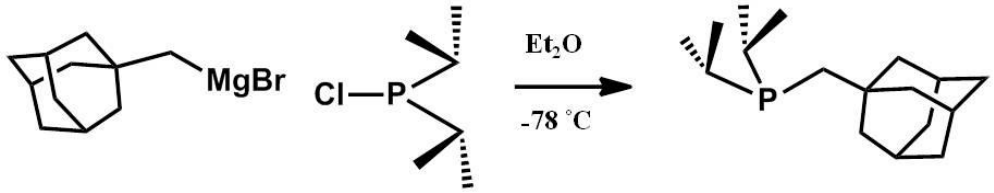

Scheme 1. 7. Synthesis of P(CH_2[1]Ad)(*i*-Pr)$_2$ from the addition of adamantylmethylene bromide to diisopropylchlorophosphine.

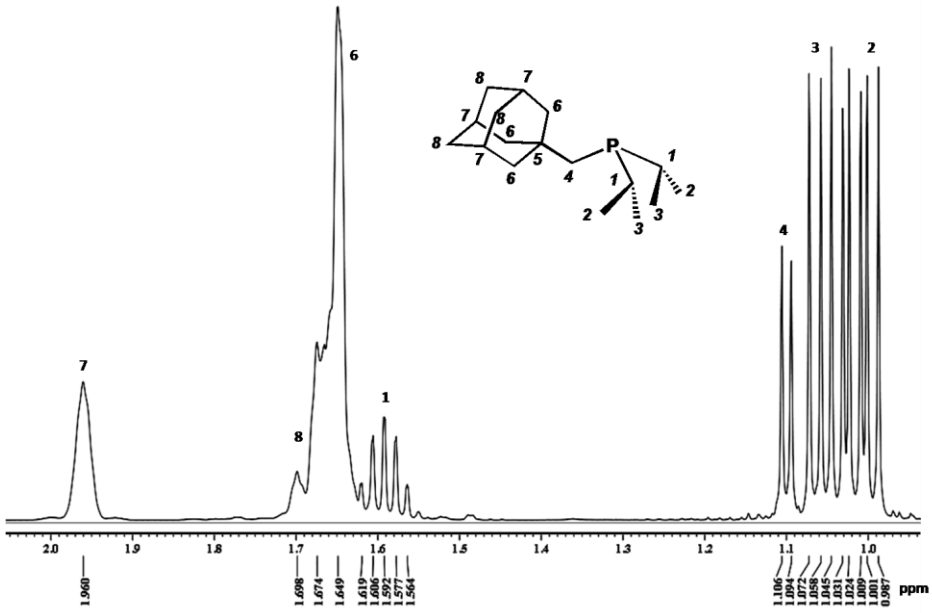

Figure 1. 4. 500 MHz ^{1}H NMR spectrum of L^{mAd} in C_6D_6 (20 °C).

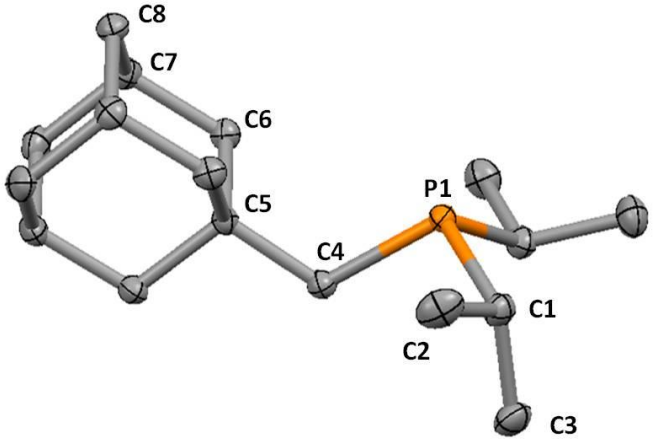

Figure 1. 5. X–ray Crystal structure of P(CH21Ad)(i-Pr)2. Hydrogens removed for clarity. Thermal ellipsoids are set to 30% probability.

1.4 Synthesis and Characterization of a Four–Coordinate Iridium(I) Monohydride

Treatment of a THF solution of $[IrCODCl]_2$ (COD = 1,5-cyclooctadience) with 1.0 equivalent of L^{mAd} generated Ir(COD)(Cl)(L^{mAd}) which was isolated and structurally characterized (Figure 1.6). The crystal structure shows the square planar geometry of the d^8 iridium(I) containing the general formula $ClIrL_3$ which mirrors that of Vaska's complex.

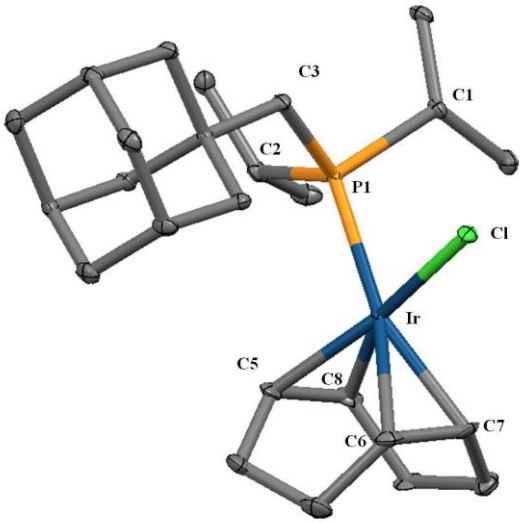

Figure 1. 6. X–ray crystal structure of complex (**1**) Ir(COD)(Cl)(L^{mAd}). Thermal ellipsoids set to 30% probability and hydrogen atoms were removed for clarity.

Treatment of a THF solution of Ir(COD)(Cl)(L^{mAd}) (**1**) with 1.0 equivalent of L^{mAd} at room temperature did not result in the binding of a second phosphine ligand. However, exposure of hydrogen gas to a mixture of Ir(COD)(Cl)(L^{mAd}) (**1**) and 1.0 equivalent of L^{mAd} results in the hydrogenation of COD to cyclooctane and the formation of $H_2Ir(Cl)(L^{mAd})_2$ (**2**) (Figure 1.7 and Figure 1.8).[68-70] Complex (**2**) is a 16–valence electron distorted square pyramid that lacks close contacts representative of an agostic interaction (closest contact Ir–H = 3.4 Å). This represents a rare example of an unsaturated, 5–coordinate iridium (III) complex that fails to engage in an agostic interaction but contains nearby sp^3 and sp^2 C–H bonds. The stability of this complex is likely from the chloride pi back donation ($Cl_{(lone\ pair)} \rightarrow Ir_{(d\text{-}orbital)}$).[71-73]

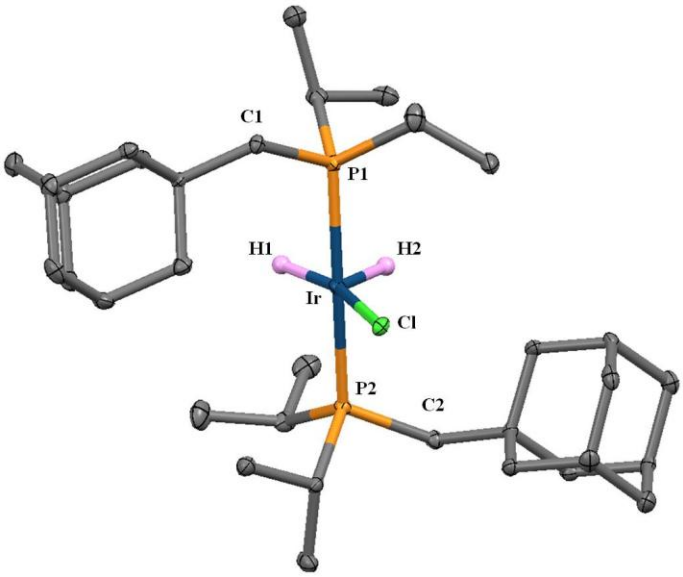

Figure 1. 7. X–ray crystal structure of complex (**2**) $H_2IrCl(L^{mAd})_2$. Thermal ellipsoids are set to 30% probability and hydrogen atoms on the ligand were removed for clarity.

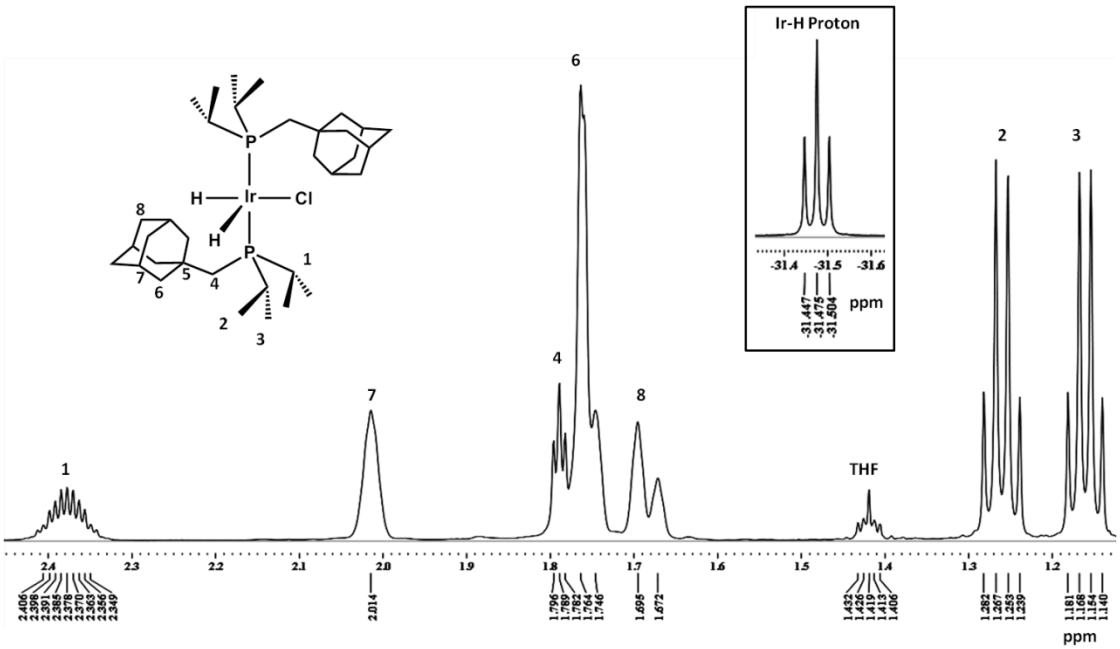

Figure 1. 8. 500 MHz ^{1}H NMR spectrum of $H_2IrCl(L^{mAd})_2$ (**2**) in C_6D_6 (20 ˚C).

Treatment of yellow complex $H_2IrCl(L^{mAd})_2$ (**2**) with 1.0 equivalent of PhMgBr in a thawing Et_2O solution under a nitrogen atmosphere furnished Vaska–type iridium(I) monohydride $HIr(N_2)(L^{mAd})_2$ (**3**) (Scheme 1.8). This complex was crystallized under a nitrogen atmosphere at –35 ˚C and characterized by ^{1}H and ^{31}P{^{1}H} NMR spectroscopy, IR

spectroscopy, and X–ray diffraction methods. Despite the difficulty involved in locating hydrogen atoms coordinated to heavy metals, the iridium hydride *trans* to N_2 was located in the electron density difference map of the X–ray crystal structure (Figure 1.9). The X–ray crystal structure of square planar complex (**3**) reveals proximal metal–proton distances of 2.710 Å and 2.729 Å. These distances are to both L^{mAd} γ-protons of the adamantyl cage and are slightly longer than what would be expected for an agostic interaction.[74]

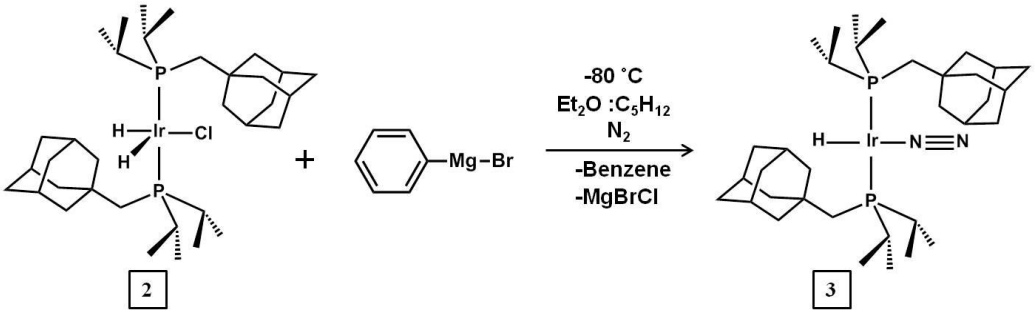

Scheme 1. 8. Synthesis of $HIr(N_2)(L^{mAd})_2$ (**3**) from $HIrCl(L^{mAd})_2$ (**2**).

It is important to note that we used C_6D_{12} to characterize monohydride complex (**3**) due to rapid decomposition or reactions with solvents, likely the result of facile C–H activation processes. The solvents that complex (**3**) were unstable in are C_6D_6, acetonitrile, chlorinated solvents, THF, and toluene. The ^1H NMR spectrum of complex (**3**) in C_6D_{12} displays a virtual triplet at –11 ppm ($^2J_{H–P}$ = 23 Hz) for the iridium–hydride resonance integrating to one proton (Figure 10).[75,76] The virtual triplet arises from the hydride coupling to the L^{mAd} phosphine ligand ($^{31}P\{^1H\}$ NMR δ = 30 ppm, 1H, vt, $^2J_{H–P}$ = 23 Hz). The small $^2J_{H–P}$ coupling constant (^2J < 50 Hz) supports both phosphines located *cis* to the hydride in a square planar geometry.

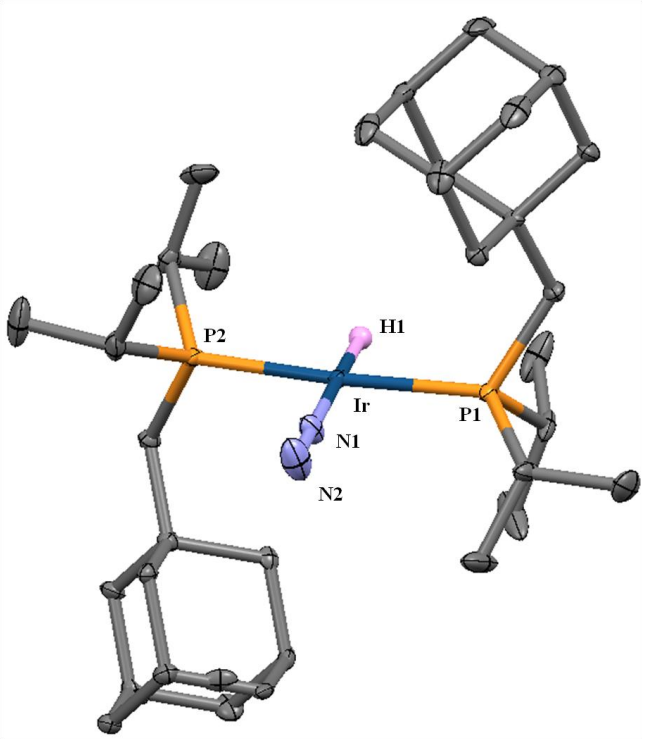

Figure 1. 9. Molecular structure of $HIr(N_2)(L^{mAd})_2$ (**3**) Selected bond distances (Å) and angles (°): Ir–H1 = 1.60(4). Ir–N1 = 1.934(2). Ir-P1 = 2.2944(6). Ir-P2 = 2.2889(6). N1–N2 = 1.108(4). P1–Ir-P2 = 168.89(2). N1–Ir–H1 = 179.3(14). P1–Ir–H1 = 83.5(13). P1–Ir–N1 = 95.90.

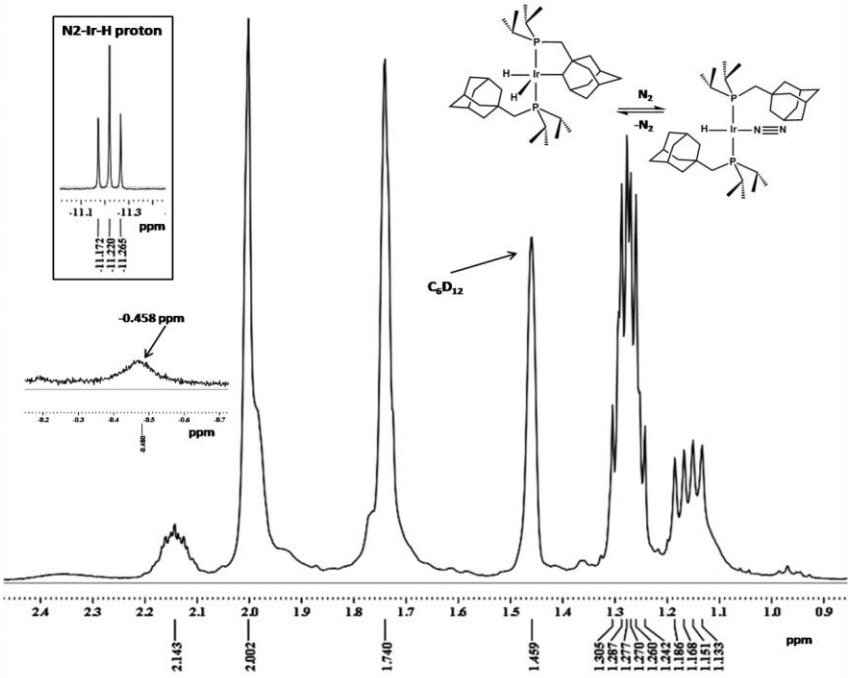

Figure 1. 10. 400 MHz ^{1}H NMR spectrum of $H_2Ir(N_2)(L^{mAd})_2$ (**3**) /$H_2Ir(\kappa^2$-*P*,*C*-$L^{mAd})(L^{mAd})$ (**4**) in C_6D_{12} (20 ˚C)

Solid–state FTIR analysis revealed two intense peaks at 2127 and 2057 cm^{-1} which are presumably the ν(Ir–H) and $\nu(N_2)$ stretching frequencies. Metal–hydride and metal–dinitrogen IR stretching frequencies exist over the range of 1900–2200 cm^{-1}, thus these two features could not be unambiguously assigned.[77-87] The inability to differentiate these features prompted us to attempt isotopic labeling experiments. The first isotopic labeling experiment was the synthesis of the monodeuteride complex $DIr(N_2)(L^{mAd})_2$. The FTIR spectroscopic features of the deutero–complex were essentially the same as the protio $HIr(N_2)(L^{mAd})$ (**3**). The use of ^2H NMR spectroscopy revealed the incorporation of deuterium into the ligand, thereby suggesting a facile ligand C–H activation process.

The second isotopic labeling experiment was performed with $^{15}N_2$ gas. FTIR spectroscopy did not provide evidence for the incorporation of $^{15}N_2$ (note that this complex was manipulated in an $^{14}N_2$ glove box for preparation of FTIR analysis). The spectroscopic features from the $^{15}N_2$ labeling experiment are identical to complex (**3**) $HIr(N_2)(L^{mAd})$ and do not show the expected shift of the ν(NN) band to lower energy upon ^{15}N labeling. One explanation would be that along with a C–H activation processes, there is also a highly labile N_2 ligand. We noticed a new complex, initially thought to be an impurity, in the $^{31}P\{^1H\}$ NMR when purified $HIr(N_2)(L^{mAd})$ (**3**) was analyzed in C_6D_6 or Et_2O. This new complex consists of approximately 40% of the phosphorus containing species in the $^{31}P\{^1H\}$ NMR in C_6D_6 at room temperature, and the percentage shifted in other solvents (C_5H_{12}, Et_2O). It was soon discovered that this new complex was in rapid equilibrium with complex $HIr(N_2)(L^{mAd})$ (**3**) (Figure 1.11 A) and can be sufficiently manipulated as the main product in solution from prolonged exposure to vacuum (Figure 1.11 B). When re–exposed to N_2 gas the equilibrium reestablishes with 40% of the phosphorus containing species being complex $HIr(N_2)(L^{mAd})$ (**3**) (Figure 1.11 C). The new complex was crystallized under an argon atmosphere and structurally characterized revealing a C–H activated iridacycle $H_2Ir(\kappa^2\text{-}P,C\text{–}L^{mAd})(L^{mAd})$ (**3**)

(Figure 1.12). Variable temperature NMR experiments reveal a 90% favorability towards $H_2Ir(N_2)(L^{mAd})_2$ (**3**) at lower temperatures, as surveyed by $^{31}P\{^1H\}$ NMR spectroscopy, correlating with the solubility of N_2 at low temperatures (Figure 1.13).[88,89]

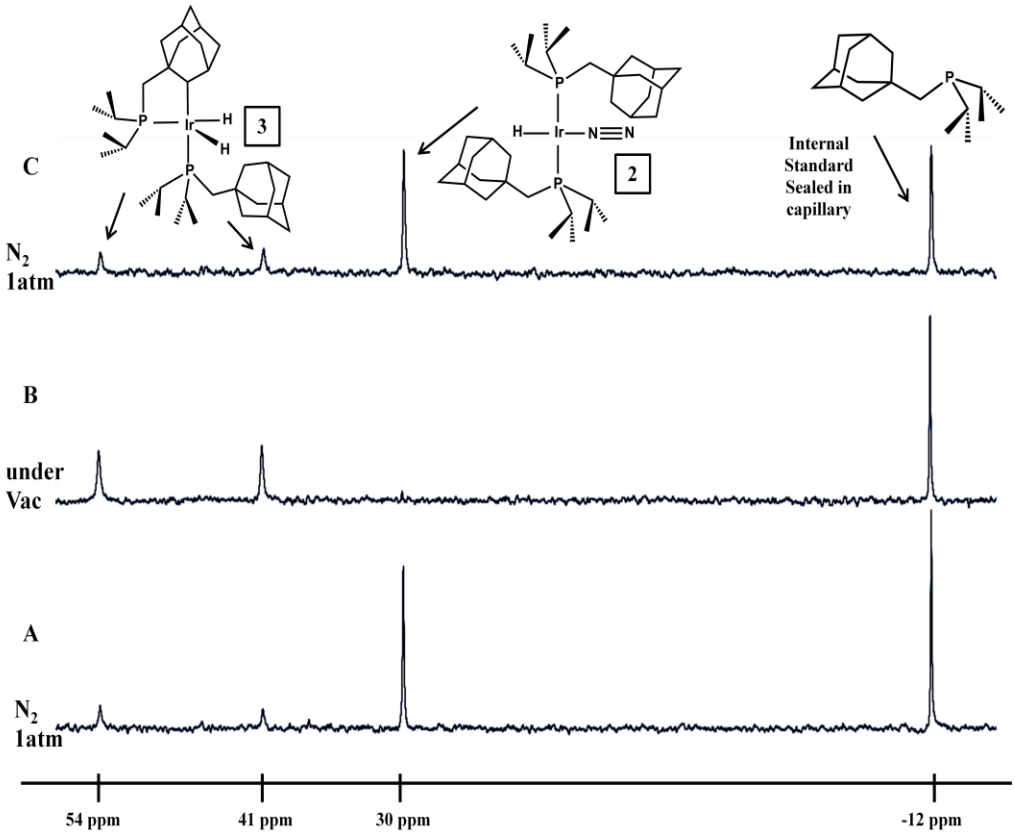

Figure 1. 11. $^{31}P\{^1H\}$ NMR data for sequential exposure of a $H_2Ir(N_2)(L^{mAd})_2$ (**3**) / $H_2Ir(\kappa^2$-*P*,*C*$L^{mAd})(L^{mAd})$ (**4**) mixture to N_2 and vacuum C_6D_{12} (20 °C). A) Initial spectrum of an equilibrium mixture of $H_2Ir(N_2)(L^{mAd})_2$ (**3**) / $H_2Ir(\kappa^2$-*P*,*C*$^{LmAd})(L^{mAd})$ (**4**) at 20 °C. B) Spectrum of identical sample in A after prolonged exposure to vacuum. Only $H_2Ir(\kappa^2$-*P*,*C*–$L^{mAd})(L^{mAd})$ (**4**) remains. C) Spectrum of identical sample in B after re–exposure to an N_2 atmosphere (20 °C). Re–exposure to N_2 re–establishes the equilibrium between $H_2Ir(N_2)(L^{mAd})_2$ (**3**) / $H_2Ir(\kappa^2$-*P*,*C*$L^{mAd})(L^{mAd})$ (**4**) .

The unsuccessful labeling experiments, which contributed to elucidating the intricate reactivity patterns, is due to a rapid equilibrium established between the four coordinate iridium monohydride $HIr(N_2)(L^{mAd})_2$ (**3**) and the five–coordinate neutral iridacycle di–hydride $H_2Ir(\kappa^2$-*P*,*C*-$L^{mAd})(L^{mAd})$ (**4**) (Figure 1.11). This equilibrium transfers the deuteride (^2H) to the ligand and the proton (^1H) to the metal due to the lower zero point energy difference of C–D bonds relative to C–H bonds.[90]

Furthermore, the lack of $^{15}N_2$ incorporation in complex (**3**) is from the significant lability of the N_2 ligand which is in direct opposition to other iridium(I) dinitrogen complexes.[91,92] We believe that N_2 either promotes coordinatively–induced C–H bond reductive elimination or efficiently traps the reactive monohydride intermediate. This equilibrium, to our knowledge, is the first example of a *reversible* process where an exogenous dinitrogen unit induces reductive elimination of a C–H bond (Scheme 1.9). [93]

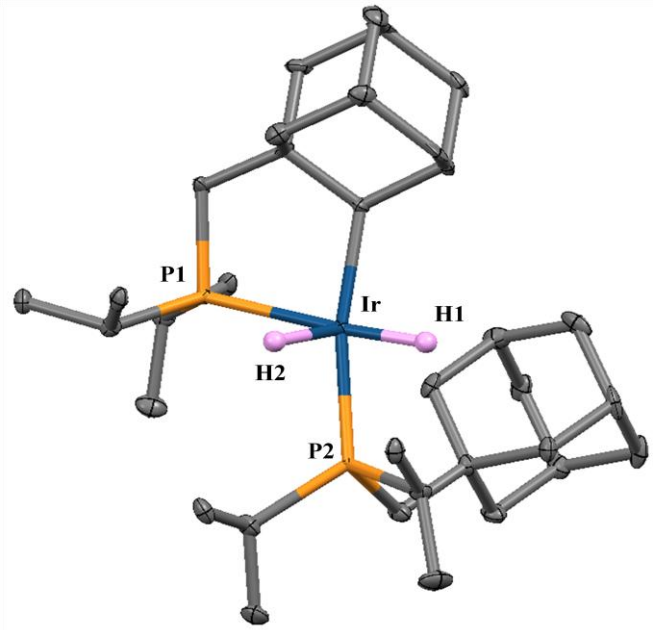

Figure 1. 12. Molecular Structure of $H_2Ir(\kappa^2\text{-}P,C\text{-}L^{mAd})(L^{mAd})$ (**3**). Selected bond distances (Å) and angles (°): C3–Ir = 2.135(6). P1–Ir = 2.3214(14). P2–Ir = 2.289(2). H1–Ir = 1.501(10). H2–Ir = 1.502(10). Ir–C3–C2 = 115.7(4). Ir–C3–C4 = 117.6(4). P1–Ir–C3 = 80.84(16). C3–Ir-P2 = 167.95(16). P1–Ir-P2 = 108.80(5). P1–Ir–H1 = 171(2). P1–Ir–H2 = 68(2).

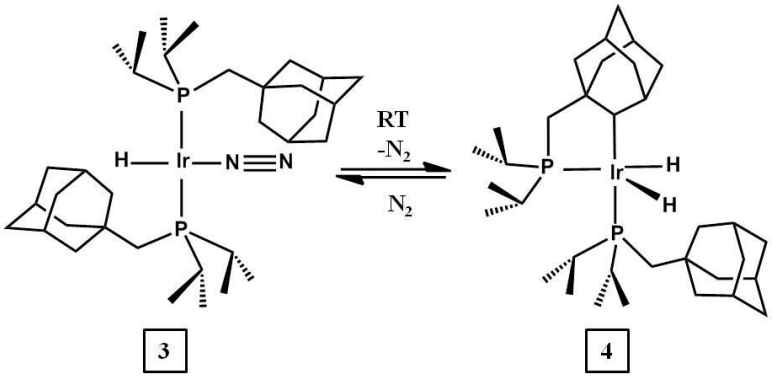

Scheme 1. 9. Rapid equilibrium between $HIr(N_2)(L^{mAd})_2$ **(3)** / $H_2Ir(\kappa^2\text{-}P,C\text{-}L^{mAd})(L^{mAd})$ (**4**).

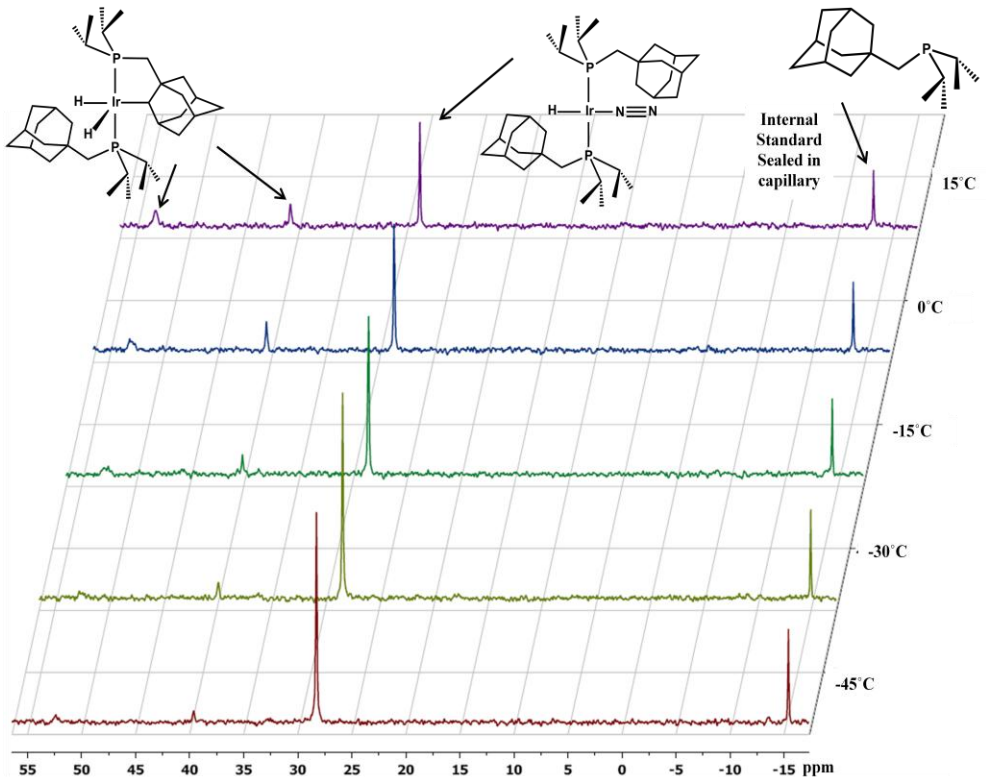

Figure 1. 13. Variable Temperature $^{31}P\{^{1}H\}f$ NMR data for $H_2Ir(N_2)(L^{mAd})_2$ **(3)** / $H_2Ir(\kappa^2\text{-}P,C^{LmAd})(L^{mAd})$ (**4**) equilibrium in C_6D_{12}.

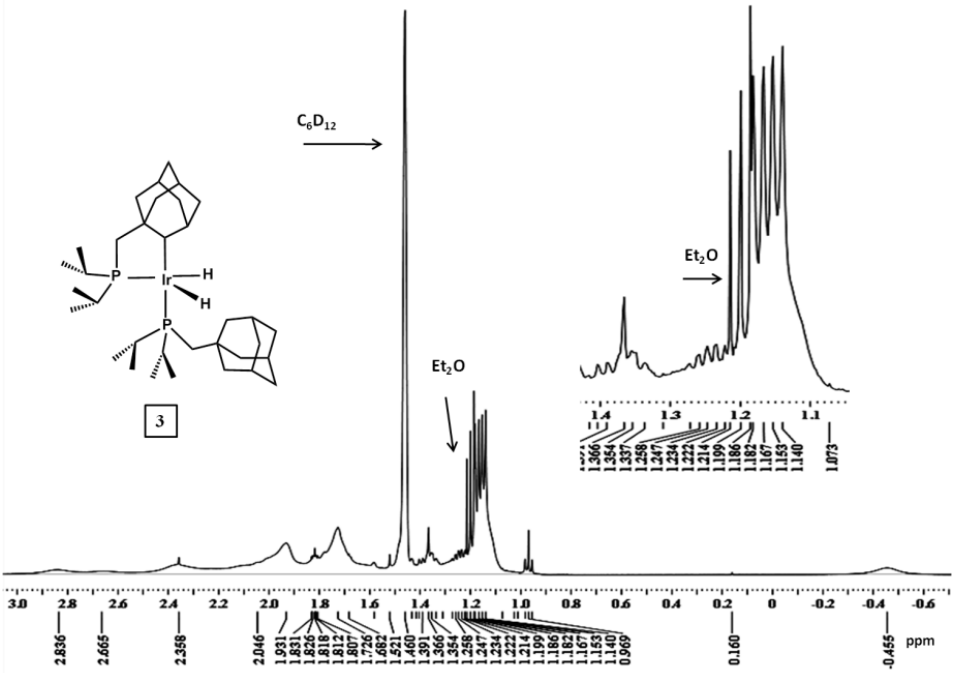

Figure 1. 14. 400 MHz ^{1}H NMR spectrum of $H_2Ir(\kappa^2\text{-}P,C\text{–}L^{mAd})(L^{mAd})$ (**4**) in C_6D_{12} (20 °C). The broadness is believed to result from rapid and reversible cyclometallation.

Because of the known difficulties in locating hydrogens from X–ray diffraction data[94-97] and the broad resonance features in the ^{1}H NMR (Figure 1.14) of complex (**3**) we wanted to confirm that complex HIr(N_2)(L^{mAd})$_2$ (**3**) was a monohydride and not a polyhydride. Synthetic access to the trihydride complex H_3Ir(L^{mAd})$_2$ (**5**) (^{31}P{^{1}H}NMR δ = 45 ppm (s), ^{1}H NMR δ = -16.13 ppm (t), ν(Ir–H) 1721 cm^{-1}) was accomplished by the addition of a thawing ether solution of Li[$HBEt_3$] to H_2IrCl(L^{mAd})$_2$ (**2**) (Scheme 1.10 and Figure 1.15).

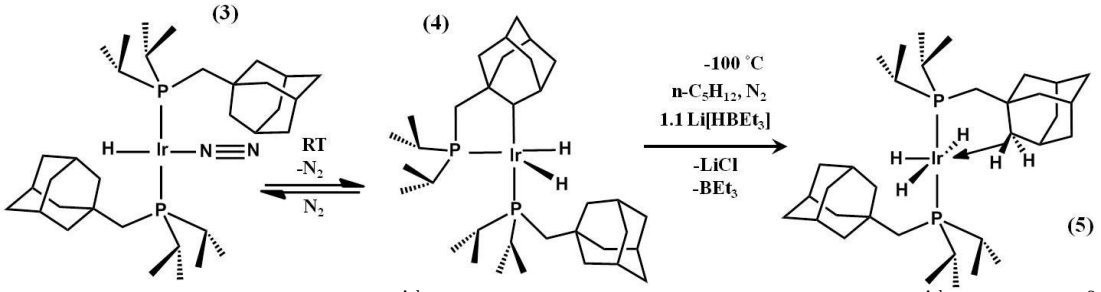

Scheme 1. 10. Synthesis of H_3Ir(L^{mAd})$_2$ (**5**) from the equilibrium mixture HIr(N_2)(L^{mAd})$_2$ (**3**) / H_2Ir(κ^2-*P*,*C*-L^{mAd})(L^{mAd}) (**4**).

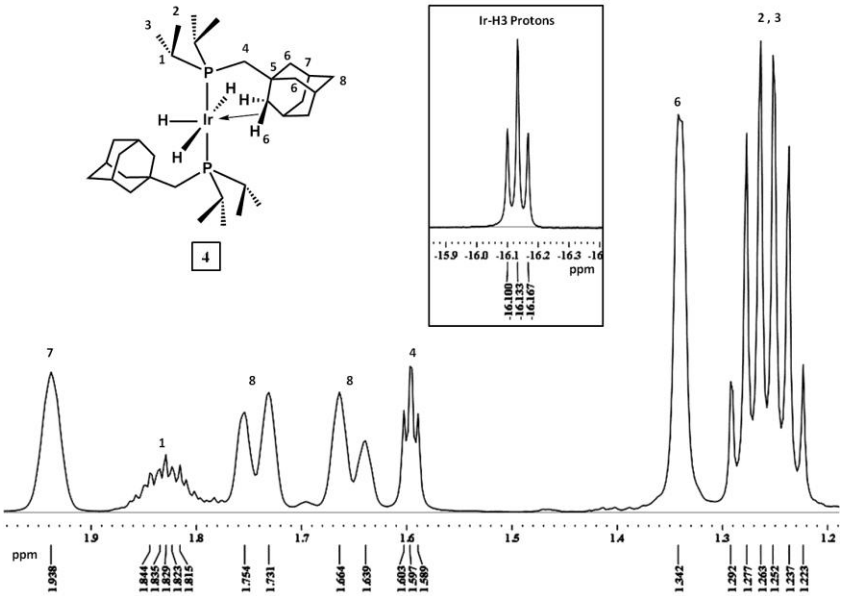

Figure 1. 15. 500 MHz ^{1}H NMR spectra of H_3Ir(L^{mAd})$_2$ (**4**) in C_6D_6 (20 °C).

The resulting tri–hydride complex (**5**) was structurally and spectroscopically distinct from the monohydride complex (**3**). A detailed examination of the X–ray crystal structure of

complex $H_3Ir(L^{mAd})_2$ (**5**) revealed close contacts from the γ-proton (of the adamantyl cage) to the iridium center, *d*(Ir–H20A) = 2.193 Å, *d*(Ir–C20) = 3.101 Å suggesting the presence of an agostic interaction. Further support for an agostic interaction was found from the comparison of spectroscopic signatures in the ^1H, ^{13}C {^1H} NMR spectrum of the trihydride complex (**5**) with other L^{mAd} complexes (Table 1.1), thereby suggesting a highly fluxional 2-Position of the adamantyl unit at 20 ˚C. This fluxionality seemingly blocks N_2 binding at pressures ranging from 1–4 atm (Figure 1.16).

Table 1.1. Comparative ^1H and ^{13}C NMR spectroscopic properties of hydido–Ir$(L^{mAd})_2$ complexes relevant to the agostic interaction in $H_3Ir(L^{mAd})_2$ (**5**) and $H_2Ir(OC_6F_5)(L^{mAd})_2$ (**10**).

Complex	^1H NMR Resonance of H6 Protons (ppm)	$^1J_{C–H}$ coupling constant of C6 Carbon atom (^{13}C NMR in Hz)
$H_3Ir(L^{mAd})_2$ (5)	**1.34**	**123**
$H_2IrCl(L^{mAd})_2$ (**2**)	1.76	127
$H_5Ir(L^{mAd})_2$ (7)	2.02	127
$H_2Ir(OH)(L^{mAd})_2$ (6)	2.08–2.04 (overlapping resonances)	126
$H_2Ir(OC_6F_5)(L^{mAd})_2$ (10)	**1.57**	**123**

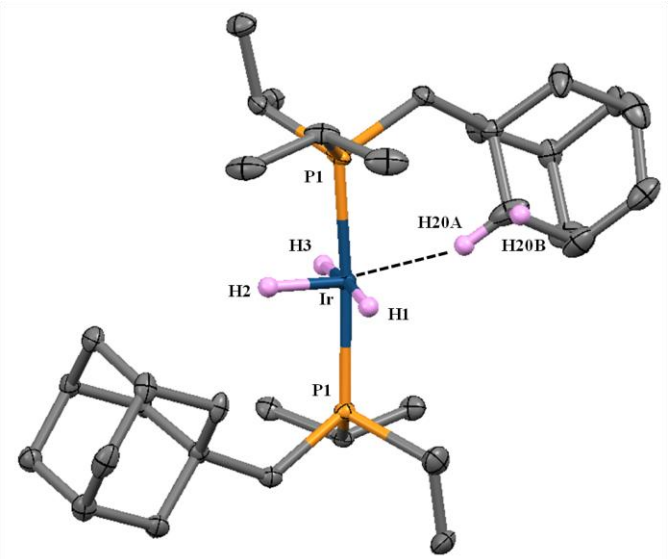

Figure 1. 16. Molecular Structure of $H_3Ir(L^{mAd})_2$ (**5**). Selected bond distances (Å) and angles (°): Ir–H1 = 1.55(2). Ir–H2 = 1.55(2). Ir–H3 = 1.55(2). Ir-P1 = 2.2550(15). Ir-P2 =2.3066(15). Ir–H20A= 2.193. Ir–C20 = 3.101. P1–Ir-P2 = 174.69(7). H1–Ir–H2 = 77(3). H1–Ir–H3 = 174(3). H2–Ir–H3= 103(3). Ir–H20A–C20 = 155.77

1.5 Reactivity Studies of an Iridium(I) Monohydrides

With the isolation of monohydride complex (**3**) we were interested to probe the reactivity towards substrates that would partake in oxidative addition reactions. In particular, we interested if the addition of H_2 would mirror that of Vaska's complex and if monohydride complex (**3**) would be capable of activating the O–H bond in water or alcohols. Even though there is an established equilibrium between complexes (**3**) and (**4**), the equilibrium mixture reacts cleanly with 1.0 equiv. of water in C_6H_6 at room temperature to produce a mononuclear $H_2Ir(OH)(L^{mAd})_2$ (**6**) complex with concomitant loss of N_2 (Scheme 1.11 and Figure 1.17). This is the first example, to our knowledge, of a dihydride–hydroxide complex, which is remarkable considering the abundance of low–valent, metal monohydrides that may be expected to induce O–H bond activation in water.

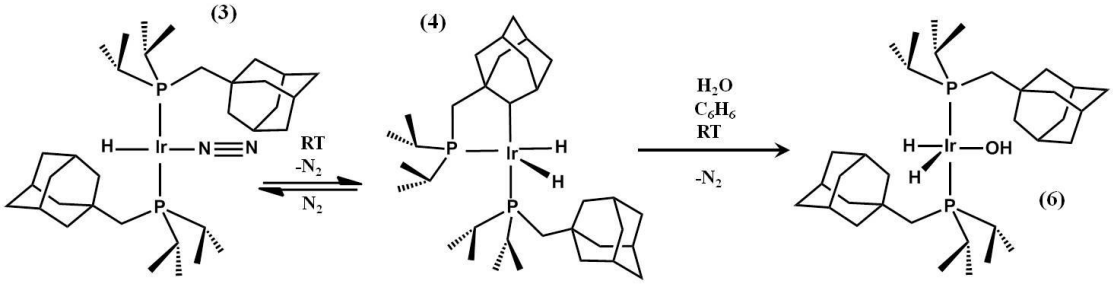

Scheme 1. 11. Synthesis of $H_2Ir(OH)(L^{mAd})_2$ (**6**) from the addition of water to $HIr(N_2)(L^{mAd})_2$ (**3**) / $H_2Ir(\kappa^2\text{-}P,C\text{–}L^{mAd})(L^{mAd})$ (**4**).

The oxidative addition of water to a single iridium metal center forming a hydride–hydroxide complex is limited to only a few examples.[98100] Milstein provided, in 1986, the first crystallographically characterized hydride-hydroxide complex *cis*-$HIr(OH)(PMe_3)_4{}^+PF_6{}^-$ synthesized from the addition of water to $[Ir(PMe_3)_4]^+[PF_6]^-$.[101] Bergman reported the oxidative addition of water to the unsaturated $Ru(PMe_3)_4$ complex producing a thermally unstable hydride-hydroxide $HRu(OH)(PMe_3)_4$ complex. Bergman also showed water activation by an analogous complex containing the heavier congener osmium. Several

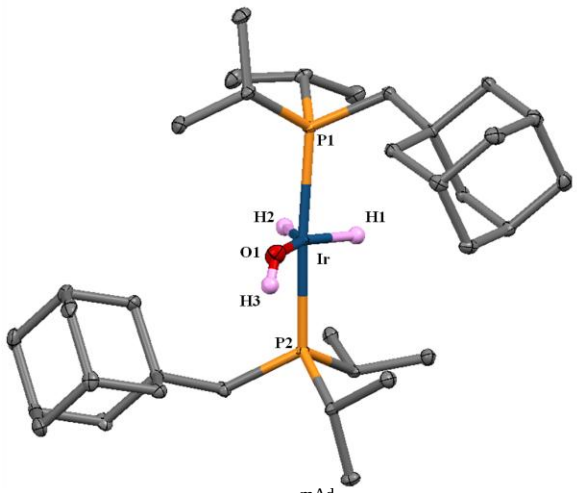

Figure 1. 17. Molecular Structure of $H_2Ir(OH)(L^{mAd})_2$ (**6**). Selected bond distances (Å) and angles (°):Ir–O1 =2.040(2). Ir-P1 = 2.2958(9). Ir-P2 = 2.2821(9). Ir–H1 = 1.553(10). Ir–H2 = 1.612(10). P1–Ir-P2 = 172.92(3). O1–Ir-P1 = 91.13(7). O1–Ir-P2 = 95.72(7). O1–Ir–H1 = 135.6. O1–Ir–H2 = 139.2. An agostic interaction between the Ir center and the L^{mAd} ligand is not observed in $H_2Ir(OH)(L^{mAd})_2$ (**6**).

rhodium hydride–hydroxide complexes were described by Gillard and co-workers, where the reduction of *trans*–$[(en)_2Rh(Cl)_2]^+$ in water lead to the formation of *trans*–$[(en)_2RhH(OH)]^+$. Although not formed by the oxidative addition of water, Potuznik and co-workers showed the addition of NaOH to $HRh(Cl)\{C_6H_3\text{-}2,6\text{-}(CH_2PBu^t_2)_2\}$ formed the hydride–hydroxide complex $HRh(OH)\{C_6H_3\text{-}2,6\text{-}(CH_2PBu^t_2)_2\}$. Jensen provided evidence for the oxidative addition of water to an iridium analogue of Potuznik's rhodium PCP pincer complex, forming $HIr(OH)\{C_6H_3\text{-}2,6\text{-}(CH_2PBu^t_2)_2\}$.[102] Otsuka and co–workers studied the oxidative addition of water to a $Pt(P(i\text{-}Pr)_3)_3$ complex yielding $HPt(OH)(P(i\text{-}Pr)_3)_2$ which readily decomposed in the absence of water.[103] Bercaw and co-workers observed the hydride-hydroxide complex $(H)Hf(OH)(Cp^*_2)$ formed from the addition of water to $H_2Hf(Cp^*_2)$ but describe the reaction as a protonolysis of the hydride instead of a base (H_2O) induced H_2 reductive elimination followed by the oxidative addition of an O–H bond from water.[98] Early metals have been shown to participate in the oxidative addition of water. Tyler and co-workers provided evidence for the low yielding synthesis of $HW(OH)(Cp^*_2)$ from the photolysis of $H_2W(Cp^*_2)$ in the presence of water.[104]

With the exception of Jensen's iridium PCP pincer complex HIr(OH){C_6H_3-2,6-($CH_2PBu^t_2$)$_2$} and Milstein's *cis* iridium hydride hydroxide complex *cis*-[HIr(OH)(PMe_3)$_4$]$^+$[PF_6]$^-$, the previously mentioned metal hydride hydroxide examples show thermal instability (either at room temperature or upon heating to 90 ˚C) with respect to the loss of H_2O or other decomposition pathways.[105,106] The dihydride–hydroxide complex H_2Ir(OH)(L^{mAd})$_2$ (**6**), shows remarkable stability in C_6D_6 solution at 90˚C for one week. Despite the thermal stability of complex (**6**), it reacts readily with 2.0 equiv. of H_2 gas undergoing rapid ejection of water and forming the pentahydride complex H_5Ir(L^{mAd})$_2$ (**7**) (Scheme 1.12 and Figure 1.18). All five hydride ligands are classical and possess a T1 = 988 ms (via non–linear saturation recovery).

Additionally, the pentahydride H_5Ir(L^{mAd})$_2$ complex (**7**) can also be formed from the monohydride complex (**3**) by the addition of 2.0 equivalents of H_2 gas to the equilibrium mixture of complexes (**3**) and (**4**), as assayed by NMR spectroscopy ($^{31}P\{^1H\}$ NMR δ = 14 ppm, ν(Ir–H)) 1966 cm^{-1}, ^{1}H NMR δ =10.30 (t, 5H, $^2J_{HP}$ = 12.5 Hz, T_1 = 988 ms (via non–linear saturation recovery)). Interestingly, the addition of 1.0 equivalent of H_2 gas to an equilibrium mixture of (**3**) / (**4**) produces a 1:1:2 mixture of HIr(N_2)(L^{mAd})$_2$ (**3**) / H_2Ir(κ^2-*P*,*C*–L^{mAd})(L^{mAd}) (**4**) to H_5Ir(L^{mAd})$_2$ (**7**) to H_3Ir(L^{mAd})$_2$ (**5**). This product ratio infers that complexes HIr(N_2)(L^{mAd})$_2$ (**3**) and H_2Ir(κ^2-*P*,*C*–L^{mAd})(L^{mAd}) (**4**) react at a similar rate with H_2 in C_6D_{12}.

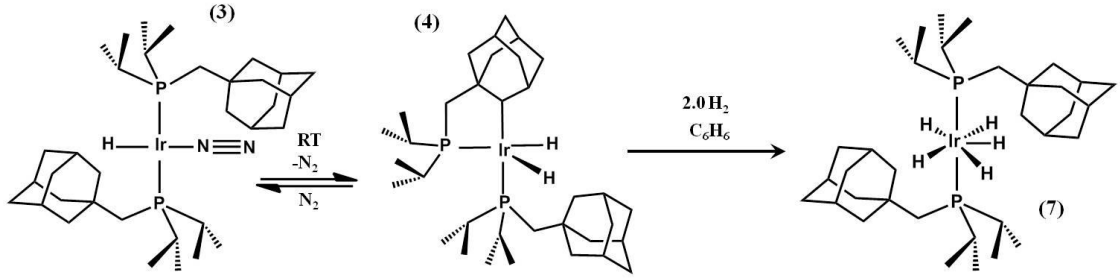

Scheme 1. 12. Synthesis of H_5Ir(L^{mAd})$_2$ (**7**) from the addition of H2 gas to the equilibrium mixture HIr(N_2)(L^{mAd})$_2$ (**3**) / H_2Ir(κ^2-*P*,*C*–L^{mAd})(L^{mAd}) (**4**).

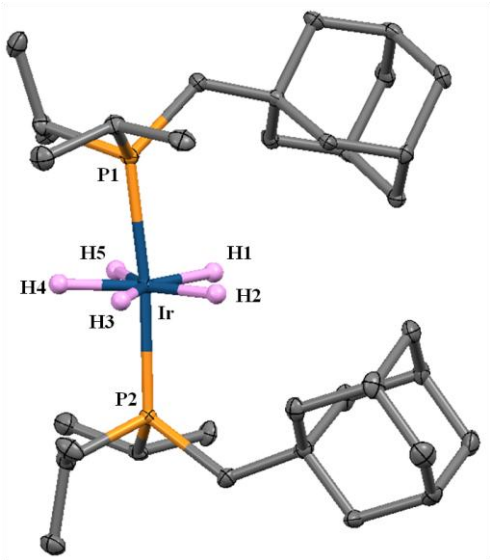

Figure 1. 18. Molecular Structure of $H_5Ir(L^{mAd})_2$ (**7**). Selected bond distances (Å) and angles (°): Ir–P1 = 2.332(2). Ir-P2 = 2.326(2). Ir–H1 = 1.5399(16). Ir–H2 = 1.540(2). Ir–H3 = 1.5399(15). Ir–H4= 1.5399(15). Ir–H5 = 1.5398(19). P1–Ir-P2 = 174.49(6). H1–Ir-P1 = 85.0(17). H1–Ir-P2 = 93.3(17).

The dihydride–hydroxide (**6**) is a rare example of an unsaturated 5–coordinate iridium complex that does not contain an agostic interaction, unlike the 5–coordinate complex $H_3Ir(L^{mAd})_2$ (**5**). We speculate this to be the result of oxygen pi-donation to the iridium center from the hydroxide ligand. Evidence for oxygen pi-donation is shown in the X–ray crystal structure by a shortened Ir–O bond length 2.038(2) Å, as compared to average Ir–O distances according to the CSD (average distance of an Ir–O bond, including examples with and without oxygen pi-bonding was 2.15 Å). An alternative route to access the iridium dihydride–hydroxide (**6**) was achieved by nucleophilic addition of OH^- from the addition of a NaOH slurry to $H_2IrCl(L^{mAd})_2$ (**2**) in THF, similar to the example by Potuznik.

To further explore the reactivity of the Vaska–type iridium(I) monohydride complex (**3**), we attempted deprotonation of the equilibrium mixture $HIr(N_2)(L^{mAd})_2$ (**3**) / $H_2Ir(\kappa_2\text{-}P,C\text{–}L^{mAd})(L^{mAd})$ (**4**) with a strong Brønsted base. Addition of *t*–butyl or *n*–butyl lithium to a solution of (**3**) / (**4**) yielded a cyclometallated iridium(I) anion $Li[HIr(\kappa^2\text{-}P,C\text{–}L^{mAd})(L^{mAd})]$ (**8**) (Scheme 1.13 and Figure 1.19). This is a second example of a four–coordinate iridium (I) monohydride, likely the result of either mechanism (i) nucleophilic addition of butyl anion to

complex (**4**), followed by C–H reductive elimination of butane or (ii) deprotonation of the Ir–H moiety by butyl anion to produce $[Ir(N_2)(L^{mAd})_2]^-$, followed by ligand C–H bond activation. Mechanistic support for nucleophilic addition of butyl anion to complex (**4**) with concomitant reductive elimination of butane was found from the analogous phosphinite system $P(O^1Ad)(i\text{-}Pr)_2$ (L^{oAd}; oAd = oxygen-1-adamantyl) (see Chapter 2). This observation is limited, as the phosphinite analogue to cyclometallated complex (**4**) is the only isolated species (no equilibrium exists with a 4–coordinate iridium(I) monohydride complex, see chapter 2).

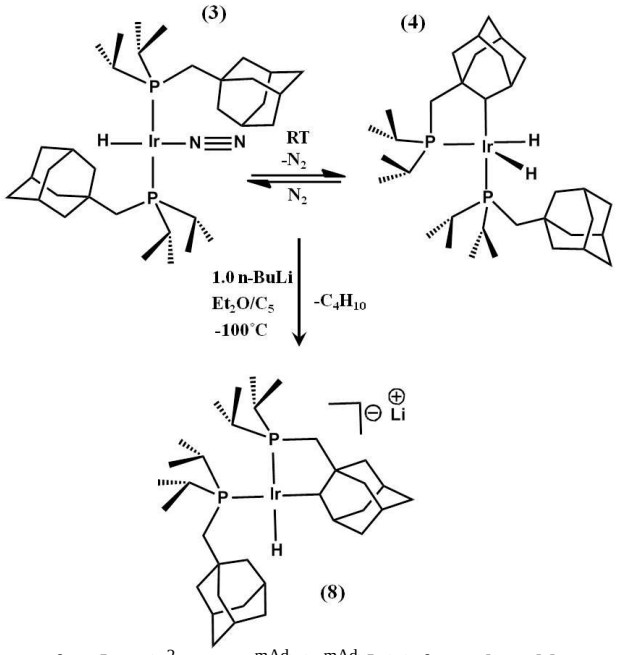

Scheme 1. 13. Formation of Li[HIr(κ^2-*P*,*C*–L^{mAd})(L^{mAd})] (**8**) from the addition of *n*–butyl lithium to the equilibrium mixture $HIr(N_2)(L^{mAd})_2$ (**3**) / $H_2Ir(\kappa_2$-*P*,*C*–L^{mAd})(L^{mAd}) (**4**).

Since the iridium(I) monohydride complex (**3**) is the major phosphorus containing species at low temperature (–50 ˚C) which were typical of reaction conditions, then we cannot rule out the potential generation of a putative d^{10} anion, $[Ir(N_2)(L^{mAd})_2]^-$ which would be expected to form from direct deprotonation. The proposed 3–coordinate (excluding agostic interactions) anion complex would be expected to readily C–H activate the adamantyl unit, thereby forming complex (**8**).

Crystallographic data reveals a contact ion-pair wherein the Li^+ ion interacts with both the Ir–C and Ir–H units. Addition of 2.0 equivalents of 12–crown–4 to (**8**) results in a slightly distorted square planar iridium(I) monohydride anion with a discrete lithium cation encapsulated by two crown ethers (**9**) (12-crown-4)$_2$Li[HIr(κ^2-*P*,*C*–L^{mAd})(L^{mAd})].

Reactivity studies involving protic reagents show the anionic monohydride (**9**) acts as a strong Brønsted base. Addition of either pentafluorophenol (C_6F_5OH) or 2,6–diisopropylaniline ($C_{12}H_{19}N$) quickly regenerates the equilibrium mixture (**3**) / (**4**) (Scheme 1.14). It is believed that the H–X units of these substrates are deprotonated by anionic complex (**9**) (12-crown-4)$_2$Li[HIr(κ^2-*P*,*C*–L^{mAd})(L^{mAd})] to produce the amide or phenoxide. NMR spectroscopy showed the fate of the deuterium from ^{2}H labeled 2,6–diisopropylaniline to reside on the L^{mAd} adamantyl γ–positions (Figure 1.20). The incorporation of deuterium results from a lower zero point energy to form the C–D bond as compared to the C–H bond.[107-110]

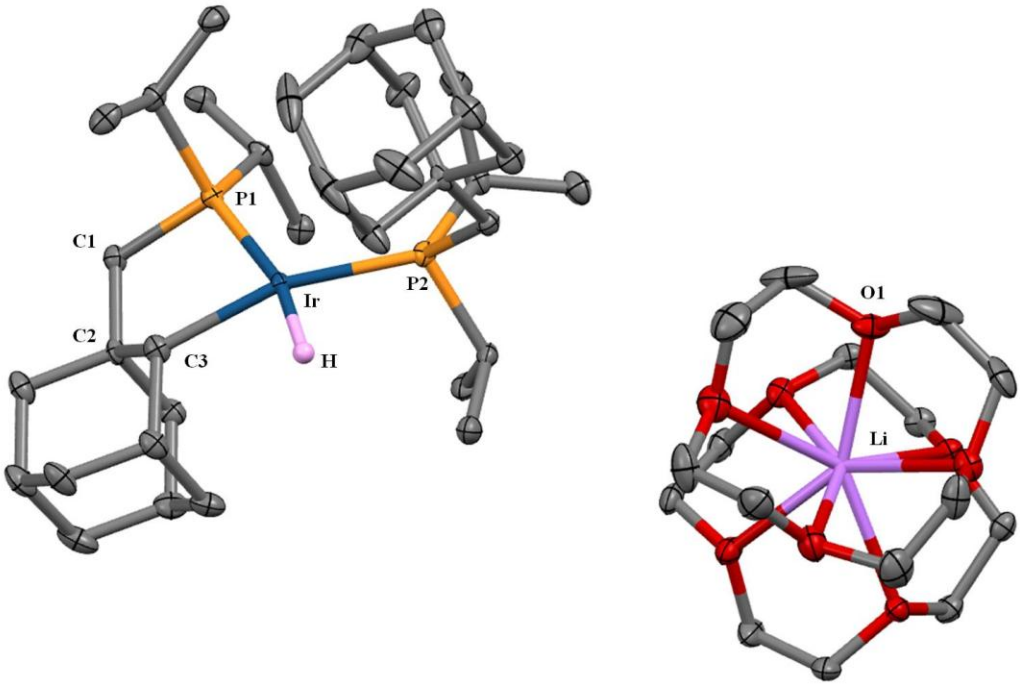

Figure 1. 19. X–ray crystal structure of Li[HIr(κ^2-*P*,*C*–L^{mAd})(L^{mAd})] (**9**). Hydrogen atoms removed for clarity. Thermal ellipsoids are set to 30% probability. Distance of iridium to lithium Ir–Li = 9.032 Å.

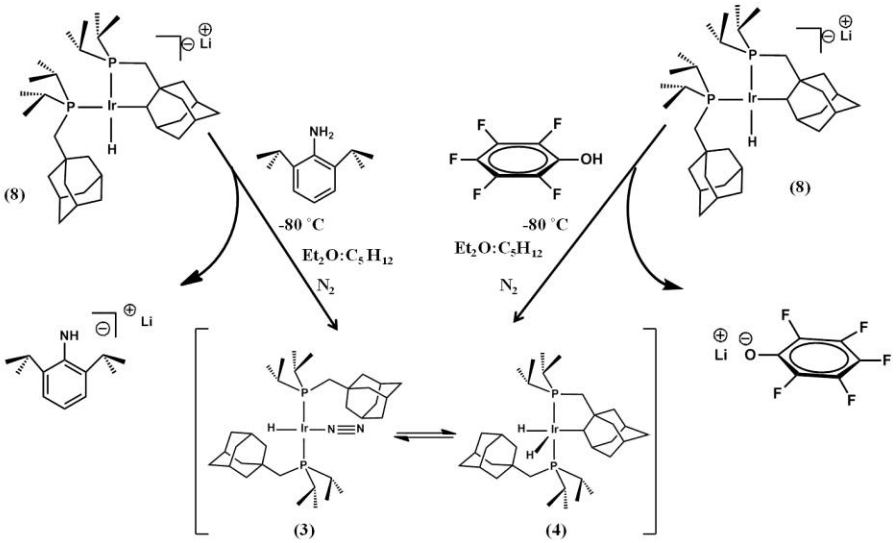

Scheme 1. 14. Reactivity of Li[HIr(κ^2-*P*,*C*–L^{mAd})(L^{mAd})] (**6**) with protic reagents aniline and pentafluorophenol.

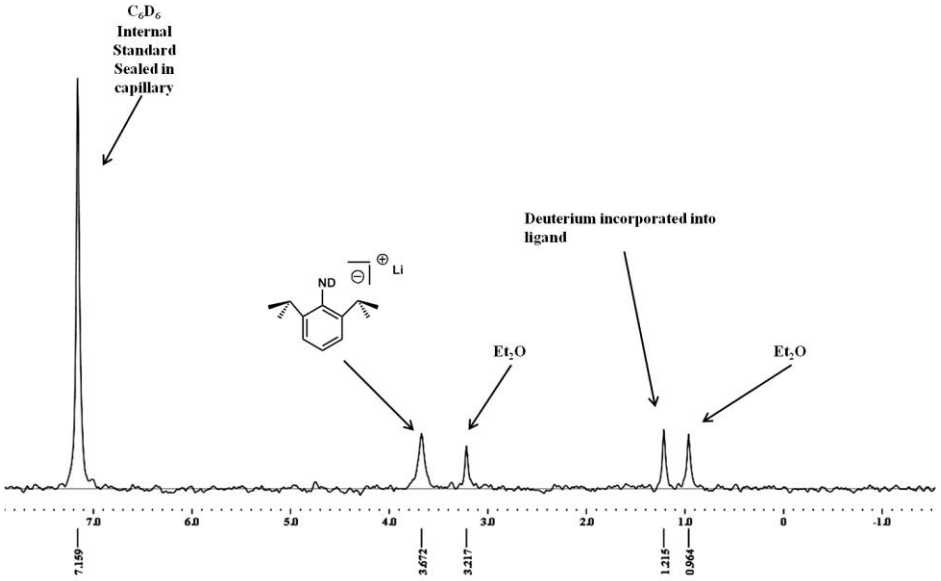

Figure 1. 20. ^{2}H NMR data for addition of D_2NDipp to [Li(12–c–4)2][HIr(κ^2-*P*,*C*–L^{mAd})(L^{mAd})] (**9**) in Et_2O (20 °C). The ^{2}H resonances for Et_2O were assigned by comparison to an authentic sample.

The addition of 2.0 equivalents of pentafluorophenol to (12-crown-4)$_2$Li[HIr(*κ*^{2}-*P*,*C*–L^{mAd})(L^{mAd})] (**9**) at room temperature cleanly provides the phenoxide bound adduct $H_2Ir(OC_6F_5)(L^{mAd})_2$ in a reaction mirroring that between $HIr(N_2)(L^{mAd})_2$ (**3**) with H_2O (Scheme 1.15). Interestingly, the crystal structure of $H_2Ir(OC_6F_5)(L^{mAd})_2$ (**10**) reveals an agostic interaction to the γ–proton located within the adamantyl cage (Figure 1.21) and contains an

elongated Ir–O bond distance of 2.181(3) Å as compared to complex $H_2Ir(OH)(L^{mAd})_2$ (**6**) Ir–O, 2.038(2) Å. This lack of oxygen pi-donation is likely the result from the five strongly electron withdrawing fluorine's on the phenyl ring thereby necessitating an agostic interaction to quench the Lewis acidity of the iridium center.

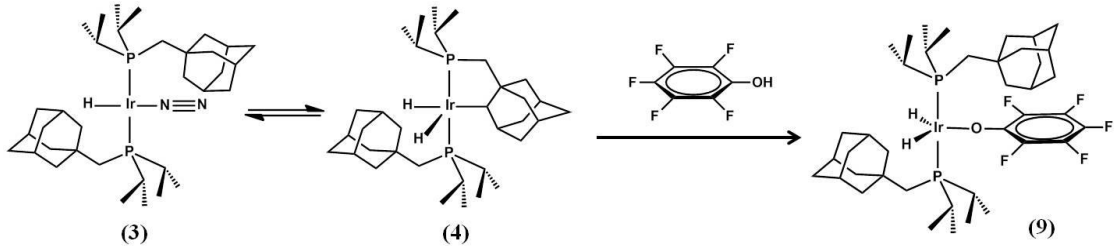

Scheme 1. 15. Synthesis of $HIr(OC_6F_5)(L^{mAd})_2$ (**10**) from the addition of 1.0 equivalent of C_6F_5OH to the equilibrium mixture $HIr(N_2)(L^{mAd})_2$ (**3**) / $H_2Ir(\kappa^2\text{-}P,C\text{–}L^{mAd})(L^{mAd})$ (**4**).

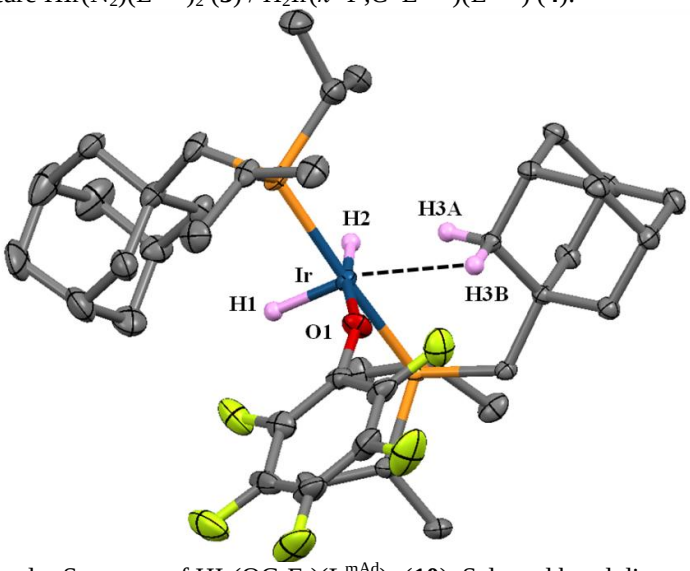

Figure 1. 21. Molecular Structure of $HIr(OC_6F_5)(L^{mAd})_2$ (**10**). Selected bond distances (Å) and angles (°): Ir–H3A = 2.091. Ir–C3 = 2.903. Ir–H3A–C3 = 137.98

1.6 Topological Studies of Highly Strained 5–Membered Iridacycles

An investigation of the structural topology of iridacycle (**4**) $H_2Ir(\kappa^2\text{-}P,C\text{–}L^{mAd})(L^{mAd})$ from X–ray diffraction data revealed several highly strained ring angles (Figure 1.22). The suggestion that angle strain plays a role in deterring intramolecular C–H bond activation was first put forth by Whitesides in cyclometallated platinum complexes.[65]

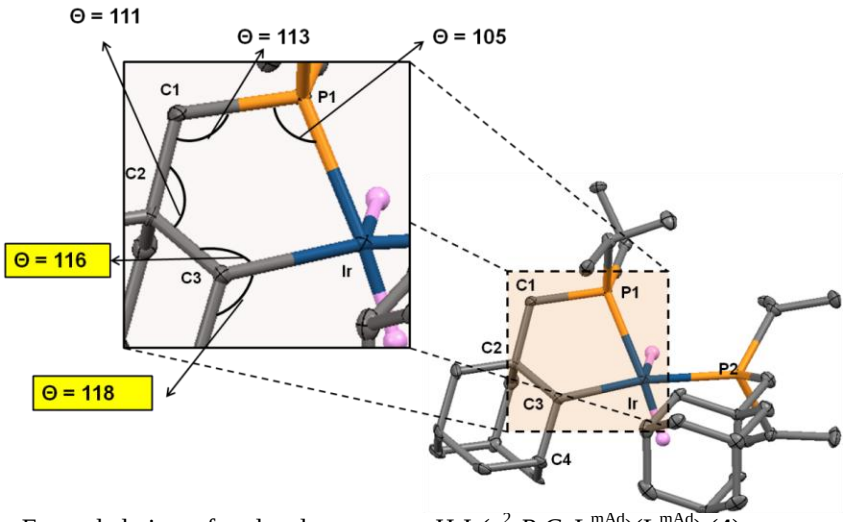

Figure 1. 22. Expanded view of molecular structure $H_2Ir(\kappa^2\text{-}P,C\text{–}L^{mAd})(L^{mAd})$ (**4**).

A Cambridge Structural Database (CSD) search was conducted for similar iridacycles to gauge the extent of strain in (**4**) $H_2Ir(\kappa^2\text{-}P,C\text{–}L^{mAd})(L^{mAd})$.[111] Specifically, the search that mimicked the general topology of $H_2Ir(\kappa^2\text{-}P,C\text{–}L^{mAd})(L^{mAd})$ with the following parameters: i) the metallacycle is a 5–membered ring, ii) the second ligating component of the ring is phosphorus and iii) the two substituents on the carbon atom coordinated to iridium are hydrogens (i.e. a methylene group, CH_2) (Figure 1.23). When criterion iii was constrained to alkyl groups (i.e. $(C(CR_3)_2)$ there were no resulting hits. A CSD inquiry for iii as a methylene group resulted in 9 hits. (CSD version 5.33, CCDC 2012 ConQuest version 1.14 (Build RC5), Nov. 2011) The parameters pertaining to angles of interest for all 9 iridacycles are compared in Table 1.2 with their corresponding CSD codes and references.

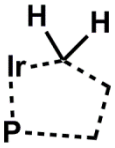

Figure 1. 23. CSD iridacycle search criteria with dashed lines representing "any bond".

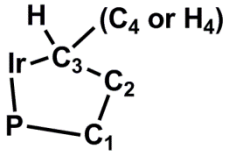

Figure 1. 24. Numerical assignments to iridacycle atoms under investigation.

Table 1.2. Comparison of iridacycle metrical parameters from the CSD search. The bolded CSD codes are complexes (**4**) and (**8**), respectively.

CSD code	C3–Ir-P	Ir-P–C1	P–C1–C2	C1–C2–C3	C2–C3–Ir	Ir–C3–(C4 or H4)	Ref.
DIPPAT	80.24	104.11	112.13	111.41	117.4	No H's	58
IBAZES	81.41	107.26	111.32	120.34	118.06	107	62
IBAZIW	82.39	106.34	111.63	120.41	117.46	107	62
IBAZOC	83.03	106.8	111.91	119.8	117.27	108	62
IBAZUI	81.94	107.10	111.10	120.29	118.31	107.71	62
IBINOX	77.60	100.76	110.93	117.16	110.01	109	60
IMESUP	83.12	102.85	105.91	109.59	113	109	63
LOMTUD	82.10	99.71	112.89	116.14	120.74	Amine	61
ZOPBOV10	77.83	113.19	110.84	110.17	120.40	107	59
ANAYUK	**80.93**	**104.38**	**112.68**	**110.98**	**115.98**	**118.07 (H–104)**	**42**
ANAZOF	**80.91**	**106.43**	**109.92**	**109.80**	**114.56**	**117.0**	**42**

The resulting CSD search provided a useful comparison of metrical parameters for all 9 different iridacycles with similar topology (Table 1.2 also includes CSD Refcodes and article references). The data from the table portrays a range of intra–ring angles for similar iridacycles, where four intra–ring angles Ir-P–C1, P–C1–C2, C1–C2–C3, C2–C3–Ir, (Table 1,columns 3–6), are 100°–120° and a fifth intra–ring angle, (Table 1, column 2), C3–Ir-P is 77°–83°. Complex $H_2Ir(\kappa^2\text{-}P,C\text{–}L^{mAd})(L^{mAd})$ (**4**) has all 5 intra–ring angles within the range of the other 9 examples, showing no indication of additional strain. This investigation exemplifies a perturbed exo–ring angle Ir–C3–C4, thus illustrating severe strain associated with the C3 carbon that connects to the rigid outer C4 carbon on the adamantyl ligand (see Figure 1.24 for numerical assignments to atoms**)**. The typical exo–ring angles Ir–C3–(C4 or H4) range from 104°–109° amongst all 9 CSD hits but for the isolated Vaska–type monohydride complexes $H_2Ir(\kappa^2\text{-}P,C\text{–}L^{mAd})(L^{mAd})$ (**4**) and $Li[HIr(\kappa^2\text{-}P,C\text{–}L^{mAd})(L^{mAd})]$ (**8)** they contain significantly expanded angles of 118˚ and 117˚, respectively (Bold entries in Table 1.2., Figure 1.22 for complex (**3**), and Figure 1.25 for complex (**8**)). We speculate the high degree of angle strain to destabilize the corresponding iridacycle $H_2Ir(\kappa^2\text{-}P,C\text{–}L^{mAd})(L^{mAd})$ and likely partakes in the driving force for allowing an exogenous dinitrogen ligand to invoke

C–H bond reductive elimination. The 9 examples from the CSD search have no mention of a reversible cyclometallation process, suggesting the ring strain in $H_2Ir(\kappa^2\text{-}P,C\text{–}L^{mAd})(L^{mAd})$ (**4**) does in fact destabilize the cyclometallated product. It should be noted that the hydrogen atoms on the ligated carbon in matallacycle complexes (**4**) and (**8**) were located from the electron density difference map. We are uncertain if the hydrogen atoms from the CSD examples were located from the electron density difference map or placed in idealized positions.[112] It is important to note that idealized positions are automatically generated with respect to a *connectivity array* from SHELXL and represent a reasonable and relaxed geometry about the ligated carbon.

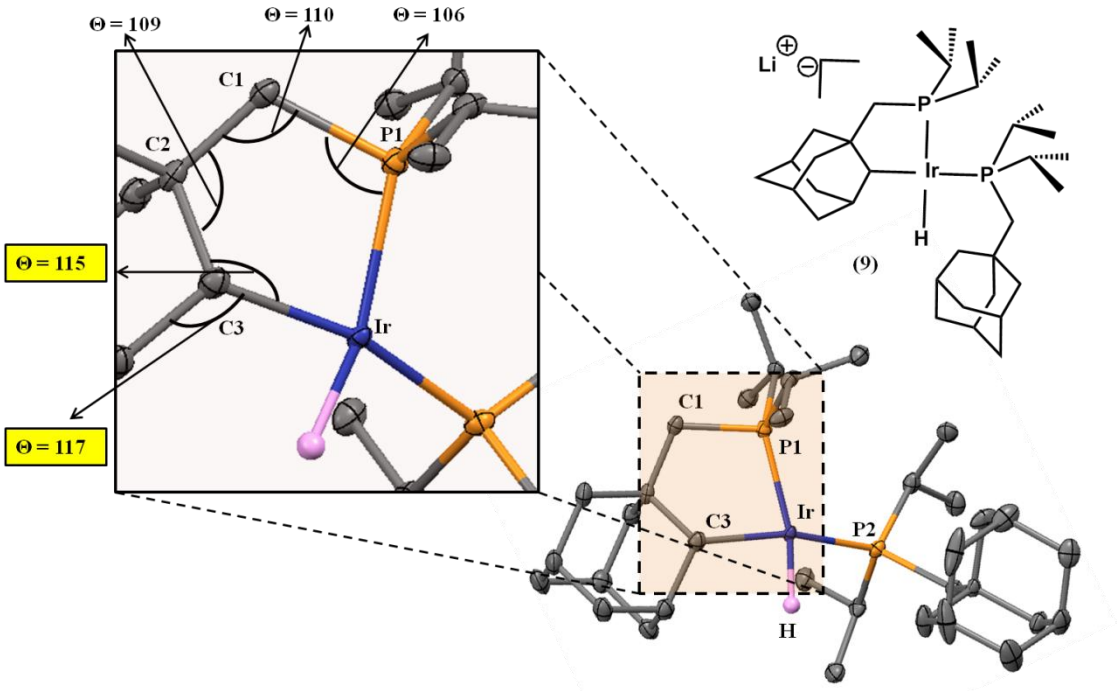

Figure 1. 25. Expanded view of 4–coordinate anionic iridium(I) monohydride $(12\text{-crown-}4)_2Li[H_2Ir(\kappa^2\text{-}P,C\text{–}L^{mAd})(L^{mAd})]$ (**9**). Thermal ellipsoids set to 30% probability. Hydrogen atoms attached to the phosphine ligand and the lithium cation were removed for clarity.

The topological examination from X–ray diffraction data of the 4–coordinate iridium (I) anion complex $(12\text{-crown-}4)_2Li[HIr(\kappa^2\text{-}P,C\text{–}L^{mAd})(L^{mAd})]$ (**9**) reveals similar exo–ring iridacycle strain, as compared to the 5–coordinate neutral iridacycle $H_2Ir(\kappa^2\text{-}P,C\text{–}L^{mAd})(L^{mAd})$ (**4**). The anionic complex $Li[HIr(\kappa^2\text{-}P,C\text{–}L^{mAd})(L^{mAd})]$ (**9**) contains an intra–ring angle Ir–C3–

C2 of 115˚ and a slightly less strained exo–ring angle Ir–C3–C4 of 117˚. However, there is no sufficient spectroscopic evidence for an equilibrium established between complex (**9**) and a putative d^{10} 3–coordinate anion $[Ir(N_2)(L^{mAd})_2]^-$.

1.7 Reactivity Studies of an Anionic Iridium(I) Monohydride

We were interested if anionic complex (12-crown-4)$_2$Li[HIr(κ^2-*P*,*C*–L^{mAd})(L^{mAd})] (**9**) could function as a source of the putative 2-coordinate bis-phosphine anion (Scheme 1.16). In this context, we added substrates to complex (**9**) to determine if a 2–coordinate bis–phosphine anion was accessible, thereby mirroring the isolobal Pd (0) and Pt (0) phosphine complexes, $Pd(PPh_3)_3$, $Pt(SO_2)(PCy_3)_2$.[2]

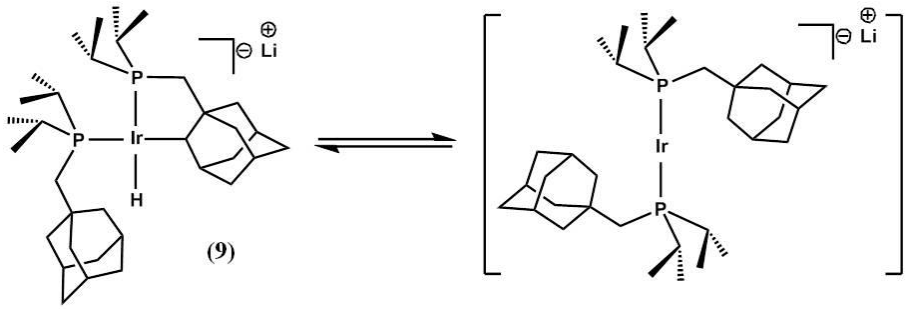

Scheme 1. 16. The formation of a putative 2–coordinate Ir (–I) anion complex from ligand C–H bond reductive elimination of complex (12-crown-4)$_2$Li[HIr(κ^2-*P*,*C*–L^{mAd})(L^{mAd})] (**9**).

The addition of a THF solution of carbamide peroxide to anionic complex (**9**) produces a 6-coordinate amidate stabilized iridium (III) complex $H_2Ir(\kappa^2$-N,*O*–$H_2NCONH)(L^{mAd})_2$ (**10**) which features a triplet integrating to two protons at δ = -29.2 ppm ($^2J_{H-P}$ = 17.26 Hz) (Scheme 1.17, Figure 1.26 and Figure 1.27). We view this reaction as a protonation event and propose that following the protonation of iridium (either by oxidative addition of peroxide or direct protonation) is ligand C–H bond reductive elimination, ejection of lithium peroxide (^{6}Li and ^{7}Li NMR spectroscopy was inconclusive) and finally, urea N–H bond oxidative addition. This reaction is reproducible but we do find it surprising that there is no oxidation by peroxide. Mirroring the reactivity of iridium(I) monohydride complex $HIr(N_2)(L^{mAd})_2$ (**3**), urea is readily ejected upon protonation by the addition of water producing

dihydride/hydroxide complex $H_2Ir(OH)(L^{mAd})_2$ (**6**) featuring a triplet at δ = -29.2 ppm ($^2J_{HP}$ = 15.3 Hz).

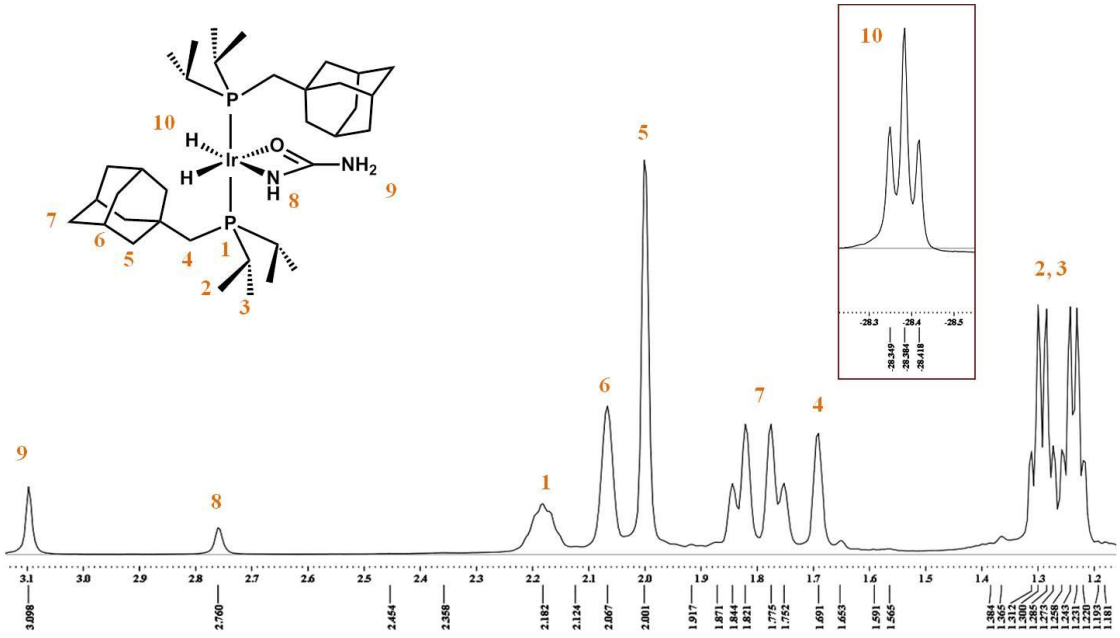

Figure 1. 26. ^{1}H NMR of complex $H_2Ir(\kappa^2\text{-N,}O\text{–}H_2NCONH)(L^{mAd})_2$ (**10**).

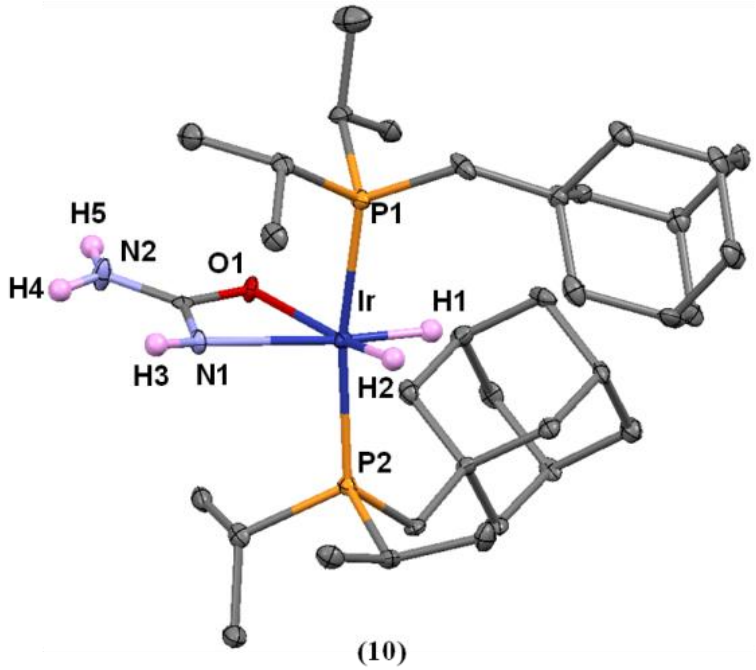

(10)

Figure 1. 27. Crystal structure of amidate complex (**11**) $H_2Ir(\kappa^2\text{-N,}O\text{–}H_2NCONH)(L^{mAd})_2$. Thermal ellipsoids are set to 30% probability. Hydrogen atoms on the phoshine ligands were removed for clarity.

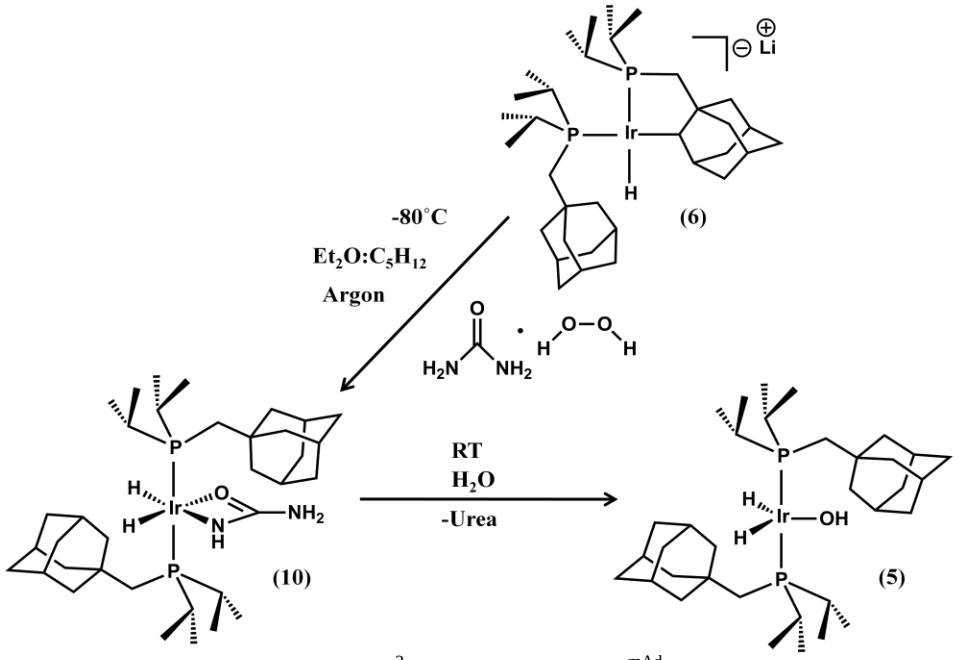

Scheme 1. 17. Synthesis of (**11**) $H_2Ir(\kappa^2\text{-N},O\text{–}H_2NCONH)(L^{mAd})_2$ from the addition of carbamide peroxide to anionic complex (**9**) $(12\text{-crown-4})_2Li[HIr(\kappa^2\text{-P},C\text{–}L^{mAd})(L^{mAd})]$.

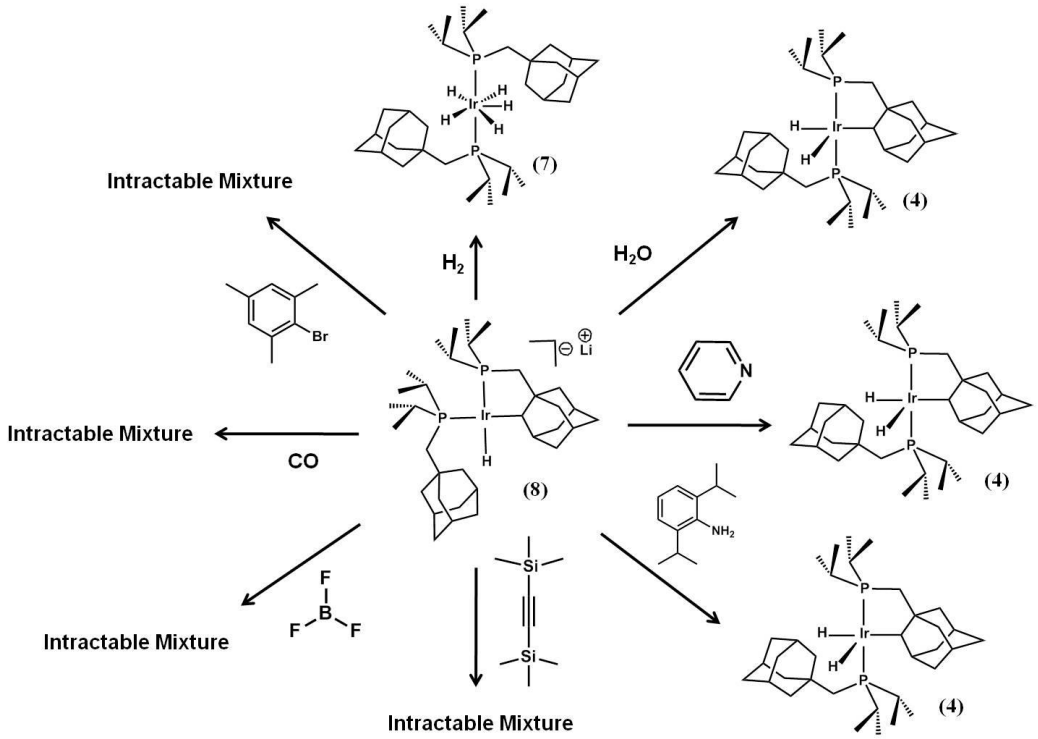

Scheme 1. 18. Reactivity pinwheel of anionic complex $(12\text{-crown-4})_2Li[HIr(\kappa^2\text{-}P,C\text{–}L^{mAd})(L^{mAd})]$ (**9**) with a variety of substrates.

Further efforts to map reactivity patterns of anionic complex (12-crown-4)$_2$Li[HIr(κ^2-*P,C*–L^{mAd})(L^{mAd})] (**9**) under an argon atmosphere resulted in, (i) a protonation event with accompanied formation of neutral iridacycle complex H$_2$Ir(κ^2-P,*C*–L^{mAd})(L^{mAd}) (**4**) or (ii) formation of an intractable mixture (Scheme 1.18). We speculate the lack of synthetic control to be from electron transfer, oxidation, or radical events; the result of an overabundance of electron density at the unsaturated anionic iridium metal center.

1.8 Conclusions

Herein we report the isolation and full characterization of a Vaska type iridium(I) monohydride complex (**3**) HIr(N$_2$)(L^{mAd})$_2$, containing to the formula HIrL$_3$. The isolation of monohydride complex (**3**) was achieved by the judicious use of the sterically encumbering phosphine ligand P(CH$_2$^{1}Ad)(*i*-Pr)$_2$(L^{mAd}). Reactivity studies of complex (**3**) HIr(N$_2$)(L^{mAd})$_2$ revealed its ability to activate an array of small molecules including: H$_2$, N$_2$, H$_2$O, pentafluorophenol (C$_6$F$_5$OH). Noteworthy, is the activation of water by the equilibrium mixture HIr(N$_2$)(L^{mAd})$_2$ (**3**) / H$_2$Ir(κ^2-*P,C*–L^{mAd})(L^{mAd}) (**4**) forming a unique dihydride/hydroxide complex HIr(OH)(L^{mAd})$_2$ (**6**). Support that monohydride complex (**3**) is not a polyhydride was found by synthetic access to the 5–coordinate trihydride complex H$_3$Ir(L^{mAd})$_2$ (**5**), which possesses an agostic interaction. The addition of 2.0 equivalents of H$_2$ gas to HIr(N$_2$)(L^{mAd})$_2$ (**3**) or 1.0 equivalent to H$_3$Ir(L^{mAd})$_2$ (**5**) formed a classical iridium penta–hydride complex H$_5$Ir(L^{mAd})$_2$. The rapid deprotonation of HIr(N$_2$)(L^{mAd})$_2$ (**3**) by the addition of strong Brønstead bases (*t*–butyl and *n*–butyl lithium) produces the anionic monohydride Li[HIr(κ^2-*P,C*–L^{mAd})(L^{mAd})] (**8**). Topological studies revealed severe ring strain within the ligand C–H activated 5–coordinate complex (**4**) and anionic 4–coordinate complex (**8**). This ring strain, imposed from the rigid adamantyl cage, may provide the thermodynamic driving force to deter ligand C–H bond activation, thereby allowing for the isolation of not only the

first isolable Vaska–type iridium(I) monohydride complex (**3**) $HIr(N_2)(L^{mAd})_2$ but also the second example, complex (**9**) (12-crown-4)$_2$Li[$HIr(\kappa^2$-*P*,*C*–$L^{mAd})(L^{mAd})$]. Reactivity studies on anionic monohydride complex (**9**) resulted in several intractable mixtures likely from an overabundance of electron density at the iridium metal center.

1.9 Synthetic Procedures

General Considerations. All manipulations were carried out under an atmosphere of dry dinitrogen or argon using standard Schlenk and glovebox techniques. Solvents were dried and deoxygenated according to standard procedures. Unless otherwise stated, reagent grade starting materials were purchased from commercial sources and used as received. 1–Adamantylbromomethane ($^1AdCH_2Br$) was prepared as previously described. [64] Isotopically labeled di–isopropylaniline $D_2N(2,6–(i\text{-}Pr)_2C_6H_3)$ (D_2NDipp) was prepared by allowing an Et_2O solution of H_2NDipp to stir with an excess of D_2O for 5 h, followed isolation and distillation under static vacuum. Benzene–d_6 and cyclohexane–d_{12} (Cambridge Isotope Laboratories) were degassed and stored over 4 Å molecular sieves for 2 d prior to use. Celite 405 (Fisher Scientific) was dried under vacuum (24 h) at a temperature above 250 ˚C and stored in the glovebox prior to use. KBr (FTIR grade from Aldrich) was stirred overnight in anhydrous THF, filtered and dried under vacuum (24 h) at a temperature above 250 ˚C prior to use.

Solution ^1H, $^{13}C\{^1H\}$, ^{13}C, $^{31}P\{^1H\}$, ^2H and $^{19}F\{^1H\}$ NMR spectra were recorded on Varian Mercury 300 and 400 spectrometers, a Varian X–Sens500 spectrometer or a JEOL ECA–500 spectrometer. ^1H and $^{13}C\{^1H\}$ chemical shifts are reported in ppm relative to $SiMe_4$ (^1H and ^{13}C δ = 0.0 ppm) and referenced to residual solvent resonances of 7.16 ppm (^1H) and 128.3 ppm (^{13}C) for benzene–d_6, 1.46 (^1H) and 26.43 (^{13}C) ppm for cyclohexane–d_{12} . $^{31}P\{^1H\}$ NMR spectra were referenced externally to 85% aqueous H_3PO_4 (δ = 0.0 ppm). $^{19}F\{^1H\}$ NMR spectra were referenced externally to neat trifluoroacetic acid, $F_3CC(O)OH$ (δ = –78.5 ppm vs.

$CFCl_3$ = 0.0 ppm). FTIR spectra were recorded on a Thermo–Nicolet iS10 FTIR spectrometer. Samples were prepared as either KBr pellets, Nujol Mulls or as C_6H_{12} solutions injected into a ThermoFisher solution cell equipped with KBr windows. For solution FTIR spectra, solvent peaks were digitally subtracted from all spectra by comparison with an authentic spectrum obtained immediately prior to that of the sample. Combustion analyses were performed by Robertson Microlit Laboratories of Madison, NJ (USA).

Synthesis of $AdCH_2MgBr$. Modifications to a published procedure were employed.[64] Step 1: Preparation of Rieke Magnesium: In a 350 mL thick–walled ampoule, a mixture of $MgCl_2$ (5.713 g, 60.0 mmol), KI (2.990 g, 18.0 mmol, 0.30 equiv) and freshly cut K metal (4.691 g, 120.0 mmol, 2.0 equiv) in 200 mL of THF was prepared. The mixture was then placed under partial vacuum and heated at 90 ˚C under vigorous stirring for 3 h. *Caution*! Activated (Rieke) magnesium prepared by this method is extremely pyrophoric.[113] The resulting black–colored mixture was then allowed to cool to room temperature. In the glovebox, the activated magnesium was collected using a filter paper–lined ceramic Buchner funnel and then dried *in vacuo* for 1 h. Step 2: Preparation of Methyleneadamantylmagnesium Bromide: The magnesium prepared above was slurried in Et_2O (400 mL) and a cold (*ca.* –60 ˚C) Et_2O solution of $^1AdCH_2Br$ (5 g, 21.82 mmol, 80 mL, 0.36 equiv vs. $MgCl_2$) was added via canula transfer over the course of 0.5 h. The resulting mixture was allowed to stir for 40 min and then filtered through Celite with a coarse porosity sintered glass frit. An H_2O quench of an aliquot of the colorless filtrate under an N_2 atmosphere indicated complete consumption of $^1AdCH_2Br$ and formation of 1–methyladamantane and 1,2–diadmantylethane in a 90:10 ratio (^1H NMR and GCMS). For stoichiometry purposes however, the filtrate was assumed to contain a 75% yield of $^1AdCH_2MgBr$ for use in subsequent steps.

Synthesis of $P(CH_2{}^1Ad)(i\text{-}Pr)_2$ (L^{mAd}). The Et_2O solution containing $^1AdCH_2MgBr$ prepared above was cooled to –78 ˚C and an equally cold Et_2O solution of $ClP(i\text{-}Pr)_2$ (2.5 g, 16.4 mmol,

0.75 equiv, 80 mL) was added via cannula over 1 h. The reaction mixture was allowed to stir for 8 h while gradually warming to room temperature. Over this period, the formation of a colorless precipitate was observed. The Et_2O was then evaporated under reduced pressure, and a small amount of unreacted $ClP(i\text{-}Pr)_2$ was removed via vacuum distillation (65 ˚C, ~20–50 mm/Hg). The resulting residue was extracted with *n*-Pentane (150 mL), filtered through Celite and evaporated to dryness again under reduced pressure. Dissolution of the resultant residue in Et_2O (30 mL), followed by storage at –35 ˚C for 1 d selectively precipitated out a small amount of 1–methyladamantane byproduct, which was filtered off. Reduction of the filtrate to a volume of 20 mL, followed by storage at –35 ˚C produced colorless crystals of $P(CH_2{}^1Ad)(i\text{-}Pr)_2$, which were dried and collected. Yield: 2.52 g, 9.46 mmol, 43%. ^{1}H NMR (500.1 MHz, C_6D_6, 20 °C): δ = 1.96 (bs, 3H, *H7*) 1.66 (m, 6H, *H8*), 1.65 (m, 6H, *H6*), 1.59 (sept, 2H, $^3J_{HH}$ = 7 Hz, $^2J_{HP}$ = 0.5 Hz, *H1*), 1.10 (d, 2H, $^2J_{HP}$ = 6 Hz, *H4*), 1.05 (dd, 6H, $^3J_{HH}$ = 7 Hz, $^3J_{HP}$ = 11 Hz, *H2* or *H3*), 1.01 (dd, 6H, $^3J_{HH}$ = 7 Hz, $^3J_{PH}$ = 11 Hz, , *H2* or *H3*). ^{13}C{^{1}H} NMR (125.7 MHz, C_6D_6, 20 °C, Resonances assigned using ^{1}H–^{13}C (HSQC): δ = 44.3 (d, $^3J_{CP}$ = 9 Hz, *C6*), 37.6 (d, $^1J_{CP}$ = 23 Hz, *C4*), 37.3 (s, *C8*), 32.3 (d, $^2J_{CP}$ = 16 Hz, *C5*), 29.4 (s, *C7*), 24.0 (d, $^2J_{CP}$ = 14 Hz, *C1*), 20.3 (d, $^1J_{CP}$ = 16 Hz, *C2* or *C3*), 19.0 (d, $^2J_{CP}$ = 11 Hz, *C2* or *C3*). ^{31}P{^{1}H} NMR (161.9 MHz, C_6D_6, 20 °C): δ = –12.5 (s) ppm. FTIR (KBr Pellet): 2959, 2945, 2908, 2844, 1450, 1359, 1097, 878, 642 cm^{-1}. Anal Calcd. for $C_{17}H_{31}P$: C, 76.64; H, 11.73. Found: C, 75.59; H, 11.48.

Synthesis of $H_2IrCl(L^{mAd})_2$ (2). In a Teflon–capped, thick–walled ampoule, a THF solution of $[IrCl(COD)]_2$ (1.466 g, 2.18 mmol, 100 mL) was added to a THF solution of L^{mAd} (2.325 g, 8.73 mmol, 4.0 equiv, 50 mL). The solution was subjected to two freeze-Pump–thaw cycles and then H_2 (1 atm) was introduced into the vessel. The reaction mixture stirred for 1 hour followed by another freeze-Pump–thaw cycle and re–introduction of H_2 (1 atm). The mixture was then allowed to stir vigorously for 13 h with intermittent manual shaking. All volatile

materials were removed *in vacuo* and the resulting residue was extracted with Et_2O (200 mL), filtered and stored at –35 ˚C to yield yellow crystals, which were collected and dried. Yield: 1.82 g, 2.39 mmol, 56%. ^{1}H NMR (400.1 MHz, C_6D_6, 20 ˚C): δ = 2.37 (d of sept, 4H, *H1*), 2.01 (bs, 6H, *H7*), 1.79 (vt, 4H, *J* = 4 Hz, *H4*), 1.76 (m, 12H, *H6*), 1.72 (m(quartet), 12H, *H8*), 1.26 (d of vt, 12H, $^3J_{HH} \approx J_{HP}$ = 8 Hz, *H2* or *H3*), 1.17 (d of vt, 12H, $^3J_{HH} \approx J_{HP}$ = 6 Hz, *H2* or *H3*), –31.5 (t, 2H, $^2J_{HP}$ = 14 Hz, Ir(*H*)$_2$) ppm. ^{13}C{^{1}H} NMR (125.7 MHz, C_6D_6, 20 ˚C): δ = 45.4 (s, *C6*), 40.3 (t, J_{CP} = 11 Hz, *C4*), 37.0 (s, *C8*), 34.5 (s, *C5*), 29.6 (s, *C7*), 26.7 (t, J_{CP} = 15 Hz, *C1*), 20.6 (s, *C2* or *C3*), 19.4 (s, *C2* or *C3*) ppm. ^{31}P{^{1}H} NMR (161.9 MHz, C_6D_6, 20 ˚C): δ = 37.5 (t, $^2J_{PH}$ = 14 Hz (coupling is observed because ^{1}H resonance is outside decoupling window) ppm. FTIR (KBr pellet): ν(IrH) 2286, 2221 and 2165 cm^{-1} also 2956, 2899, 2845, 1459, 1383, 1100, 1043, 825, 655 cm^{-1}. Anal Calcd. for $C_{34}H_{64}ClIrP_2$: C, 53.56; H, 8.46. Found: C, 53.83; H, 8.36.

Synthesis of HIr(N$_2$)(L^{mAd})$_2$ (3). To a cold (–45 ˚C) 80:20 Et_2O/*n*-Pentane mixture of $H_2IrCl(L^{mAd})_2$ (0.505 g, 0.663 mmol, 80 mL total) was added a cold (–78 ˚C) Et_2O solution of C_6H_5MgBr (0.120 g, 0.663 mmol, 1.0 equiv, 60 mL total) over the course of 25 min. The reaction mixture was allowed to warm to room temperature and stirred for an additional 2 h. All volatile materials were then removed *in vacuo*. The resulting residue was then extracted into *n*-Pentane (2 x 8 mL), filtered through Celite and evaporated again to dryness. Dissolution of the resulting solid in an *n*-Pentane/Et_2O mixture (4:1, 10 mL total), followed by storage at –35 °C resulted in orange crystals, which were collected and dried *in vacuo*. Yield: 0.103 g, 0.136 mmol, 21%. ^{1}H NMR (400.1 MHz, C_6D_{12}, 20 ˚C): δ = 2.14 (d of sept, 4H, P(C*H*(CH$_3$)$_2$)$_2$), 2.00 (m, 18H, *^{1}Ad*), 1.74 (m, 12H, *^{1}Ad*), 1.27 (d of vt, 24H, P(CH(C*H*$_3$)$_2$)$_2$), –11.2 (t, 1H, $^1J_{HP}$ = 23 Hz, Ir–*H*) ppm. ^{13}C{^{1}H} NMR (100.6 MHz, C_6D_6, 20 ˚C): δ = 45.1 (*C6*), 38.6 (t, J_{CP} =12 Hz, *C4*), 37.2 (s, *C8*), 32.8 (s, *C5*), 29.4 (*C7*), 27.4 (t, J_{CP} = 15 Hz, *C1*), 20.6 (*C2* or *C3*), 19.7 (*C2* or *C3*) ppm. ^{31}P{^{1}H} NMR (121.5 MHz, C_6D_{12}, 20 ˚C): δ = 29.8 (s) ppm.

FTIR (KBr Pellet): □(IrH) and □(NN) 2129 and 2057 cm^{-1} also 2956, 2897, 2845, 1459, 1246, 1100, 1040, 823, 654 cm^{-1}. Anal. Calcd. For $C_{34}H_{63}N_2IrP_2$: C, 54.16; H, 8.42. Found: C, 53.96; H, 8.29.

Synthesis and Isolation of $H_2Ir(\kappa^2$-*P,C*–$L^{mAd})(L^{mAd})$ (4). In a Teflon–capped ampoule, a C_6D_{12} solution of $HIr(N_2)(L^{mAd})_2$ (0.130 g, 0.172 mmol, 15 mL) was subjected to three freeze-Pump–thaw cycles, heated at 30 ˚C for 10 min and then subjected to two additional freeze-Pump–thaw cycles. This process resulted in a color change of the sample from orange to light yellow. All volatile materials were then removed under reduced pressure. The resulting solid was then introduced to an argon atmosphere, washed with *n*-Pentane (3 x 2 mL) and dried again *in vacuo*. Dissolution of the resulting residue in Et_2O (2 mL) and storage at –35 ˚C under argon resulted in light yellow crystals, which were collected and dried *in vacuo*. Yield: 0.084 g, 0.116 mmol, 66%. ^{1}H NMR (500.1 MHz, C_6D_{12}, 20 ˚C): δ = 2.84 (bs, Ad), 2.66 (bs, Ad), 2.36 (bs, Ad), 1.93 (bs, Ad or C*H*$(CH_3)_2$), 1.73 (bs, Ad), 1.17 (dd, CH(C*H*$_3)_2$), 1.15 (dd, CH(C*H*$_3)_2$), –0.455 (bs, 1H, Ir–*H*),–32.4 (bs, 1H, Ir–*H*) ppm. We believe the broadness of the ^{1}H resonances for this complex is due to rapid and reversible cyclometallation of both L^{mAd} ligands. ^{13}C{^{1}H} NMR (125.7 MHz, C_6D_{12}, 20 ˚C): δ = 48.1 (b), 44.1 (b), 38.0 (b), 32.2–30.4 (several peaks), 20.8 (b) ppm. ^{31}P{^{1}H} NMR (161.9 MHz, C_6D_{12}, 20 ˚C): δ = 53.6 (bs) and 40.9 (bs) ppm. FTIR (KBr Pellet): ν(CH–agostic) 2287 (m) cm^{-1}, ν(IrH) 2012 (s) cm^{-1} also 2922, 2853, 2732, 1452, 1360, 1241, 1027, 643 cm^{-1}. Anal. Calcd. for $C_{34}H_{63}IrP_2$: C, 56.25; H, 8.75. Found: C, 56.52; H, 8.55 (performed under argon).

Synthesis of $H_3Ir(L^{mAd})_2$ (5). To a thawing 1:1 *n*-pentane/Et_2O mixture of $H_2IrCl(L^{mAd})_2$ (0.130 g, 0.171 mmol, 5 mL) was added a thawing Et_2O solution of $Li[HBEt_3]$ (0.018 g, 0.171 mmol, 2 mL, 1.0 equiv). The reaction mixture was stirred for 45 min while warming to room temperature. The reaction mixture was then filtered and all volatiles were removed under reduced pressure. Dissolution of the resulting solid in Et_2O (5 mL), followed by filtration and

storage at –35 °C resulted in yellow crystals, which were collected and dried *in vacuo*. Yield: 0.102 g, 0.140 mmol, 82%. ^{1}H NMR (400.1 MHz, C_6D_6, 20 ˚C): δ = 1.94 (bs, 6H, *H7*), 1.83 (d of sept, 4H, *H1*), 1.70 (m(quartet), 12H, *H8*), 1.60 (t, 4H, $^{2}J_{HP}$ = 3 Hz, *H4*), 1.34 (m, 12H, *H6*), 1.26 (dd of vt, 24H, *H2* and *H3*),–16.13 (t, 3H, $^{2}J_{HP}$ = 17 Hz, Ir–*H*) ppm. ^{13}C{^{1}H} NMR (125.7 MHz, C_6D_6, 20 ˚C): δ = 42.4 (s, *C6*), 41.8 (t, J_{CP} = 11 Hz, *C4*), 36.9 (s, *C8*), 34.9 (s, *C5*), 29.6 (s, *C6*), 28.5 (t, J_{CP} = 16 Hz, *C1*), 19.9 (*C2* and *C3*) ppm. ^{31}P{^{1}H} NMR (161.9 MHz, C_6D_6, 20 ˚C): δ = 46 (s) ppm. FTIR (KBr Pellet): ν(CH–agostic) 2312 (m) cm^{-1}, ν(IrH) 1721 (vs) cm^{-1} also 2972, 2952, 2907, 2893, 2868, 2845, 1452, 1360, 1241, 1027, 643 cm^{-1}. Anal. Calcd. for $C_{34}H_{65}IrP_2$: C, 56.09; H, 9.00. Found: C, 55.89; H, 8.90.

Synthesis of $H_2Ir(OH)(L^{mAd})_2$ (6). Method A – from $HIr(N_2)(L^{mAd})_2$: A C_6D_6 solution of $HIr(N_2)(L^{mAd})_2$ (0.010 g, 0.013 mmol, 0.4 mL) in a J. Young NMR tube was subjected to three freeze-Pump–thaw cycles. A C_6D_6 solution of H_2O (0.004 g, 0.022 mmol, 400 μL, 1.65 equiv, in 0.2 mL of C_6D_6) was then vacuum transferred into the NMR tube. ^{1}H NMR analysis of the reaction mixture *ca*. 10 min after addition revealed exclusive production of $H_2Ir(OH)(L^{mAd})_2$. Method B – from $H_2IrCl(L^{mAd})_2$. To a THF solution of $H_2IrCl(L^{mAd})_2$ (0.255 g, 0.334 mmol, 30 mL) was added a THF slurry of NaOH (0.134 g, 3.34 mmol, 10 equiv, 10 mL). The reaction mixture was allowed to stir for 5 d, after which all volatile materials were removed under reduced pressure. The resulting residue was extracted with *n*-Pentane, filtered through Celite and dried *in vacuo*. Dissolution of the resulting solid in Et_2O (10 mL), followed by filtration and storage at –35 °C resulted in yellow crystals, which were collected and dried. Yield: 0.230 g, 0.309 mmol, 93%. ^{1}H NMR (500.0 MHz, C_6D_6, 20 ˚C): δ = 3.70 (s, 1H, Ir–O*H*), 2.08–2.04 (m (overlapping resonances) 22H, *H1*, *H6*, *H7*), 1.79 (m(quartet), 12H, *H8*), 1.56 (t, 4H, $^{2}J_{HP}$ = 3 Hz, *H4*), 1.23 (d of vt, 24H, $^{3}J_{HH} \approx J_{HP}$ = 8 Hz, *H2* or *H3*), 1.18 (d of vt, 24H, $^{3}J_{HH} \approx J_{HP}$ = 8 Hz, *H2* or *H3*), –29.3 (t, 2H, $^{2}J_{HP}$ = 14 Hz, Ir–*H*). ^{13}C{^{1}H} NMR (125.7 MHz, C_6D_6, 20 ˚C): δ = 45.1 (s, *C6*), 38.6 (t, J_{CP} = 11 Hz, *C4*), 37.3 (s, *C8*), 33.8 (s, *C*5), 29.7 (s, *C7*), 26.5 (t, J_{CP}

= 15 Hz, *C1*), 20.2 (s, *C2* or *C3*), 19.0 (s, *C2* or *C3*). ppm. $^{31}P\{^{1}H\}$ NMR (121.95 MHz, C_6D_6, 20 ˚C): δ = 32.2 (t, $^{2}J_{PH}$ = 14 Hz, (coupling is observed because ^{1}H resonance is outside decoupling window)) ppm. FTIR (KBr Pellet): ν(Ir–H) 2247 and 2198 cm^{-1} also 2955, 2900, 2846, 2725, 1453, 1384, 1361, 850, 772 cm^{-1}. FTIR (Nujol): ν(OH) 3644 cm^{-1} (w) , ν(Ir–H) 2246 and 2202 cm^{-1}. Anal. Calcd. for $C_{34}H_{65}IrOP_2$: C, 54.88; H, 8.80. Found: C, 55.04; H, 8.58.

Synthesis of $H_5Ir(L^{mAd})_2$ (7).

Method A – from $HIr(N_2)(L^{mAd})_2$. To a degassed C_6H_{12} solution of $HIr(N_2)(L^{mAd})_2$ (0.012 g, 0.016 mmol, 0.85 mL) was added H_2 (0.797 mL, 0.033 mmol, 1 atm, 2.05 equiv) via syringe. The reaction mixture quickly changed in color from bright to faint yellow. ^{1}H NMR analysis of the mixture *ca*. 10 min after addition revealed exclusive production of $H_5Ir(L^{mAd})_2$.

Method B – from $H_2Ir(OH)(L^{mAd})_2$. To a degassed C_6D_6 solution of $H_2Ir(OH)(L^{mAd})_2$ (0.100 g, 0.0134 mmol, 8 mL) was added H_2 (6.74 mL, 1 atm, 0.275 mmol, 2.05 equiv). The color quickly changed from bright yellow to faint yellow. The reaction mixture was stirred for 1 h and then all volatile materials were removed *in vacuo*. The resulting residue was extracted with Et_2O (40 mL) and then stirred over activated 4Å molecular sieves for 8 h. The solution was then filtered, concentrated to a volume of 8 mL and filtered again. Storage of the resulting solution at –35 ˚C overnight yielded light yellow crystals, which were dried and collected. Yield: 0.073 g, 0.100 mmol, 75%. ^{1}H NMR (500.1 MHz, C_6D_6, 20 ˚C): δ = 2.05 (bs, 6H, *H7*), 2.02 (m, 12H, *H6*), 1.77 (m(quartet), 12H, *H8*), 1.56 (d of sept, 4H, *H1*), 1.43 (t, 4H, $^{2}J_{HP}$ = 4 Hz, *H4*), 1.17 (d of vt, 12H, $^{3}J_{HH} \approx J_{HP}$ = 7 Hz, *H2* or *H3*), 1.05 (d of vt, 12H, $^{3}J_{HH} \approx J_{HP}$ = 7 Hz, *H2* or *H3*), –10.30 (t, 5H, $^{2}J_{HP}$ = 12.5 Hz, T_1 = 988 ms (via non–linear saturation recovery), Ir–*H*). $^{13}C\{^{1}H\}$ NMR (125.7 MHz, C_6D_6, 20 ˚C): δ = 44.41 (s, *C6*), 38.3 (t, J_{PC} = 13 Hz, *C4*), 37.4 (s, *C8*), 34.3 (s, *C5*), 29.9 (t, J_{CP} = 17 Hz, *C1*), 29.6 (s, *C7*), 19.3 (s, *C2* or *C3*), 19.05 (s, *C2* or *C3*) ppm. $^{31}P\{^{1}H\}$ NMR (161.95 MHz, C_6D_6, 20 °C): δ = 14.1 (s) ppm. FTIR (KBr

Pellet): ν(Ir–H) 1966 cm^{-1} also 2957, 2889, 2848, 1452, 1379, 1246, 1032, 904, 643 cm^{-1}. Anal. Calcd. for $C_{34}H_{67}IrP_2$: C, 55.94; H, 9.25. Found: C, 55.65; H, 9.24.

Synthesis of Li[HIr(κ^2-*P*,*C*–L^{mAd})(L^{mAd})] (8). Method A – From a HIr(N_2)(L^{mAd})$_2$/H_2Ir(κ^2-*P*,*C*–L^{mAd})(L^{mAd}) Mixture: To a thawing Et_2O solution of HIr(N_2)(L^{mAd})$_2$ (0.014 g, 0.019 mmol, 1.1 mL; Note that HIr(N_2)(L^{mAd})$_2$ establishes an equilibrium with H_2Ir(κ^2-*P*,*C*–L^{mAd})(L^{mAd}) in Et_2O) was added *n*–BuLi (0.0176 mmol, 11 μL of a 1.6 M solution in hexanes, 0.95 equiv). The reaction mixture was allowed to warm to room temperature. Analysis of the reaction mixture by $^{31}P\{^1H\}$ NMR indicated clean formation of Li[HIr(κ^2-*P*,*C*–L^{mAd})(L^{mAd})]. A second experiment was performed under identical conditions, but the sample was allowed to thaw in an NMR probe. $^{31}P\{^1H\}$ NMR acquisition at –45 ˚C indicated that no reaction had taken place. Warming the probe by 5 ˚C steps indicated that the sample fully converts to Li[HIr(κ^2-*P*,*C*–L^{mAd})(L^{mAd})] at –20 ˚C.

Method B – From H_2IrCl(L^{mAd})$_2$: To a thawing 4:1 *n*-Pentane/Et_2O mixture of H_2IrCl(L^{mAd})$_2$ (0.501 g, 0.657 mmol, 100 mL) was added a thawing *n*-Pentane solution of *n*–BuLi (1.58 mmol, 0.986 mL of a 1.6 M solution in hexane diluted to 15 mL with *n*-Pentane, 2.4 equiv). The reaction mixture was stirred for 3 h and then filtered through Celite. All volatiles were removed under reduced pressure and the resulting solid was extracted with Et_2O (6 mL) and filtered again. Storage of this solution at –35 ˚C overnight resulted in the formation of red crystals which were dried and collected. Yield: 0.341 g, 0.466 mmol, 71%. ^1H NMR (500.0 MHz, C_6D_6, 20 ˚C): δ = 2.85 (d, *Ad*), 2.69 (bs, Ad), 2.54 (bs, *Ad*), 2.21 (s, *Ad*), 2.10 (s, *Ad*), 2.05–1.64 (m), 1.44–1.12 (m), –4.19 (broad doublet, $J_{(HPtrans)}$ = 120 Hz, (cis coupling not observed), Ir–*H*), $^{31}P\{^1H\}$ NMR (161.9 MHz, C_6D_6, 20 °C): δ = 53.3 (bs), 33.5 (bs) ppm. FTIR (KBr Pellet): ν(IrH) 1930 (m) cm^{-1}, also 2970, 2900, 2815, 1444, 1365, 1289, 1304, 1244, 1137, 1096, 1025, 925, 857 cm^{-1}. Anal. Calcd. for $C_{34}H_{62}P_2IrLi$: C, 55.79; H, 8.54. Found: C, 56.13; H, 8.58.

Synthesis of [Li(12–c–4)$_2$][HIr(κ^2-*P*,*C*–L^{mAd})(L^{mAd})] (9). To an *n*-Pentane solution of Li[HIr(κ^2-*P*,*C*–L^{mAd})(L^{mAd})] (**8**) (0.456 g, 0.623 mmol, 150 mL) was added an *n*-pentane solution of 12–crown–4 (0.360 g, 1.87 mmol, 3.29 equiv) and resulted in the formation of a red precipitate. The reaction mixture was then filtered and the solid material washed with *n*-pentane (3 x 10 mL). Dissolution of the resulting solid in an 80:20 *n*-pentane/Et_2O mixture (9mL), followed by filtration and storage at –35 ˚C resulted in brick red crystals, which were collected and dried *in vacuo*. Yield: 0.486 g, 0.448 mmol, 72%. ^{1}H NMR (500.0 MHz, C_6D_6, 20 ˚C): δ = 3.34 (s, 32H, 12–c–4), 3.10 (s, 1H, Ad) 2.99 (d, 1H, Ad), 2.67 (d, 1H, Ad), 2.58 (s, 1H, Ad), 2.46 (m, 1H), 2.35–2.27 (m, 4H), 2.18 (s, 6H, Ad), 2.11–1.88 (m, 8H), 1.79 (m(quartet), 6H), 1.69–1.28 (m, 28H), –3.65 (dd, 1H, $^2J_{(HPtrans)}$ = 100.6 Hz, $^2J_{(HPcis)}$ = 20 Hz, Ir–*H*). ^{13}C{^{1}H} NMR (125.7 MHz, C_6D_6, 20 ˚C): δ = 70.1(s), 47.7(d), 47.5(d), 47.5(d), 46.2(m), 45.9(d) 45.7(m), 45.3(bs), 44.1(m), 39.1(s), 39.0(s), 37.6(s), 35.9(d), 33.1(s), 33.0(s), 32.0(s), 30.3(s), 29.9(s), 29.8(s), 29.6(s), 26.4(s), 26.3(d), 25.6(s), 25.5(d), 22.5(d), 22.3(d), 21.7(d), 20.8 (s), 20.8(d), 20.3(d), 19.5(d), 18.4 (d) ppm. ^{31}P{^{1}H} NMR (161.9 MHz, C_6D_6, 20 ˚C): δ = 53.9 (bs), 42.2 (bs) ppm. FTIR (KBr Pellet): ν(IrH) 1882 (s) cm^{-1}, also 2960, 2891, 2800, 2751, 1483, 1446, 1365, 1289, 1136, 1908, 1024, 922, 856, 646, 624 cm^{-1}. Anal. Calcd. for $C_{50}H_{95}O_8LiIr$: C, 54.88; H, 8.81. Found: C, 55.04; H, 8.68.

Synthesis of $H_2Ir(OC_6F_5)(L^{mAd})_2$ (10). To a thawing Et_2O solution of [Li(12–c–4)$_2$][HIr(κ^2-*P*,*C*–L^{mAd})(L^{mAd}) (0.076 g, 0.070 mmol, 10 mL) was added an Et_2O solution of HOC_6F_5 (0.026 g, 0.140 mmol, 5 mL, 2.0 equiv). An immediate color change from brick red to light yellow was observed and the reaction mixture was allowed to stir for 15 min while warming to room temperature. All volatile materials were then removed *in vacuo* and the resulting residue was extracted with *n*-Pentane (15 mL), filtered through Celite and dried again under reduced pressure. Dissolution of the resulting solid in an Et_2O/*n*-Pentane mixture (20:1, 2 mL total), followed by filtration and storage at –35 °C for 3 d resulted in yellow

crystals, which were collected and dried *in vacuo*. Yield: 0.053 g, 0.058 mmol, 83%. ^{1}H NMR (500.2 MHz, C_6D_6, 20 ˚C): δ = 2.00 (bs, 6H, *H7*), 1.95 (d of sept, 4H, *H1*), 1.70 (m(quartet), 12H, *H8*), 1.65 (t, 4H, J_{HP} = 3 Hz, *H4*), 1.57 (m, 12H, *H6*), 1.08 (dd of vt, 12H, $^{3}J_{HH} \approx J_{HP}$ = 7 Hz, *H2* and *H3*), –32.4 (t, 2H, $^{2}J_{HP}$ = 15 Hz, Ir–*H*). ^{13}C{^{1}H} NMR (125.8 MHz, C_6D_6, 20 ˚C): δ = 145.5(m), 142.9(m), 141.0(m), 140.4(m), 138.4(m), 45.23 (s, *C6*), 40.49 (t, J_{CP} = 10 Hz, *C4*), 36.8 (s, *C8*), 34.4 (s, *C5*), 29.6 (s, *C7*), 27.6 (t, J_{CP} = 15 Hz, *C1*), 19.9 (s, *C2* or *C3*), 19.3 (s, *C2* or *C3*) ppm. ^{31}P{^{1}H} NMR (202.5 MHz, C_6D_6, 20 ˚C): δ = 39.2 (t, $^{2}J_{PH}$ = 15 Hz, coupling is observed because ^{1}H resonance is outside decoupling window) ppm. ^{19}F{^{1}H} NMR (470.6 MHz, C_6D_6, 20 ˚C): δ = –164.9 (d, 2F, *J* = 22 Hz, *o–F*), –169.3 (t, 2F, *J* = 22 Hz, *m–F*), –183.5 (bs, 1H, *p*–F) ppm. FTIR (KBr Pellet): ν(CH–agostic) 2659 (w) cm^{-1}, ν(IrH) 2304 (w), 2268 (w), 2212 (w) cm^{-1} also 2958, 2904, 2848, 1649, 1607, 1500, 1476, 1242, 1172, 1008, 980, 884, 644 cm^{-1}. Anal. Calcd. for $C_{40}H_{64}F_5OIrP_2$: C, 52.79; H, 7.09. Found: C, 52.51; H, 7.18.

Reaction of [Li(12–c–4)$_2$][HIr(κ^2-*P*,*C*–L^{mAd})(L^{mAd})] with 1.0 equiv HOC$_6$F$_5$. To a thawing Et_2O solution of [Li(12–c–4)$_2$][HIr(κ^2-*P*,*C*–L^{mAd})(L^{mAd})] (0.209 g, 0.193 mmol, 10 mL) was added a thawing Et_2O solution of HOC_6F_5 (0.036 g, 0.193 mmol, 10 mL, 1 equiv). An immediate color change from brick red to yellow–orange was observed and the reaction mixture was allowed to stir for 30 min while warming to room temperature. All volatiles were then removed under reduced pressure. Dissolution of the resulting residue in C_6D_{12} followed by analysis by ^{1}H NMR spectroscopy indicated production of a HIr(N$_2$)(L^{mAd})$_2$/H$_2$Ir(κ^2-*P*,*C*–L^{mAd})(L^{mAd}) equilibrium mixture.

Synthesis of H$_2$Ir(*κ*^{2}-N,*O*–H$_2$NCONH)(L^{mAd})$_2$ (10). A thawing Et_2O slurry of carbamide peroxide (0.006 g, 0.0602 mmol, 1.07 equiv) was added to a thawing 2:1 ratio Et_2O:C_5H_{12} solution in of Li[HIr(*κ*^{2}-P,*C*–L^{mAd})(L^{mAd})] (**8**) (0.061 g, 0.056 mmol, 60 mL). The reaction mixture was stirred for 12 hrs followed by removal of most volatile materials under reduced

pressure to approximately 0.5 ml. The resulting solution was filtered and solvent was completely removed. The resulting residue was washed three times with pentane (5 mL each), filtered in pentane (2 ml) and the filtrate was collected and dried under reduced pressure, dissolved in Et_2O (1 ml), filtered, and stored at -35 ˚C to yield yellow crystals, collected and dried. Yield: 0.012 g, 0.0056 mmol, 27%. ^{1}H NMR (500.16 MHz, C_6D_6, 20 ˚C): δ = 3.10 (s, 2H, N*H*$_2$), 2.76 (s, 1H, Ir-N*H*), 2.18 (bs, 3H, Ad), 2.07 (s, 4H, Ad), 2.0 (s, 10H), 1.80 (m (pseudo q), 12H, Ad), 1.69 (s 3H), 1.29 (d of vt, 12H, $^3J_{HH} \approx J_{HP}$ = 6 Hz, *H2* or *H3*), 1.24 (d of vt, 12H, $^3J_{HH} \approx J_{HP}$ = 5 Hz, *H2* or *H3*), -28.38 (t, 2H, $^2J_{HP}$ = 18 Hz, Ir(*H*)$_2$). ^{31}P{^{1}H} NMR (161.964 MHz, C_6D_6, 20 ˚C): δ = 18.0 (s) ppm.

Reaction of [Li(12–c–4)$_2$][HIr(κ^2-*P*,*C*–L^{mAd})(L^{mAd})] with H_2NDipp (Dipp = 2,6–(*i*-Pr)$_2$C$_6$H$_3$). To a thawing Et_2O solution of [Li(12–c–4)$_2$][HIr(κ^2-*P*,*C*–L^{mAd})(L^{mAd})] (0.063 g, 0.058 mmol, 1 equiv) was added an Et_2O solution of H_2NDipp (0.010 g, 0.058 mmol, 1 equiv). An immediate color change from brick red to yellow–orange was observed and the reaction mixture was allowed to stir for 30 min while warming to room temperature. All volatiles were then removed under reduced pressure. Dissolution of the resulting residue in C_6D_{12} followed by analysis by ^{1}H NMR spectroscopy indicated production of a HIr(N$_2$)(L^{mAd})$_2$/H$_2$Ir(κ^2-*P*,*C*–L^{mAd})(L^{mAd}) equilibrium mixture. When this reaction was repeated with D_2NDipp, ^{2}H NMR analysis in Et_2O indicated deuterium incorporation into the L^{mAd} resonances associated with the HIr(N$_2$)(L^{mAd})$_2$/ H$_2$Ir(κ^2-*P*,*C*–L^{mAd})(L^{mAd}) mixture.

1.10 Crystallographic Structure Determinations

General. Single crystal X–ray structure determinations were carried out at low temperature on a Bruker P4, Platform or Kappa Diffractometer equipped with a Bruker APEX II detector. All structures were solved by direct methods with SIR 2004 [114] and refined by full–matrix least–squares procedures utilizing SHELXL–97. [115] Molecular structures of all complexes are depicted in Figures.

Crystallographic data collection and refinement information is listed in Tables 1.3–1.6.Hydride Treatment. With the exception of $HIr(N_2)(L^{mAd})_2$ **(3)**, peaks in the electron density difference map corresponding the appropriate number of hydride ligands were found for all iridium–hydride complexes. Upon positive identification, these hydride atoms were subjected to one cycle of free refinement and then restrained to an Ir–H bond distance of 1.55(± 0.02) Å for all subsequent refinements. In order to produce a chemically sensible geometry, the hydride units of the hydroxide complex $H_2Ir(OH)(L^{mAd})_2$ (**6**) were additionally restrained to an H···H bond distance of 2.15(± 0.05) Å. The hydride ligand in monohydride $HIr(N_2)(L^{mAd})_2$ **(3)** was located from the electron density difference map and refined without restraints in all cycles.

Positional Disorder. One full methylene adamantane group in $HIr(N_2)(L^{mAd})_2$ **(3)** possessed a two–site positional disorder which was readily modeled and refined with 50:50 occupancy of the components. Trihydride $H_3Ir(L^{mAd})_2$ (**5**) possessed a two–site positional disorder involving the Ir center and one L^{mAd} ligand for which a 91:9 site occupancy of major and minor components lead to stable refinement. The cyclometallated complex $H_2Ir(\kappa^2\text{-}P,C\text{–}L^{mAd})(L^{mAd})$ (**4**) also possessed a two–site positional disorder involving the Ir center and one L^{mAd} ligand for which a 90:10 site occupancy of major and minor components lead to stable refinement.

Disordered Solvent Molecules of Co–Crystallization. The structures of both $H_2Ir(Cl)(L^{mAd})_2$ (**2**) and $[Li(12\text{–}c\text{–}4)_4][HIr(\kappa^2\text{-}P,C\text{–}L^{mAd})(L^{mAd})]$ contained several disordered Et_2O molecules of co–crystallization that could not be easily modeled. To account for this disorder and the underlying electron density, the crystallographic routine SQUEEZE [116] was employed and the solvent–free refinement information is detailed within each CIF file.

Table 1.3. Crystallographic Data Collection and Refinement Information for L^{mAd}, $H_2IrCl(L^{mAd})_2$•0.5(Et_2O), $HIr(N_2)(L^{mAd})_2$.

Compound	L^{mAd}	$H_2IrCl(L^{mAd})_2$•0.5(Et_2O)	$HIr(N_2)(L^{mAd})_2$
Formula	$C_{17}H_{31}P$	$C_{36}H_{69}ClIrO_{0.50}P_2$	$C_{34}H_{63}IrN_2P_2$
Crystal System	Monoclinic	Triclinic	Monoclinic
Space Group	*C*2/*c*	*P*–1	$P2_1/n$
a, Å	20.8279(4)	10.3140(16)	15.6940(9)
b, Å	15.5918(3)	12.6360(19)	13.1160(7)
c, Å	10.3665(2)	13.910(2)	17.2375(9)
α, deg	90	97.399(2)	90
β, deg	110.9470(10)	95.803(2)	102.6540(10)
γ, deg	90	92.354(2)	90
V, $Å^3$	3143.98(10)	1785.9(5)	3462.0(3)
Z	8	2	4
Radiation (λ, Å)	Cu–Kα, 1.54178	Mo–Kα, 0.71073	Mo–Kα, 0.71073
ρ (calcd.), g/cm^3	1.126	1.487	1.447
μ (Mo Kα), mm^{-1}	1.381	3.928	3.973
Temp, K	100(2)	100(2)	100(2)
θ max, deg	68.26	25.40	25.05
data/parameters	2632 / 168	6507 / 359	6146 / 455
R_1	0.0269	0.0295	0.0172
wR_2	0.0718	0.0562	0.0462
GOF	1.040	1.004	1.014

Table 1.4. Crystallographic Data Collection and Refinement Information for $H_3Ir(L^{mAd})_2$, $H_2Ir(\kappa^2\text{-}P,C\text{–}L^{mAd})(L^{mAd})$, $H_5Ir(L^{mAd})_2$.

Compound	$H_3Ir(L^{mAd})_2$	$H_2Ir(\kappa^2\text{-}P,C\text{–}L^{mAd})(L^{mAd})$	$H_5Ir(L^{mAd})_2$
Formula	$C_{34}H_{65}IrP_2$	$C_{34}H_{62}IrP_2$	$C_{34}H_{67}IrP_2$
Crystal System	Monoclinic	Monoclinic	Monoclinic
Space Group	$P2_1/n$	$P2_1$	$P2_1/c$
a, Å	13.1354(9)	10.9025(4)	10.776(13)
b, Å	11.1154(8)	11.8348(4)	12.182(14)
c, Å	22.9070(16)	13.4097(5)	26.90(3)
α, deg	90	90	90
β, deg	100.9830(10)	111.181(2)	98.916(15)
γ, deg	90	90	90
V, Å^3	3283.3(4)	1613.35(10)	3489(7)
Z	4	2	4
Radiation (λ, Å)	Mo–Kα, 0.71073	Mo–Kα, 0.71073	Mo–Kα, 0.71073
ρ (calcd.), g/cm^3	1.473	1.492	1.390
μ (Mo Kα), mm^{-1}	4.185	4.258	3.938
Temp, K	100(2)	100(2)	100(2)
θ max, deg	25.07	25.31	25.58
data/parameters	5797 / 359	5031 / 358	6484 / 349
R_1	0.0345	0.0273	0.0452
wR_2	0.0689	0.0641	0.0949
GOF	1.053	1.048	1.034

Table 1.5. Crystallographic Data Collection and Refinement Information for $H_2Ir(OH)(L^{mAd})_2$, $Li[HIr(\kappa^2\text{-}P,C\text{–}L^{mAd})(L^{mAd})]\bullet Et_2O$, $Li[HIr(\kappa^2\text{-}P,C\text{–}L^{mAd})(L^{mAd})]\bullet 4(Et_2O)$.

Compound	$H_2Ir(OH)(L^{mAd})_2$	$Li[HIr(\kappa^2\text{-}P,C\text{–}L^{mAd})(L^{mAd})]\bullet Et_2O$	$Li[HIr(\kappa^2\text{-}P,C\text{–}L^{mAd})(L^{mAd})]\bullet 4(Et_2O)$
Formula	$C_{34}H_{65}C_{l0}IrOP_2$	$C_{38}H_{72}IrLiOP_2$	$C_{66}H_{134}IrLiO_{12}P_2$
Crystal System	Triclinic	Orthorhombic	Triclinic
Space Group	*P*–1	$P2_12_12_1$	*P*–1
a, Å	10.429(5)	10.918(3)	13.1359(11)
b, Å	13.741(5)	16.463(5)	14.0399(12)
c, Å	13.801(5)	21.628(7)	15.8641(14)
α, deg	116.142(5)	90	87.9760(10)
β, deg	90.733(5)	90	86.6690(10)
γ, deg	105.160(5)	90	89.3790(10)
V, $Å^3$	1694.8(12)	3887(2)	2918.9(4)
Z	2	4	2
Radiation (λ, Å)	Mo–Kα, 0.71073	Mo–Kα, 0.71073	Mo–Kα, 0.71073
ρ (calcd.), g/cm^3	1.458	1.377	1.402
μ (Mo Kα), mm^{-1}	4.057	3.543	2.397
Temp, K	100(2)	100(2)	100(2)
θ max, deg	25.40	25.31	27.54
data/parameters	6200 / 363	6947 / 403	12952 / 580
R_1	0.0199	0.0437	0.0365
wR_2	0.0420	0.1050	0.0721
GOF	1.040	1.046	1.045

Table 1.6. Crystallographic Data Collection and Refinement Information for $H_2Ir(OC_6F_5)(L^{mAd})_2$.

Compound	$H_2Ir(OC_6F_5)(L^{mAd})_2$
Formula	$C_{40}H_{64}F_5IrOP_2$
Crystal System	Triclinic
Space Group	*P*–1
a, Å	10.3320(10)
b, Å	13.2640(12)
c, Å	16.4940(17)
α, deg	104.8080(10)
β, deg	93.1770(10)°.
γ, deg	110.7050(10)°.
V, $Å^3$	2017.4(3)
Z	2
Radiation (λ, Å)	Mo–Kα, 0.71073
ρ (calcd.), g/cm^3	1.498
μ (Mo Kα), mm^{-1}	3.441
Temp, K	100(2)
θ max, deg	25.03
data/parameters	7041 / 458
R_1	0.0286
wR_2	0.0754
GOF	1.041

1.11 References

1. Manriquez, M. J.; Fagan, P. J.; Marks, T. J. *J. Am. Chem. Soc* **1978,** *100,* 3941-3942.

2. Cotton, F. A.; Wilkinson, G. *Advanced Inorganic Chemistry,* 5th ed.;, 1988; Vol. Chpt. 28 and Chpt. 19 (pg 918).

3. Keith, J. A.; Henry, P. M. *Angew. Chemie Int. Ed* **2009,** *48,* 9038-9049.

4. Milstein, D. *Acc. Chem. Res.* **1984,** *17,* 221-226.

5. Godard, C.; Duckett, S. B.; Henry, C.; Polas, S.; Toose, R.; Whitewood, A. *Chem. Commun* **2004,** 1826-1827.

6. Jensen, C. M.; Trogler, W. C. *J. Am. Chem. Soc.* **1986,** *108,* 723-729.

7. Fisher, B. J.; Eisenberg, R. *Organometallics* **1983,** *2,* 764–767.

8. Kunin, A. J.; Eisenberg, R. *J. Am. Chem. Soc.* **1986,** *108,* 535–536.

9. Kunin, A. J.; Eisenberg, R. *Organometallics* **1988,** *7,* 2124–2129.

10. Housecroft, C. E. Iridium: Inorganic & Coordination Chemistry. *Encyclopedia of Inorganic Chemistry* **2006**.

11. Vitale, A. A.; San Filippo, J. *J. Organomet. Chem.* **1985,** *286,* 91–101.

12. Bernard, K. A.; Rees, W. M.; Atwood, J. D. *Organometallics* **1986,** *5,* 390–391.

13. Zhao, J.; Hesslink, H.; Hartwig, J. F. *J. Am. Chem. Soc.* **2001,** *123,* 7220–7227.

14. Crabtree, R. H. *J. Chem. Soc., Dalton Trans.* **2001,** 2437–2450.

15. Fawcett, J. P.; Harrod, J. F. *J. Organomet. Chem.* **1976,** *113,* 245–248.

16. Geoffroy, G. L.; Pierantozzi, R. *J. Am. Chem. Soc.* **1979,** *98,* 8054–8059.

17. Harrod, J. F.; Yorke, W. *J. Inorg. Chem.* **1981,** *20,* 1156–1159.

18. Drouin, M.; Harrod, J. F. *Inorg. Chem.* **1983,** *22,* 999–1001.

19. Johnson, C. E.; Eisenberg, R. *J. Am. Chem. Soc.* **1985,** *107,* 3148–3160.

20. Muir, K. W.; Ibers, J. A. *Journal of Organometallic Chemistry* **1969,** *18,* 175-187.

21. Farber, E. *Chymia* **1962,** *8,* 165-180.

22. Wurtz, A. *Compt. rend.* **1845,** *18,* 702.

23. Graham, T. *Pilos. Trans. R. Soc.* **1866,** *156,* 415.

24. Sabatier, P. *J. Chem. Ed.* **1926,** *18,* 1005.

25. Hieber, W.; Leutert, F. *Naturwissenshaften* **1931,** *19,* 360.

26. Wilkinson, G.; Birmingham, J. M. *J. Am. Chem. Soc.* **1955,** *77,* 3421.

27. Chatt, J.; Duncanson, L. A.; Shaw, B. L. *Proc. Chem. Soc* **1957,** 343.

28. Duncanson, L. A. Joseph Chatt FRS. *Biogr. Mems. Fell. R. Soc.* **1996,** 1748-8494.

29. Fernandez-Megia, E. *Synlett* **1999,** *7,* 1179.

30. Cornils, B.; Herrmann, W. A.; Rasch, M. *Angew. Chem. Int.Ed. Engl.* **1994,** *33,* 2144-2163.

31. Cornish, A. J.; Gartner, K.; Yang, H.; Peters, J. W.; Hegg, E. L. *J. Biol. Chem* **2011,** *19,* 1038-1052.

32. Kaesz, H. D.; Saillant, R. B. *Chem. Rev.* **1971,** *72,* 231-281.

33. Ahmad, N.; Robinso, D. S.; Uttley, M. F. *Dalton Trans* **1972,** 843-847.

34. Empsell, H. D.; Hyde, E. M.; Mentzer, E. S. B.; Uttley, M. *Dalton Trans* **1976,** 2069-2074.

35. Ciechanowicz, M.; Skapski, A. C.; Troughton, P. *Acta Cryst.* **1976,** *B32,* 1673-1680.

36. Zanella, R.; Canziani, F.; Ros, R.; Graziani, M. J. *Organomet. Chem.* **1974,** *67,* 449-454.

37. Giustiniani, M.; Dolcetti, G.; Nicolini, M.; Belluco, U. *J. Chem. Soc. A* **1969,** 1961-1962.

38. Balzani, V.; Moggi, L.; Manfrin, M. F.; Bolletta, F.; Gleria, M. *Science* **1975,** *189,* 852-856.

39. Casey, C. P.; Whiteker, G. T.; Melville, M. G.; Petrovich, L. M.; Gavney, J. A.; Powell,

D. R. *J. Am. Chem. Soc.* **1992,** *114,* 5535-5543.

40. Casey, C. P.; Paulsen, E. L.; Beuttenmueller, E. W.; Proft, B. R.; Matter, B. A.; Powell, D. R. *J. Am. Chem. Soc.* **1999,** *121,* 63-70.

41. Benson, M. T.; Cundari, T. R. *Inorganica Chimica Acta* **1997,** *259,* 91-100.

42. Millard, M. D.; Moore, C. E.; Rheingold, A. L.; Figueroa, J. S. *J. Am. Chem. Soc.* **2010,** *132,* 8921-8923.

43. Diluzio, J. W.; Vaska, L. *J. Am. Chem. Soc.* **1961,** *83,* 2784-2785.

44. Diluzio, J. W.; Vaska, L. *J. Am. Chem. Soc.* **1962,** *84,* 679-680.

45. Rhodes, R. E.; Vaska, L. *J. Am. Chem. Soc.* **1965,** *87,* 4970-4971.

46. Nishihara, Y.; Takemura, M.; Osakada, K. *Inorganica Chimica Acta* **2009,** 2951-2956.

47. Cundari, T. R. *J. Am. Chem. Soc.* **1994,** *116,* 340-347.

48. Gray, H. B.; Ballhausen, C. J. *J. Am. Chem. Soc.* **1962,** *85,* 260-265.

49. Aba-Hasanayn, F.; Goldman, A. S.; Krogh-Jespersen, K. *Inorg Chem.* **1994,** *33,* 5122-5130.

50. Yoshida, T.; Thorn, D. L.; Okano, T.; Otsuka, S.; Ibers, J. A. *J. Am. Chem. Soc.* **1980,** *102,* 6451-6457.

51. Freeman, M. A.; Young, D. A. *Inorg. Chem.* **1986,** *25,* 1556-1560.

52. Vinas, C.; Flores, M. A.; Rosario, N.; Teixidor, F.; Kivekas, R.; Sillanpaa, R. *Organometallics* **1998,** *17,* 2278-2289.

53. Stradiotto, M.; Fujkala, K. L.; Tilley, T. D. *Helvetica Chimica Acta* **2001,** *84,* 2958-2971.

54. Burgess, K.; van der Donk, W. A.; Westcott, S. A.; Marder, T. B.; Baker, R. T.; Calabrese, J. C. *J. Am. Chem. Soc.* **1992,** *114,* 9350-9359.

55. Douglas, S.; Lowe, J. P.; Mahon, M. F.; Warren, J. E.; Whittlesey, M. K. *J. of Organomet. Chem.* **2005,** *690,* 5027-5035.

56. Hoffman, R. *Angew. Chem. Int. Ed.* **1982,** *21,* 711-800.

57. Jean, Y. *Molecular Orbitals of Transition Metal Complexes;* Oxford: New York, 2005; pp P 53-P 54.

58. Dahlenburg, J.; Hock, N. *Inorg. Chim. Acta* **1985,** *104,* L29-L30.

59. Benvenutti, M. H. A.; Hitchcock, P.; Nixon, J. F.; Vargas, M. D. *J. Chem. Soc., Dalton Trans.* **1996,** 739.

60. Termaten, A. T.; Nijbacker, T.; Ehlers, A. W.; Schakel, M.; Spek, A. L.; McKee, M. L.; Lammertsma, K. *Chem-Eur. J.* **2004,** *10,* 4063.

61. Yano, T.; Moroe, Y.; Yamashita, M.; Nozaki, K. *Chem. Lett.* **2008,** *37,* 1300.

62. Campos, J.; Alvarez, E.; Carmona, E. *New J. Chem.* **2011,** *35,* 2122.

63. Garcia-Camprubi, A.; Martin, M.; Sola. *E. Inor. Chem.* **2012,** *49,* 10649.

64. Bochmann, M.; Wilkinson, G.; Young, B. G. *J. C. S. Dalton Trans.* **1980,** *10,* 1879-1887.

65. Hackett, M.; Whitesides, G. M. *Organometallics* **1987,** *6,* 403-410.

66. Silverman, G. *Handbook of Grignard Reagents;* Chemical Industries, 1996; Vol. P 9-21.

67. Rieke, R. D.; Bales, S. E. *J Am. Chem. Soc.* **1974,** *96,* 1775-1781.

68. Vrieze, D.; Stufkens, D.; Heitkamp, S. *Journal of Organometallic Chemistry* **1978,** *152,* 347-357.

69. Rossi, M.; Giannaccaro, P.; Gargano, M. *Inorganica chimica Acta* **1973,** *7,* 409-412.

70. Morris, G.; Fillebeen-Khan, T.; Felkin, H.; Crabtree, R. *Journal of Organometallic Chemistry* **1979,** *168,* 183-195.

71. Albiniti, A.; Bakhmutov, V. I.; Caulton, K. G.; Clot, E.; Eckert, J.; Eisenstein, O.; Gusev, D. G.; Grushin, V. V.; Hauger, B. E.; Klooster, W. T.; Koetzle, T.; Mcmullan, R. K.; O'Loughlin, T. J.; Pelissier, M.; Ricci, J. S.; Sigalas, M. S.; Vymenitis, A. *J. Am. Chem. Soc* **1993,** *115,* 7300-7312.

72. Cooper, A. C.; Clot, E.; Huffman, J. C.; Streib, W. E.; Maseras, F.; Eisenstein, O.; Caulton, K. G. *J. Am. Chem. Soc.* **1999,** *121,* 97-106.

73. Clot, E.; Eisenstein, O.; Dube, T.; Faller, J. W.; Crabtree, R. H. *Organometallics* **2002,** *21,* 575-580.

74. Brookhart, M. G. M. L. H. P. *G. PNAS* **2007,** *104,* 6908-6914.

75. Crabtree, R. H. *The Organometallic Chemistry of the Transition Metals;* Wiley: New Jersey, 2005; pp P276-P279.

76. Green, J. C. a. M. L. H. *Comprehensive Inorganic Chemistry;* Pergamon: Oxford, 1973; p Chpt. 48.

77. Bath, S. S.; Vaska, L. *J. Am. Chem. Soc.* **1963,** *85,* 3500-3501.

78. Collman, J. P.; Kubota, M.; Vastine, F. D.; Sun, J. Y.; Kang, J. W. *J. Am. Chem.Soc.* **1968,** *90,* 5430-5437.

79. Chatt, J. *Pure Appl. Chem* **1970,** *24* (No. 2), 425-442.

80. Stroshane, R. M.; Taniguchi, M.; Rinehart Jr., K. L. *J. Am. Chem. Soc.* **1976,** *98,* 3027-3028.

81. Milstein, D.; Clabrese, J. C. *J. Am. Chem. Soc.* **1982,** *104,* 3773-3774.

82. Morris, R. H. *Inorg. Chem.* **1992,** *31,* 1471-1478.

83. Rampt, F. A.; Spiegler, M.; Herrmann, W. A. *J. Organomet. Chem.* **1999,** *582,* 204-210.

84. Fryzuk, M. D.; Johnson, S. A. *Coord. Chem. Rev.* **2000,** 200-202, 379-409.

85. Shaver, M. P.; Fryzuk, M. D. *Adv. Synth. Catal.* **2003,** *345,* 1061-1076.

86. Ghosh, R.; Kanzelberger, M.; Emge, T. J.; Hall, G. S.; Goldman, A. S. *Organometallics* **2006,** *25,* 5668-5671.

87. Bottcher, C. H.; Graf, M.; Mayer, P.; Sunkel, K. Z. *Anorg. Allg. Chem.* **2008,** *634,* 1241-1243.

88. Fischer, K.; Wilken, M. *J. Chem. Thermodynamics* **2001,** *33,* 1285-1308.

89. Battino, R.; Rettich, T. R.; Tominaga, T. *J. Phys. Chem. Ref. Data* **1984,** *13,* 563-600.

90. Churchill, D. G.; Janak, K. E.; Wittenberg, J. S.; Parkin, G. *J. Am. Chem. Soc.* **2003,** *125,* 1403–1420.

91. Van der Boom, M. E.; Milstein, D. *Chem. Rev.* **2003,** *103,* 1759–1792.

92. Lee, D. W.; Jensen, C. M.; Morales-Morales, D. *Organometallics* **2003,** *22,* 4744–4749.

93. Pool, J. A.; Lobkovsky, E.; Chirik, P. J. *J. Am. Chem. Soc.* **2003,** *125,* 2241–2251.

94. Allen, F. *Acta Cryst.* **1986,** *B42,* 515-522.

95. Cochran, W. *Acta Cryst.* **1951,** *4,* 408.

96. Cruickshank, D. W. *J. Acta Cryst.* **1949,** *2,* 65.

97. Cruickshank, D. W. *J. Acta Cryst.* **1949,** *2,* 154.

98. Ozerov, O. V. *Chem. Soc. Rev.* **2009,** *38,* 83–88.

99. Blum, O.; Milstein, D. *J. Am. Chem. Soc.* **2002,** *124,* 11456–11467.

100. Piers, W. E. *Organometallics* **2011,** *30,* 13-16.

101. Milstein, D.; Clabrese, J. C.; Williams, I. D. *J. Am. Chem. Soc.* **1986,** *108,* 6387-6389.

102. Morales-Morales, D.; Lee, D. W.; Wang, Z.; Jensen, C. M. *Organometallics* **2001,** *20,* 1144.

103. Yoshida, T.; Matsuda, T.; Okano, T.; Kitani, T.; Otsuka, S. *J. Am. Chem. Soc.* **1979,** *101,* 2027.

104. Yoon, M.; Tyler, D. R. *Chem. Commun.* **1997,** 639.

105. Burn, M. J.; Fickes, M. G.; Hartwig, J. F.; Hollander, F. J.; Bergman, R. G. *J. Am. Chem. Soc.* **1993,** *115,* 5875–5876.

106. Blum, O.; Milstein, D. *Angew. Chem., Int. Ed. Engl.* **1995,** *34,* 229–231.

107. Janowicz, A. H.; Bergman, R. G. *J. Am. Chem. Soc.* **1983,** *105,* 3929-3939.

108. Brookhart, M.; Green, M. *Journal of Organometallic Chemistry* **1983,** *250,* 395-408.

109. Jones, W. D.; Rosini, G. P.; Maguire, J. A. *Organometallics* **1999,** *18,* 1754-1760.

110. Jones, W. D. *Acc. Chem. Res.* **2003,** *36,* 140-146.

111. Allen, F. H. *Acta Cryst* **2002,** *B58,* 380-388.

112. Sheldrick, G. M. *Acta Cryst.* **2008,** *A64,* 112-122.

113. Rieke, R.; Bales, S. *J. Am. Chem. Soc.* **1974,** *96,* 1775-1781.

114. Burla, M. C.; Caliandro, R.; Camalli, M.; Carrozzini, B.; Cascarano, G. L.; De Caro, L. *J. Appl. Cryst.* **2005,** *38,* 381-388.

115. Sheldrick, G. M. *Acta Cryst.* **2008,** *A64,* 112-122.

116. van der Sluis, P.; Spek, A. L. *Acta Cryst.* **1990,** *A46,* 194-201.

Chapter 1: Much of the material for this chapter comes directly from a manuscript entitled "Four–Coordinate Iridium(I) Monohydrides: Reversible Dinitrogen Binding, Bond Activations, and Deprotonations" by Matthew D. Millard, Joshua S. Figueroa, Curtis E. Moore, and Arnold L. Rheingold, which has been published in *Journal of the American Chemical Society,* **2010**, 132 (16), pp 8921-8923

Chapter 2

Elucidating the Reactivity of Lewis Acidic Phosphinite Iridium Hydrides

2.1 Introduction

Vaska–type iridium (I) monohydrides are challenging to characterize due to the ease of proximal C–H bond activation and substrate oxidative addition. However, we were able to exploit the phosphine L^{mAd} framework $P(CH_2{}^1Ad)(i\text{-}Pr)_2$, allowing for the isolation and full characterization of a Vaska–type iridium (I) monohydride $H_2Ir(N_2)(L^{mAd})_2$ (**2**) (see chapter 1). Through these efforts we were inspired to install a phoshinite framework as a route to circumvent uncontrolled oxidation of the anionic monohydride complex $Li[HIr(\kappa^2\text{-}P,C\text{–}L^{mAd})(L^{mAd})]$, which often yielded intractable mixtures upon reaction with small molecules (Chapter 1). Phosphinites are organophosphorus compounds comprised of the formula $P(OR)R_2$ and are widely installed onto metal complexes for their electronic effects relative to phosphines. For example, Brookhart showed the bis-phosphinite PCP pincer complex $\{C_6H_3\text{-}2,6\text{-}[OP(t\text{Bu})_2]_2\}IrH_2$ to be roughly one order of magnitude more active in dehydrogenating alkanes than the benchmark diphosphine pincer catalyst $\{C_6H_3\text{-}2,6\text{-}[CH_2P(t\text{Bu})_2]_2\}IrH_2$.[1] We chose the $P(O^1Ad)(i\text{-}Pr)_2$ (L^{oAd}; oAd = oxy-1-adamantyl) ligand manifold because of the σ–donor/π–acceptor properties and the topological resemblance to L^{mAd} phosphine $P(CH_2{}^1Ad)(i\text{-}Pr)_2$.

2.2 Desire to Attenuate Metal-Based Electron Density in Four-Coordinate Iridium Monohydride Complexes

The previously synthesized Vaska-type iridium (I) monohydride complex (**3**) $HIr(N_2)(L^{mAd})_2$ (Chapter 1) displayed reactivity towards an array of substrates, in particular, strong Brønsted bases.[2] Deprotonation of an equilibrium mixture of $H_2Ir(N_2)(L^{mAd})_2$ (**3**)

/$H_2Ir(\kappa^2$-*P*,*C*-$L^{mAd})(L^{mAd})$ (**4**) with *n*-butyl lithium or *t*-butyl lithium cleanly affords the anionic complex Li[$HIr(\kappa^2$-P,*C*–$L^{mAd})(L^{mAd})$] (**8**) that can be readily protonated back to the equilibrium mixture (**3**) / (**4**) upon addition of 2,6–diisopropylaniline ($C_{12}H_{19}N$) or pentafluorophenol (C_6F_5OH) (Scheme 1.14, Chapter 1). Examination of the geometric structure of anionic complex (**8**) reveals a d^8 square planar geometry with double occupation of the four nonbonding d_{xz}, d_{yz}, d_{xy}, and d_z^2 orbitals.

With many routes available to structurally or electronically modify the modonodentate phosphine L^{mAd}, we decided that it was crucial to preserve the steric properties of the *iso*-propyl groups and the C-H resistivity of the adamantyl moiety. These structural scaffolds successfully suppress C–H bond activation allowing for the isolation of the monohydride complex (**3**) $H_2Ir(N_2)(L^{mAd})_2$ and anionic complex (**8**) Li[$HIr(\kappa^2$-P,*C*–$L^{mAd})(L^{mAd})$]. In this context, we desired to avoid oxidation events as seen from reactivity studies on complex (**8**) with an array of substrates (Chapter 1). We turned to the convenient and elementary electronic modification approach pioneered by Tolman. [3, 4]

Seminal studies by Tolman uncovered the electron donor-acceptor relationships in organophosphorus ligands using the nickel complex $Ni(CO)_3P(X_1X_2X_3)$ (where X = alkyl or alkoxide groups). [5] Each systematic insertion of an oxygen atom between an alkyl group (X_1, X_2, and X_3) and the phosphorus atom resulted in a 5 cm^{-1} increase in the carbonyl (CO) stretching frequency. Carbonyl groups attached to metal complexes, as in the nickel complex studied by Tolman, are well known to give valuable IR spectroscopic fingerprints for correlating the electron donor-acceptor properties of ligands. [6] An increase in the carbonyl IR stretching frequency is a result of reduced $d_{Ni} \rightarrow \pi^*_{CO}$ back donation and therefore reduced electron density at the metal center. Phosphinite ligands serve as electron withdrawing surrogates to phosphines (PR_3), without compromising the strong σ–donation character. [6]

The general route to phosphinites is the replacement of the methylene carbon with an oxygen atom. The incorporation of an oxygen atom leads to an accessible P-O σ* orbital. This typically increases the Lewis acidity at the iridium metal center via ($d_{Ir} \rightarrow \sigma^*_{P\text{-}O}$) π back donation, ultimately serving to attenuate the electron density at iridium and stabilize lower oxidation states, as seen from previously mentioned studies by Tolman. Other electronic effects are possible, especially in phosphinite PCP pincer complexes. For example, the incorporation of an oxygen atom into the methylene positions of the PCP pincer complex (κ^3-2,6-$C_6H_3(CH_2PR_2)_2$)Ir increases the electron density at the metal center, which is in direct contrast to the L^{oAd} phosphinite. This increase of electron density is due to inductive effects from the aryl backbone directly bound to the iridium center in (κ^3-2,6-$C_6H_3(OPR_2)_2$)Ir. In the monodentate phosphinite L^{oAd}, we would expect the lowering of P–O bonding and antibonding orbital energies, as compared to the corresponding P–C bond energies. This is a consequence of the increased electronegativity and orbital overlap from oxygen (Figure 2.1).

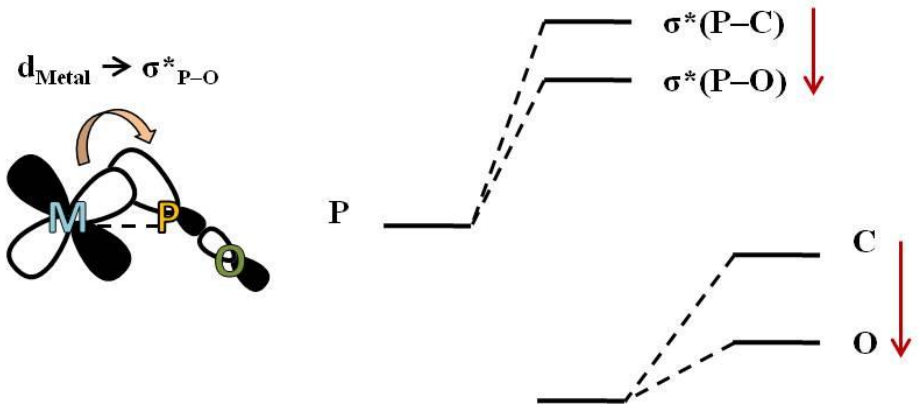

Figure 2. 1. Depiction of $d_{Metal} \rightarrow \sigma^*_{P\text{-}O}$ π back donation in phosphinites.

The electronic effects that phosphinites impart on metal complexes has been utilized in important bond activations, [7, 8] hydrogenations, [9-101112] dehydrogenations, [13-1415 16] and asymmetric catalysis. [17] Bergman demonstrated the usefulness of a phosphinite ancillary ligand with the isolation of and characterization of a preagostic Rh-H interaction and C-H

bond functionalization from a rhodium(I) phopshinite complex [RhCl(*i*-Pr_2POXy)(PPh_3)]$_2$. [18] Therefore, we employed the electronic modification of replacing a methylene group with an oxygen atom, thereby synthesizing the monodentate phosphinite L^{oAd} P(O^1Ad)(*i*-Pr)$_2$.

2.3 Synthetic Access to a Phosphinite Analogue of L^{mAd}

We reasoned that the simple replacement of the methylene group in L^{mAd} with an oxygen atom would provide a ligand with comparable topological properties but enhanced pi–acceptor characteristics. Therefore, we targeted the ligand P(O^1Ad)(*i*-Pr)$_2$ as a phosphinite analogue to the trialkyl phosphine L^{mAd}. Synthetic access to P(O^1Ad)(*i*-Pr)$_2$ (L^{oAd}; oAd = oxy-1-adamantyl) was achieved by the addition of a THF slurry of LiO^1Ad (O^1Ad = adamantoxide, $OC_{10}H_{15}$) to $[(CH_3)_2CH]_2PCl$ (di–isopropylchlorophosphine) followed by multiple crystallizations in pentane at –35 ˚C (synthesis is Scheme 2.4). Attempts at purifying the phosphinite L^{oAd} by protonation with HCl or distillation resulted in Michaelis-Arbuzov–type rearrangements [19] or decomposition to a phosphine oxide product, as determined by $^{31}P\{^1H\}$ NMR. Thus, multiple fractional crystallization was the only reliable method to purify L^{oAd}. As expected, $^{31}P\{^1H\}$ NMR spectroscopy revealed the L^{oAd} chemical shift to be deshielded (δ = 119 ppm) as compared to L^{mAd} (δ = -12 ppm) (X-ray crystal structure shown in Figure 2.2, ^1H NMR shown in Figure 2.3).

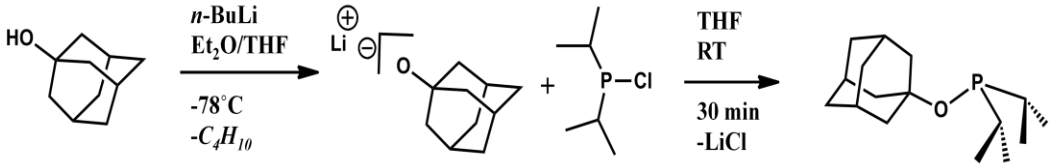

Scheme 2. 1. Synthesis of phosphinite ligand P(O^1Ad)(i-Pr)$_2$ (L^{oAd}; oAd = oxygen-1-adamantyl).

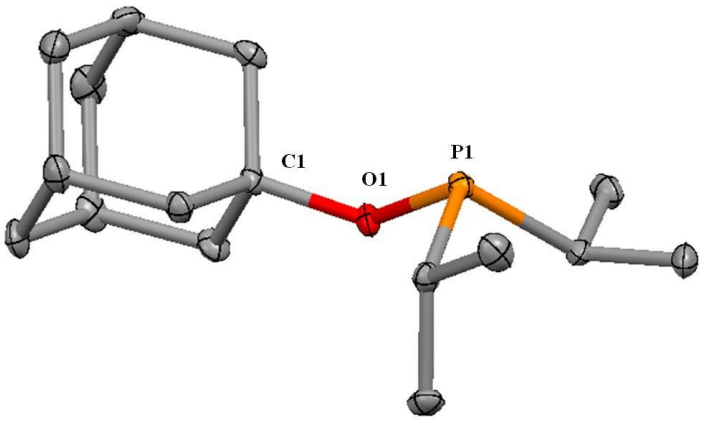

Figure 2. 2. X-ray crystal structure of phosphinite L^{oAd}. Thermal parameters are set to 30% probability and hydrogen atoms were removed for clarity.

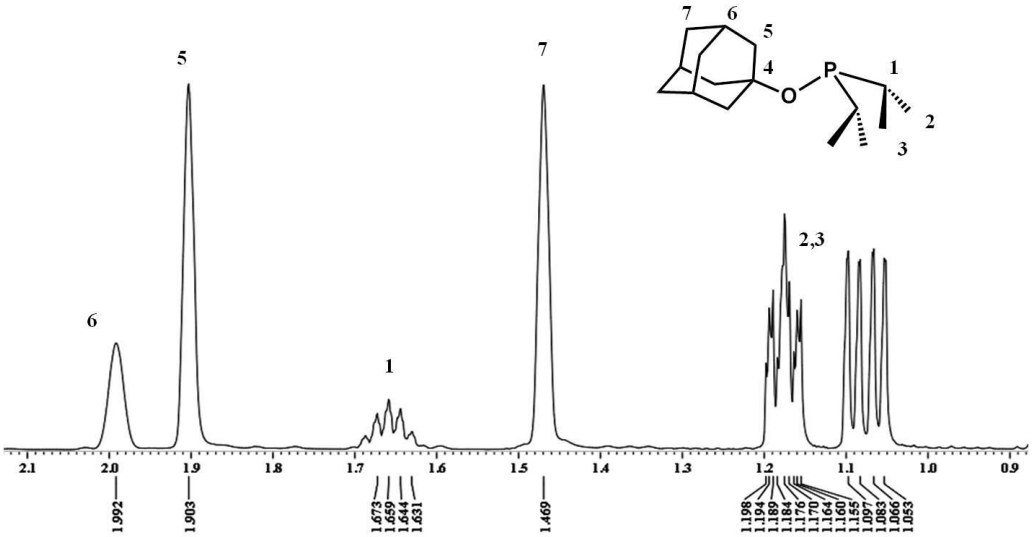

Figure 2. 3. ^{1}H NMR of phosphinite L^{oAd} $P(O^1Ad)(i\text{-}Pr)_2$.

Treatment of a THF solution of 4.0 equivalents of phosphinite L^{oAd} with 1.0 equivalent of $[Ir(COD)Cl]_2$ under an H_2 atmosphere provided $H_2IrCl(L^{oAd})_2$ (**11**) in 49% yield (Scheme 2.2). X–ray crystallographic data obtained for (**11**) $H_2IrCl(L^{oAd})_2$ is shown in Figure 2.4 and contains similar topological parameters when compared to L^{mAd} complex (**2**) $H_2IrCl(L^{mAd})$. The main difference in L^{oAd} complex (**11**) is the shorter bond distances to the adamantyl unit P–O (1.626(5) Å), $O–C_{adamantyl}$ (1.472(8) Å) as compared to L^{mAd} $P–C_{methylene}$ (1.842(4) Å), $C_{methylene}–C_{adamantyl}$ (1.532(5) Å) (comparison of bond distances shown in Table 2.1).

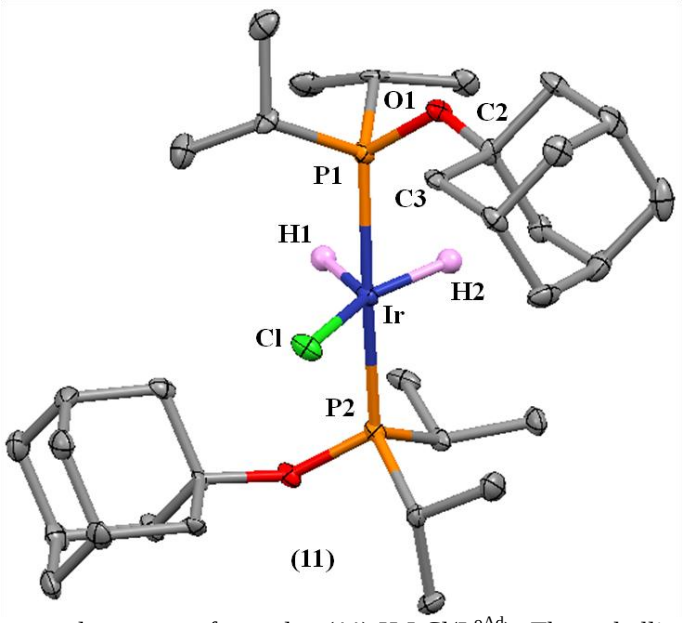

Figure 2. 4. X–ray crystal structure of complex (**11**) $H_2IrCl(L^{oAd})_2$. Thermal ellipsoids are set to 30% probability. Hydrogen atoms on the phosphinite ligand were removed for clarity.

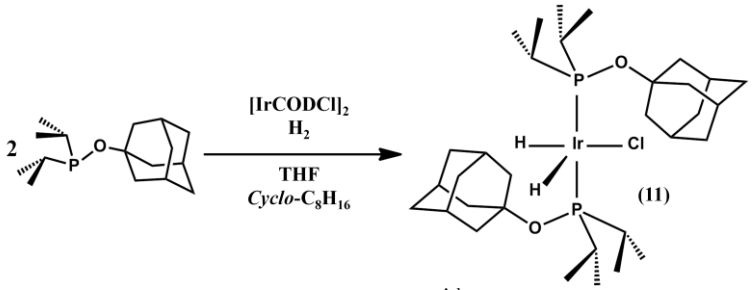

Scheme 2. 2. Synthetic access to complex (**11**) $H_2IrCl(L^{oAd})_2$.

Table 2. 1. Comparison of metrical parameters for complexes (**1**) and (**11**). E = C1 for phosphine or O1 for phosphinite and C2 = ^{1}Ad, i.e. the bridgehead carbon in the adamantyl cage.

Selected Bond	$H_2IrCl(L^{mAd})_2$ (2)	$H_2IrCl(L^{oAd})_2$ (11)
Ir-Cl	2.442(1) Å	2.407(2) Å
Ir-P	2.300(1) Å	2.287(2) Å
P-E	1.842(4) Å	1.626(5) Å
E-C2	1.532(5) Å	1.472(8) Å
Ir-E	3.462(1) Å	3.418(1) Å
Ir-C3	3.314(1) Å	3.469(1) Å

We wanted to assess the behavior of L^{oAd} complexes with reactions previously established for the L^{mAd} system. In attempts to synthesize an analogue of monohydride complex (**3**) $H_2Ir(N_2)(L^{mAd})_2$, a thawing 1:1 Et_2O:C_5H_{12} solution of 1.0 equivalent of *n*-BuLi

was added to complex (**11**) under an N_2 atmosphere affording iridacycle complex (**12**) $H_2Ir(\kappa^2$-*P*,*C*-$L^{oAd})(L^{oAd})$. Crystallization at –35 ˚C produced X–ray quality single crystals (Scheme 2.3 and Figure 2.5). Cyclometallated complex (**12**) appears to closely parallel the analogous L^{mAd} iridacycle complex (**4**). Both complexes contain broad features in the ^{1}H NMR at room temperature and possess severe *exo* ring strain in the solid state structures (Figure 2.11 shows a comparison of ring strain and NMR data for complex (**12**) is shown in Figure 2.6 and complex (**4**) shown in chapter 1, Figure 1.14).

The crystal structures (**12**) $H_2Ir(\kappa^2$-*P*,*C*-$L^{oAd})(L^{oAd})$ and (**4**) $H_2Ir(\kappa^2$-*P*,*C*-$L^{mAd})(L^{mAd})$ contain a bound adamantyl carbon with bond distances for (**12**) $Ir–C_{1(adamantyl)}$ = 2.140 Å and (**4**) $Ir–C_{1(adamantyl)}$ = 2.135 Å. Moreover, these complexes may contain an η^2-H,C agostic interaction with bond distances for (**12**) $Ir–C_{4(agostic)}$ = 2.900 Å and (**4**) $Ir–C_{4(agostic)}$ = 2.943 Å. Unlike L^{mAd} iridacycle complex (**4**), there is no evidence that supports the existence of an

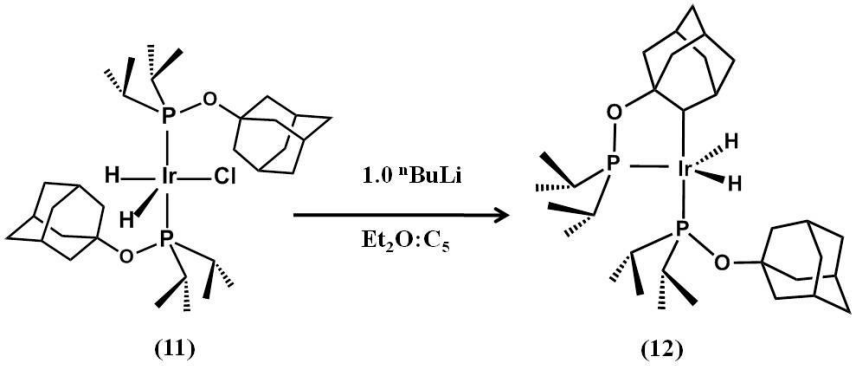

(**11**) (**12**)

Scheme 2. 3. Synthesis of (**12**) $H_2Ir(\kappa^2$-*P*,*C*-$L^{oAd})(L^{oAd})$ from the addition of 1.0 equivalents of *n*-BuLi to complex (**11**) $H_2IrCl(L^{oAd})_2$.

equilibrium between neutral iridacycle (**12**) $H_2Ir(\kappa^2$-*P*,*C*-$L^{oAd})(L^{oAd})$ and an N_2 bound Vaska–type iridium (I) monohydride $HIrN_2(L^{oAd})_2$. This result is likely a consequence from ($d_{Ir} \rightarrow \sigma^*_{P\text{-}O}$) π back donation. Support for π back donation is found from the shortened agostic interaction in iridacycle L^{oAd} complex (**12**). The bond distance is reduced by 0.043 Å, as compared to L^{mAd} complex (**4**), alluding to slightly more electron deficient metal center and a

more tightly bound adamantyl carbon. The increase in Lewis acidity at the metal center may not permit ligand C–H bond reductive elimination.

The ^{31}P and ^{1}H NMR of complex (**12**) contains the broad features and suggests the existence of a dynamic process in solution. Exposure of complex (**12**) to vacuum or increased pressures of N_2 gas were unsuccessful at manipulating the broad features in both the ^{1}H and ^{31}P NMR, unlike the ^{31}P NMR of L^{mAd} phosphine complex (**4**) which can be sufficiently manipulated (Chapter 1). The broad features in the ^{1}H NMR are also persistent in solution for L^{mAd} complex (**4**), but because of the instability of complex (**4**) in NMR solvents, it was unknown if the broad features were from the reversible binding of an exogenous N_2 ligand or another phenomenon in solution. Interestingly, the L^{oAd} iridacycle complex (**12**) is considerably stable in a solution of d^8 toluene, thereby allowing for the investigation into the nature of the two broad singlets in the ^{31}P NMR located at δ = 160.2 ppm and 156.1 ppm

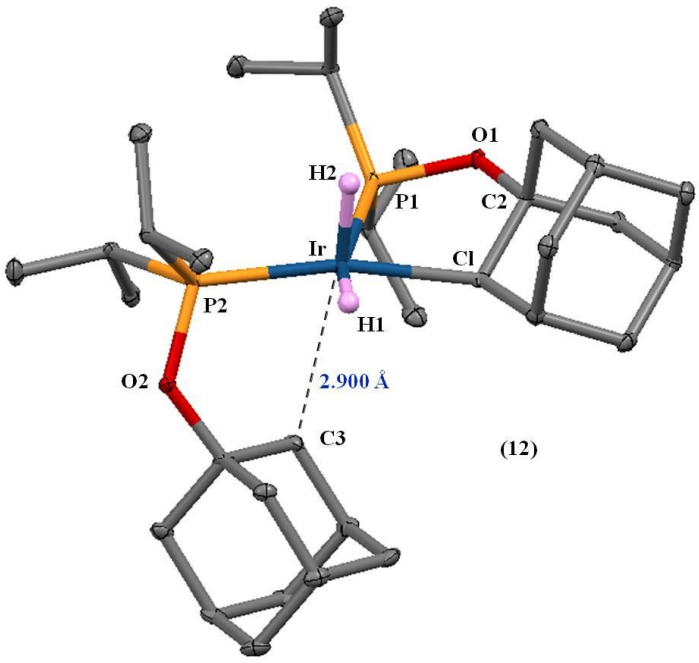

Figure 2. 5. Crystal structure of phosphinite complex (**12**) $H_2Ir(\kappa^2\text{-}P,C\text{-}L^{oAd})(L^{oAd})$. Hydrogen atoms removed for clarity. Thermal ellipsoids are set at 30% probability.

(25˚C, C_6D_{12}) and the broad features in the ^{1}H NMR. We found that the broad features in the NMR represent an intramolecular dynamic process established amongst the three agostically–bound adamantyl methylene groups at the 2–position within the cage (^{1}H NMR shown in Figure 2.6).

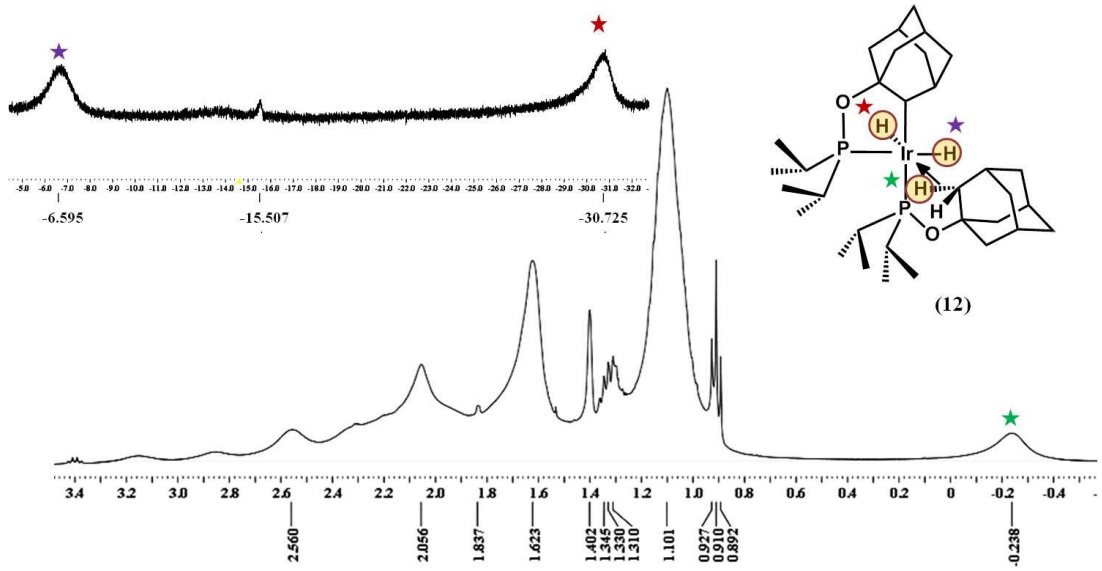

Figure 2. 6. 400 MHz ^{1}H NMR of complex (**12**) $H_2Ir(\eta^2$-P,C-$L^{oAd})(L^{oAd})$ at 298 K in C_6D_{12}. Colored stars represent the corresponding three proton signals. See text for further details.

2.4. VT NMR Studies of the Cyclometallated L^{oAd} Complex (12)

The ability of complex (**4**) to reversibly bind N_2 is attributed to the interplay between two unfavorable phenomenon, *exo* ring strain and the instability inherent in the formed low–coordinate Vaska–type iridium (I) monohydride complex (**3**). In stark contrast to L^{mAd} complex (**3**), L^{oAd} complex (**12**) is stable in a solution of d_8–toluene. This stability allows for the use of VT NMR methods to further elucidate the broad features in the NMR. The ^{31}P and ^{1}H Variable Temperature (VT) NMR studies of complex (**12**) in d_8–toluene were performed in the temperature range –80 ˚C to 25 ˚C and revealed the existence of one complex in solution which contains an agostic interaction. Resolution of the broad features in the NMR and J-coupling values occurred upon cooling to –60 ˚C, providing evidence that at room temperature

one of the adamantyl ligands is undergoing rapid exchange (Figure 2.7, Figure 2.8, Figure 2.9). The broad features at δ = –0.45 ppm $^{1}J_{CH}$ = 123 Hz (Figure 2.7) in the ^{1}H NMR at room temperature correspond to the agostic interaction. Based on integration values, this represents six protons and is constant throughout the temperature range –60 ˚C to 25 ˚C. According to these integration values the dynamic equilibrium at room temperature is a result of all three methylene groups located at the 2–position of one adamantyl unit undergoing rapid exchange for the agostic interaction. The eventual resolution of the single agostic proton occurs at –60 ˚C (integration 5:1, see Figure 2.7). We speculate that at lower temperatures, below –60˚C, other issues become problematic, e.g. poor solubility and shimming difficulties.

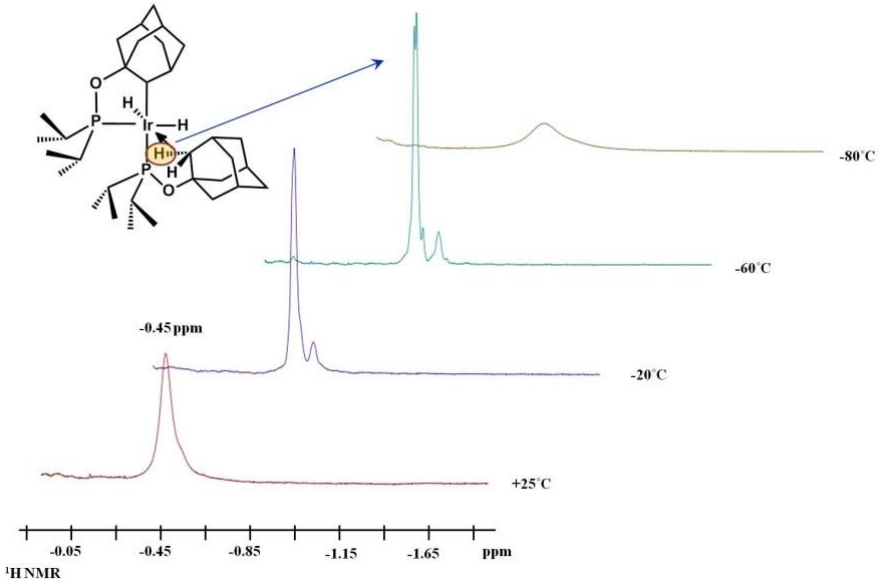

Figure 2. 7. 500 MHz ^{1}H VT NMR of phosphinite iridacycle complex (**12**) $H_2Ir(\eta^2\text{-P,C-L}^{oAd})(L^{oAd})$ in d_8–toluene revealing a dynamic equilibrium at 25 ˚C that becomes more static at –60˚C. The region of the spectrum corresponds to the highlighted agostically bound protons.

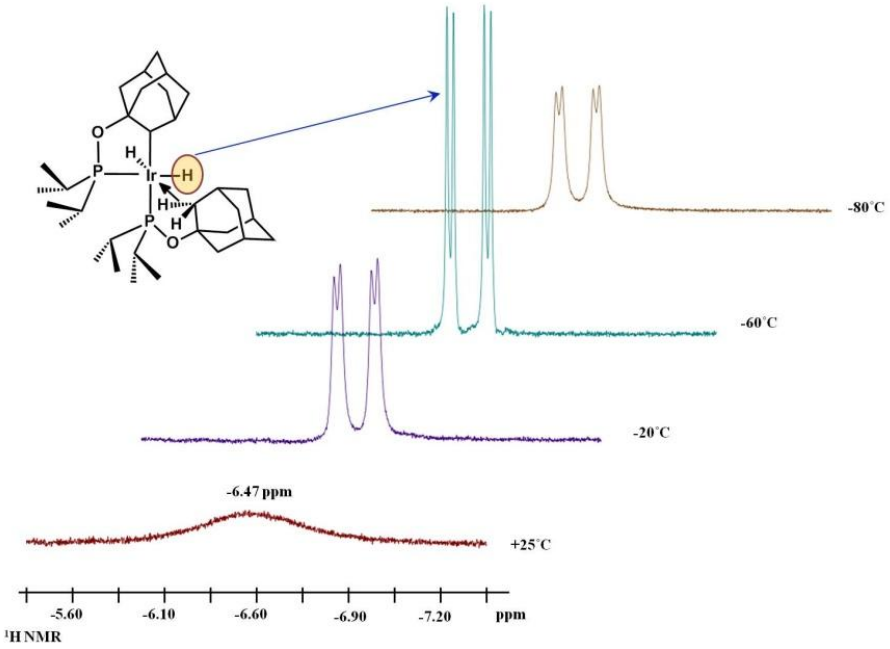

Figure 2. 8. 500 MHz 1H VT NMR of phosphinite iridacycle complex (**12**) $H_2Ir(\eta^2\text{-P,C-L}^{oAd})(L^{oAd})$ in d^8–toluene revealing a dynamic equilibrium at 25 ˚C that becomes more static at –60˚C. Resolution of both trans $^2J_{HP}$ = 137 Hz and cis $^2J_{HP}$ = 23 Hz coupling. The hydride region of the spectrum shown corresponds to the highlighted proton.

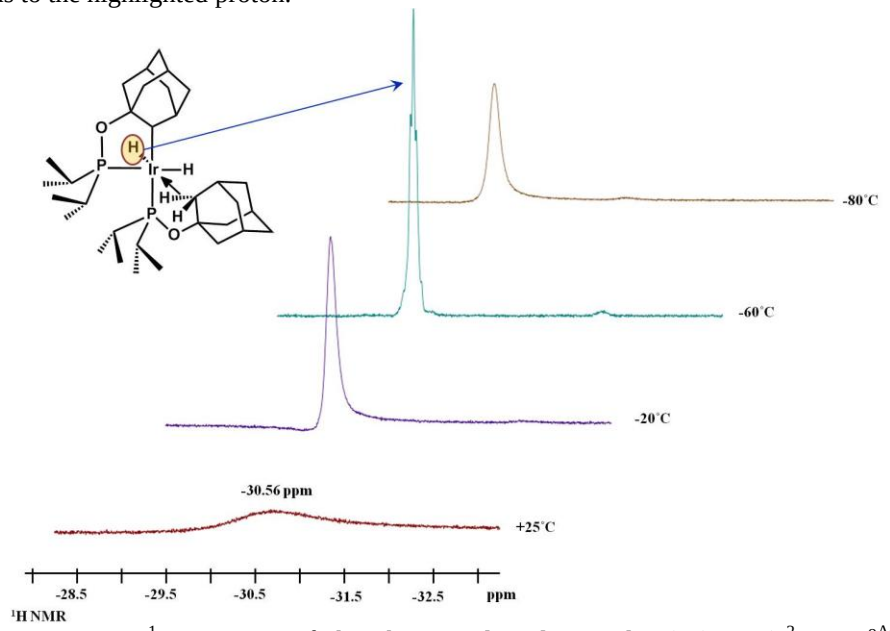

Figure 2. 9. 500 MHz ^{1}H VT NMR of phosphinite iridacycle complex (**12**) $H_2Ir(\eta^2\text{-P,C-L}^{oAd})(L^{oAd})$ in d_8–toluene revealing a dynamic equilibrium at 25 ˚C that becomes more static at -60˚C. Slight resolution of coupling to cis phosphorus ($^2J_{HP}$ = 10Hz) at -60˚C. The hydride region of the spectrum corresponds to the highlighted protons.

Since the agostic interaction is limited to six methylene protons on the adamantyl cage throughout the temperature range of -80 ˚C to 25 ˚C, then N_2 may not have the opportunity to bind to L^{oAd} complex (**12**). No changes to the NMR spectra of (**12**) were observed, even under increased pressures of N_2 gas (up to 4 atm). Thus, we speculate that the L^{oAd} version of the Vaska type Iridium (I) monohydride is perhaps fleetingly formed in solution at 25 ˚C or that N_2 binding does not occur due to obstruction by the agostic interaction, mirroring that of the phosphine tri–hydride complex (**5**) $IrH_3(L^{mAd})_2$ (Chapter 1).

Table 2. 2. Comparison of X–ray metrical parameters , ^{1}H and ^{13}C spectroscopic properties relevant to the agostic interaction in $H_2Ir(\eta^2$-P,C-$L^{oAd})(L^{oAd})$ (**12**). Agostic complexes are highlighted with bold

Complex	^{1}H NMR Resonance of 2–Ad position (ppm)	$^1J_{CH}$ coupling constant of C6 carbon atom ^{13}C NMR, in Hz	Distance to agostic bound Carbon X–ray data *d*(Ir–C) in Å
$H_2Ir(\kappa^2$-*P*,*C*-$L^{oAd})(L^{oAd})$ (12)	**-0.45**	**123**	**2.900**
$H_2Ir(\kappa^2$-*P*,*C*-$L^{mAd})(L^{mAd})$ (4)	**-0.45**	**Not Amenable**	**2.943**
$IrH_3(L^{mAd})_2$ (5)	**1.34**	**123**	**3.101**
$H_2Ir(OC_6F_5)(L^{mAd})_2$ (10)	**1.57**	**123**	**2.903**
$H_2IrCl(L^{oAd})_2$ (11)	2.05	131	3.470
$H_2IrCl(L^{mAd})_2$ (2)	1.76	127	3.315

Despite the shortened agostic bond distance and the stability in NMR solvents, iridacycle complex (**12**) readily activates the O–H bond in water to form complex (**13**) $H_2Ir(OH)(L^{oAd})_2$. The oxidative addition of water to L^{oAd} complex (**12**) $H_2Ir(\eta^2$-P,C-$L^{oAd})(L^{oAd})$ was accomplished by the addition of 1.0 equivalents of H_2O in C_6D_6, which closely parallels the reactivity of L^{mAd} complex (**4**) $H_2Ir(\eta^2$-P,C-$L^{mAd})(L^{mAd})$. Furthermore, L^{mAd} complex (**6**) $H_2Ir(OH)(L^{mAd})_2$ and L^{oAd} complex (**13**) $H_2Ir(OH)(L^{oAd})_2$ have similar metrical parameters as seen from the X–ray crystal structure (Figure 2.10). The spectroscopic features of complex (**13**) reveals a downfield shift of the metal–hydride to -28.3 (t, 2H, $^2J_{HP}$ = 14 Hz), and a slightly weaker IR feature at 2226 cm^{-1} (for comparison, L^{mAd} complex (**6**) $H_2Ir(OH)(L^{mAd})_2$ (Chapter

1) contains a metal–hydride resonance in the ^{1}H NMR at -29.3 (t, 2H, $^{2}J_{HP}$ = 14 Hz) and the IR feature for the Ir–H is located at 2247 cm^{-1}).

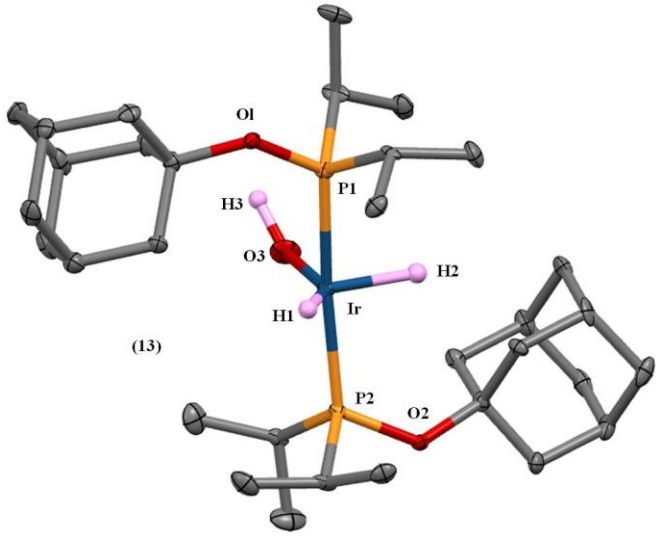

Figure 2. 10. X-ray crystal structure of complex (**13**) $H_2Ir(OH)(L^{oAd})$. Thermal ellipsoids are set to 30% probability. Hydrogen atoms are removed for clarity except the two located on the iridium metal center and the hydroxide proton, which were found from the electron density difference map.

The topological and spectroscopic similarities between iridacycles (**4**) $H_2Ir(\kappa^2$-*P*,*C*-$L^{mAd})(L^{mAd})$ and (**12**) $H_2Ir(\kappa^2$-*P*,*C*-$L^{oAd})(L^{oAd})$, as compared by X-ray crystallography (Figure 2.11) and NMR data, further highlight the uniqueness of the phosphine L^{mAd} ligand manifold in stabilizing a Vaska-type iridium (I) monohydride complex (**3**) $HIr(N_2)(L^{mAd})_2$. The inability to isolate a L^{oAd} phosphinite Vaska-type monohydride is likely the result of an electronically satisfied iridium metal center. We speculate N_2 promotes C-H bond reductive elimination in cyclometallated L^{mAd} complex (**4**) $H_2Ir(\kappa^2$-*P*,*C*-$L^{mAd})(L^{mAd})$. Thus, the stabilization of L^{mAd} complex (**3**) is from the ability of N_2 to act as a pi-acid towards an electron rich metal center. For phosphinite L^{oAd} complex (**12**) $H_2Ir(\kappa^2$-*P*,*C*-$L^{oAd})(L^{oAd})$, the ligand attenuates electron density thereby rendering the binding of N_2 unnecessary. Furthermore, L^{oAd} iridacycle complex (**12**) allows for the use of VT NMR methods which confirmed the agostic interaction

in solution (Table 2.2) and future studies may reveal the existence of a phosphinite Vaska-type iridium (I) monohydride at increased temperatures.

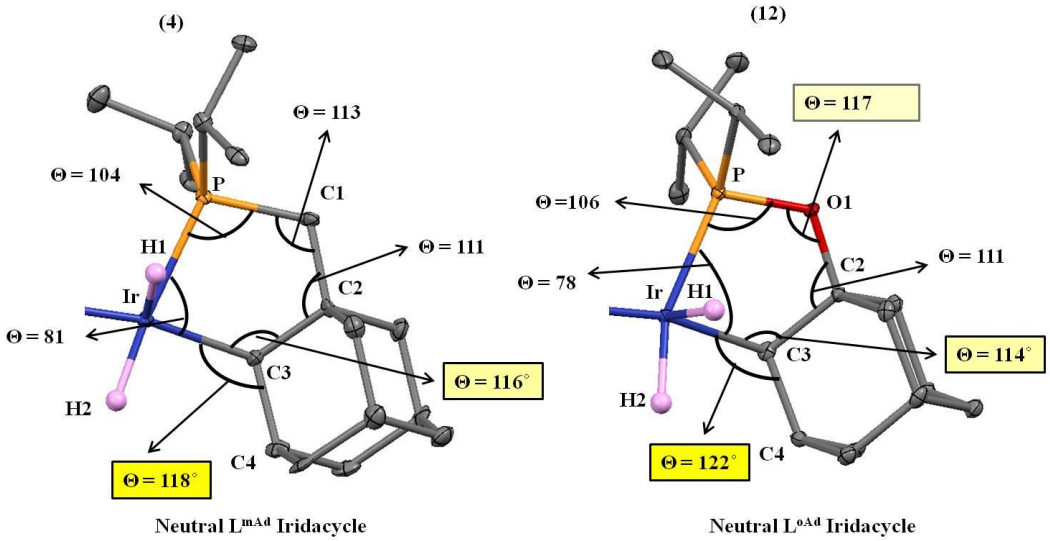

Figure 2. 11. Comparison of metrical parameters complex (**4**) $H_2Ir(\kappa^2\text{-}P,C\text{-}L^{mAd})(L^{mAd})$ and complex (**12**) $H_2Ir(\kappa^2\text{-}P,C\text{-}L^{oAd})(L^{oAd})$. Thermal ellipsoids are set to 30% probability. Hydrogen atoms were removed for clarity except those bound to the iridium metal center.

2.5 Alkyl Anion Binding to an Iridium Phosphinite Complex

Attempts to synthesize the L^{oAd} analogue of L^{mAd} complex (**9**) $Li[12\text{-}c\text{-}4)_2][H_2Ir(\kappa^2\text{-}P,C\text{–}L^{mAd})(L^{mAd})]$ by deprotonation of (**12**) $H_2Ir(\kappa^2\text{-}P,C\text{-}L^{oAd})(L^{oAd})$ with 1.0 equivalent of *n*-BuLi or 1.0 equivalent of CH_3Li provides instead the 6-coordinate anions (**14**) $Li[12\text{-}c\text{-}4)_2][H_2Ir(C_4H_9)(\kappa^2\text{-}P,C\text{–}L^{oAd})(L^{oAd})]$ and (**15**) $Li[12\text{-}c\text{-}4)_2][H_2Ir(CH_3)(\kappa^2\text{-}P,C\text{–}L^{oAd})(L^{oAd})]$ with accompanied alkyl binding (Scheme 2.4 and Figure 2.12). Anionic complex (**14**) consists of an arrested *n*-butyl group still intact upon isolation and, similarly, anionic complex (**15**) possesses an intact methyl group. This was not observed for the L^{mAd} system and lends supports to one proposed mechanism for metal hydride deprotonation; nucleophilic addition followed by C–H bond reductive elimination.

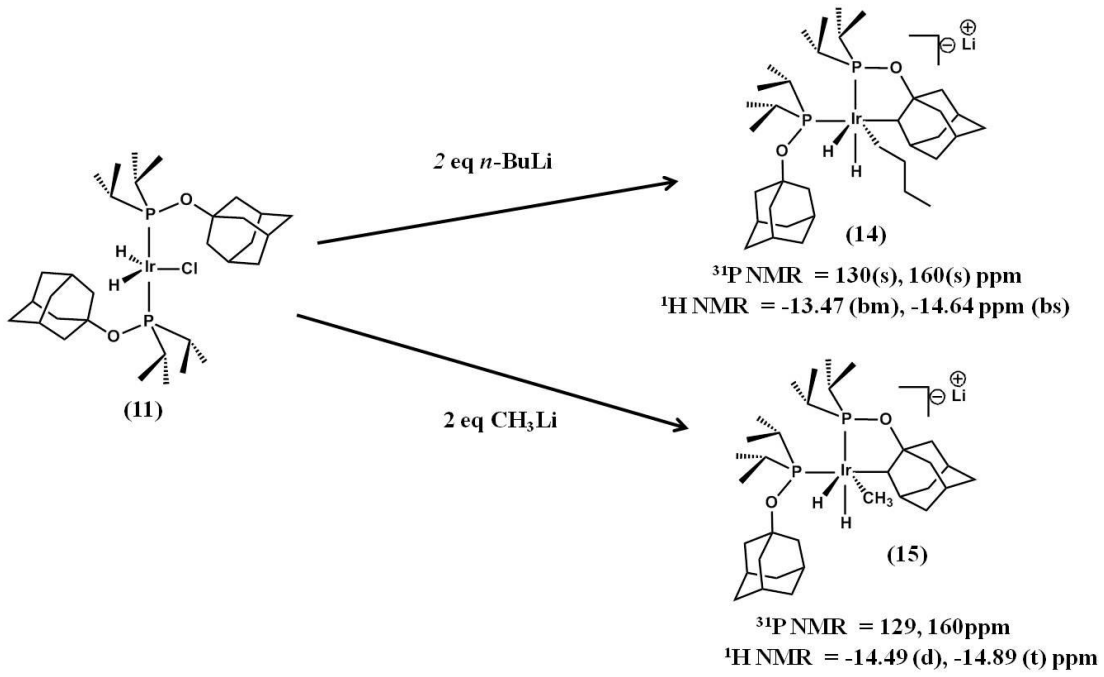

Scheme 2. 4. Formation of anionic complexes *n*–butyl (**14**) and methyl (**15**) from the addition of *n*-BuLi and CH_3Li to complex (**11**) $H_2Ir(Cl(L^{oAd})_2$.

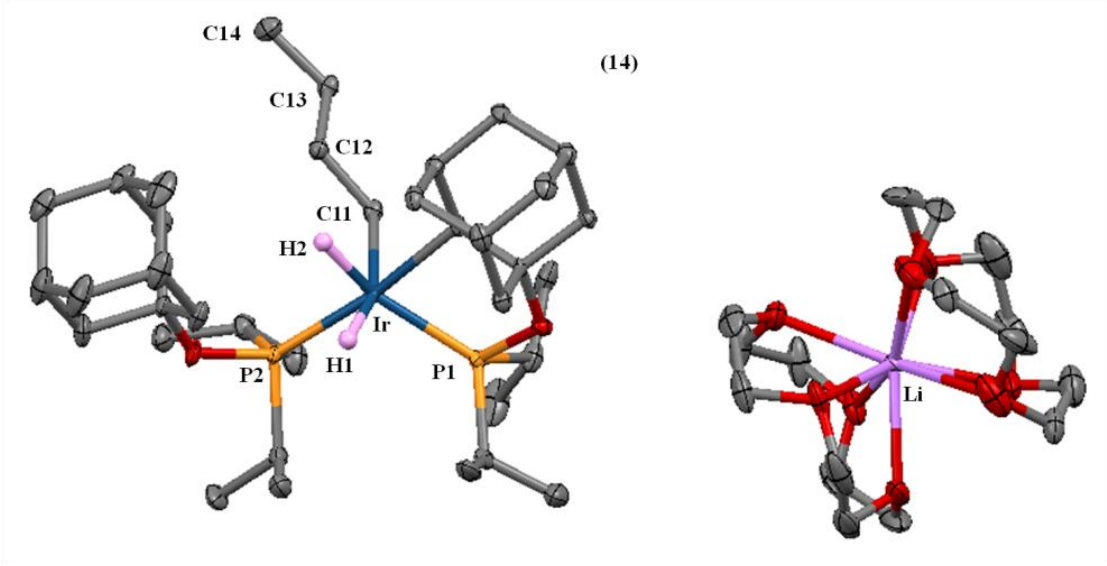

Figure 2. 12. X-ray crystal structure of complex (**14**) Li[12-c-4)$_2$][$H_2Ir(C_4H_9)(\kappa^2$-P,*C*–$L^{oAd})(L^{oAd})$]. Thermal ellipsoids are set to 30% probability. Hydrogen atoms are removed for clarity except the two located on the iridium metal center which was found from the electron density difference map.

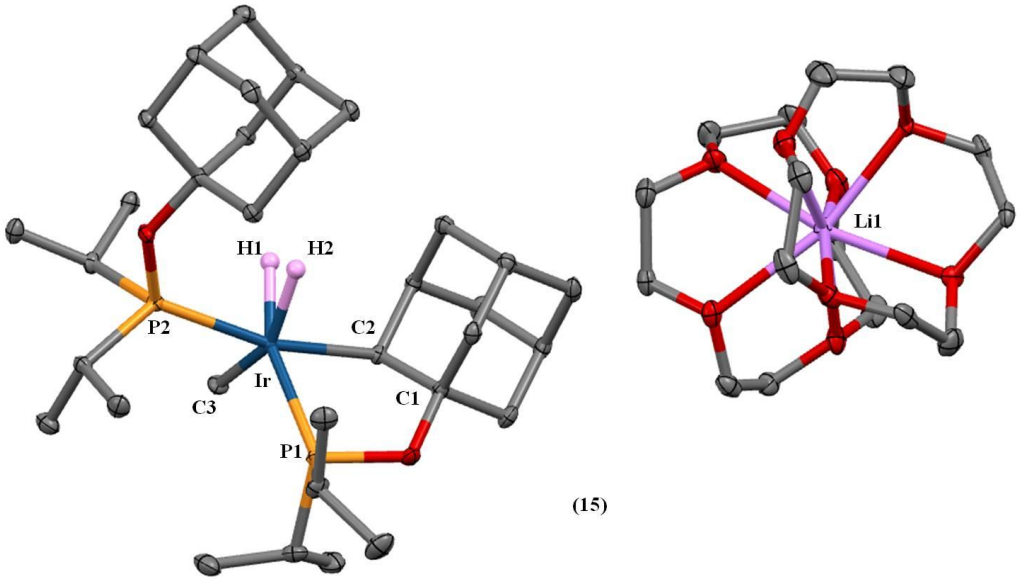

Figure 2. 13. X-ray crystal structure of complex (**15**) Li[12-c-4)$_2$][H$_2$Ir(CH$_3$)(κ^2-P,*C*–L^{oAd})(L^{oAd})]. Thermal ellipsoids are set to 30% probability. Hydrogen atoms are removed for clarity except the two located on the iridium metal center which was found from the electron density difference map.

Reductive elimination of *n*–butane from *n*–butyl anion (**14**) occurs upon heating to 45 ˚C (several hours to completion) or 100 ˚C (several minutes to completion) in pentane, cyclohexane, toluene, or benzene with concomitant formation of neutral iridacycle (**12**) H$_2$Ir(κ^2-*P*,*C*-L^{oAd})(L^{oAd}), as assayed by ^{31}P and ^{1}H NMR. Exposure of anionic complex methyl (**15**) Li[12-c-4)$_2$][H$_2$Ir(CH$_3$)(κ^2-P,*C*–L^{mAd})(L^{mAd})] to 45 ˚C or 100 ˚C heat in pentane, cyclohexane, toluene or benzene produces C–H bond reductive elimination, thus ejecting methane followed by what is likely a protonation event to form complex (**12)** H$_2$Ir(κ^2-*P*,*C*-L^{oAd})(L^{oAd}) (more rapid than *n*–butyl anion (**14**)). These studies were performed at 45 ˚C and 100 ˚C with deuterated solvents d$_6$–benzene (C$_6$D$_6$), d$_8$–toluene (C$_7$D$_8$), and d$_{12}$–cyclohexane (C$_6$D$_{12}$). Anionic complexes *n*–butyl (**14**) and methyl (**15**) rapidly incorporate deuterium into the formed neutral iridacycle complex (**12**) H$_2$Ir(κ^2-*P*,*C*-L^{oAd})(L^{oAd}) upon exposure to heat as evidenced by ^{2}H NMR spectroscopy. Isotopic incorporation into the ligand substantiates the C–H bond reductive elimination of butane and methane from *n*–butyl (**14**) and methyl (**15**),

respectively, with the concomitant formation of a fleeting 4-coordiate anionic iridium monohydride complex (**16**) Li[HIr(κ_2-P,*C*–L^{oAd})(L^{oAd})]$^-$ (Scheme 2.5).

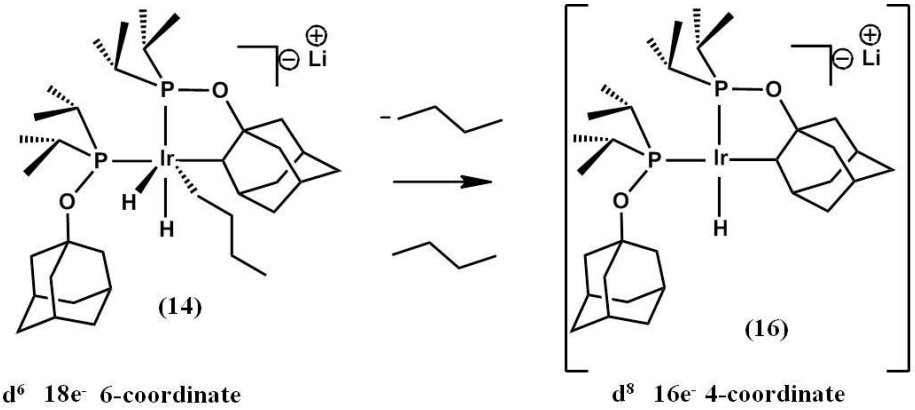

Scheme 2. 5. Putative 2–coordinate L^{oad} anion complex (**16**) Li[HIr(κ_2-P,*C*–LmAd)(L^{oAd})]$^-$ produced from the C-H bond reductive elimination of butane.

2.6 Oxidative Behavior of Anionic Phosphinite Complexes Methyl (15) and *n*-Butyl (14)

Although protonation of the metal center is consistently observed, it was unexpected when the addition of 1.0 equivalent of iodine (I_2) to methyl anion complex (**15**) at low temperatures resulted in the formation of complex (**17**) $H_2IrI(L^{oAd})_2$ (right side of Scheme 2.6). We view this reaction as the result of both protonation and oxidation events. Furthermore, a protonation event occurs upon the addition of pyridine to complex (**15**) Li[12-c-4)$_2$][$H_2Ir(CH_3)$(κ^2-P,*C*–L^{oAd})(L^{oAd})] yielding neutral iridacycle (**12**) $H_2Ir(\kappa^2$-*P*,*C*-L^{oAd})(L^{oAd}) (left side of Scheme 2.6). [20]

In efforts to combine the oxidation route provided by I_2 and the protonation reactivity of pyridine, we combined the two reagents in a 1:1 ratio in a thawing C_5H_{12}:Et_2O solution affording a previously studied pyridine–I_2 adduct. [21, 22] Treatment of this freshly prepared reagent to a thawing Et_2O:C_5H_{12} solution of methyl anion complex (**15**) afforded a doubly C–H activated bis-iridacycle complex (**18**) $HIr(\kappa^2$-*P*,*C*-$L^{oAd})_2$ (Scheme 2.6, Scheme 2.7, Figure 2.14) One proposed route to complex (**18**) is oxidatively induced reductive elimination with the ejection of methane and formation of a coordinated cation intermediate (Scheme 2.7).

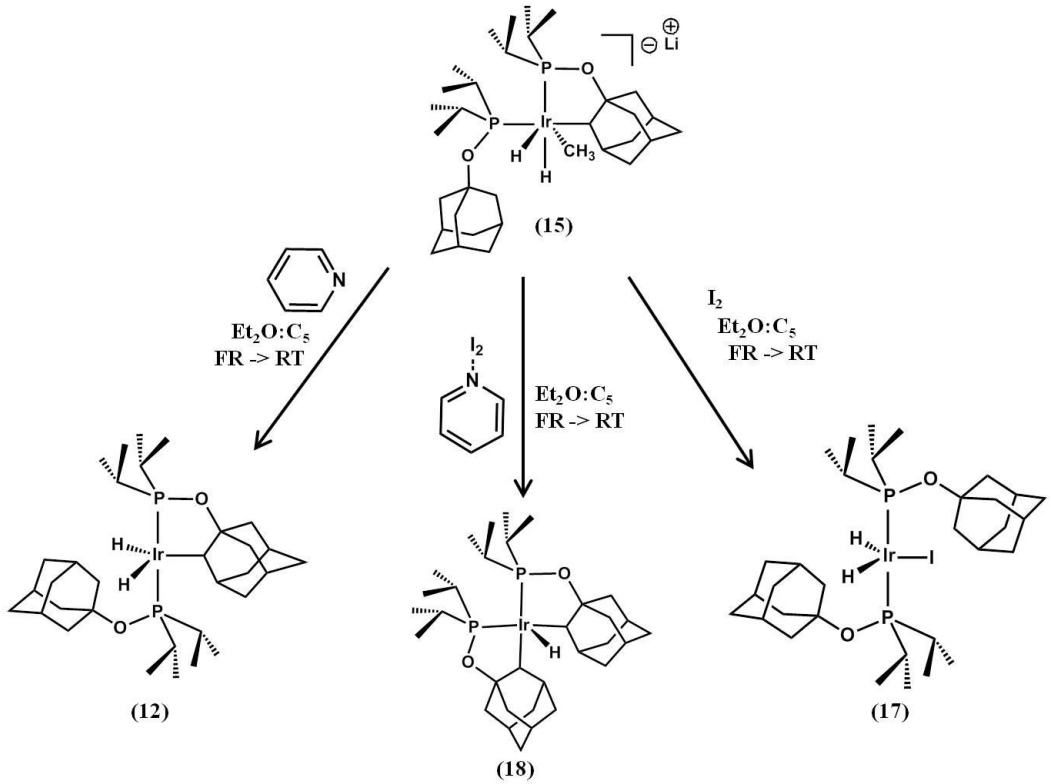

Scheme 2. 6. Formation of complex (**18**) HIr(κ^2-*P*,*C*-L^{oAd})$_2$ from the addition of a pyridine-I_2 adduct to complex (**15**) Li[12-c-4)$_2$][$H_2Ir(CH_3)(\kappa^2$-P,*C*–L^{oAd})(L^{oAd})].

The coordinated cation contains a strongly Brønsted basic pyridine group (either bound to the iodine or in solution) that could engage in H–atom abstraction. In this context, the coordinated cation would participate in substrate induced reductive elimination with the elimination of insoluble pyridinium iodide and the formation of a 3-coordinate iridium phosphinite species (Scheme 2.7). This highly reactive 14–electron T–shaped iridium (I) species would be expected to undergo facile intramolecular C–H bond oxidative addition forming complex (**18**) (Figure 2.14 and proposed mechanism shown in Scheme 2.7). It is the *in-situ* formed pyridine-I_2 adduct that serves as an attenuated oxidant with Brønsted base character that allows for the second intramolecular C–H bond activation, as opposed to oxidation or an intermolecular protonation event. [23-2425]

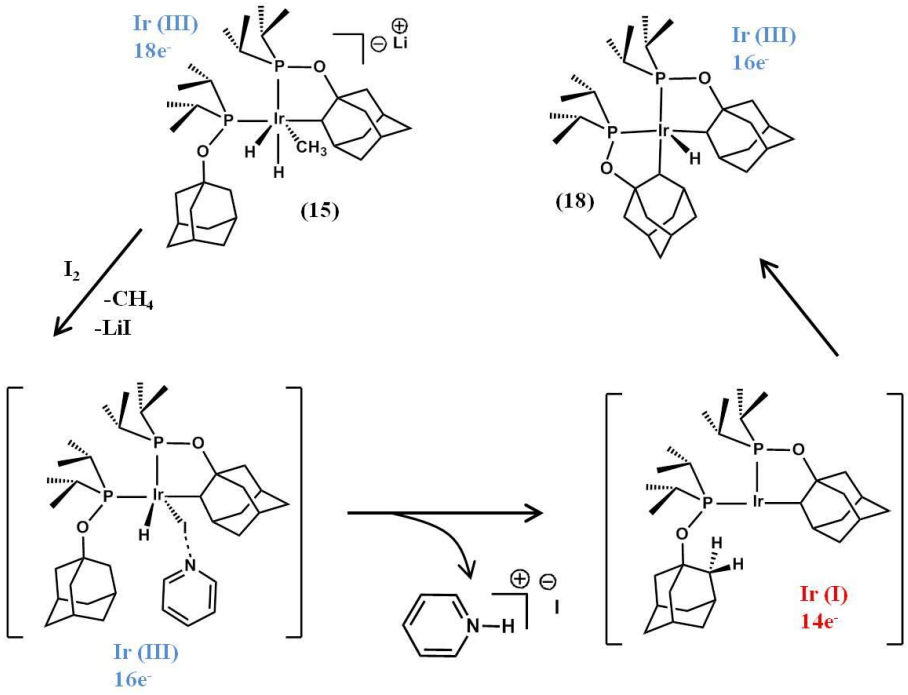

Scheme 2. 7. Proposed mechanism for the formation of complex (**18**) HIr(κ^2-*P*,*C*-L^{oAd})$_2$.

Intramolecular C–H bond activations with the formation of an isolable five membered metallacycle are not uncommon amongst low valent, late transition metal complexes. The uniqueness of the highly distorted square–pyramidal complex (**18**) HIr(κ^2-*P*,*C*-L^{oAd})$_2$ arises because it is the first example of an isolable doubly ligand C–H activated product. A Cambridge Structural Data Base search for doubly C–H activated complexes, including both phosphines and phosphinites, produced zero results. A search for similar phosphinite iridacycles resulted in 2 hits (Ref codes CAHPOS and KAKDIK), of which both are PCP pincer complexes. [26, 27]

Complex (**18**) shows a high aptitude towards oxidative addition of substrates, with the probable driving force emanating from severe ring strain (Figure 2.14). Complex (**18**) HIr(κ^2-*P*,*C*-L^{oAd})$_2$ undergoes rapid substrate induced ligand C–H bond reductive elimination with the addition of an Et$_2$O solution of HCl providing neutral iridacycle complex (**19**) HIr(Cl)(κ^2-*P*,*C*-L^{oAd})(L^{oAd}) (Scheme 2.8). The facile C–H bond reductive elimination of the adamantyl

ancillary ligand is likely the result of severe *exo*-ring strain, although we cannot rule out the alternate mechanism of direct protonation of the C–H bond.

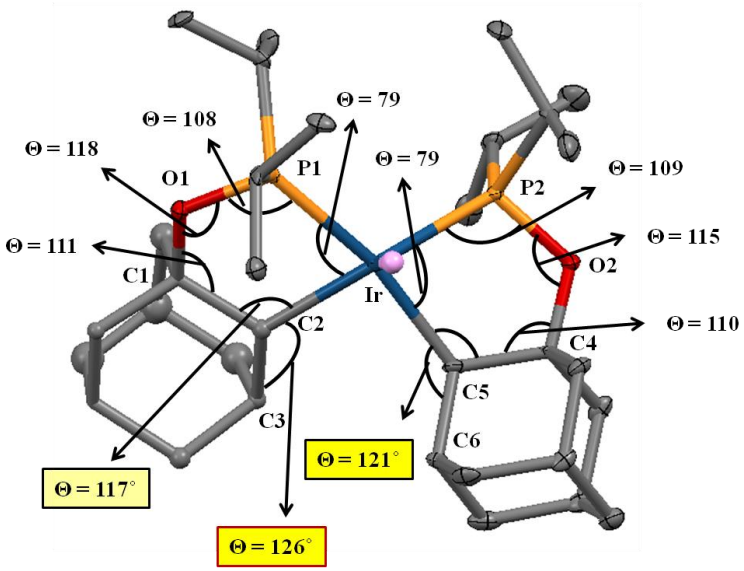

Figure 2. 14. Severe angle strain highlighted in the X-ray crystal structure of complex (**18**) HIr(κ^2-*P*,*C*-L^{oAd})$_2$. Thermal ellipsoids set at 30% probability.

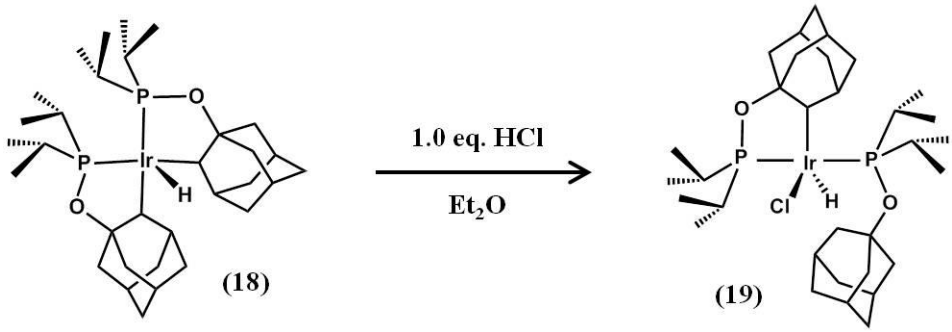

Scheme 2. 8. Synthesis of complex (**19**) HIr(Cl)(κ^2-*P*,*C*-L^{oAd})(L^{oAd}) from the addition of HCl to complex (**18**) HIr(κ^2-*P*,*C*-L^{oAd})$_2$.

2.7 Formation of 4-Coordinate L^{oAd} Anion Monohydrides

In further attempts to isolate a 4-coordinate L^{oAd} anion and a route to probe the nature of the cation, we employed the nucleophilic reagent Me_2Zn. Addition of 2.0 equivalents of Me_2Zn in Et_2O to complex (**11**) $H_2IrCl(L^{oAd})$ provided the rare hetero–bimetallic complex (**20**) $HIr(ZnCH_3)(\kappa^2\text{-}P,C\text{-}L^{oAd})(L^{oAd})$ featuring an iridium-zinc covalent interaction (Scheme 2.9 and Figure 2.15). To our knowledge, this represents the first crystallographically characterized

iridium–zinc covalent bond (based on CSD search using version 5.33 2011). [28] Complex (**20**) contains an agostic interaction with an Ir–C3 bond distance of 3.128(9) Å and an Ir–H bond distance of 2.256 Å. We view the zinc in complex (**20**) to be undergoing a Z-type interaction with iridium, which is formally operating in the +1 oxidation state. The 5–coordinate zinc stabilized anion (**20**) HIr($ZnCH_3$)(κ^2-*P*,*C*-L^{oAd})(L^{oAd}) emulates the reactivity patterns of 6-coordinate anions butyl (**14**) and methyl (**15**), thereby forming neutral iridacycle (**12**) H_2Ir(κ^2-*P*,*C*-L^{oAd})(L^{oAd}) upon exposure to 70 ˚C heat in cyclohexane–d_{12}.

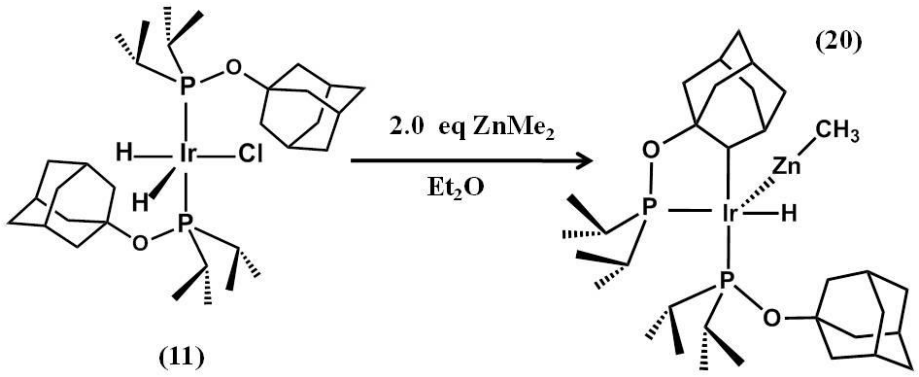

Scheme 2. 9. Formation of (**20**) HIr($ZnCH_3$)(κ^2-*P*,*C*-L^{oAd})(L^{oAd}) from the addition of $ZnMe_2$ to complex (**11**) H_2IrCl(L^{oAd}).

Selected Bond Lengths	
Ir-Zn	2.3344 (6) Å
Ir-P1	2.2934(9) Å
Ir-C3	2.132(3) Å
Ir-C5	3.128(9) Å

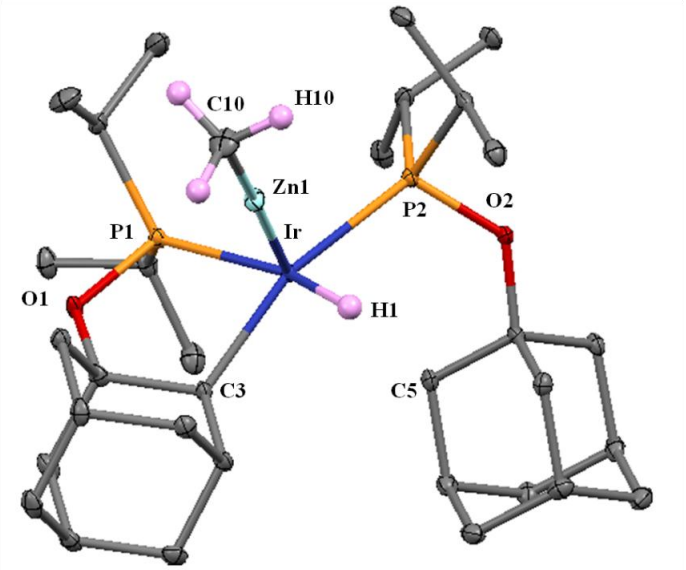

Figure 2. 15. X-ray crystal structure of rare hetero–bimetallic complex (**20**) HIr($ZnCH_3$)(κ^2-*P*,*C*-L^{oAd})(L^{oAd}). Thermal ellipsoids set to 30% probability.

We anticipated that *t*–butyl lithium ($(CH_3)_3CLi$) would form a 4-coordinate L^{oAd} anion, similar to purported complex (**16**), because the sterically encumbered *iso*–butyl group discourages binding. Questioning if the product would be isolable, we proceeded with the addition of 2.0 equivalents of $(CH_3)_3CLi$ to complex (**11**) $H_2IrCl(L^{oAd})$. It was with great excitement that the product was the 4-coordinate hydrido complex (**21**) $[Li_2(12\text{-c-}4)_2][HIr(\kappa^2\text{-P},C\text{–}L^{oAd})(L^{oAd})]_2$ (Figure 2.17, Scheme 2.10) ^1H NMR studies, as expected, did not reveal elimination of hydrogen gas (H_2) at 45 ˚C or 100 ˚C from anionic hydrido complex (**21**) $Li[12\text{-c-}4)_2][HIr(\kappa^2\text{-P},C\text{–}L^{mAd})(L^{mAd})]$. The incorporation of deuterium into the adamantyl unit was observed upon heating hydrido complex (**21**) in deuterated solvents d_6–benzene (C_6D_6), d_8–toluene (C_7D_8), and d_{12}–cyclohexane (C_6D_{12})

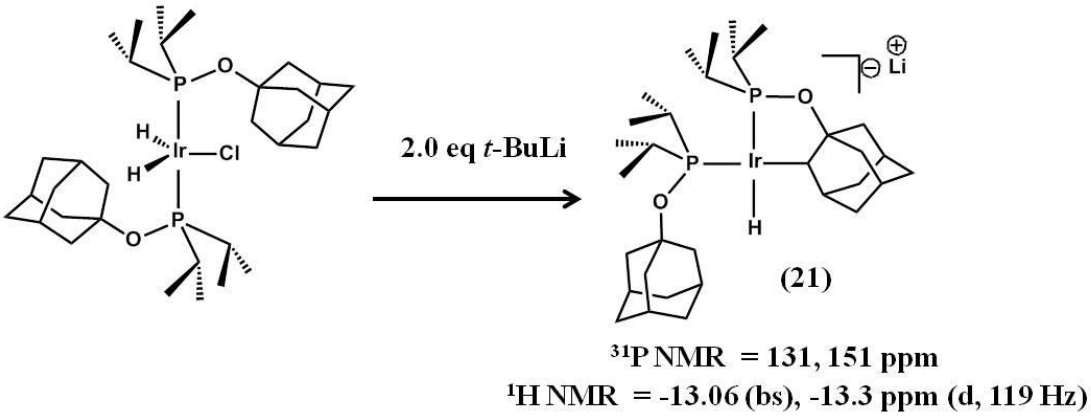

Scheme 2. 10. Synthesis of (**21**) $Li[12\text{-c-}4)_2][HIr(\kappa^2\text{-P},C\text{–}L^{oAd})(L^{oAd})]$ from the addition of 2.0 eq. of $(CH_3)_3CLi$ to complex (**11**) $H_2IrCl(L^{oAd})$.

The solid state X–ray crystal structure for the isolable 4–coordinate anion monohydride complex (**21**) reveals a lithium cation that is bridged by two metal hydrides. Complex (**21**) mirrors the 4–coordinate analogous L^{mAd} anion complex (**8**) $Li[HIr(\kappa_2\text{-P},C\text{–}L^{mAd})(L^{mAd})]^-$ (Chapter 1) and we speculate this to closely resemble the fleeting intermediate formed from heating anionic complexes butyl (**14**) and methyl (**15**). The speculated intermediate that is formed from butyl (**14**) and methyl (**15**) rapidly undergoes a protonation event possibly by deprotonating pentane (C_5H_{12}), cyclohexane (C_6H_{12}), toluene (C_7H_8), or

benzene (C_6H_6) and yields iridacyle complex (**12**) $H_2Ir(\kappa^2\text{-}P,C\text{-}L^{oAd})(L^{oAd})$ and the accompanied alkyl or aryl lithium salt. This is supported from reactivity seen with monohydride complex (**21**), as we notice the formation of neutral iridacycle (**12**) produced over time, even at room temperature during routine NMR characterization. We speculate that the alkyl lithium product RLi (where R = pentyl (C_5H_{11}), cyclo–hexyl (C_6H_{11}), phenyl (C_6H_5), benzyl (C_7H_8)) does not deprotonate newly formed neutral iridacycle (**12**)

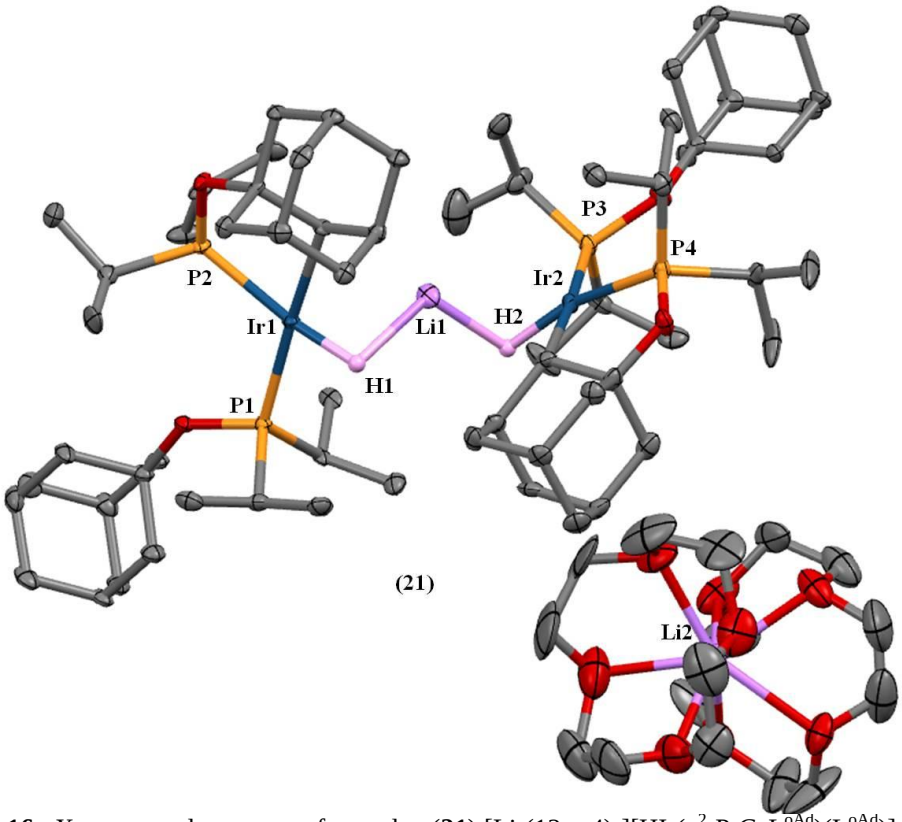

Figure 2. 16. X-ray crystal structure of complex (**21**) $[Li_2(12\text{-}c\text{-}4)_2][HIr(\kappa^2\text{-}P,C\text{–}L^{oAd})(L^{oAd})]_2$. Thermal ellipsoids are set to 30% probability. Hydrogen atoms are removed for clarity except the two located on the iridium metal center which was found from the electron density difference map.

$H_2Ir(\kappa^2\text{-}P,C\text{-}L^{oAd})(L^{oAd})$ because the utilization of 12-crown-4 ether. The use of crowned lithium anions *n*–butyl (**14**), methyl (**15**), and hydrido (**21**) renders the alkyl or aryl lithium product, produced from heating, insoluble in pentane (C_5H_{12}) and cyclo–hexane (C_6H_{12}) upon ejection. Furthermore, formed benzyl lithium or phenyl lithium may be capable of

deprotonating complex (**12**) but the dilute solution these complexes were studied in disfavors this process as seen by unsuccessful attempts at deprotonating complex (**12**) with a concentration of 0.0003M (prototypical concentration of a routine reactivity study) at 298 ˚C in a solution of Et_2O:C_5 by 1.0 equivalent of phenylmagnesiumbromide (PhMgBr). Moreover, attempts at deprotonating complex (**12**) with 1.0 equivalent of methyl lithium in a dilute solution of a 1:1 Et_2O:C_5H_{12} mixture took over 3 days with vigorous mixing. Alternatively, it has been suggested that since we were unable to characterize the RLi product, protonation events could originate from adventitious proton sources such as decomposition of the crown ether or those found in the groups that make up the surface of the silicate glass of the reaction vials. Although future experiments should encompass the use of trimethyl silyl–protected glassware and further attempts at isolating the RLi species, we were successful at isolating a masked 4-coordinate L^{oAd} anion complex zinc (**20**) $HIr(ZnCH_3)(\kappa^2\text{-}P,C\text{-}L^{oAd})(L^{oAd})$ and 4-coordinate L^{oAd} anion complex hydrido (**21**) $Li[12\text{-}c\text{-}4)_2][H_3Ir(\kappa^2\text{-}P,C\text{–}L^{oAd})(L^{oAd})]$.

2.8 Conclusions

An elementary electronic modification approach was employed to attenuate the electron richness at an iridium metal center. The increase in Lewis acidity allowed for the isolation of 6-coordinate anionic complexes (**14**) $Li[12\text{-}c\text{-}4)_2][H_2Ir(C_4H_9)(\kappa^2\text{-}P,C\text{–}L^{oAd})(L^{oAd})]$ and (**15**) $Li[12\text{-}c\text{-}4)_2][H_2Ir(CH_3)(\kappa^2\text{-}P,C\text{–}L^{oAd})(L^{oAd})]$. Mechanistic insight into the formation of phosphine analogue complex (**6**) $Li[HIr(\kappa^2\text{-}P,C\text{–}L^{mAd})(L^{mAd})]$ was accomplished with the isolation of highly reactive, alkyl arrested, phosphinite intermediates (**14**) and (**15**). Although the reactivity array for complexes (**14**) and (**15**) were consistent with an eventual protonation event, the addition of a pyridine-I_2 adduct, an attenuated oxidant with Brønsted base character, to anionic complex (**15**) provided the highly strained, double ligand C–H activated complex (**18**) $HIr(\kappa^2\text{-}P,C\text{-}L^{oAd})_2$. It was with the use of $(CH_3)_2Zn$ and $Li(CH_3)_3CLi$ that we were able to successfully isolate 4-coordinate and pseudo 4-coordinate L^{oAd} anion complexes hydrido (**21**)

$[Li_2(12\text{-c-}4)_2][HIr(\kappa^2\text{-P},C\text{–}L^{oAd})(L^{oAd})]_2$ and (**20**) $HIr(ZnCH_3)(\kappa^2\text{-}P,C\text{-}L^{oAd})(L^{oAd})$, respectively. Future experiments will encompass expanding the substrate scope towards the anionic arsenal *n*–butyl (**14**), methyl (**15**), hydrido (**21**), and zinc (**20**) and to evaluate the ability of double iridacycle (**18**) $HIr(\kappa^2\text{-}P,C\text{-}L^{oAd})_2$ to catalytically activate water and dehydrogenate alkanes.

2.9 Synthetic Procedures

General Considerations. All manipulations were carried out under an atmosphere of dry dinitrogen or argon using standard Schlenk and glovebox techniques. Solvents were dried and deoxygenated according to standard procedures. Unless otherwise stated, reagent grade starting materials were purchased from commercial sources and used as received. Benzene–d_6 and cyclohexane–d_{12} (Cambridge Isotope Laboratories) were degassed and stored over 4 Å molecular sieves for 2 d prior to use. Celite 405 (Fisher Scientific) was dried under vacuum (24 h) at a temperature above 250 ˚C and stored in the glovebox prior to use. KBr (FTIR grade from Aldrich) was stirred overnight in anhydrous THF, filtered and dried under vacuum (24 h) at a temperature above 250 ˚C prior to use.

Solution ^1H, $^{13}C\{^1H\}$, ^{13}C, $^{31}P\{^1H\}$, ^2H and $^{19}F\{^1H\}$ NMR spectra were recorded on Varian Mercury 300 and 400 spectrometers, a Varian X–Sens500 spectrometer or a JEOL ECA–500 spectrometer. ^1H and $^{13}C\{^1H\}$ chemical shifts are reported in ppm relative to $SiMe_4$ (^1H and ^{13}C δ = 0.0 ppm) and referenced to residual solvent resonances of 7.16 ppm (^1H) and 128.3 ppm (^{13}C) for benzene–d_6, 1.46 (^1H) and 26.43 (^{13}C) ppm for cyclohexane–d_{12} . $^{31}P\{^1H\}$ NMR spectra were referenced externally to 85% aqueous H_3PO_4 (δ = 0.0 ppm). $^{19}F\{^1H\}$ NMR spectra were referenced externally to neat trifluoroacetic acid, $F_3CC(O)OH$ (δ = –78.5 ppm vs. $CFCl_3$ = 0.0 ppm). FTIR spectra were recorded on a Thermo–Nicolet iS10 FTIR spectrometer. Samples were prepared as either KBr pellets, Nujol Mulls or as C_6H_{12} solutions injected into a ThermoFisher solution cell equipped with KBr windows. For solution FTIR spectra, solvent peaks were digitally subtracted from all spectra by comparison with an authentic spectrum

obtained immediately prior to that of the sample. Combustion analyses were performed by Robertson Microlit Laboratories of Madison, NJ (USA).

Synthesis of L^{oAd}. A thawing 90:10 THF:Et_2O solution of freshly prepared LiAd (4.350 g, 27.5 mmol, 1.5 equiv, 150 mL) was dropwise added over a five minute period to a thawing THF solution of $ClP(i\text{-}Pr)_2$ (2.787 g, 18.33 mmol, 1.0 equiv, 20 mL). The solution was allowed to stir for 3 hours followed by the removal of all volatile materials *in vacuo* and washed five times (30 mL each) with pentane. The resulting residue was extracted with pentane (16 mL), filtered and stored at -35 ˚C. Multiple crystallizations yielded colorless crystals, which were collected and dried. Melting point ~25 ˚C. Yield: 2.32 g, 8.65 mmol, 47%. ^{1}H NMR (499.8 MHz, C_6D_6, 20 ˚C): δ = 2.0 (s, 3H, *H6*), 1.9 (s, 6H, *H5*), 1.66 (d of sept, 2H, *H1*) 1.47 (s, 6H, *H7)*, 1.17 (m, 6H, $^3J_{HH} \approx J_{HP}$ = 8 Hz, *H2* or *H3*), 1.08 (m(dd), 6H, $^3J_{HH}$ = 15 Hz, J_{HP} = 7 Hz, *H2* or *H3)*. $^{13}C\{^1H\}$ NMR (125.7 MHz, C_6D_6, 20 ˚C): δ = 77.9 (d, J_{CP} = 10 Hz, *C4*), 45.1 (d, J_{CP} = 8 Hz *C5*), 36.2 (s, *C7*), 29.6 (s, *C8*), 27.8 (d, J_{CP} = 17 Hz, *C1*), 18.8 (d, J_{CP} = 11 Hz, *C2* or *C3*), 17.7 (d, J_{CP} = 9 Hz, *C2* or *C3*) ppm. $^{31}P\{^1H\}$ NMR (161.9 MHz, C_6D_6, 2 0 ˚C): δ = 119.3 (s) ppm. FTIR (KBr pellet): 2909, 2852, 1455, 1352, 1302, 1105, 1067, 974, 945, 818, 798, 764, 664 cm^{-1}. Anal Calcd. for $C_{16}H_{29}PO$: C, 71.61; H, 10.89. Found: C, 53.83; H, 8.36.

Synthesis of $H_2IrCl(L^{oAd})_2$ (11). In a Teflon-capped, thick-walled ampoule, a THF solution of $[IrCl(COD)]_2$ (1.964 g, 2.92 mmol, 110 mL) was added to a 90:20 THF:Et_2O solution of L^{oAd} (3.134 g, 11.69 mmol, 4.0 equiv, 20 mL). The solution was subjected to two freeze-pump-thaw cycles and then H_2 (1 atm) was introduced into the vessel. The reaction mixture stirred for 4 hours followed by another freeze-pump-thaw cycle and re-introduction of H_2 (1 atm). The mixture was then allowed to stir vigorously for 6 h with intermittent manual shaking followed by another freeze-pump-thaw cycle and re-introduction of H_2 (1 atm). The reaction mixture was vigorously stirred for 11 hours. All volatile materials were removed *in vacuo* and the resulting residue was extracted with Et_2O (200 mL), filtered and stored at -35 ˚C to yield

yellow crystals, which were collected and dried. Yield: 2.194 g, 2.86 mmol, 49%. ^{1}H NMR (400.1 MHz, C_6D_6, 20 ˚C): δ = 2.54 (d of sept, 4H, *H1*), 2.05 (s, 18H, *H5*, *H6*), 1.53 (m(quartet), 12H, *H7*), 1.28 (d of vt, 12H, $^{3}J_{HH} \approx J_{HP}$ = 7 Hz, *H2* or *H3*), 1.17 (d of vt, 12H, $^{3}J_{HH} \approx J_{HP}$ = 8 Hz, *H2* or *H3*), -31.5 (t, 2H, $^{2}J_{HP}$ = 15 Hz, Ir(*H*)$_2$) ppm. ^{13}C{^{1}H} NMR (125.7 MHz, C_6D_6, 20 ˚C): δ = 77.9 (s, *C4*), 45.1 (s, *C5*), 36.2 (s, *C7*), 29.6 (s, *C6*), 26.7 (t, J_{CP} = 15 Hz, *C1*), 20.6 (s, *C2* or *C3*), 19.4 (s, *C2* or *C3*) ppm. ^{31}P{^{1}H} NMR (161.9 MHz, C_6D_6, 20 ˚C): δ = 139.26 (t, $^{2}J_{PH}$ = 12 Hz (coupling is observed because ^{1}H resonance is outside decoupling bandwidth) ppm. FTIR (KBr pellet): ν(IrH) 2313 (m), 2261 (m) cm^{-1} also 1454, 1353, 1065, 981, 820, 684, 620, 545 cm^{-1}. Anal Calcd. for $C_{32}H_{60}ClIrP_2O_2$: C, 52.31; H, 8.78. Found: C, 53.83; H, 8.36.

Synthesis of $H_2Ir(\kappa^2$-*P,C*-$L^{oAd})(L^{oAd})$ (12). A thawing 1:1 Et_2O:C_5H_{12} mixture of PhMgBr (0.145 μL, 0.44 mmol, 1.03 equiv, 4 mL) was added to a 1:1 Et_2O:C_5H_{12} solution of $H_2IrCl(L^{oAd})_2$ (**11**) (0.325 g, 0.42 mmol, 15 mL). The reaction mixture was stirred for 2 h followed by removal of all volatile materials under reduced pressure. The resulting residue was washed three times with pentane (5 mL each), filtered. Then solvent removed under reduced pressure. The product was dissolved in Et_2O (4 ml), filtered, and stored at -35 ˚C to yield yellow crystals, which were collected and dried. Yield: 0.103 g, 0.141 mmol, 33%. ^{1}H NMR (500.16 MHz, C_7D_8, –50 ˚C): δ = 3.36 (s, 1H, Ad), 3.21 (s, 1H, Ad), 2.75 (d, 1H, Ad), 2.63 (d, 1H, Ad), 2.58 (d, 3H, Ad), 2.38 (s, 1H, Ad), 2.28 (d, 1H, Ad), 2.16 (s, 1H, Ad), 2.12 (m, 2H), 2.05 (m, 2H, Ad), 1.96 (m, 6H), 1.86 (d, 4H, Ad), 1.73 (m, 5H), 1.63 (t, 2H), 1.54 (d, 2H),1.42 (m, Ad), 1.31 (m, 10H), 1.01 (m), 0.92 (dd, 5H), –0.52 (m, 4H, Agostic Ir–H), –6.61 (dd, 1H, trans Ir–H, $^{2}J_{HP(trans)}$ = 137 Hz, $^{2}J_{HP(cis)}$ = 24 Hz), –30.08 (vt, 1H, $^{2}J_{HP(cis)}$ = 11 Hz, Cis Ir–H) ppm. ^{13}C{^{1}H} NMR (125.7 MHz, C_6D_6, 20 ˚C): δ = 83.2 (s), 75.2 (s), 66.1 (s), 49.3 (s), 48.7 (s), 46.5 (m), 45.1 (s), 41.81 (s), 40.93 (s), 38.3 (s), 35.7 (s), 35.3 (s), 34. (d, 22 Hz), 32.6 (d, 14 Hz), 32.1 (d, 23 Hz) 31.0 (s), 29.3 (d, 28 Hz), 18.8 (m), 18.5 (d, 10 Hz), 17.9 (s), 17.0

(s), 16.2 (s), 15.8 (s) ppm. $^{31}P\{^{1}H\}$ NMR (161.9 MHz, C_6D_6, 20 ˚C): δ = 160.5 (bs), 155.8 (bs) ppm. FTIR (KBr pellet): ν(Ir–H, Agostic) 2645 (m), ν(Ir–H) 2297 (s), ν(Ir–H) 2036 cm^{-1} also 1457, 1376, 1361, 1102, 1066, 952, 824, 670, 566 cm^{-1}. Anal Calcd. for $C_{32}H_{59}IrP_2O_2$: C, 52.65; H, 8.15. Found: C, 52.84; H, 7.96.

Synthesis of $H_2Ir(OH)(L^{oAd})_2$ (13).

Method A – From $H_2Ir(\kappa^2$-*P,C*-$L^{oAd})(L^{oAd})$ (12): A C_6D_6 solution of $H_2Ir(\kappa^2$-*P,C*-$L^{oAd})(L^{oAd})$ (0.010 g, 0.014 mmol, 0.5 mL) in a New Era CAV tube was subjected to three freeze-pump-thaw cycles. A C_6D_6 solution of H_2O (0.004 g, 0.022 mmol, 400 μL, 1.65 equiv, in 0.2 mL of C_6D_6) was then vacuum transferred into the NMR tube. 1H NMR analysis of the reaction mixture *ca.* 20 min after addition revealed exclusive production of $H_2Ir(OH)(L^{oAd})_2$.

Method B - From $H_2IrCl(L^{oAd})_2$ (11): A THF slurry of NaOH (0.160 g, 4 mmol, 10 equiv, 10 mL) was added to a THF solution of $H_2IrCl(L^{oAd})_2$ (11) (0.305 g, 0.4 mmol, 10 mL). The solution was vigorously stirred for 5 d followed by removal of all volatile materials *in vacuo* and the resulting residue was washed three times with pentane (5 mL each). The product was extracted with pentane (10 mL), filtered and stored at -35 ˚C to yield yellow crystals, which were collected and dried. Yield: 0.160 g, 0.217 mmol, 54%. ^{1}H NMR (500.16 MHz, C_6D_6, 20 ˚C): δ = 4.35 (s, 1H, Ir-OH) 2.33 (s, 12H, *H5, H6*), 2.18 (m(d of sept), 2H, *H1*), 2.10 (s, 2H), 1.58 (m, 12H, *H7*), 1.31 (d of vt, 12H, $^{3}J_{HH} \approx J_{HP}$ = 7 Hz, *H2* or *H3*), 1.24 (d of vt, 12H, $^{3}J_{HH} \approx J_{HP}$ = 7 Hz, *H2* or *H3*), -28.31 (t, 2H, $^{2}J_{HP}$ = 14 Hz, Ir(*H*)$_2$) ppm. $^{13}C\{^{1}H\}$ NMR (125.7 MHz, C_6D_6, 20 ˚C): δ = 77.28 (s, *C4*), 45.3 (s, *C5*), 36.4 (s, *C7*), 31.8 (s, *C6*), 31.3 (t, J_{CP} = 19 Hz, *C1*), 18.4 (s, *C2* or *C3*), 18.1 (s, *C2* or *C3*) ppm. $^{31}P\{^{1}H\}$ NMR (161.9 MHz, C_6D_6, 20 ˚C): δ = 131.62 (s) ppm. FTIR (KBr pellet): ν(Ir-OH) 3639 (s), ν(Ir-H) 2226 (bs) cm^{-1} also 1455, 1354, 1302, 1032, 1103, 1062, 980, 883, 808, 766, 668, 624, 548 cm^{-1}. Anal Calcd. for $C_{32}H_{61}IrP_2O_3$: C, 53.50; H, 9.10. Found: C, 53.83; H, 8.36.

Synthesis of (12-crown-4)$_2$Li[(H$_2$)Ir(C$_4$H$_9$)(κ^2-P,*C*–L^{oAd})(L^{oAd})] (14). A thawing Et_2O solution of $Li(CH_2)_3CH_3$ (15 ml, 1.35 mmol, 2.4 equiv) was added to a thawing pentane:Et_2O solution in a 4:1 ration of $H_2IrCl(L^{oAd})_2$ (**11**) (0.430 g, 0.564 mmol, 80 mL). The reaction mixture was stirred for 5 hrs followed by removal of all volatile materials under reduced pressure. The resulting residue was washed three times with pentane (5 mL each), filtered in Et_2O (40 ml), and 12-crown-4 (1.86 mmol, 3.3 equiv) was added dropwise. After stirring for 20 min, all Et_20 was removed under reduced pressure, washed three times with pentane (15ml) and filtered in pentane (60 ml). The light yellow filtrate was collected, dried under reduced pressure. Yield: 0.130 g, 0.046 mmol, 20%. Crystallization was accomplished with stirring a solution of 10 ml Et_2O with 0.080 g for 45 min followed by filtration and storage at -35 ˚C for 15 days to yield light yellow crystals. ^{1}H NMR (500.16 MHz, C_6D_6, 20 ˚C): δ = 3.29 (bs, 23H, 12-crown-4), 3.02 (m, 1H), 2.917 (m), 2.8 (m, 1H), 2.54 (bs, 1H), 2.43-2.01 (m, 19H), 1.79 (s, 2H), 1.65-1.2 (m, 32H),–13.47 (bm, 1H), –14.64 (bs, 1H) ppm. ^{31}P{^{1}H} NMR (161.964 MHz, C_6D_6, 20 ˚C): δ = 160.4 (s), 129.5 (d, 42 Hz) ppm. Anal Calcd. for $C_{37}H_{72}IrP_2O_3Li$: C, 53.80; H, 8.79. Found: C, 50.03; H, 8.07.

Synthesis of (12-crown-4)$_2$Li[H$_2$Ir(CH$_3$)(κ^2-P,*C*–L^{oAd})(L^{oAd})] (15). A thawing Et_2O slurry of $LiCH_3$ (20 ml, 0.043 mmol, 4.7 equiv) was added to a thawing Et_2O solution of $H_2IrCl(L^{oAd})_2$ (**11**) (0.705 g, 0.920 mmol, 70 mL). The reaction mixture was stirred for 24 hrs followed by removal of all volatile materials under reduced pressure. The resulting residue was washed three times with pentane (8 mL each), filtered in Et_2O (40 ml), and 12-crown-4 (0.9 mmol, 0.95 equiv) was added dropwise. After stirring for 20 min, all Et_20 was removed under reduced pressure, washed three times with pentane (15ml) and filtered in pentane (60 ml). The light yellow filtrate was collected, dried under reduced pressure, dissolved in Et_2O (15 ml), filtered, and stored at -35 ˚C to yield light yellow crystals. Yield: 0.625 g, 0.051 mmol, 56%. ^{1}H NMR (500.16 MHz, C_6D_{12}, 20 ˚C): δ = 3.64 (q, 4H, Et_2O)3.02 (d, 1H, 11 Hz), 2.69 (d, 1H,

11 Hz), 2.50 (m, 1H), 2.38 (m, 2H), 2.25 (s, 2H, Ad), 2.16 (s, 6H, Ad), 2.06 (m, 6H, Ad), 1.93 (s, 1H), 1.8 (m, 4H), 1.65 (m, 9H), 1.30 (t, 6H, Et_2O), 1.30-1.0 (m, 24H), -0.512 (s, 3H, Ir–CH_3), -14.49 (d, 1H, trans Ir–H, $^2J_{HP(trans)}$ = 126 Hz,-14.89 (t, 1H Cis Ir–H $^2J_{HP(cis)}$ = 15 Hz). $^{13}C\{^1H\}$ NMR (125.7 MHz, C_6D_{12}, 20 ˚C): δ = 82.9 (t), 81.8 (d, 19 Hz)), 67.56 (s, Et_2O), 46.7 (s), 46.6 (s), 45.5 (d, 6 Hz), 44.8 (d, 6 Hz), 44.2 (s), 44.0 (d, 8 Hz), 41.0 (s), 37.7 (s), 37.0 (s), 35.6 (d, 20 Hz), 35.1 (s) 34.6 (s) 33.3 (s), 32.8 (d, 17 Hz), 32.1 (d, 26 Hz), 31.4 (s), 23.4 (s), 21.9 (d, 4 Hz), 21.5 (s), 21.4 (s), 20.5 (d, 9 Hz), 19.6 (d, 3 Hz), 19.4 (d, 2 Hz), 18.8 (d, 4 Hz), 15.8 (s, Et_2O), ppm. $^{31}P\{^1H\}$ NMR (161.964 MHz, C_6D_6, 20 ˚C): δ = 160.4 (s), 129.0 (s) ppm. FTIR (KBr pellet): ν), ν(Ir–H) 2047 (s), 1893 cm^{-1} also 1446, 1376, 1354, 1288, 1065, 936, 742, 641, 492 cm^{-1}. Anal Calcd. for $C_{37}H_{72}IrP_2O_3Li$: C, 53.80; H, 8.79. Found: C, 50.03; H, 8.07.

Synthesis of (12-crown-4)$_2$Li[HIr(κ^2-P,*C*–L^{oAd})(L^{oAd})] (16). A thawing pentane slurry of $LiC(CH_3)_3$ (20 ml, 0.0913 mmol, 2.0 equiv) was added to a thawing Et_2O:C_5H_{12} solution in a 1:2 ratio of $H_2IrCl(L^{oAd})_2$ (**11**) (0.348 g, 0.046 mmol, 60 mL). The reaction mixture was stirred for 3 hrs followed by removal of all volatile materials under reduced pressure. The resulting residue was washed four times with pentane (15 mL each), filtered in Et_2O (40 ml), and 12-crown-4 (0.096 mmol, 2.0 equiv) was added dropwise. After stirring for 20 min, all Et_20 was removed under reduced pressure, washed three times with pentane (15 ml each) and filtered in pentane (60 ml). The light yellow filtrate was collected, dried under reduced pressure. Yield: 0.222 g, 0.046 mmol, 45%. Crystallization was accomplished with stirring a solution of 10 ml Et_2O with 0.080 g for 45 min followed by filtration and storage at -35 ˚C for 15 days to yield light yellow crystals. ^1H NMR (500.16 MHz, C_6D_{12}, 20 ˚C): δ = 3.75 (s, 28H, 12-crown-4), 3.25 (d, 1H, 11 Hz), 2.85 (d, 1H, 11 Hz), 2.66 (s, 1H), 2.27 (m, 9H, Ad), 2. 09 (m, 6H, Ad), 2.00 (s, 1H), 1.9 (m, 3H), 1.74 (m (sept), 2H), 1.61 (m, 15H), 1.30 (s, 29H), 1.23-0.98 (m, 19H), 0.894 (m, 12H), -13.06 (bs (possible vt, 2H, cis Ir-*H*), -13.3 (d, 1H, trans Ir–H, $^2J_{HP(trans)}$

= 119 Hz), ppm. $^{13}C\{^{1}H\}$ NMR (125.7 MHz, C_6D_{12}, 20 ˚C): δ = 81.9 (s), 78.54 (s), 78.4 (s), 71.8 (s, 12-crown-4), 46.8 (d, 8 Hz), 46.5 (s), 43.7 (s), 43.6 (d, 8 Hz), 40.6 (s), 38.5 (d, 18 Hz), 38.2 (s), 37.0 (d, 24 Hz), 35.9 (s), 33.8 (s), 33.4 (s), 33.3 (s), 31.4 (s), 31.0 (d, 13 Hz), 30.8 (s), 29.5 (d, 22 Hz), 24.4 (s), 24.0 (s), 22.3 (s), 21.9 (s), 20.6 (s), 19.5 (d, 10 Hz), 13.2 (s), 16.8 (d, 5 Hz), 15.3 (dm 10 Hz), 15.2 (s) ppm. $^{31}P\{^{1}H\}$ NMR (161.964 MHz, C_6D_6, 20 ˚C): δ = 151.4 (m (pseudo q), ~9 Hz), 130.8 (s) ppm. FTIR (KBr pellet): ν), ν(Ir–H) 1959 cm^{-1} also 1700, 1452, 1353, 1289, 1244, 1136, 1098, 1024, 984, 936, 885, 816, 758, 653 cm^{-1}. Anal Calcd. for $C_{37}H_{72}IrP_2O_3Li$: C, 53.80; H, 8.79. Found: C, 50.03; H, 8.07.

Synthesis of HIr(κ^2-*P*,*C*-L^{oAd})(L^{oAd})(ZnCH$_3$) (18). A thawing 3:2 Et_2O:C_5H_{12} solution of $Zn(CH_3)_2$ (0.535 μL from a 1M solution, 0.535 mmol, 2.09 equiv) was added to a thawing Et_2O solution of $H_2IrCl(L^{oAd})_2$ (**11**) (0.196 g, 0.256 mmol, 8 mL). The reaction mixture was stirred for 45 min followed by removal of all volatile materials under reduced pressure. The resulting residue was washed three times with pentane (5 mL each), filtered in cold Et_2O (2 ml). Insoluble filtrate was collected, dried under reduced pressure, dissolved in Et_2O (6 ml), filtered, and stored at -35 ˚C to yield yellow crystals, collected and dried. Yield: 0.038 g, 0.037 mmol, 18%. ^{1}H NMR (500.16 MHz, C_6D_6, 20 ˚C): δ = 3.26 (bd, 2H, 48 Hz), 2.61 (t, 2H, Ad), 2.38 (d, 3H, Ad, 11 Hz), 2.27 (s, 1H, Ad), 2.17 (m, 2H), 2.02 (m, 6H, Ad), 1.22 (m (4 features), 9H), 1.11 (m (4 features), 4H), 1.04 (m (4 features), 6H), 0.878 (m, 6H), 0.273 (s, 3H), -4.44 (dd, 1H, trans Ir–H, $^{2}J_{HP(trans)}$ = 106 Hz, Cis Ir–H $^{2}J_{HP(cis)}$ = 18 Hz). $^{13}C\{^{1}H\}$ NMR (125.7 MHz, C_6D_6, 20 ˚C): δ = 82.6 (t), 74.5 (d, 4 Hz)), 65.9 (s), 62.85 (s), 62.3 (s), 47.8 (s), 47.5 (d, 9 Hz), 46.2 (s), 41.6 (d, 6 Hz), 38.3 (s), 36.9 (d, 21 Hz), 36.4 (s), 36.0 (s), 32.7 (s) 32.4 (s) 32.0 (d, 21 Hz), 31.4 (s), 31.0 (d, 32 Hz), 30.2 (s), 28.3 (d, 32 Hz), 20.2 (s), 19.4 (d, 3 Hz), 19.3 (s), 19.3 (s), 18.8 (d, 2 Hz), 18.8 (s), 18.7 (s), 17.2 (s), 17.0 (s), 16.9 (d, 4Hz), 16.2 (d, 3 Hz), 15.6 (s), -6.3 (s, Zn*C*H$_3$) ppm. $^{31}P\{^{1}H\}$ NMR (161.964 MHz, C_6D_6, 20 ˚C): δ = 175.8 (d, 30 Hz), 149.3 (s) ppm. FTIR (KBr pellet): ν(Ir–H, Agostic) 2675 (m), ν(Ir–H) 1938

(s), cm^{-1} also 1455, 1375, 1312, 1245, 1086, 1066, 1015, 979, 953, 883, 829, 771, 661, 557 cm^{-1}. Anal Calcd. for $C_{33}H_{61}IrP_2O_3$: C, 48.97; H, 7.60. Found: C, 48.68; H, 7.32.

Synthesis of $H_2Ir(I)(L^{oAd})_2$ (19). A pentane solution of I_2 (0.0014 g, 0.0055 mmol, 0.95 equiv, 2 mL) was added to a pentane solution of (12-crown-4)$_2$Li[HIr(κ^2-P,*C*–L^{oAd})(L^{oAd})] (16) (0.0066 g, 0.006 mmol, 16 mL) at 23 ˚C. The solution was stirred for 30 min followed by removal of all volatile materials *in vacuo* and the resulting residue was washed three times with pentane (3 mL each). The product was extracted with pentane (1 mL), filtered and stored at -35 ˚C to yield purple precipitate, which was collected and dried. Yield: 0.004 g, 0.0047 mmol, 78%. ^{1}H NMR (500.16 MHz, C_6D_6, 20 ˚C): δ = 2.81 (d of sept, 4H), 2.02 (bs, 6H, Ad), 1.87 (s, 12H, Ad), 1.50 (m(quartet), 12H, Ad), 1.22 (m, 24H) -27.68 (t, 2H, $^2J_{HP}$ = 15 Hz, Ir(*H*)$_2$) ppm. ^{13}C{^{1}H} NMR (125.7 MHz, C_6D_6, 20 ˚C): δ = 78.1 (s), 43.9 (s), 31.7 (s), 31.3 (t, J_{CP} = 20 Hz), 18.4 (s), 18.1 (s) ppm. ^{31}P{^{1}H} NMR (161.9 MHz, C_6D_6, 20 ˚C): δ = 140.1 (s) ppm. FTIR (KBr pellet): ν(Ir-H) 2298, 2201 cm^{-1} also 1457, 1379, 1354, 1243, 1064, 988, 955, 874, 821, 769, 672, 630, 544 cm^{-1}. Anal Calcd. for $C_{32}H_{61}IrP_2O_3$: C, 53.50; H, 9.10. Found: C, 53.83; H, 8.36.

Synthesis of HIr(κ^2-*P,C*-L^{oAd})$_2$ (20). A thawing toluene solution was added pyridine C5H5N (0.036g, 0.07 mmol, 4 equiv.) and iodine I2 (0.069 mg, 0.0274 mmol, 1.5 equiv). The thawing toluene mixture (2 ml total) containing the iodine-pyridine adduct was added dropwise to a thawing toluene solution of (12-crown-4)$_2$Li[H_2Ir(CH_3)(κ^2-P,*C*–L^{oAd})(L^{oAd})] (**15**) (0.222 g, 0.0183 mmol, 8 mL). The reaction mixture was stirred for 20 min followed by removal of all volatile materials under reduced pressure. The resulting residue was washed three times with pentane (2 mL each), filtered in pentane (4 ml), and stored at -35 ˚C to yield light yellow crystals. Yield: 0.030 g, 0.04 mmol, 23%. ^{1}H NMR (500.16 MHz, C_6D_{12}, 20 ˚C): ppm. ^{31}P{^{1}H} NMR (161.964 MHz, C_6D_6, 20 ˚C): δ = 123.5 (s), 110.2 ppm

Synthesis of HIr(Cl)(κ^2-*P*,*C*-L^{oAd})(L^{oAd}) (21). A solution of HCl in Et2O (23 µl, 0.0235 mmol, 4.0 equiv) was added to a C_6D_6 solution of HIr(κ^2-*P*,*C*-L^{oAd})$_2$ (**20**) (0.047 g, 0.00584 mmol, 2 mL). The reaction mixture was stirred for 1min. The light yellow solution was characterized by NMR methods: ^{1}H NMR (500.16 MHz, C_6D_{12}, 20 ˚C): δ = 2.01 (bm), 1.55 (bm),1.36 (m), -38.8 (d of t, 1H, $^2J_{HP}$ = 60 Hz, $^2J_{HP(cis)}$ = 15 Hz). ^{31}P{^{1}H} NMR (161.964 MHz, C_6D_6, 20 ˚C): δ = 124.6 (s), 120.8 ppm.

2.10 Crystallographic Structure Determinations

General. Single crystal X–ray structure determinations were carried out at low temperature on a Bruker P4, Platform or Kappa Diffractometer equipped with a Bruker APEX II detector. All structures were solved by direct methods with SIR 2004 [29] and refined by full–matrix least–squares procedures utilizing SHELXL–97. [30] Molecular structures of all complexes are depicted in Figures.

Crystallographic data collection and refinement information is listed in Tables 2.3–2.5. Metal hydrides were located from the electron density difference map and the appropriate number of hydride ligands were found for all iridium–hydride complexes. Upon positive identification, these hydride atoms were subjected to one cycle of free refinement and then restrained to an Ir–H bond distance of 1.55(± 0.02) Å for all subsequent refinements. In order to produce a chemically sensible geometry, the hydride units of the hydroxide complex $H_2Ir(OH)(L^{mAd})_2$ (**6**) were additionally restrained to an H···H bond distance of 2.15(± 0.05) Å.

Table 2.3. Crystallographic Data Collection and Refinement Information for $H_2IrCl(L^{oAd})_2$, $HIr(OH)(L^{oAd})_2$.

Compound	$H_2IrCl(L^{oAd})_2$	$H_2Ir(OH)(L^{oAd})_2$
Formula	$C_{32}H_{60}ClIrO_2P_2$	$C_{32}H_{61}IrO_3P_2$
Crystal System	Triclinic	Monoclinic
Space Group	*P*–1	$P2_1/n$
a, Å	10.264(3)	10.350(2)
b, Å	16.408(5)	23.672(4)
c, Å	20.484(6)	13.871(2)
α, deg	103.574(4)	90
β, deg	90.868(4)	96.751(2)
γ, deg	95.538(4)	90
V, Å^3	3335.2(16)	3374.9(10)
Z	4	4
Radiation (λ, Å)	Mo–Kα, 0.71073	Mo–Kα, 0.71073
ρ (calcd.), g/cm^3	1.526	1.487
μ (Mo Kα), mm^{-1}	4.206	4.235
Temp, K	100(2)	100(2)
θ max, deg	25.70	25.090
data/parameters	11519 / 2 / 712	5957 / 1 / 371
R_1	0.0332	0.0458
wR_2	0.0727	0.1077
GOF	1.065	1.060

Table 2.4. Crystallographic Data Collection and Refinement Information for $H_2Ir(\kappa^2\text{-}P,C\text{–}L^{oAd})(L^{oAd})$, $(12\text{-crown-4})_2Li[(H_2)Ir(C_4H_9)(\kappa^2\text{-}P,C\text{–}L^{oAd})(L^{oAd})]$, and $(12\text{-crown-4})_2Li[H_2Ir(CH_3)(\kappa^2\text{-}P,C\text{–}L^{oAd})(L^{oAd})]$

Compound	$H_2Ir(\kappa^2\text{-}P,C\text{–}L^{oAd})(L^{oAd})$	$(12\text{-crown-4})_2Li[(H_2)Ir(C_4H_9)(\kappa^2\text{-}P,C\text{–}L^{oAd})(L^{oAd})]$	$(12\text{-crown-4})_2Li[H_2Ir(CH_3)(\kappa^2\text{-}P,C\text{–}L^{oAd})(L^{oAd})]$
Formula	$C_{32}H_{59}IrO_2P_2$	$C_{52}H_{99}IrLiO_{10}P_2$	$C_{49}H_{85}IrLiO_{10}P_2$
Crystal System	Triclinic	Monoclinic	Monoclinic
Space Group	P -1	P 2_1/c	P 2_1/n
a, Å	11.2245(6)	11.3001(6)	16.938(3)
b, Å	11.6282(6)	19.0751(11)	16.534(3)
c, Å	12.6015(7)	25.6851(13)	19.933(4)
α, deg	100.0370(10)	90	90
β, deg	93.9700(10)	95.848(3)	111.368(8)
γ, deg	99.8100(10)	90	90
V, Å^3	1587.59(15)	5507.6(5)	5198.7
Z	2	4	4
Radiation (λ, Å)	Mo–Kα, 0.71073	Mo–Kα, 0.71073	Mo–Kα, 0.71073
ρ (calcd.), g/cm^3	1.527	1.384	1.400
μ (Mo Kα), mm^{-1}	4.332	2.537	2.683
Temp, K	100(2)	100(2)	100(2)
θ max, deg	27.593	30.593	31.015
data/parameters	6880 / 354	15563/ 652	15783/ 778
R_1	0.0308	0.0552	0.0301
wR_2	0.0557	0.1245	0.0692
GOF	0.997	1.072	1.072

Table 2.5. Crystallographic Data Collection and Refinement Information for (12-crown-4)$_2$Li[HIr(κ^2-P,*C*–L^{oAd}) (L^{oAd})], HIr(κ^2-*P*,*C*-L^{oAd})(L^{oAd})(ZnCH$_3$), HIr(κ^2-*P*,*C*-L^{oAd})$_2$.

Compound	(12-crown-4)$_2$Li [HIr(κ^2-P,*C*–L^{oAd}) (L^{oAd})]	HIr(κ^2-*P*,*C*-L^{oAd})(L^{oAd}) (ZnCH$_3$)	HIr(κ^2-*P*,*C*-L^{oAd})$_2$
Formula	$C_{80}H_{147}Ir_2Li_2O_{12}P_4$	$C_{33}H_{61}IrO_2P_2Zn$	$C_{34}H_{43}IrO_2P_2$
Crystal System	Triclinic	Monoclinic	Triclinic
Space Group	P -1	P 2_1/c	P -1
a, Å	15.5317(10)	15.896(4)	11.205(5)
b, Å	16.9245(10)	10.441(3)	11.476(5)
c, Å	19.1631(12)	21.592(6)	12.293(5)
α, deg	103.982(3)	90	99.655(5)
β, deg	94.082(3)	108.482(3)	94.953(5)
γ, deg	106.538(3)	90	97.350(5)
V, Å^3	4632.5(5)	3398.5(16)	1536.1(11)
Z	2	4	2
Radiation (λ, Å)	Cu–Kα, 1.54178	Mo–Kα, 0.71073	Mo–Kα, 0.71073
ρ (calcd.), g/cm^3	1.307	1.582	1.502
μ (Mo Kα), mm^{-1}	2.990	4.739	4.474
Temp, K	100(2)	100(2)	100(2)
θ max, deg	28.613	27.926	24.294
data/parameters	20813 / 925	7807/ 365	4903/ 313
R_1	0.0521	0.0255	0.0451
wR_2	0.1058	0.0565	0.1062
GOF	0.926	1.037	1.161

2.11 References

1. Gottker-Schnetmann, I.; White, P.; Brookhart, M. *J. Am. Chem. Soc.* **2004,** *126,* 1804-1811.

2. Millard, M.; Moore, C.; Rheingold, A.; Figueroa, J. *J. Am. Chem. Soc* **2010,** *132,* 8921-8923.

3. Tolman, C. *Chem. Rev.* **1977,** *77,* 313-348.

4. Manzer, L.; Tolman, C. *J. Am. Chem. Soc* **1975,** *97,* 1955-1956.

5. Tolman, C. *J. Am. Chem. Soc.* **1970,** *92,* 2953-2956.

6. Crabtree, R. *The Organometallic Chemistry of the Transition Metals;* Wiley-Interscience, 2005.

7. Wetherby, A.; Mucha, N.; Waterman, R. *ACS Catal.* **2012,** *2,* 1404-1407.

8. Chakraborty, S.; Patel, Y. J.; Krause, J. A.; Guan, H. *Polyhedron* **2012,** *32,* 30-34.

9. Chan, S. C. A.; Wenhao, H.; C., P.; Lau, C. *J. Am. Chem. Soc.* **1997,** *119,* 9570-9571.

10. Kallstrom, K.; Hedberg, C.; Brandt, P.; Bayer, A.; Andersson, P. *J. Am. Chem. Soc.* **2004,** *126,* 14308-14309.

11. Bell, S.; Wustenberg, B.; Kaiser, S.; Menges, F.; Netscher, T.; Pfaltz, A. *Science* **2006,** *311,* 642-644.

12. Roseblade, S.; Pfaltz, A. *C. R. Chimie* **2007,** *10,* 178-187.

13. Zhu, K.; Achord, P.; Zhang, X.; Krogh-Jespersen, K.; Goldman, A. *J. Am. Chem. Soc.* **2004,** *126,* 13044 - 13053.

14. Gottker-Schetmann, I.; White, P.; Brookhart, M. *J. Am. Chem. Soc.* **2004,** *126,* 1804-1811.

15. Arunachalampillai, A.; Olsson, D.; Wendt, O. *Dalton Transactions* **2009,** 8626-8630.

16. Gottker-Schnetmann, I.; Brookhart, M. *J. Am. Chem. Soc.* **2004,** *126,* 9330-9338.

17. Fernandez-Perez, H.; Etayo, P.; Panossian, A.; Vidal-Ferran, A. *Chem. Rev.* **2011,** *111,* 2119-2176.

18. Lewis, J. C.; Wu, J.; Bergman, R. G.; Ellman, J. *Organometallics* **2005,** *24,* 5737-5746.

19. Bhattacharya, A. K.; Thygarajan, G. *Chem. Rev.* **1981,** *81,* 415-430.

20. Woltermann, C. J.; Schwindeman, J. A. *Fine Chemistry* **2002,** *Nov/Dec,* 5-8.

21. Cundari, T. R. *J. Am. Chem. Soc.* **1994,** *340-347,* 116.

22. Ming-Der, S.; San-Yan, C. *J. Phys. Chem. A* **1998,** *102,* 10159-10166.

23. Rimmer, E. L.; Bailey, R. D.; Pennington, W. T.; Hanks, T. W. *J. Chem. Soc., Perkin Trans. 2* **1998,** 2557–2562.

24. Aronson, S.; Epstein, P.; Aronson, D. B.; Wieder, G. *J. Phys. Chem.* **1982,** *86,* 1035-1037.

25. Kronick, P. L. *J. Phys. Chem.* **1965,** *9,* 3178-3179.

26. Ruhland, K.; Herdtweck, E. *Adv. Synth. Catal.* **2005,** *347,* 398-404.

27. Jonasson, K. J.; Ahlsten, N.; Wendt, O. F. *Inorganica Chimica Acta* **2011,** *379,* 76-80.

28. Fletcher, D. A.; McMeeking, R. F.; Parkin, D. J. The United Kingdom Chemical Databse. *J. Chem. Inf. Comput. Sci.* **1996,** *36,* 746-749.

29. Burla, M. C.; Caliandro, R.; Camalli, M.; Carrozzini, B.; Cascarano, G. L.; De Caro, L. *J. Appl. Cryst.* **2005,** *38,* 381-388.

30. Sheldrick, G. M. *Acta Cryst.* **2008,** *A64,* 112-122.

Chapter 3

Coordination of Alkanes to an Unsaturated Cobalt Complex – an X–ray Crystallographic Endeavor

3.1 Introduction

Of all metal–ligand interactions, it is the coordination of an alkane C–H bond to a transition metal that is one of the most difficult. While such interactions have been observed, they are not well-understood. A continued effort to isolate and characterize alkane σ–complexes stems from a desire to control alkane C–H bond transformations, a significant synthetic challenge with high economic benefit. Herein we report the X–ray characterization of coordinated alkanes, *n*–hexane and *n*–heptane, to a cobalt metal complex.

Alkanes have had a long standing reputation for being unreactive, hence their original name "paraffin", meaning "lacking affinity" or "lacking reactivity". The inert nature of the C–H bond in alkanes likely stems from high bond strengths (90-104 kcal/mol),[1] high pKa values (~50), and low polarizability. These factors complicate functionalizing alkanes and there are few industrial processes that efficiently and selectively convert alkanes to valuable synthons. Currently, these industrial processes require high temperatures and pressures, for example, ethylene is one of the largest chemical commodities (annual production estimated 141 million tonnes in 2011)[2] and is produced by steam cracking short chain hydrocarbons. Despite the lack of synthetic control and energy inefficiency, alkanes are continually used as a major industrial chemical feedstock, as they are the least expensive and most abundant hydrocarbon resource.[3,4]

Historically, the functionalization of alkanes has been accomplished by metal–free radical or electrophilic reactions, i.e., chlorine atom radicals or superacids, respectively.[1]

Although these routes accomplish alkane functionalization, they are limited by poor selectivity, favoring tertiary C–H bonds over secondary and primary (3˚ > 2˚ > 1˚). Currently, research has been focused on selective functionalization of alkanes with the use of transition metal complexes, wherein the metal center promotes the activation of an alkane C–H bond. By this methodology, the C–H bond must first come into close proximity to the metal center. It is proposed that along this reaction trajectory, prior to oxidative addition, the C–H bond donates electron density into an empty metal d–orbital; thereby forming a three–center, two–electron M···H···C interaction, known as an alkane σ–complex (Scheme 3.1).[5,6] It is the investigation of this fleetingly formed η^2-H,C interaction that may provide relevant information pertaining to the controlled activation and functionalization of C–H bonds.

Scheme 3. 1. Formation of a η^2-H,C alkane σ–complex prior to oxidative addition.

As outlined in a thorough review by Crabtree,[7] the ideas of alkane coordination and activation by a metal complex can be traced back to Pauling's 1939 book "*The Nature of the Chemical Bond*".[8] Based on short M–C bond distances, Pauling proposed that carbon engages in multiple bonding (currently known as metal to ligand π back-donation) with nickel in $Ni(CO)_4$. Although Lagmuir had suggested this as early as 1921, it was not well received at the time. This proposal of π back-bonding by Pauling seethed a cauldron of debate that lead to the currently accepted Dewer–Chatt bonding model, which was proposed in publications from the 1960's, veering away from then accepted Werner coordination theory (simple lone pair donation). The Dewer–Chatt bonding model describes both the ligand to metal σ–interaction, as well as the metal to ligand π back-donation. This bonding description was crucial for the

interpretation and understanding of non–classical H_2 σ–complexes, established by Kubas,[9] and, furthermore, the understanding of both borane (B–H) and silane (Si–H) σ–complexes.[10]

The ongoing quest to understand the nature of the η^2-H,C σ–type interaction was further developed in the late 1960's by Trofimenko with the isolation of the first transition metal complex that had conspicuously close contacts to an intra–molecular C–H bond, [{Et_2Bpz_2}$Mo(CO)_2$(2–methyl–allyl)] (Scheme 3.1).[11] This complex was fully investigated by Cotton and Stanislowski, in which they estimated the C–H/Mo binding energy to be 17 kcal/mol.[12]

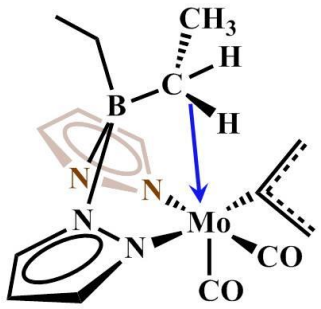

Scheme 3. 2. Trofimenko's bis-parazyl borate complex [{Et_2Bpz_2}$Mo(CO)_2$(2–methyl–allyl)] that contains an η^2-H,C σ–type interaction.

Currently, there are many examples of structurally characterized transition metal complexes containing intra–molecular ligand C–H bond coordination. The intra–molecular ligand C–H coordination by a metal center is formally known as an "agostic" interaction, a term coined by Maurice Brookhart and Malcolm Green which means "to clench ones shield". These agostic complexes are estimated to contain bond strengths of 10–15 kcal/mol and typical M–H distances of 1.8–2.3 Å and M–H–C angles of 90–140°.[13–15]

Both agostic and alkane σ–complexes contain a Lewis basic η^2-H,C σ–type interaction to a metal center. The alkane σ–complex coordinates the C–H bond independently, without assistance from an ancillary ligand. In stark contrast, agostic complexes require tethered ligand platforms which assist in positioning the C–H bond in close proximity to the metal center. Being deficient in any stabilization energy from tethering effects, it was no surprise

that theoretical studies on rhenium–alkane σ–complexes revealed binding energies slightly lower than that found for agostic complexes, in the range between 5–12 kcal/mol[16,17]. Unlike agostic complexes, alkane σ–complexes can potentially undergo several coordination modes (Scheme 3.2).

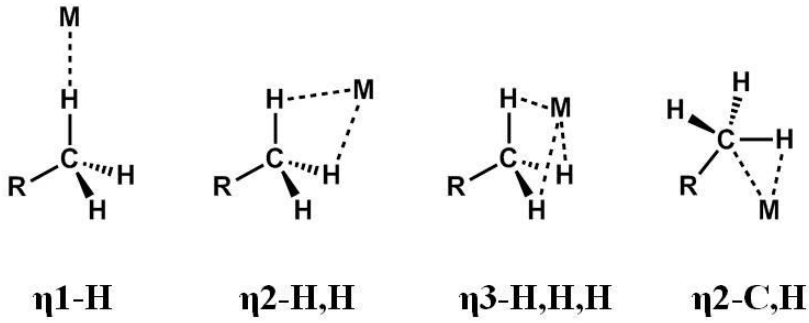

Scheme 3.3. Four different binding modes for alkane σ–complexes. (R = alkyl).

Following the full characterization of several complexes containing agostic interactions, Perutz and Turner in the 1970's were successful at coordinating alkanes to metal carbonyl complexes $M(CO)_5$ (M = Cr, Mo, W) with matrix assisted photoextrusion of CO.[18,19] Proposed around the same time by Kelly et al. was the cyclohexane bound $Cr(CO)_5$ complex inferred from infrared spectroscopic studies.[20] A major advancement supporting alkane functionalization was the electrophilic C–H activation from a platiunum (II) complex unveiled by Shilov (1970's)[21] and further developed by Labinger and Bercaw (2002)[6] These studies by Shilov portrayed, for the first time, deuterium and halogen incorporation into alkanes starting from the platinum complex $[PtCl_4]^{-2}$.

A big breakthrough in the early 1980's performed by Breckenridge was the binding of methane to $Cr(CO)_5$ formed via pulsed laser photolysis investigations from the saturated $Cr(CO)_6$ complex under a methane matrix.[22,23] Shortly thereafter, in 1985, isotopic data became available with the accompanied spectroscopic support of time–resolved infrared spectroscopy (TRIR), providing convincing evidence for the existence of a cyclohexane bound chromium complex $(C_6H_{12})Cr(CO)_5$.[17] The result of these seminal studies inferred

coordination of the alkane C–H bond to a transition metal center but lacked direct support (^{1}H or ^{13}C NMR spectroscopy) for the controlled activation of the C–H bond. Direct C–H bond activation was finally achieved, with great excitement, by the oxidative addition of an alkane C–H bond from *cyclo*–C_6H_{12} to a transition metal center reported by Bergman and independently by Graham in 1982 ($(H_5C_5)(PMe_3)Ir$ and $(H_5C_5)(CO)Ir$, respectively).[24,25] Interestingly, low temperature flash kinetic spectroscopy studies of metal complexes that undergo C–H bond oxidative addition, as in the examples from Bergman and Graham, lack evidence for the existence of an alkane σ–complex. These studies propose an uninserted transient alkane σ–complex but there are no assignable carbonyl absorptions.[26-28]

Since these early discoveries, it has become evident that understanding both the kinetic and structural features of the coordination of a C–H bond to a metal center, prior to oxidative addition, is an area of considerable importance. Exhaustive efforts aimed at the controlled activation of alkanes have been ongoing for decades with some more recent studies highlighting direct evidence for the persistence of an alkane σ–complex in solution. The use of low temperature (T < 200K) NMR methods has recently been reported in remarkable studies by Ball,[29–34] George, Perutz,[35,36] and Brookhart.[37] X–ray crystallographic characterization of alkane σ–complexes is limited to three examples of which two were solution–derived. Reed et al. reported the first example of a solution derived alkane σ–type interaction characterized by X–ray diffraction methods, where a methyl group of *n*–heptane was in close contact (Fe–C distance of 2.5 and 2.8 Å) to an iron (II) porphyrin metal complex Fe(DAP) (DAP = double A–frame porphyrin).[38] Meyer et al. isolated the second example of a crystallographically characterized, solution derived uranium (III) complex $[U(ArO)_3tacn]$ (Ar = 2,5–(*t*–Bu)$_2C_6H_2$; tacn = triazacyclononane) containing long C–H σ–type contacts from several cycloalkanes (distances U–C = 3.864(7) Å and U–H = 3.192 Å).[39] The third structurally characterized example was a non–solution derived norbornane σ–bound adduct reported by Weller et al.,

and was produced by gas–solid reaction from the *in situ* hydrogenation of a crystalline norbornadiene rhodium (I) complex [Rh(^{i}Bu$_2$PCH$_2$CH$_2$P^{i}Bu$_2$)($\eta^2\eta^2$–C$_7$H$_8$)[BAr$^F_4$] (Ar^F = 3,5–(CF$_3$)$_2$C$_6$H$_3$)].[40] Unfortunately, these three examples suffer from crystallographic challenges of low resolution or positional disorder. Currently, alkane σ–complexes that have been spectroscopically characterization by NMR methods lack accompanied crystallographic data. Further complicating matters is the fact that the two crystallographically characterized solution derived σ–complexes from Reed and Meyer are paramagnetic (not amenable to NMR methods) and the third example, the Rh(I) complex studied by Weller, is only stable in the crystalline state.

Desiring to isolate a diamagnetic transition metal complex containing the necessary metal d–orbital manifold to bind alkanes, we drew inspiration from early studies of metal carbonyl complexes. These unsaturated metal carbonyl complexes M(CO)$_5$ (M = Cr, Mo, W) contain a highly Lewis acidic metal centers as the result of coordination to 5 strongly π–basic CO ligands. The *in situ* formed metal carbonyl complex M(CO)$_5$ (where M = Cr, Mo, W) contains a vacant d_z^2 orbital of proper symmetry to accept electron density from a C–H bond in a σ–type of interaction (Figure 3. 1).[41]

The reactive nature of these unsaturated metal carbonyl complexes is exemplified by their propensity to coordinate or activate the matrix they are formed in. Although these metal complexes elicit C–H bond activation, their short half lives and instability obviate the direct structural elucidation of the fleetingly formed alkane σ–complex. Therefore, we employed an isocyanide ligand that acts as a surrogate to carbon monoxide with increased stability, more specifically, provides the kinetic stabilization towards bimolecular decomposition.[42-44] Building on the isolobal relationship between isocyanides and carbon monoxide, both possess strong σ–donation in addition to being π–acceptors. Unlike carbonyl moieties, isocyanides

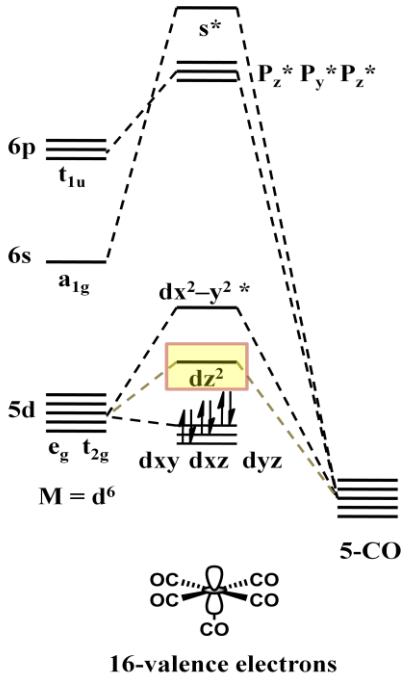

Figure 3. 1. Qualitative molecular orbital diagram for $M(CO)_5$ where M = Cr, Mo, W.

can be structurally modified to encompass desired electronic or steric properties.[45-47] We employed the previously reported $CNAr^{Mes2}$ ligand, an isocyanide modified with the 2,6–dimesitylphenyl framework, which serves to sterically protect the metal center (Ar = Aryl, Mes = mesityl = 2,4,6–$Me_3C_6H_2$ and Me = methyl, CH_3).[48]

3.2 Synthetic Studies of a Cobalt Tris–Isocyanide Monoanion Complex

Previous studies in our group have shown that complex (**1**) (η^2–PPN)($Co(CNAr^{Mes2})_3$ (PPN = $(C_6H_5)_3P=N=P(C_6H_5)_3$) functions as a source of cobalt tris–isocyanide monoanion species $[Co(CNAr^{Mes2})_3]^-$ and reacts with electrophiles.[49] The addition of trimethylchlorosilane (Me_3SiCl; TMSCl) to a toluene solution of complex (**1**) (η^2–PPN)($Co(CNAr^{Mes2})_3$ (PPN = $(C_6H_5)_3P=N=P(C_6H_5)_3$) under a nitrogen atmosphere produces insoluble [PPN]Cl and diamagnetic complex (**2**) $(N_2)Co(SiMe_3)(CNAr^{Mes2})_3$ as assayed by ^1H NMR (C_6D_6, 20 ˚C), FTIR (KBr pellet) spectroscopy as well as X–ray crystallography (Scheme 3.3 and Figure 3.2).

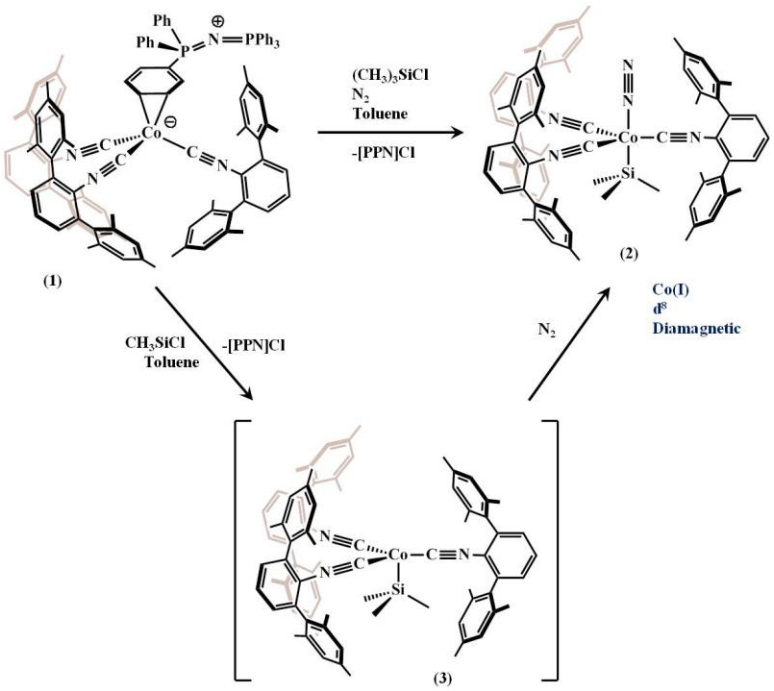

Scheme 3. 4. Synthesis of complex (**2**) under a dinitrogen atmosphere from the addition of $(CH_3)_3SiCl$ to complex (**1**).

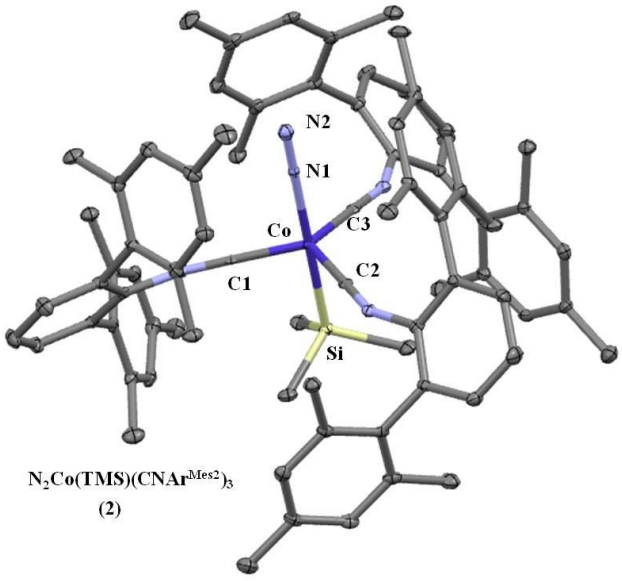

Figure 3. 2. Molecular structure of complex (**2**) $N_2Co(SiMe_3)(CN^{ArMes2})_3$. Thermal ellipsoids are shown at 30% probability and hydrogen atoms are excluded for clarity.

Attempts to remove N_2 by vacuum (8 mtorr) or by repeated pentane (C_5H_{12}) washes followed by exposure to vacuum were unsuccessful. Therefore, we employed an argon

atmosphere throughout the entire synthesis in attempts at isolating the coordinatively unsaturated [$Co(SiMe_3)(CNAr^{Mes2})_3$] complex (**3**). Employing a crystallization solvent DME (DME = dimethoxyethane) resulted in the formation of complex (**4**) (DME)$Co(SiMe_3)(CNAr^{Mes2})_3$. We speculate that complex (**3**) is formed *in situ* and if there is a potentially coordinating solvent nearby, it will bind to this highly Lewis acidic cobalt metal center. Synthetic support for the existence of complex (**3**) in solution was found by the broad array of adducts formed upon substrate addition: carbon monoxide $(CO)Co(SiMe_3)(CNAr^{Mes2})$ (**5**), water $(H_2O)Co(SiMe_3)(CNAr^{Mes2})_3$ (**6**), 1–hexene $(C_6H_{12})Co(SiMe_3)(CNAr^{Mes2})_3$ (**7**), hydrogen $(H_2)Co(SiMe_3)(CNAr^{Mes2})_3$ (**8**), pyridine $(C_5H_5N)Co(SiMe_3)(CNAr^{Mes2})_3$, ammonia $(NH_3)Co(SiMe_3)(CNAr^{Mes2})_3$ (Figure 3.3, Figure 3.4, Figure 3.5, and Scheme 3.4).[50]

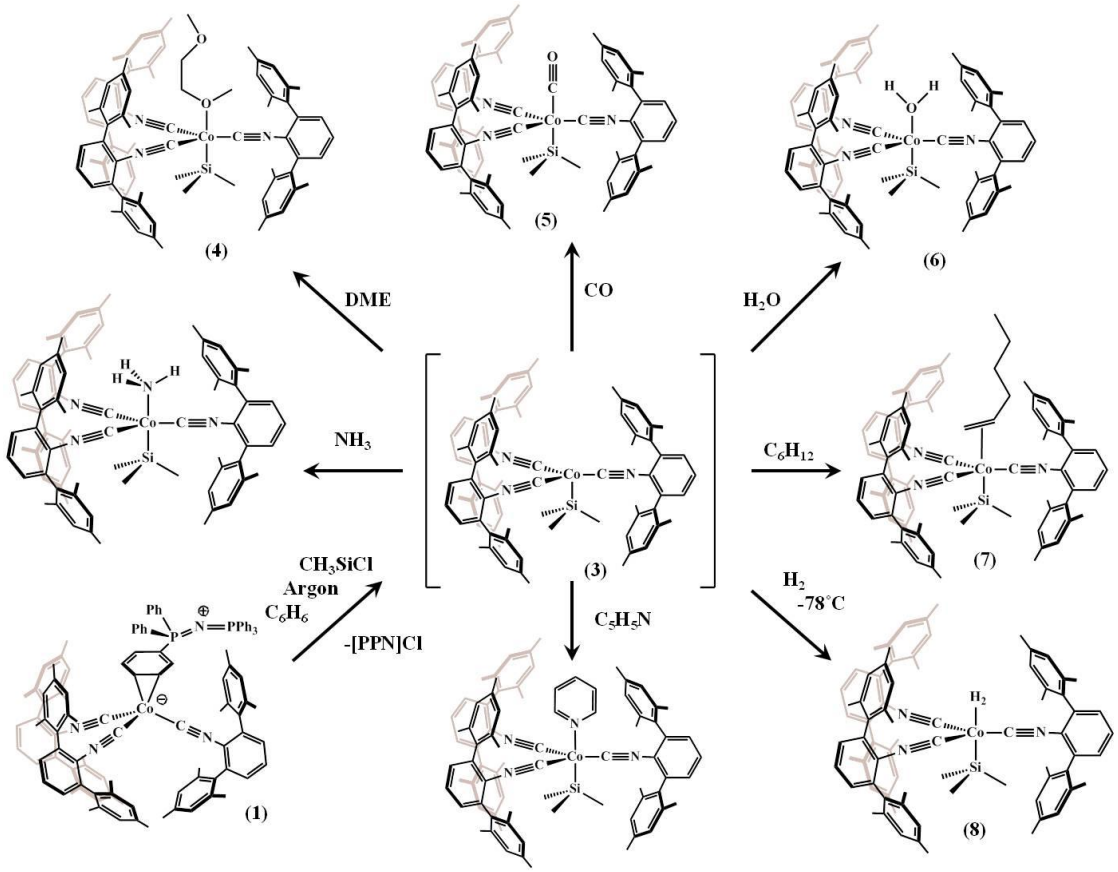

Scheme 3. 5. Reaction pinwheel of unsaturated complex (**3**) $Co(TMS)(CNAr^{Mes2})_3$.

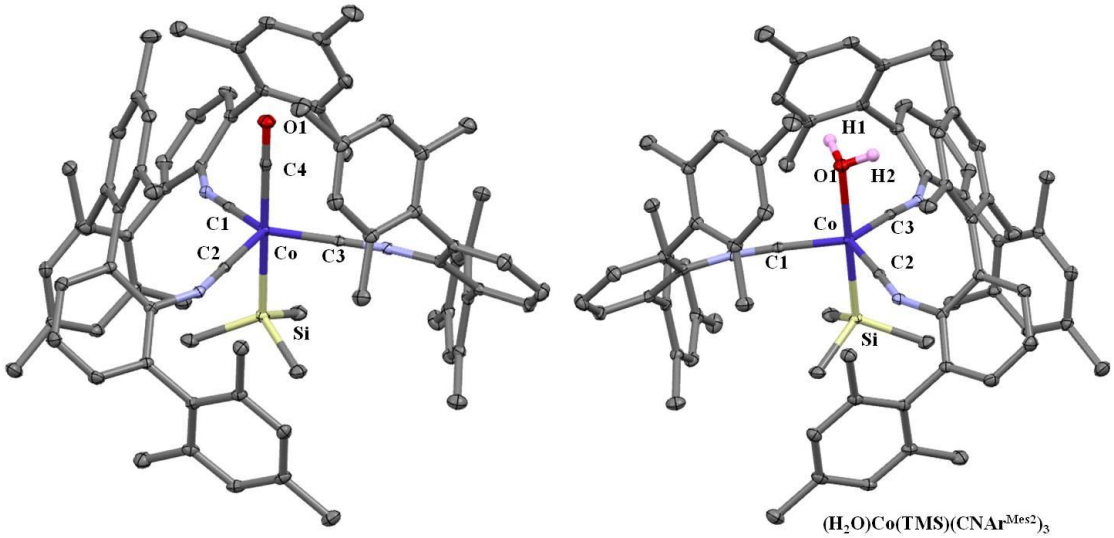

(CO)Co(TMS)(CNAr^{Mes2})$_3$ (5)

(H$_2$O)Co(TMS)(CNAr^{Mes2})$_3$ (6)

Figure 3. 3. X–ray crystal structures of complexes (**5**) and (**6**). Thermal ellipsoids are shown at 30% probability and hydrogen atoms were excluded for clarity except H_2O protons.

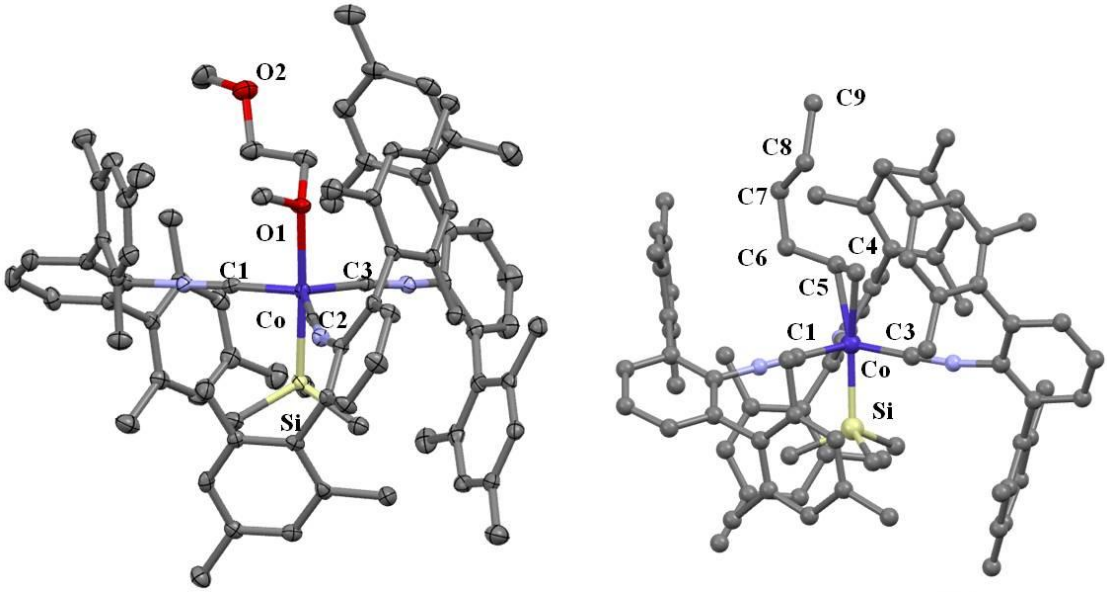

(DME)Co(TMS)(CNAr^{Mes2})$_3$ (4)

(C$_6$H$_{12}$)Co(TMS)(CNAr^{Mes2})$_3$ (7)

Figure 3. 4. X–ray crystal structures of complexes (**4**) and (**7**). Thermal ellipsoids are shown at 30% probability and hydrogen atoms were excluded for clarity for structure (**4**) Structure (**7**) was only isotropically refined.

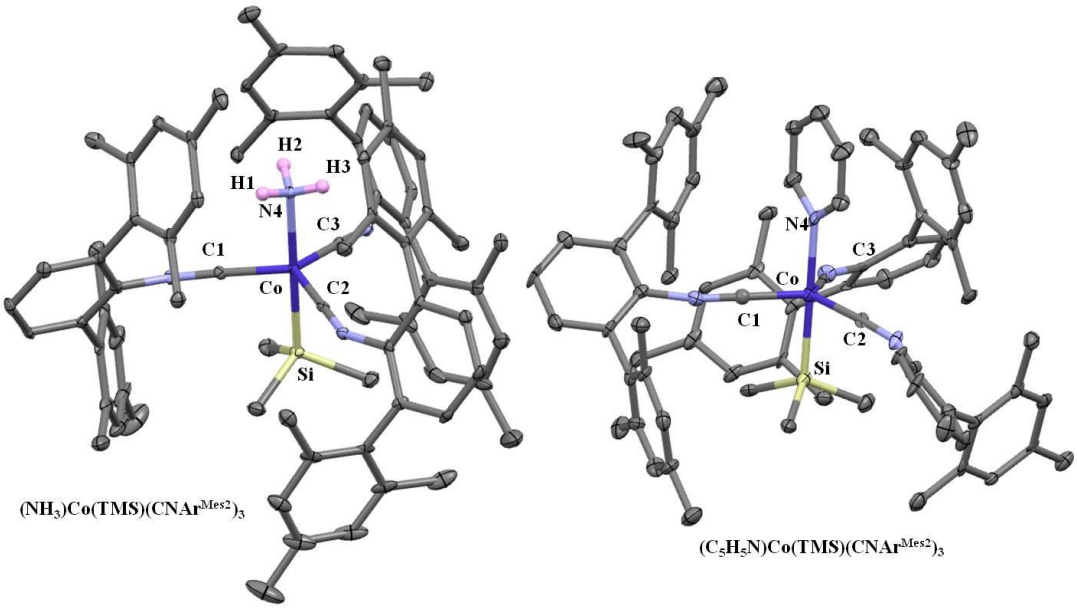

Figure 3. 5. X–ray crystal structures of ammonia and pyridine bound cobalt isocyanide complexes. Thermal ellipsoids are shown at 30% probability and hydrogen atoms were excluded for clarity except.

3.3 The Coordination of *n*–hexane and *n*–heptane to $Co((CH_3)_3Si)(CNAr^{Mes2})_3$

The addition of $(CH_3)_3SiCl$ to a benzene solution of zwitterionic complex (**1**) under an argon atmosphere produces the diamagnetic complex $Co(SiMe_3)(CNAr^{Mes2})_3$ (**3**) (Scheme 3.4) assayed by ^1H NMR (cyclohexane [D_{12}], 20 ˚C) and FTIR (KBr pellet) spectroscopy. We speculate that complex (**3**) persists in solution as the highly dynamic solvent bound complex, as evidenced by several NMR competition experiments. The ^1H NMR spectroscopic signal for the TMS group (TMS = trimethylsilyl, $Si(CH_3)_3$) in complex (**3**) is located at $\delta = -1.112$ ppm in *cyclo*–C_6D_{12}. This spectroscopic feature (singlet) undergoes a shift upon addition of 5% v/v of a stronger Lewis basic solvent, following the binding trend, *cyclo*–C_6D_{12} < C_6D_6 < DME. For example, the addition of more than ~5% v/v of C_6D_6 to a solution of complex (**3**) in *cyclo*–C_6D_{12} (35 μL of C_6D_6 in a volume of 0.8 ml of *cyclo*–C_6D_{12}) correspondingly shifts the TMS signature to $\delta = -1.070$ ppm. Furthermore, the addition of ~3% v/v of DME to a solution of complex (**3**) in C_6D_6 (21 μL of DME in a volume of 0.8 mL of C_6D_6) shifts the TMS peak

from δ = –0.690 ppm to δ = –0.751 ppm. We speculate that complex (**3**) binds NMR solvents C_6D_6, and *cyclo*–C_6D_{12}. Moreover, these solvents can be displaced upon adding a solvent with increased Lewis basicity. When less than 5% v/v of C_6D_6 was added to a *cyclo*–C_6D_{12} solution of complex (**3**), no detectable change occurred in the TMS region. The coordinative competition shown in these NMR experiments are similar to the competition between hydrocarbons and rare gas atoms in the flash kinetic studies performed on the rhodium complex Cp*Rh(CO) reported by Bergman and co-workers.[51]

In attempts to synthesize a non–solvated complex (**3**), we employed a "non–coordinating" crystallization solvent mixture of 95:5 v/v of *n*–hexane (*n*–C_6H_{14}) and benzene (C_6H_6). Indeed, an alkane σ–complex was observed! X–ray quality dark red single crystals were formed after 60–70 hours at 238K comprising the formula μ^2–(η^2-H, C–($CH_3(CH_3(CH_2)_4CH_3)$)[$Co(SiMe_3)(CNAr^{Mes2})_3$]$_2$·(*n*–$C_6H_{14}$)·2($C_6H_6$) (**9**·(*n*–$C_6H_{14}$)·2($C_6H_6$)) (see Figure 3.6). X–ray diffraction methods at 90K were refined to 0.80 Å in the space group P–1. There is one molecule of *n*–hexane and two molecules of benzene located in the periphery, of which all three co–crystallization solvents lack close contacts to the metal center (less than 3Å, which is longer than the van der Waals radii of hydrogen in alkanes (r_{vdW}(H) = 1.20 Å))[52]. It is the presence of 5 vol% of C_6H_6 that allows for the reproducibility of X–ray quality crystals from a *n*–hexane solution of (**9**)·(*n*–C_6H_{14})·2(C_6H_6). Although crystals are produced in the absence of C_6H_6, they were amorphous and not amenable to X–ray diffraction.

Further support for the binding of alkanes to complex (**3**) was found with the crystallization solvent mixture of 95:5 v/v of *n*–heptane (*n*–C_7H_{16}) and benzene (C_6H_6). This solvent mixture produced X–ray quality dark red single crystals after 100 hours at 238 K of the similar *n*–heptane adduct μ^2–(η^2-H,C–($CH_3(CH_3(CH_2)_5CH_3)$)[$Co(SiMe_3)(CNAr^{Mes2})_3$]$_2$·(*n*–$C_7H_{16}$) (**10**·(*n*–$C_7H_{16}$)) (shown in Figure 3.7). X–ray diffraction methods at 90K were refined to 0.82 Å in the space group $P2_1/n$. Located in the periphery is one solvent molecule of *n*–

heptane which lacks close contacts to the metal center (less than 3Å). Although benzene is not present in this crystal structure, its presence of 5 vol% is necessary for the reproducibility of X–ray quality crystals. Similar to complex (**9**·(*n*–C_6H_{14})·2(C_6H_6)), amorphous crystals of (**10**·(*n*–C_7H_{16})) are produced in the absence of C_6H_6 that were not amenable to X–ray diffraction methods.

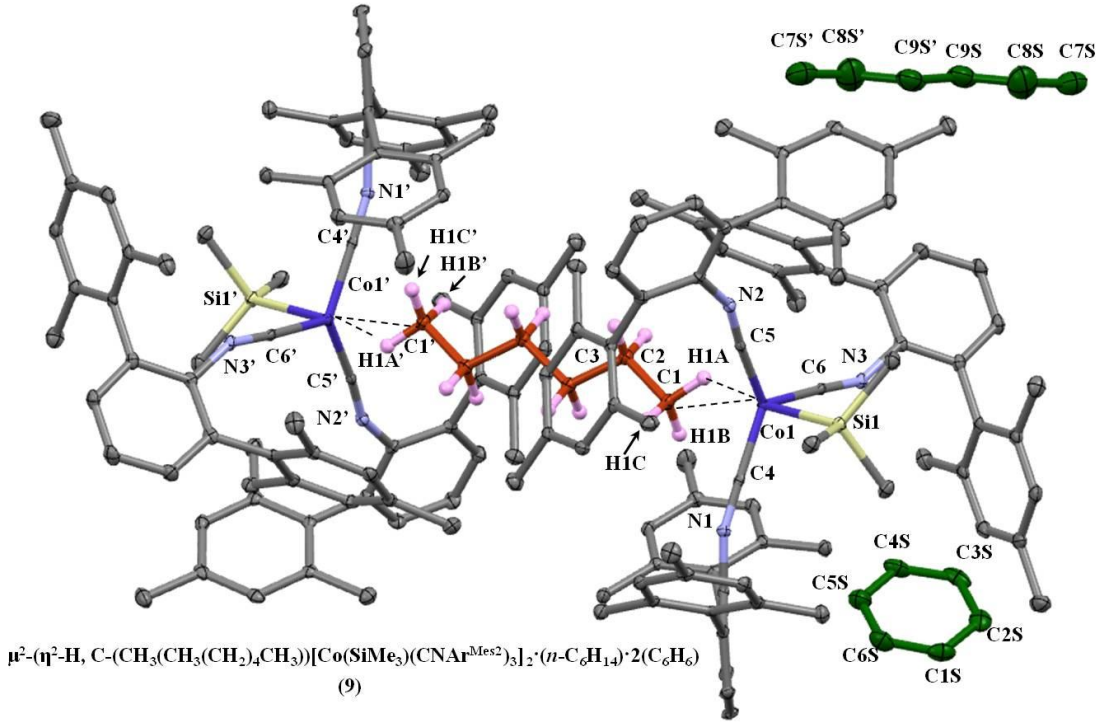

Figure 3. 6. X–ray crystal structure of complex (**9**)·(*n*–C_6H_{14})·2(C_6H_6) showing co–crystallization solvent molecules. Thermal ellipsoids are shown at 30% probability. Hydrogen atoms belonging to the $CNAr^{Mes2}$ ligands and co–crystallization solvent molecules have been omitted for clarity. A peripherally located benzene co–crystallization solvent molecular has been removed for clarity. Interior *n*–hexane molecule colored red and peripherally located solvent molecules *n*–hexane (C_6H_{14}) and benzene (C_6H_6) colored green for clarity. Hydrogen atoms of the bound *n*–hexane molecule were found in the electron density difference map and are colored pink for clarity.

X–ray crystallographic characterization of solution–derived alkane σ–complexes (μ^2–(η^2-H,C–($CH_3(CH_3(CH_2)_4CH_3)$)[$Co(SiMe_3)(CNAr^{Mes2})_3$]$_2$·(*n*–$H_{14}$)·2($C_6H_6$)(**9**·(*n*$C_6H_{14}$)·2($C_6H_6$)) and μ^2–(η^2-H,C–($CH_3(CH_3(CH_2)_5CH_3)$)[$Co(SiMe_3)(CNAr^{Mes2})_3$]$_2$·(*n*–$C_7H_{16}$) (**10**·(*n*–$C_7H_{16}$)) consists of two monovalent cobalt metal centers sandwiching a well ordered hexane (**9**·(*n*–C_6H_{14})·2(C_6H_6)) or a partially positional disordered inner *n*–heptane molecule (**10**·(*n*–C_7H_{16}))

(the heptane molecule in close proximity to cobalt). These coordinatively unsaturated Co (I) metal centers [$Co(SiMe_3)(CNAr^{Mes2})_3$] are formally 16 valence–electron, low spin organometallic fragments with an electron deficient d_z^2 orbital aligned *trans* to the apical trimethylsilyl ($Si(CH_3)_3$) group. The high Lewis acidity at the cobalt metal center is the result of a low–lying empty d_z^2 orbital oriented towards the open coordination site. The interplay between the sterically encumbering π–acidic ligands and the apically oriented vacant coordination site allows for the appropriate combination of electronic structure and geometry to bind alkanes in a σ–type of fashion, similar to the carbonyl complexes previously mentioned ($M(CO)_5$ where M = Cr, Mo, W). The structural parameters for (**9**·(*n*–C_6H_{14})·2(C_6H_6)) and (**10**·(*n*–C_7H_{16})) are comparable with previously studied complexes possessing a bona fide η^2-H,C alkyl agostic interaction to a transition metal center.[13,15] All hydrogen atoms in the well–ordered interior *n*–hexane molecule of (**9**)·(*n*–C_6H_{14})·2(C_6H_6) were located in the electron–density difference map and freely refined. Complex (**9**)·(*n*–C_6H_{14})·2(C_6H_6) crystallizes in the space group P–1 with the inversion center positioned at the mid–point of the sandwiched interior *n*–hexane molecule. The hydrogen atoms of the interior *n*–heptane molecule in (**10**)·(*n*–C_7H_{16}) were located in the electron–density difference map and freely refined, except for the two hydrogen atoms belonging to one of the terminal ends. These two hydrogen atoms contain disorder about atom C7 over 2–positions. These two hydrogen atoms, not in close contact with the cobalt metal center, were modeled but, importantly, the hydrogen atom in close contact with Co (1.982(20) Å) was located in the electron density difference map and freely refined (Figure 3.7).

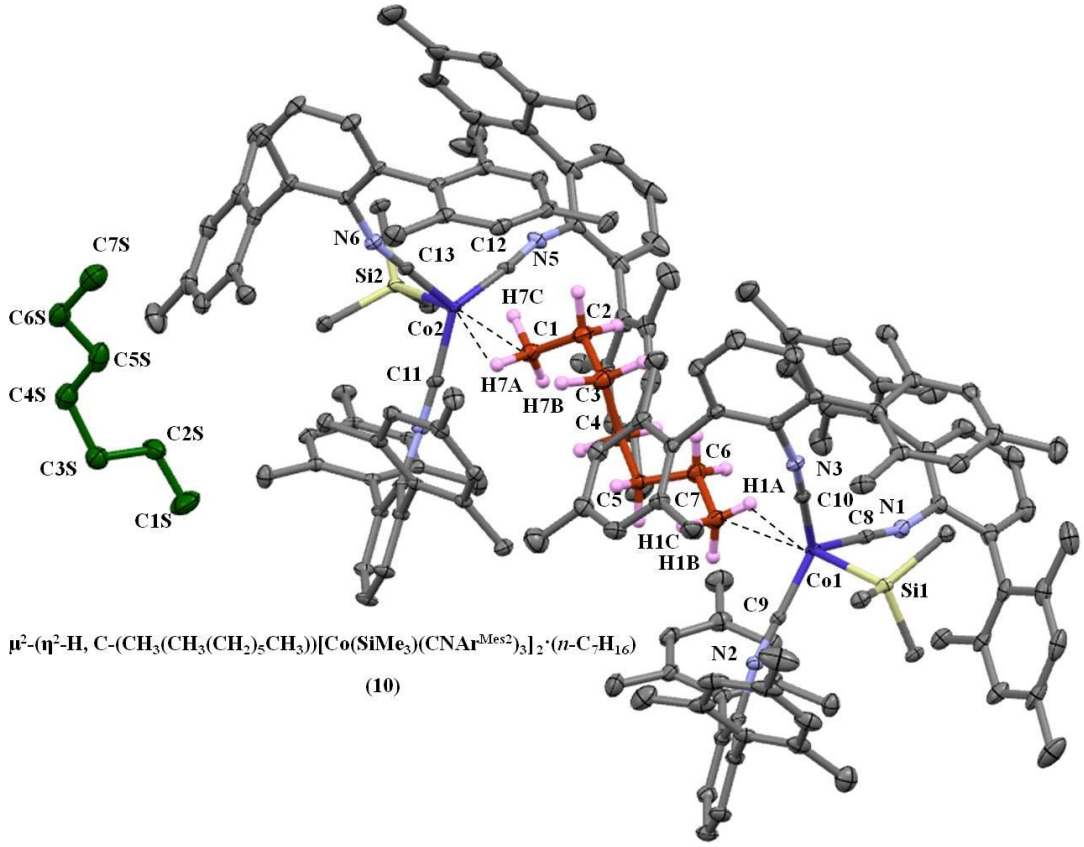

Figure 3. 7. X–ray crystal structure of complex (**10**)·(*n*–C_7H_{16}) showing co–crystallization solvent molecule. Thermal ellipsoids are shown at 30% probability. Hydrogen atoms belonging to the $CNAr^{Mes2}$ ligands and the co–crystallization solvent molecule have been omitted for clarity. Interior *n*–hexane molecule colored red and peripherally located solvent molecule *n*–heptane (C_7H_{16}) colored green for clarity. Hydrogen atoms located on interior *n*–heptane are colored pink.

3.4 Topological Examination of Complexes (9·(n–C_6H_{14})·2(C_6H_6)) and (10·(*n*–C_7H_{16}))

A topological examination of complex (**9**)·(*n*–C_6H_{14})·2(C_6H_6) reveals an η^2-H,C σ–type of interaction from the C–H bond of the terminal *n*–hexane methyl group to the cobalt metal center. Related by an inversion center, both cobalt metal centers possess a Co1–H1A distance of 1.995(30) Å and Co1–C1 distance of 2.718(3) Å with a Co1–H1A–C1 angle of 125.82(20) ˚. These parameters fall within the range for structurally characterized η^2-H,C alkyl agostic complexes (d(M–H) = 1.8 – 2.3 Å; (M–H–C angle) = 90–140).[15,13] The close contacts representing an alkane σ–complex finds computational support from previous studies

on σ–type interactions with propane and *n*–pentane.[13,34,53] Although subtle, there is a slight lengthening (0.04–0.05 Å) of the *n*–hexane terminal methyl C1–H1A bond (C1–H1A 1.02(2) Å, C1–H1B 0.98(3) Å, C1–H1C 0.97(3) Å) that is in close proximity to cobalt (Co1–H1A 1.995(30) Å, Co1–H1B 2.760(30) Å, and Co1–H1C 3.011(30) Å)) (Figure 3.8). The lengthening of the C–H bond by metal π–back donation to the C–H σ* orbital of the alkane is consistent with the Dewer–Chatt–Duncanson bonding model. [54] This minor elongation is at the limit of detection and may be considered insignificant based on the 3σ error criterion for crystallographic metrical parameters. [55] Support for the lengthening of a C–H bond is provided by *ab initio* and DFT methods of the C–H bond in η^2-H,C alkane σ–complexes.[14,29,56,57] This slight C–H bond lengthening was not noted in complex (**10**)·(*n*–C_7H_{16}).

A topological examination of complex (**10**)·(*n*–C_7H_{16}) reveals a σ–type interaction between the cobalt metal center and the C–H bond of the terminal *n*–heptane methyl groups. Close contacts of (**9**·(*n*–C_6H_{14})·2(C_6H_6)) and (**10**·(*n*–C_7H_{16})) are compared in Table 3. 1 with close contacts from complex (**10**·(*n*–C_7H_{16})) having the following: Co1–H1A distance of 2.117(30) Å and Co1–C1 distance of 2.719(3) Å with the Co1–H1A–C1 angle of 122.60(20)˚ (Figure 3.9). Interestingly, the second terminal methyl group of the internal *n*–heptane molecule possesses disorder about two positions, C7A and C7B, but both carbon positions commonly share one hydrogen atom H7, which is in close proximity to cobalt (Co2–H7A 1.982(30) Å, Co2–C7A 2.798(3) Å, Co2–C7B 2.779(3) Å, Co1–H7A–C7A angle of 130.88(20)˚, Co1–H7A–C7B angle of 141.34(20)˚) (Figure 3.10).

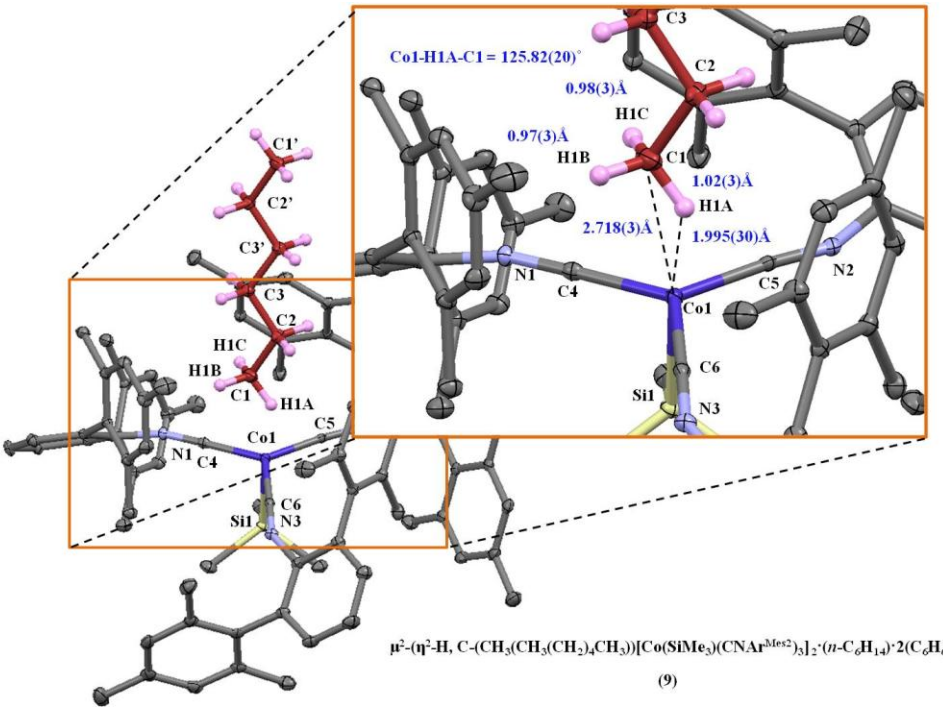

Figure 3. 8. Expanded view of complex (**10**·(n–C_7H_{16})) with selected metrical parameters. Thermal ellipsoids set to 30% probability. Inner n–hexane molecule colored red for clarity. Hydrogen atoms belonging to the $CNAr^{Mes2}$ ligands and the co–crystallization solvent molecules have been omitted for clarity.

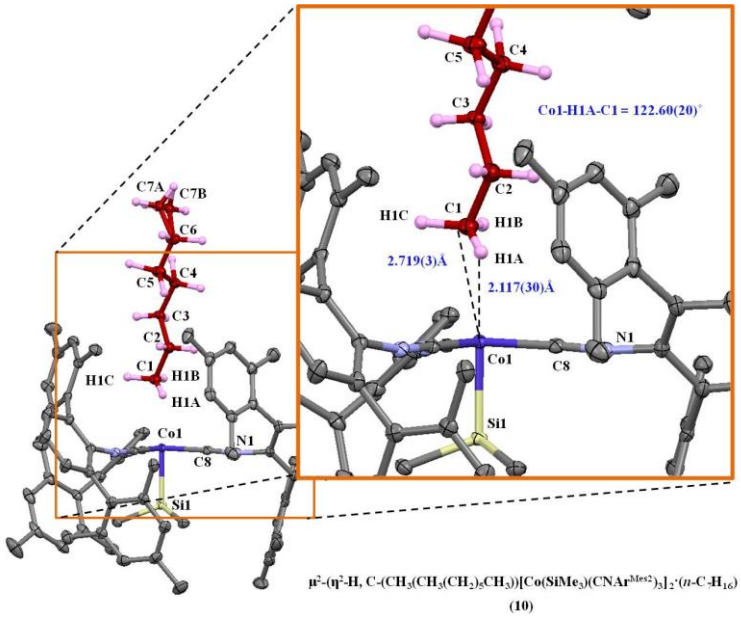

Figure 3. 9. Expanded view of complex (**10**·(n–C_7H_{16})) showing the well–ordered terminal n–heptane methyl group with selected metrical parameters. Thermal ellipsoids set to 30% probability. Inner n–heptane molecule colored red for clarity. Hydrogen atoms belonging to the $CNAr^{Mes2}$ ligands, co–crystallization solvent molecule, and the second cobalt metal center have been omitted for clarity.

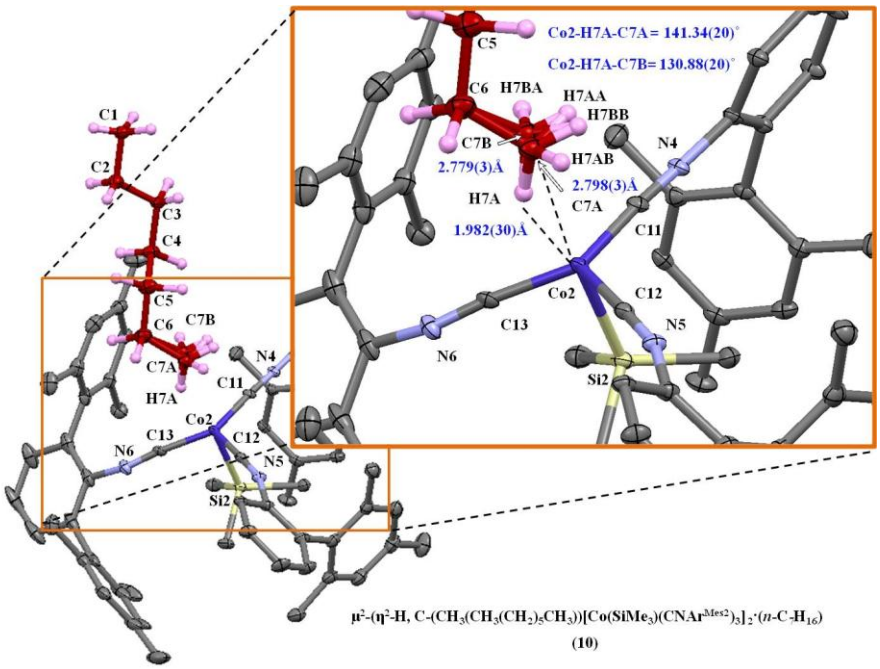

Figure 3. 10. Expanded view of complex (**10**·(*n*–C_7H_{16})) showing the disordered terminal *n*–heptane methyl group with selected metrical parameters. Thermal ellipsoids set to 30% probability. Inner *n*–heptane molecule colored red for clarity. The second cobalt metal center, the co–crystallization solvent molecule, and the hydrogen atoms belonging to the $CNAr^{Mes2}$ ligands have been omitted for clarity.

3.5 Support for a σ–type Interaction from the Crabtree r_{bp} Parameter

Crabtree's r_{bp} structural criterion for the interaction of C–H bonds with transition metal centers was used to determine the alkane σ–interaction for complexes (**9**·(*n*–C_6H_{14})·2(C_6H_6)) and (**10**·(*n*–C_7H_{16})).[58] Crabtree's r_{bp} parameter accounts for the inaccuracy in determining hydrogen atom positions by X–ray diffraction methods. The r_{bp} parameter is used as a standard method in measuring the degree of C–H to metal bonding interaction in η^2–H,C alkyl σ–complexes. The r_{bp} parameter encompasses variations in covalent radii for transition metal centers (r_M), as well as the *ca.* 0.1 Å under–determination of hydrogen–element bonds by X–ray diffraction techniques. This r_{bp} value effectively describes the covalent radius of the C–H bonding electrons with a transition metal. The lower bound for r_{bp} values representing single M–C and M–H covalent interactions is 0.4 Å and the upper bound for values representing distances appropriate for electrostatic interactions and/or simple van der Waals contacts is 1.9 Å.[58]

The following equations were used to calculate the r_{bp} values for complexes (**9**·(*n*–C_6H_{14})·2(C_6H_6)) and (**10**·(*n*–C_7H_{16})).

$$r_{bp} = d_{bp} - r_M \quad \textbf{(E3.1)}$$

Where M = Co

$$d_{bp} = [{d_{MH}}^2 + r^2{d_{CH}}^2 - r({d_{MH}}^2 + {d_{CH}}^2 - {d_{MC}}^2)]^{1/2} \quad \textbf{(E3.2)}$$

where the constant r = 0.28 is the ratio of r_M(H) to the standard C–H distance (1.09Å)

$$d_{MH} = l_{MH} + 0.1\left\{\frac{l_{CH^2} + l_{MH^2} - d_{MC^2}}{2l_{CH}l_{MH}}\right\} \quad \textbf{(E3.3)}$$

$$d_{CH} = l_{CH} + 0.1 \quad \textbf{(E3.4)}$$

Definitions

r = radius

d = bond distance

l = bond length

An r_{bp} value of less than 1.0 Å is typical for strong η^2-H,C alkyl agostic interactions. Crabtree categorized the most strongly bound η^2-H,C agostic complexes to possess an r_{bp} range of 0.59 – 0.69 Å (less is more). Complexes that have definitive η^2-H,C agostic interactions possess an r_{bp} range of 0.69 – 1.12 Å. Utilizing equations (**E3.1**)–(**E3.4**), complex (**9**·(*n*–C_6H_{14})·2(C_6H_6)) possesses an r_{bp} values of 0.76–1.029 Å. This range of values incorporates the uncertainty surrounding published covalent radii available for cobalt.[859-62] Calculated r_{bp} values for Complex (**10**·(*n*–C_7H_{16})) were split into three categories: (i) the well ordered carbon C1, (ii) positional disordered carbon C7A and (iii) positional disordered carbon C7B (Table 3. 1).

Table 3. 1. Calculated r_{bp} values for complexes (**9**·(*n*–C_6H_{14})·2(C_6H_6)) and (**10**·(*n*–C_7H_{16})).

Parameter	Value for Complex 9 (Å)	Value for Complex 10 (Å)	Value for Complex 10 (Å) Disordered C7(A)	Value for Complex 10 (Å) Disordered C7(B)
l_{MH}	1.995	2.117	1.982	1.982
l_{CH}	1.02	0.912	0.961	1.043
d_{MC}	2.718	2.719	2.798	2.779
d_{CH}	1.12	1.012	1.061	1.143
d_{MH}	1.936	2.063	1.903	1.916
d_{bp}	2.125	2.220	2.139	2.132
r_{bp}	0.76–1.029	0.840–1.110	0.759–1.029	0.753–1.022

r_M(Co) (Å)	Complex (9) r_{bp} (Å)	Complex (10) C1 r_{bp} (Å)	Complex (10) C7A r_{bp} (Å)	Complex (10) C7B r_{bp} (Å)	Ref. #
1.11	1.02	1.11	1.03	1.02	59
1.15	0.97	1.07	0.99	0.98	60
1.25	0.87	0.97	0.89	0.88	8
1.25	0.86	0.96	0.88	0.87	61
1.38	0.74	0.84	0.76	0.75	62

The upper bound of r_{bp} values calculated for complexes (**9**·(*n*–C_6H_{14})·2(C_6H_6)) and (**10**·(*n*–C_7H_{16})) fall well within the range accepted for definitive η^2-H,C agostic interactions as defined by Crabtree. The upper limit for an r_{bp} value, that accounts for the most contracted cobalt covalent radii (r_M), is comparable to Green's well–defined η^2-H,C agostic titanium–ethyl complex ($Me_2PCH_2CH_2PMe_2$)$TiEtCl_3$ (r_{bp} = 0.98 Å).[13,15,58,63]

3.6 Van der Waals Interactions in Complexes (9·(n–C_6H_{14})·2(C_6H_6)) and (10·(*n*–C_7H_{16}))

Careful examination of X–ray crystal structures (**9**·(*n*–C_6H_{14})·2(C_6H_6)) and (**10**·(*n*–C_7H_{16})) revealed potential van der Waals (vdW) interactions from the coordinated *n*–hexane and *n*–heptane to the Ar^{Mes2} framework. We speculate the binding of the *n*–hexane to be assisted by weak C···H and H···H vdW interactions. The three vdW interactions in complex (**9**·(*n*–C_6H_{14})·2(C_6H_6)) are symmetric about the C3 carbon atom of the bridging *n*–hexane molecule. This symmetry is strictly enforced by a crystallographic inversion center. The

shortest sub–vdW contact is the H···H distance of 2.389 Å arising from H3A (located on *n*–hexane) and H74 (located on the Ar^{Mes2} ligand). This distance is slightly shorter than the sum of the vdW radii (r_{vdW}) for hydrogen atoms in alkanes (r_{vdW}(H) = 1.20 Å).[52] The two remaining vdW interactions are C···H contacts that are slightly shorter than the sum of the vdW radii for carbon and hydrogen bonds in alkanes (r_{vdW}(C) = 1.70 Å)[52] These sub–vdW interactions are located between H2B and the adjacent mesityl ring carbon atoms C25 and C26 at a distance of 2.708Å and 2.833Å, respectively (Figure 3.11). These weak interactions from the Ar^{Mes2} ligands may energetically assist the alkane molecule into the protective mesityl pocket on the pathway to forming the η^2-H,C σ–type interaction. This assistance may be comparable to the chelate effect found in agostic complexes (see section 3.12 for further details). Similarly, host–guest interactions have been observed in the solid state for the iron and uranium systems of Reed[38] and Meyer. [39]

Complex (**10**·(*n*–C_7H_{16})) contains several vdW interactions from the coordinated *n*–heptane to the Ar^{Mes2} ligand. These vdW interaction are found on all five interstitial carbon atoms within the encapsulated *n*–heptane. The C···H and H···H distances are as follows: H2B···C129 = 2.80 Å, H3B···C144 = 2.851 Å, H4A···C56 = 2.888 Å, H4B···H28 = 2.386 Å, H5A···H131 = 2.358 Å, H6A···H73A = 2.370 Å, H6A···C73 = 2.787 Å, H6A···C68 = 2.638 Å, H6A···C69 = 2.806 Å, H6B···H33C = 2.368 Å, H6B···C33 = 2.741 Å , H6B···C28 = 2.882 Å (underlined hydrogens belong to the inner *n*–heptane) (Figure 3.11). Interestingly, there is an increased amount of vdW close contact interactions on the terminal end that contains disorder (see section 3.15 for further details).

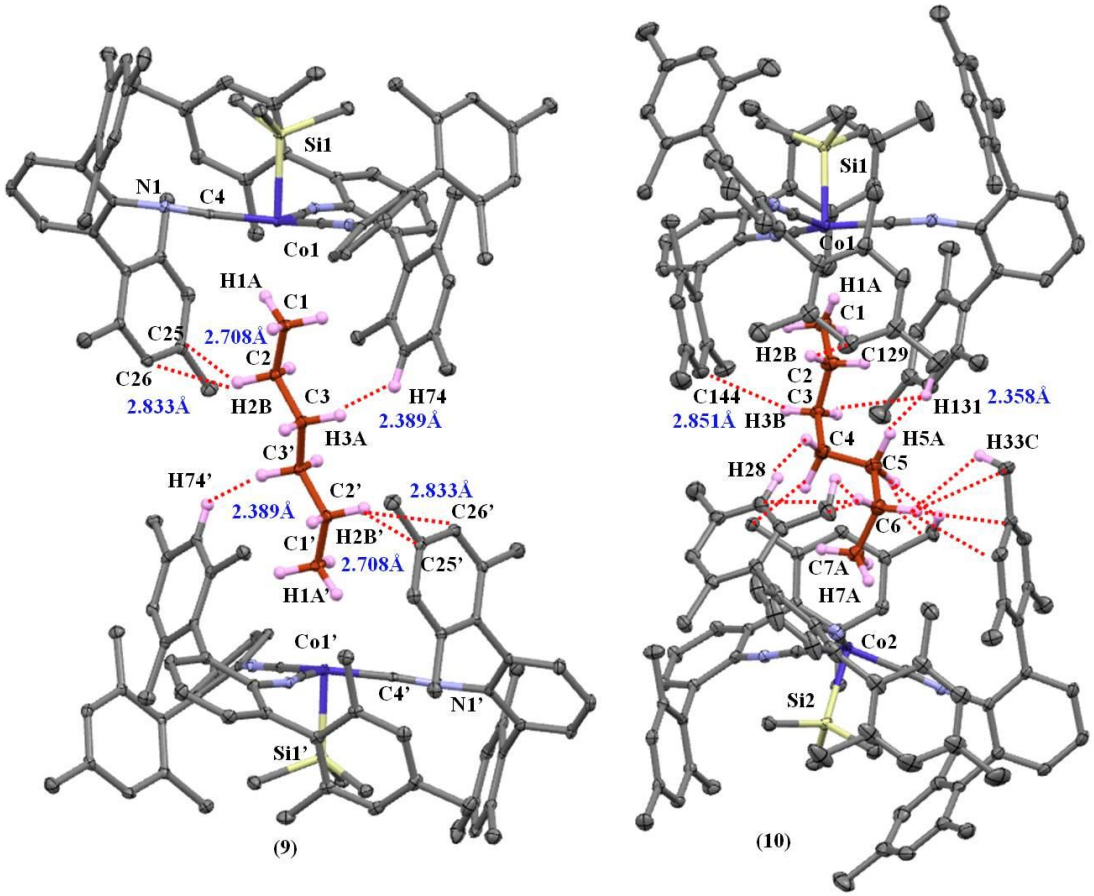

Figure 3. 11. Depiction of sub–van der Waals interactions for alkane σ–complexes (**9**·(*n*–C_6H_{14})·2(C_6H_6)) and (**10**·(*n*–C_7H_{16})). Complex (**9**·(*n*–C_6H_{14})·2(C_6H_6)) has 2 mesityl groups removed for clarity. Thermal ellipsoids set at 30% probability. Only selected distances are shown for complex (**10**·(*n*–C_7H_{16})).

3.7 Computational Support at the DFT Level of Theory

The σ–alkane interaction in complex (**9**·(*n*–C_6H_{14})·2(C_6H_6)) was examined by DFT calculations at the PBE0/6–31G**/SDD level of theory on a monomeric model complex (η^2-H,C–($CH_3(CH_2)_4CH_3$))Co($SiMe_3$)($CNXyl)_3$ (**11**, where Xyl = 2,6–$Me_2C_6H_3$) (see section 3.21 for details). The optimized model complex (**11**) has slightly elongated (ca. 0.1Å) hydrogen–element bond distances when compared to experimentally determined parameters for complex (**9**·(*n*–C_6H_{14})·2(C_6H_6)). This elongation can be accounted for with the ca. 0.1 Å underestimation of hydrogen–element X–ray data. Even though complex (**11**) is missing the

flanking Ar^{Mes2} groups, which likely provides host–guest stabilization contacts, the σ–type interaction to the cobalt metal center is computationally preserved (Table 3. 2).

Table 3. 2. Metrical parameter comparison between experimentally derived complex (**9**·(*n*–C_6H_{14})·2(C_6H_6)) and computationally determined complex (**11**).

Parameter	Complex (9) Exp. (X–ray)	Complex (11) Calculated (DFT)	% Difference
Co1–H1A	1.995(30) Å	1.909 Å	4.3
Co1–C1	2.718(3) Å	2.793 Å	2.8
C1–H1A	1.02(2) Å	1.115 Å	9.7
C1–H1B	0.98(3) Å	1.094 Å	11.5
C1–H1C	0.97(3) Å	1.092 Å	11.2
Co–(H1A–C1)$_{centroid}$	2.329 Å	2.326 Å	0.1
Co1–Si1	2.2550(2) Å	2.245 Å	0.5
Co–C4	1.7952(1) Å	1.785 Å	0.6
Co–C5	1.8168(1) Å	1.785 Å	1.8
Co–C6	1.8994(1) Å	1.789 Å	1.1
Co1–H1–C1	125.86˚	133.21˚	5.8
Si1–Co1–H1	172.0(2)˚	168.10˚	2.3
Si1–Co1–(H1A–C1)	176.0(5)˚	178.2˚	1.3

3.8 Computational Support by the Atoms in Molecules Method

Complex (**11**) was also investigated computationally by the Atoms in Molecules (AIM) method.[64] A topological examination of the electron density with AIM on complex (**11**) reveals a (3,–1) bond critical point (BCP) is present between the Co metal center and the H1 atom on the *n*–hexane methyl group (Figure 3.12, Table 3. 3). The values of the electron density (ρ) and Laplacian of the electron density ($\nabla^2\rho$) at this BCP are 0.034 a.u. and 0.134 a.u., respectively. These values are close to the lower threshold currently accepted for complexes possessing definitive η^2–H alkyl agostic interactions (ρ = 0.035 – 0.050 a.u.; $\nabla^2\rho$ = 0.150 – 0.250).[65–6667] The AIM analysis on complex (**11**) revealed a weak metal/H–C bond relative to η^2-H,C alkyl agostic complexes but it should be noted that model complex (**11**) has an elongated (0.075 Å) bond distance between Co and the *n*–hexane methyl carbon when compared to experimental parameters, as well as, lacks any contributions in stabilization energy from the chelate effect (two monomeric metal complexes chelating one molecule of *n*–

hexane). Furthermore, despite the weak interaction based on the BCP, complex (**11**) does show a depletion of electron density for the Co–bound C–H bond relative to the unbound C–H units in the peripherally located *n*–hexane methyl groups (ρ = 0.259 vs. 0.280 vs. 0.281 a.u.). Thus, support from computational methods, both DFT and AIM, indicate a weakening of the terminal methyl C–H bonds in the sandwiched *n*–hexane molecule upon binding to the cobalt metal center.

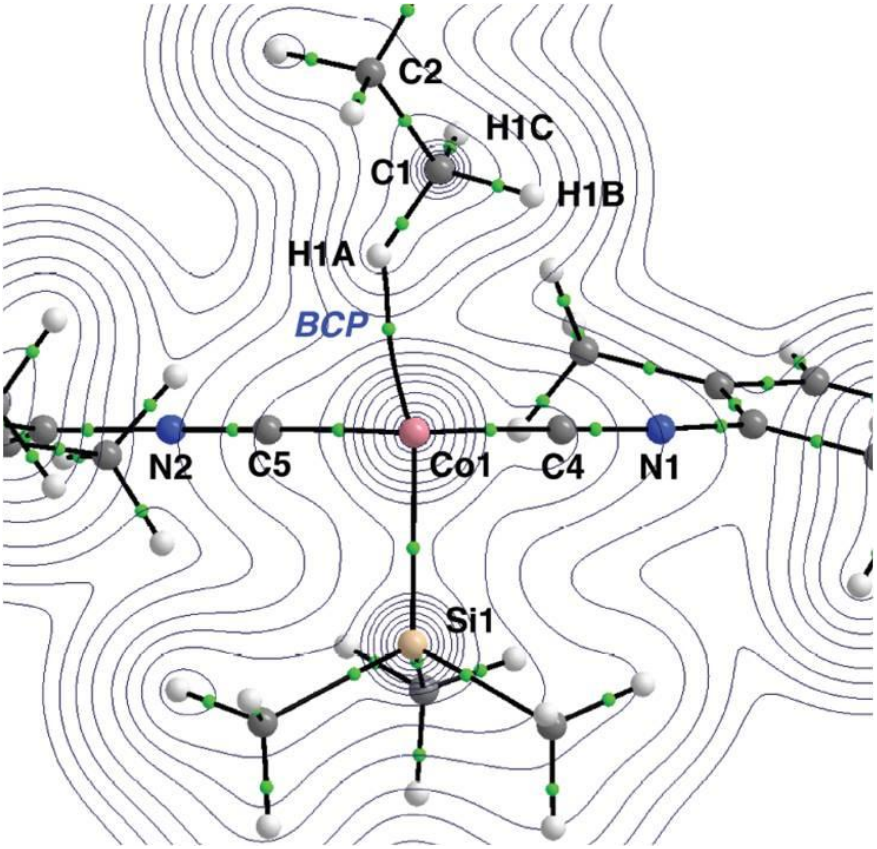

Figure 3. 12. Electron density (ρ) topology plot for model complex (**11**) in the H1A–Co–C4 plane. Bond paths are represented by black lines and bond critical points (BCP) are represented as green spheres.

Table 3. 3. Topological Features of the Electron Density in model complex (**11**) from AIM Analysis (from single point calculation using PBE0/6–311++G(3df,2pd)/SDD(ECP))

Bond	ρ_{BCP} (a.u)	$\nabla^2\rho_{BCP}$ (a.u.)	ε_{BCP}	H_{BCP}
Co1–H1A	0.034	0.143	0.021	–0.001
C1–H1A	0.259	–0.861	0.009	–0.264
Co1–Si1	0.085	–0.097	0.003	–0.047
Co1–C4	0.149	0.518	0.016	–0.068
Co1–C5	0.150	0.519	0.014	–0.070
Co1–C6	0.150	0.519	0.012	–0.070
N1 – C4	0.291	–0.622	0.062	–0.432
N2 – C5	0.291	–0.604	0.063	–0.433
N3 – C6	0.291	–0.619	0.062	–0.432

3.9 NMR Studies in Alkane Solvents

The use of low temperature (T < 200K) NMR methods to detect alkane σ–complexes has recently been reported by Ball,[29–34] George, Perutz,[35,36] and Brookhart.[37] These studies definitively show the coordination of alkanes to a transition metal according to the spectroscopic features in the NMR belonging to the η^2-H,C alkyl bound unit. The ^{1}H NMR studies of these complexes have revealed that the shielded η^2-H,C alkyl proton is located in the range 0.5 ppm to –6.5 ppm and the ^{13}C displays a shielded feature in the range –17 ppm to –43 ppm. These studies reveal that alkyl binding occurs not only at the terminal ends but throughout the entire alkane. For example, Ball et al. showed the binding of *n*–pentane to the metal complex (*i*-PrCp)Re(CO)$_2$ displayed three shielded ^{1}H spectroscopic features assigned to the three possible *n*–pentane complexes, wherein the metal is bound to C1, C2, or C3.[30]

Attempts with ^{1}H Nuclear Magnetic Resonance spectroscopy to resolve spectroscopic features belonging to the bound η^2-H,C alkyl protons in complex (**9**) have been unsuccessful to date. Initial attempts using detection methods that isolate the η^2-H,C alkyl region of the spectrum and avoid detection of the protio *n*–hexane solvent peak (δ = 1.43 (CH_2), 1.04 (CH_3)) via digital filtration were unsuccessful due to residual protio solvent magnetization that was present in the observed region.[68] To circumvent the dynamic range issue, we employed shaped

pulses to limit the irradiation bandwidth to the chemical shift region where we would expect the η^2-H,C alkyl feature (more shielded, up-field of 0 ppm). This method was chosen over the more widely employed solvent suppression techniques such as WATERGATE because dynamic exchange of the bound *n*–hexane with the free *n*–hexane would preclude the detection of the η^2-H,C alkyl feature. The pulse shapes found to be most effective at isolating the detection region and avoiding excitation of the free *n*–hexane were adiabatic WURST or non–adiabatic EBURP2 pulse schemes (Figure 3.13). Although these techniques allowed us to overcome the dynamic range issues presented by the protio solvent mixture, the resonances of the η^2-H,C alkyl ligand were not observed (Figure 3.14).

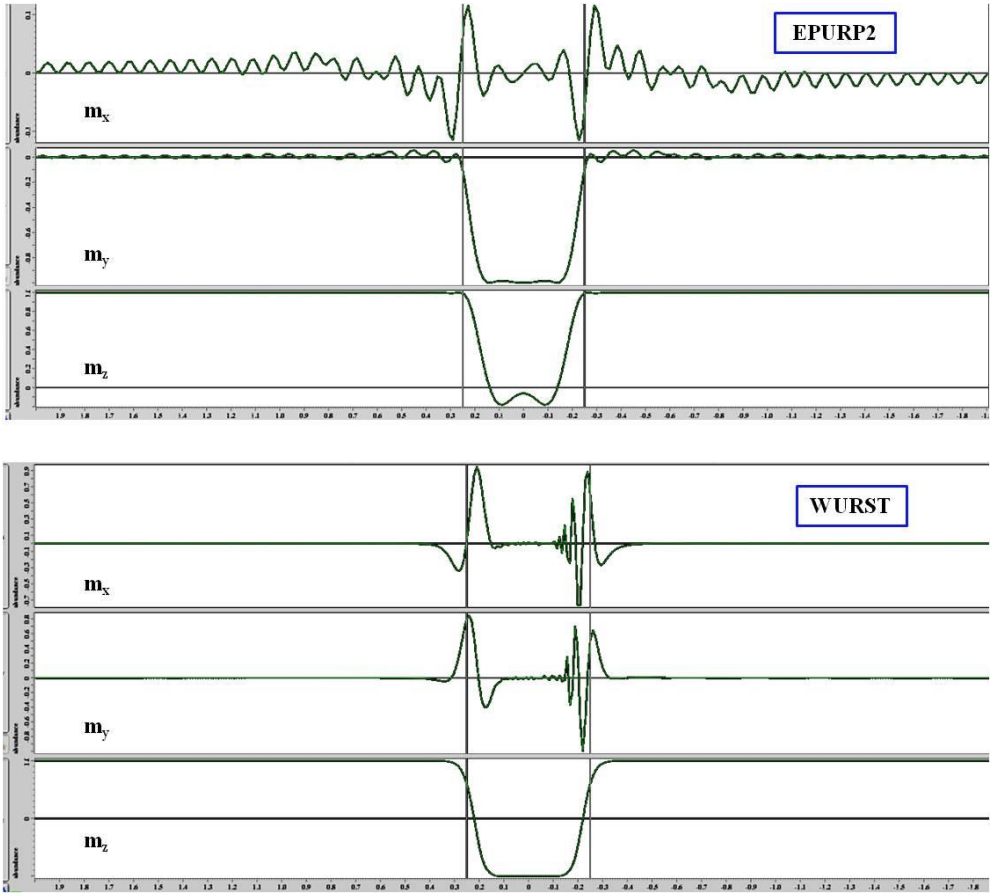

Figure 3. 13. Pulse schemes shown are adiabatic WURST (bottom) and non–adiabatic EBURP2 (top). Magnetization planes m_x, m_y, and m_z labeled on the left side.

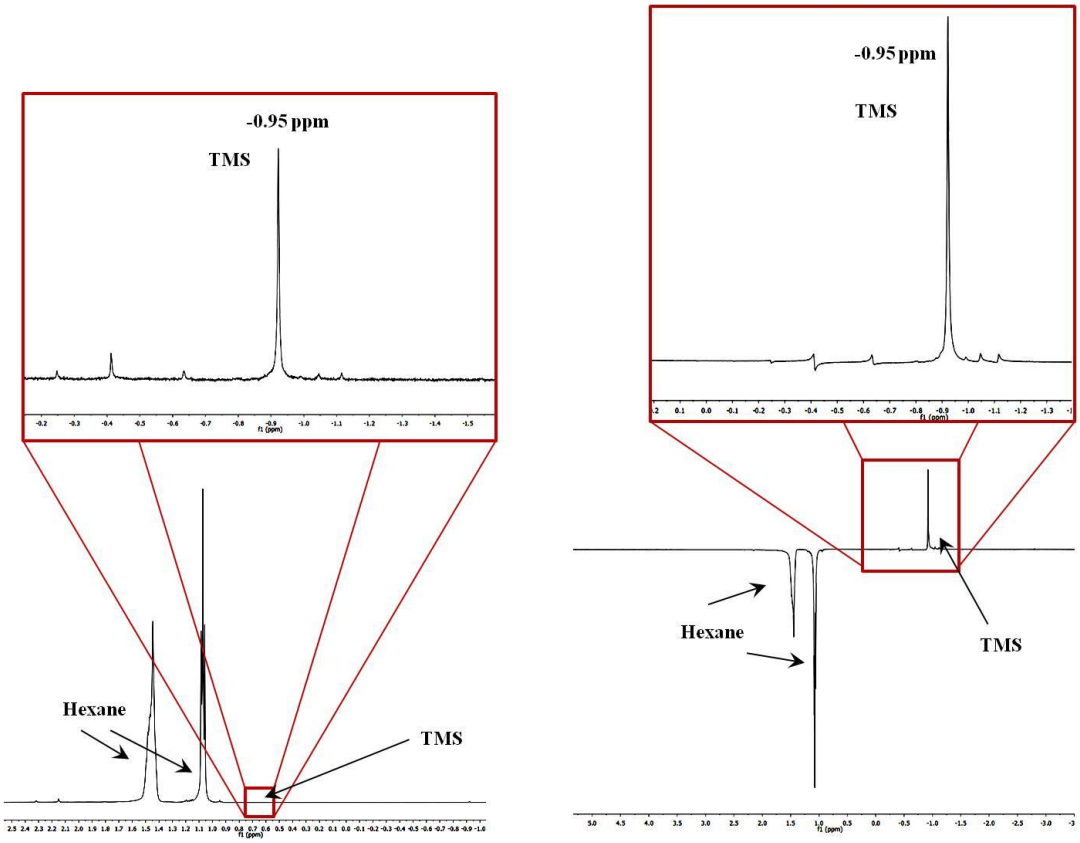

Figure 3. 14. Successful attenuation of the protio *n*–hexane resonance employing the pulse shape EBURP2. Complex (**3**) dissolved in a solvent mixture of 90:10 C_6H_{14}:C_6D_{14} at –80˚C. Left spectrum is normal ^{1}H NMR, 32 scans. Right spectra is the same sample as left, 32 scans, but resolution has been significantly enhanced from the selective irradiation EBURP2 pulse scheme focused at -1.3 ppm with a 1ppm bandwidth.

Single crystals of complex (**9**·(*n*–C_6H_{14})·2(C_6H_6)) were dissolved in a mixture of C_6H_{14}:C_6D_{14} at a ratio of 85:15 (after a cold *n*–hexane wash/vacuum cycle) and examined by ^{1}H NMR spectroscopy in the temperature range from –90˚C to +10˚C. The three deshielded (downfield) resonances in the enlarged NMR spectrum in Figure 3.14, as compared to the $Si(CH_3)_3$ peak located at δ = –0.95 ppm, are decomposition products.[69] Interestingly, as shown in Figure 3.15, the three resonances upfield of the $Si(CH_3)_3$ protons shows a conformational equilibrium involving complex (**3**) at low temperatures. The ^{1}H NMR in Figure 3.15 shows resonances corresponding to the nine protons located on the three equivalent methyl groups belonging to the apically bound $Si(CH_3)_3$ (TMS) ligand, forming a spectroscopic fingerprint for complex (**3**) at δ = –0.95 ppm. Variable-Temperature (VT) ^{1}H NMR studies of complex (**9**)

show a minimum of four species in solution at –80 ˚C as shown by the methyl, aryl, and TMS regions of the ^{1}H NMR data (Figure 3.15, Figure 3.16, Figure 3.17). The four resonances may correspond to a conformational equilibrium wherein three of the $Si(CH_3)_3$ group resonances correspond to different binding modes of the alkane to the cobalt metal center. The ligand *n*–hexane has three unique carbon sites (C1, C2 and C3) that could undergo coordination with the metal center accounting for three of the four species in solution, with the fourth corresponding to the major product at –80˚C, uncoordinated complex (**3**) but this is purely speculation. Two–dimensional NMR experiments EXSY, COSY, and DOSY were attempted at low temperatures but the results did not provide sufficient evidence of exchange (EXSY) or close contacts (COSY). In attempts to differentiate the several chemical species present at low temperatures and determine if complex (**9**) formed a dimer in solution we employed a DOSY NMR experiment. The DOSY experiment was performed at –40˚C and revealed what appears to be two species in equilibrium with each other with a possible third species in solution. We were unable to definitively assign any spectroscopic features belonging to a η^2-H,C alkyl feature. Full characterization of the highly dynamic alkyl–bound complex (**9**) will likely require the capability to access temperatures below what is capable with the present equipment at UCSD (VT limit of the JOEL ECA500 is –100˚C) as all known fully resolved alkane σ–complexes were performed below –110˚C.[70]

It is possible that the nine protons belonging to the $(CH_3)_3Si$ group are observable because they are less dynamic at temperatures above –100˚C, allowing for the detection of alkyl binding. When alkyl binding occurs, the cobalt dz^2 orbital directly influences the methyl resonance of the methyl protons in $(CH_3)_3Si$ via the electronic contribution to the paramagnetic shielding tensor.[71] Therefore, we speculate that the proton resonance for the $(CH_3)_3Si$ group in complex (**3**) might be exploited as an independent reporter for the binding of *n*–hexane.

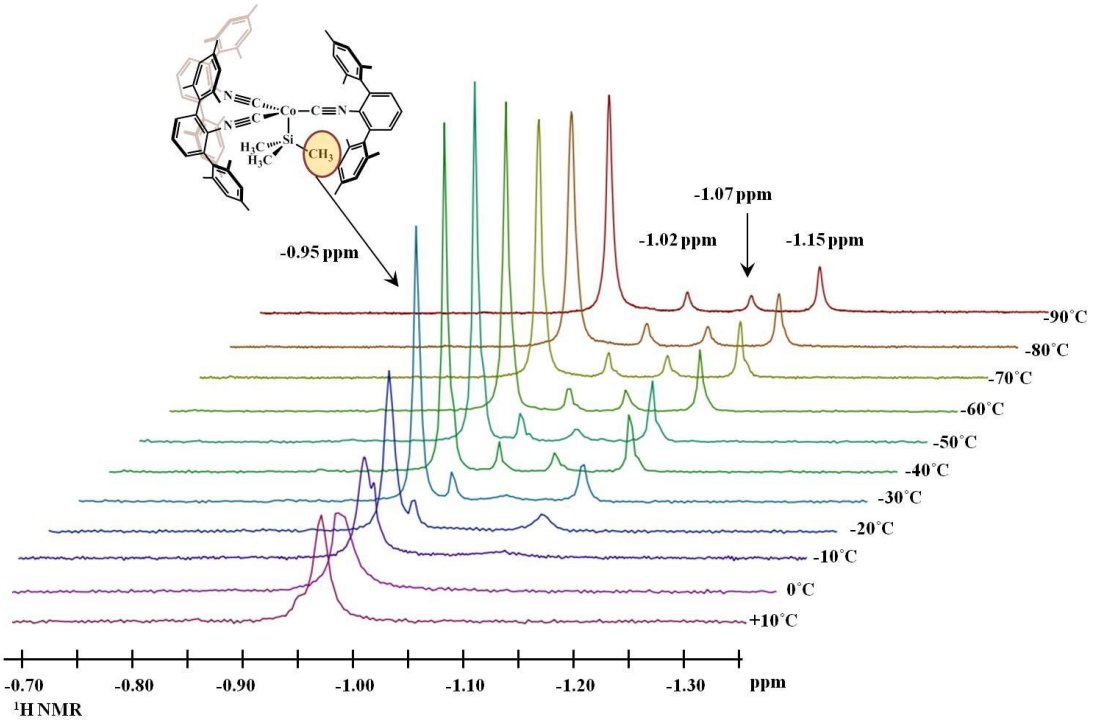

Figure 3. 15. VT ^{1}H NMR studies on complex (**3**) in a mixture of C_6H_{14}:C_6D_{14} at a ratio of 85:15 from 10˚C to –90˚C. Pictured is the region corresponding to the methyl proton resonances of the TMS group.

Support for rapid molecular movement of the bound *n*–hexane molecule in the temperature range studied by NMR methods was found from a solid–state X–ray crystal structure of complex (**9**·(*n*–C_6H_{14})·2(C_6H_6)) performed at 210K (–63˚C). Interestingly, increasing the temperature of single crystal (**9**·(*n*–C_6H_{14})·2(C_6H_6)) from 90K to 210K resulted in crystal structure (**21**) which contains positional disorder of the bound inner *n*–hexane molecule. In contrast, the crystal structure at 90K does not contain disorder (Figure 3.6). The crystal structure obtained at 210K has disorder about the C1 carbon which is in close proximity to the cobalt metal center. The positional disorder was directly related to the increase in temperature lending credence to the prospect that η^2-H,C alkyl binding may be NMR silent (due to rapid exchange) at temperatures ranging from –80˚C to +10˚.[72–75] Ongoing efforts in our laboratory are focused on characterizing complex (**9**) with NMR methods at low temperature (–150˚C).

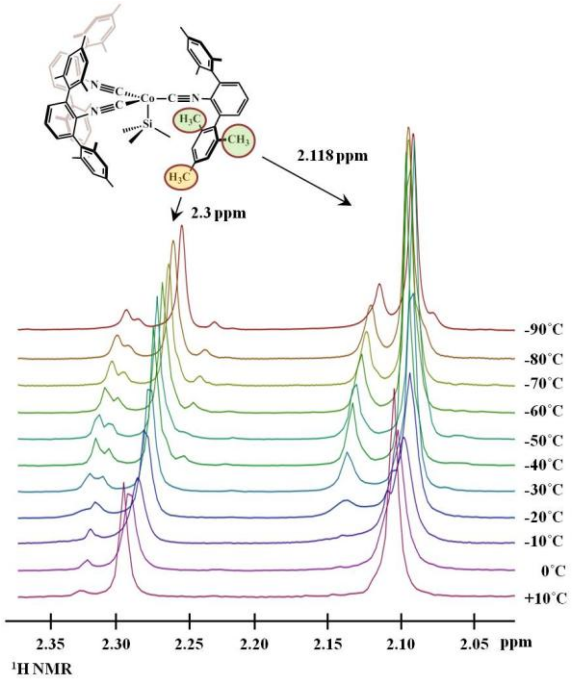

Figure 3. 16. VT ^{1}H NMR studies on complex (**3**) in a mixture of C_6H_{14}:C_6D_{14} at a ratio of 85:15 from 10˚C to –90˚C. Pictured is the region corresponding to the $CNAr^{Mes2}$ mesityl methyl proton resonances.

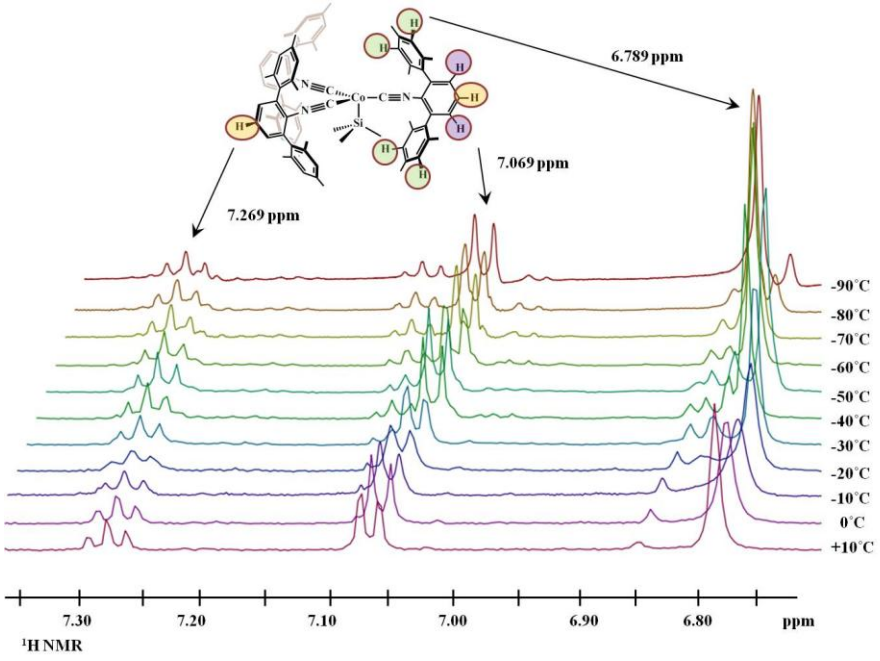

Figure 3. 17. VT ^{1}H NMR studies on complex (**3**) in a mixture of C_6H_{14}:C_6D_{14} at a ratio of 85:15 from 10˚C to –90˚C. Pictured is the region corresponding to the $CNAr^{Mes2}$ aryl proton resonances.

In addition to characterizing the η^2-H,C interaction, we speculate that the apically bound silicon nuclei can be utilized as an independent reporter for the degree of Lewis basicity

of the trans–bound ligand. The total NMR shielding tensor for a nuclei is calculated by summing contributions from paramagnetic (σ_{para}), diamagnetic (σ_{dia}), and spin orbit (σ_{SO}) components.[7677] The Lewis basic ligand that binds to complex (**3**) will electronically contribute to the dz^2 orbital, directly influencing the trans bound silicon nuclei. This contribution will directly influence the σ_{para} shift tensor of the *trans* located silicon nucleus. The 29 Si isotope possesses a spin ½ nucleus and has a relative sensitivity of 0.00784 (relative to ^1H = 1.00) making it detectable by NMR methods. The low sensitivity of ^{29}Si (less than 2% of sample by mass) combined with the time sensitivity of complex (**3**) to decomposition ($T_{1/2}$ ~ 3 h at RT for complex 3 in C_6D_{12}) required the use of Distortionless Enhancement Polarization Transfer (DEPT) and VT NMR. The use of DEPT was successful at enhancing the signal to noise in the ^{29}Si NMR and most adducts of complex (**3**) are stable below –35˚C for several weeks.[78] Laboratory efforts are focused on characterizing a series of complexes by ^{29}Si NMR that we speculate will possess a relationship between the $(CH_3)_3Si$ group chemical shift and the electron donating ability of the trans–bound substrate. The ^{29}Si NMR spectroscopic shifts are as follows: $(C_6H_{14})Co(SiMe_3)(CNAr^{Mes2})$ δ = 52.5 ppm, $(N_2)Co(SiMe_3)(CNAr^{Mes2})$ δ = 40.7 ppm, $(C_5H_5N)Co(SiMe_3)(CNAr^{Mes2})$ δ = 35.6 ppm, $(CO)Co(SiMe_3)(CNAr^{Mes2})$ δ = 35.5 ppm, $(NH_3)Co(SiMe_3)(CNAr^{Mes2})$ δ = 16.1 ppm

3.10 Isolation of a Pseudo–Unsaturated $XCoL_3$ Complex

We were unsuccessful to date in isolating other alkane complexes with attempts in *n*–pentane (C_5H_{12}), cyclopentane (C_5H_{10}) and octane (C_8H_{18}) both with and without added benzene (C_6H_6). Reluctantly, based on the high boiling point (151˚C), we used nonane as the crystallization solvent. Surprisingly, the use of nonane allowed for the X–ray structural characterization of complex (**12**) comprising the formula $(Ar)_{1/7}Co(SiMe_3)(CNAr^{Mes2})_3$ (the 1/7 stoichiometric ratio is based on occupancy of the Q-peak in found in the electron density difference map). X–ray diffraction methods at 90K were refined to 0.83 Å in the space group

$P2_1/n$. Noteworthy is the lack of co–crystallization solvent in crystal structure (**12**). A topological examination of complex (**12**) after adding hydrogens and anisotropically refining all fully occupied atoms, revealed a Q-peak (Q = 2.5 electrons) located at a distance of 2.279 Å away from the cobalt metal center (Figure 3.18) and electron density surrounding Q-peak shown in Figure 3.19). Although the Q-peak electron density might be represented by several atoms at partial or full occupancy we speculate that it is argon based on bond distance, oxidation state, geometry, and single crystal to single crystal (SC–SC) transformation experiments

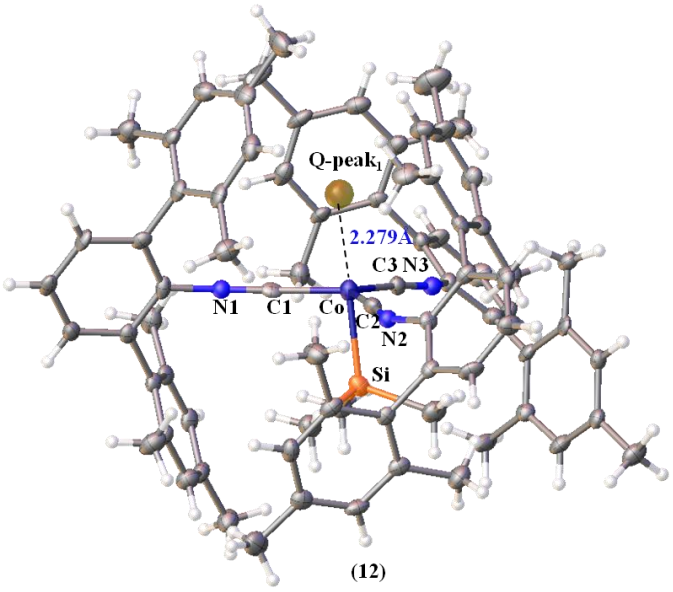

Figure 3. 18. Molecular structure of complex (**12**) with labelled Q-peak1. Thermal ellipsoids set to 50% probability.

We quickly ruled out positional disorder about the apical ($Si(CH_3)_3$) group based on angle discrepancy (Si–Co–Q_{peak} = 176.54 (not linear)) and occupancy criteria; where the Q-peak freely–refines to an occupancy of 18% when assigned as a silicon atom. This is too high an occupancy to be positional disorder about the TMS group because the Si1 atom freely–refines to 100% occupancy. If disordered, we would expect a free–refinement of ~82% occupancy for the Si1 atom. Additionally, there is no evidence for residual electron density

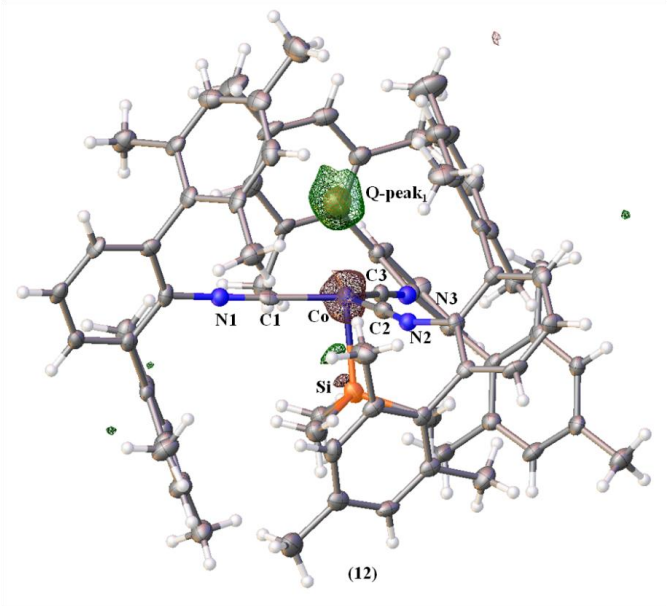

Figure 3. 19. Molecular structure of complex (**12**) displaying positive electron density around Q-peak$_1$. Image rendered from the electron density difference map feature in Olex2 version 1.12. Thermal ellipsoids set at 50% probability

around the Q-peak corresponding to the methyl groups of ($Si(CH_3)_3$). Based on the electron density of the Q-peak, there should be a corresponding methyl residual Q-peaks amounting to ~ 1 electron. The bond length of 2.279 Å does not correlate with an oxygen atom from a coordinated water molecule, as evidenced by complex (**6**) (Co–O = 2.144 Å.) A CSD (CSD = Cambridge Structural Database) search on Co–Cl bond distances resulted in 2093 hits showing a median bond length of 2.266 Å which correlates well with the Q-peak distance to cobalt. Contrastingly, when assigned as a chlorine atom, the Q-peak occupancy reports as ~20% and, although not impossible, would be an extremely rare example of an isolable d^7 cobalt (II) complex in the trigonal–bypyramidal geometry, where all other examples that lack tethered ligand platforms prefer square pyramidal geometry.[79,80] Although chlorine and argon atoms have similar covalent radii (Cl = 0.99 Å,[59,81] 1.02 Å[61] and Ar = 0.96 Å,[59] 0.97 Å,[81] 1.06 Å[61]), published data for the covalent radii of argon are likely extrapolated from neighboring non–metals. Thus, if the Q-peak is a chlorine atom with an occupancy of 20%, then 80% of the remaining cobalt metal centers within the crystal are unoccupied and should readily bind N_2

forming complex (**2**) and leaving the original residual Q-peak = 2.5 electrons at 2.279 Å. Alternatively, if the Q-peak is an argon atom in close proximity to the cobalt metal center, then as previously revealed in synthetic studies, should be easily displaced by the intercalation of N_2. This would result in 100% occupancy of N_2 with no stray residual Q-peaks at a distance of 2.279 Å from the cobalt metal center.

3.11 Single Crystal to Single Crystal Dinitrogen Intercalation Experiments

An initial X–ray data collection of single crystal (**12**) at 90K was utilized as the starting point (standard) for Q-peak size comparison. Single crystal (**12**), while still mounted on the goniometer pin under a Bruker Kryoflex N_2 stream, had the temperature raised to 300K and exposed for 2 hours under the N_2 stream at a flow rate of 3 L/min. After 2 hours, the Bruker Kryoflex was lowered to 90K for a second X–ray data collection producing crystal structure (**13**) (Figure 3.20). The initial residual Q-peak (referred to as Q-peak$_1$) in crystal structure (**13**) increased from ~3.1 to ~3.9 electrons and decreased in length from 2.277 to 2.138 Å with the appearance of a second Q-peak$_2$ = 1.6 electrons at a distance of 0.976 Å away from Q-peak$_1$. The increased electron density indicates molecular nitrogen uptake and consequent binding. There is a noticeable increase in thermal parameters suggesting increased molecular movement. Single crystal (**13**) was subjected to a second round of exposure of dinitrogen under the Bruker Kryoflex at 300K for 2 hours followed by a data collection at 90K resulting in structure (**14**) (Figure 3.21). Crystal structure (**14**) shows that dinitrogen is in fact intercalating into the crystal and binding to the cobalt metal center as evidenced by the increase in occupancy for dinitrogen Q-peak$_1$ = 4.84 electrons, ~ 84% N–atom occupancy, and Q-peak$_2$ = 3.42 electrons, ~ 54% N–atom occupancy. Complex (**14**) displays more reasonable bond lengths of Co–N = 2.039 Å and N–N 1.011 Å as well as increased cooperation from thermal parameters.

Crystal (**14**) was subjected to a third and final round of dinitrogen exposure at 300K for 10 hours followed by a data collection at 90K producing crystal structure (**15**) (Figure 3.22). The two Q-peaks in crystal structure (**15**) are refined at full occupancy to dinitrogen and correlate well with independently synthesized complex (**2**), Co–N = 1.940 Å, N–N = 1.073Å Noteworthy, is the lack of evidence corresponding to the initial Q-peak at 2.279 Å from the cobalt metal center. An overlay of all three rounds of exposure to dinitrogen for data collections (**12**), (**13**) and (**15**) portraying structural changes over time is shown in Figure 3.23.

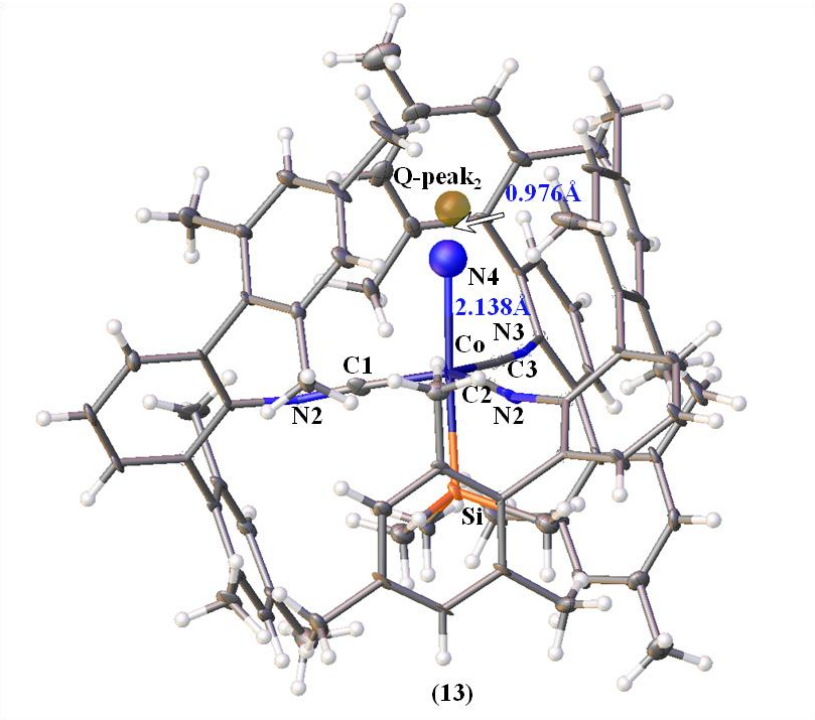

Figure 3. 20. Exposure of complex (**12**) to dinitrogen for 2 hours results in the molecular structure (**13**). Thermal ellipsoids are set to 50% probability.

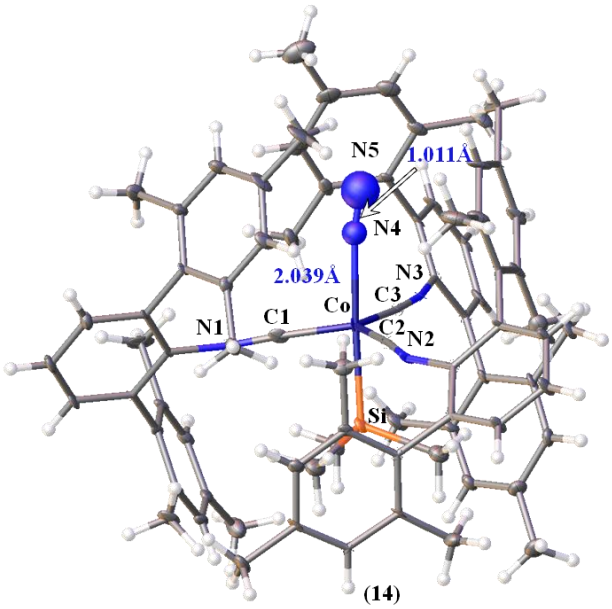

Figure 3. 21. Exposure of complex (**13**) to dinitrogen for 2 hours results in molecular structure (**14**). Thermal ellipsoids are set to 50% probability.

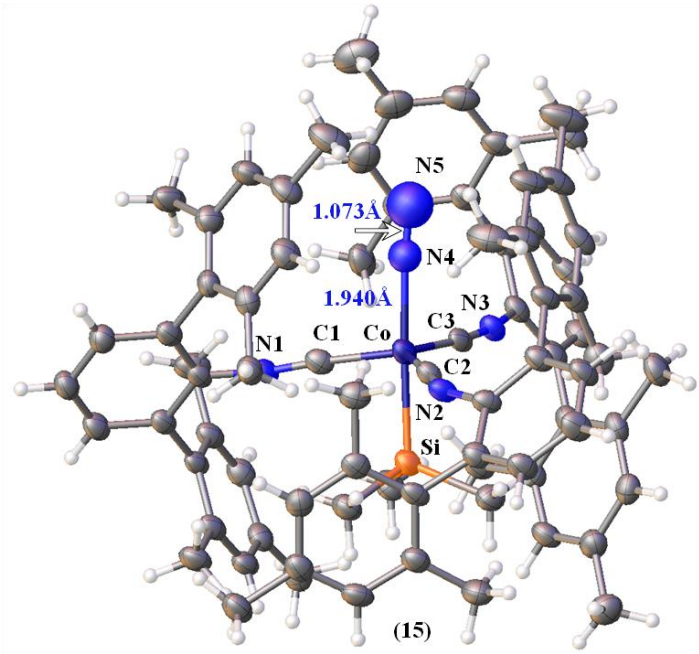

Figure 3. 22. Exposure of complex (**14**) to dinitrogen for 10 hours results in molecular structure (**15**). Thermal ellipsoids set at 50% probability.

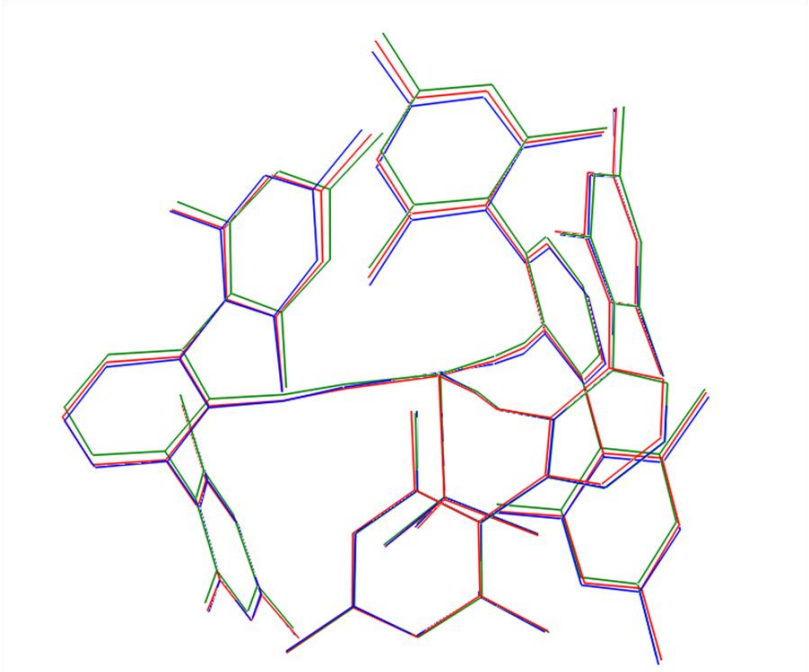

Figure 3. 23. Overlay of molecular structures (**13**), (**14**), and (**15**) showing structural changes over time.

We speculate the Q-peak in complex (**12**) is an argon atom that partially occupies the open coordination site ~14% of time. Although it would be considered in close proximity to cobalt, we wonder if complex (**12**) mimics clathrates with the ability to encapsulate argon by weak intramolecular vdW forces.[8284] In analogy to complex (**3**), there are several examples of unsaturated metal complexes that coordinate alkanes, in addition to noble gases, in solution (supported by TRIR, FTIR, and NMR studies).[85–89] A more accurate description from further investigations is necessary in determining the nature of the Q-peak interaction in complex (**12**) but based on the experiments reported herein, the Q-peak is readily displaced upon addition of dinitrogen.

3.12 The formation of a flexible $CNAr^{Mes2}$ pocket in $Co(TMS)(Ar^{Mes})_3$

Success at the stabilization of alkane σ–complexes (**9**·(*n*–C_6H_{14})·2(C_6H_6)), (**10**·(*n*–C_7H_{16})) and the ~20% entrapment of argon in complex (**12**) may be aided by the sub VdW

interactions unique to the $CNAr^{Mes2}$ ligand framework. There is compelling evidence that suggests the preferential formation of a $CNAr^{Mes2}$ pocket to the volume and shape of the substrate bound to the cobalt metal center. This phenomenon is similar to the flexible cavity formed in the supramolecular host assembly $[Ga_4L_6]^{12-}$ reported by Bergman and Raymond.[90] We compared topological parameters of several derivatives synthesized from complex (**3**) $Co(CNAr^{Mes2})_3$ with a series of ligands bound to the vacant coordination site. These complexes contain the formulation (**X**)Co($(CH_3)_3Si$)$(CNAr^{Mes2})_3$ where **X** represents the following: (**CO) =** complex (**5**), (**Ar)** = complex (**12**), (**H_2O**) = complex (**6**), (**N_2**) = complex (**2**) , (**DME**) = complex (**4**), (**C_6H_{14}**) = complex (**9**), (**C_7H_{16}**) = complex (**10**) and, for comparison purposes, previously synthesized from our group complex (**H**)Co(**CO**)$(CNAr^{Mes2})_3$. A rough correlation was found between the $CNAr^{Mes2}$ pocket volume and the summation of all three $CNAr^{Mes2}$ ligand torsion angles (Figure 3.24, Figure 3.25 and Figure 3.26).

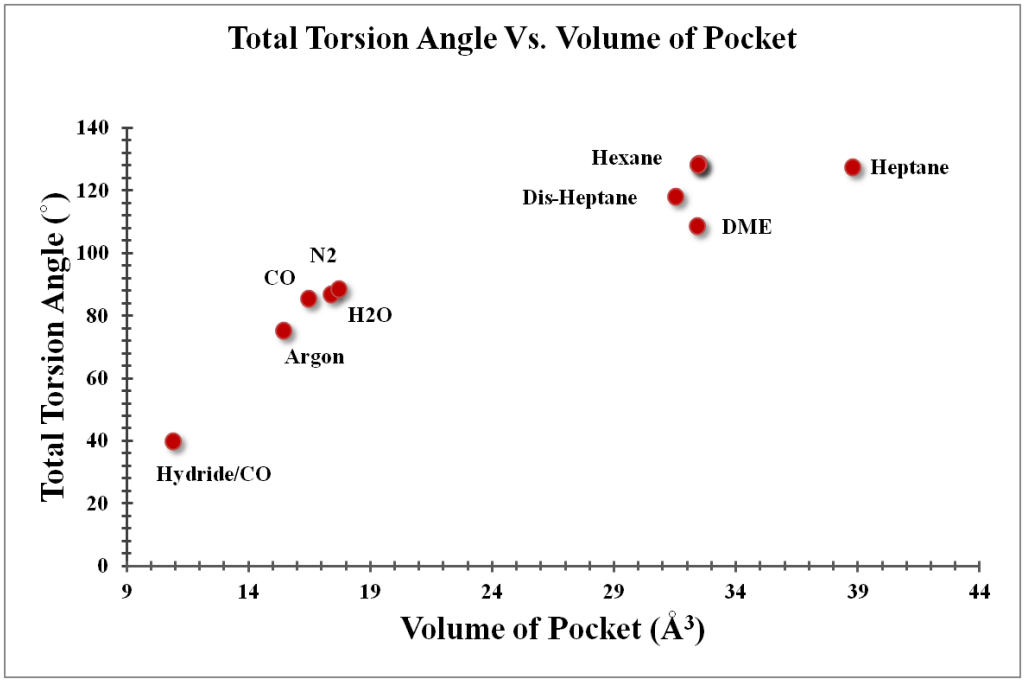

Figure 3. 24. Correlation for the different adducts of complex (**3**). The ordinate axis consists of the summation of torsion angles of the three $CNAr^{Mes2}$ ligands and the abscissa is the $CNAr^{Mes2}$ pocket volume.

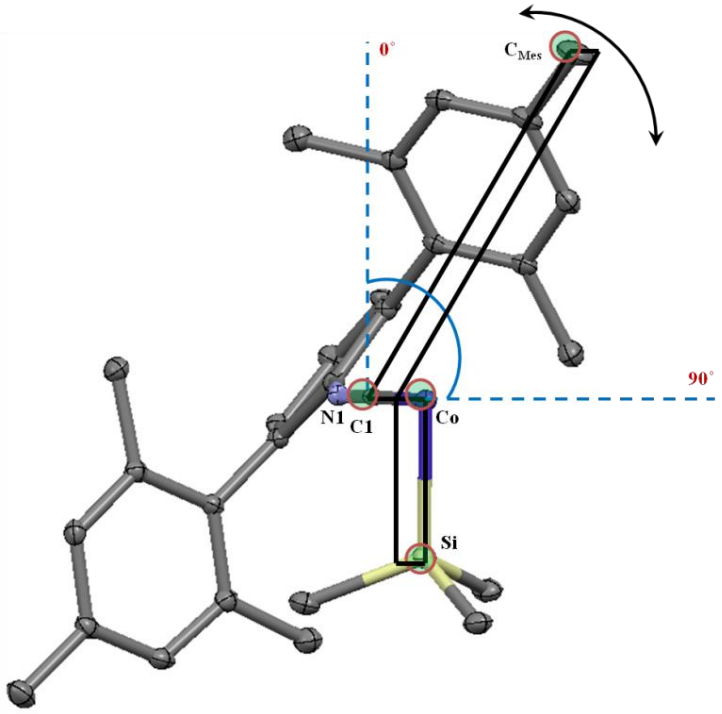

Figure 3. 25. View of how the torsion angle was measured for all three CNAr^{Mes2} ligands. Two CNAr^{Mes2} ligands and the hydrogens have been removed for clarity

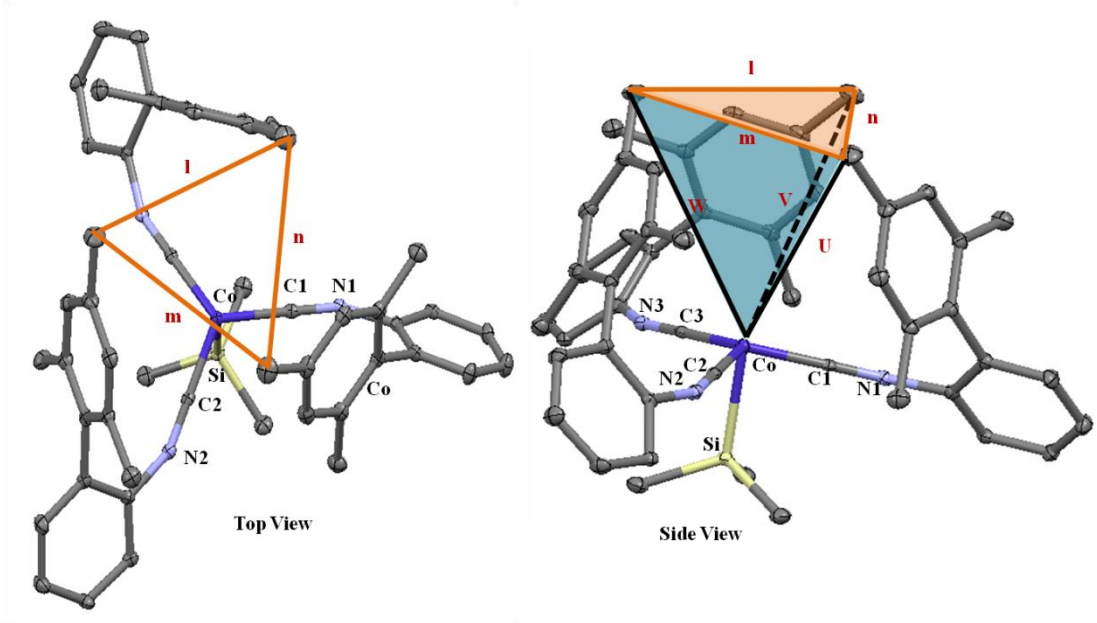

Figure 3. 26. Top and side view of the tetrahedron formed by the three CNAr^{Mes2} ligands.

The sterically encumbering *m*–terphenyl CNAr^{Mes2} ligand contains a near linear backbone that minimally sways from 180˚ (+/– 16˚), although it should be noted that these *m*–

terphenyl isocyanides are not completely rigid. Surprisingly, they have a range of flexibility, particularly a breathing type motion (movement about the Mes_{p-CH3}–C_{ipso}–Mes_{p-CH3} angle) and differentiation of length between the cobalt metal center and the *ipso*–carbon of the phenyl ring. As might be anticipated, the volume of the pocket formed by the three $CNAr^{Mes2}$ ligands increases with the size of the substrate bound to cobalt. The $CNAr^{Mes2}$ ligand has limited degrees of freedom to accommodate larger substrates and therefore, the framework attempts to achieve thermodynamic stability by either increasing the torsion angle (Si–Co–C_1–Mes_{CH3}, range from 0˚ – 60˚, Figure 3.25) or adjusting the APS angle (where APS = Apical Point of Sterics i.e. the overbearing angle Si–Co–Mes_{p-CH3}, range from 187˚ – 137˚, Figure 3.27).

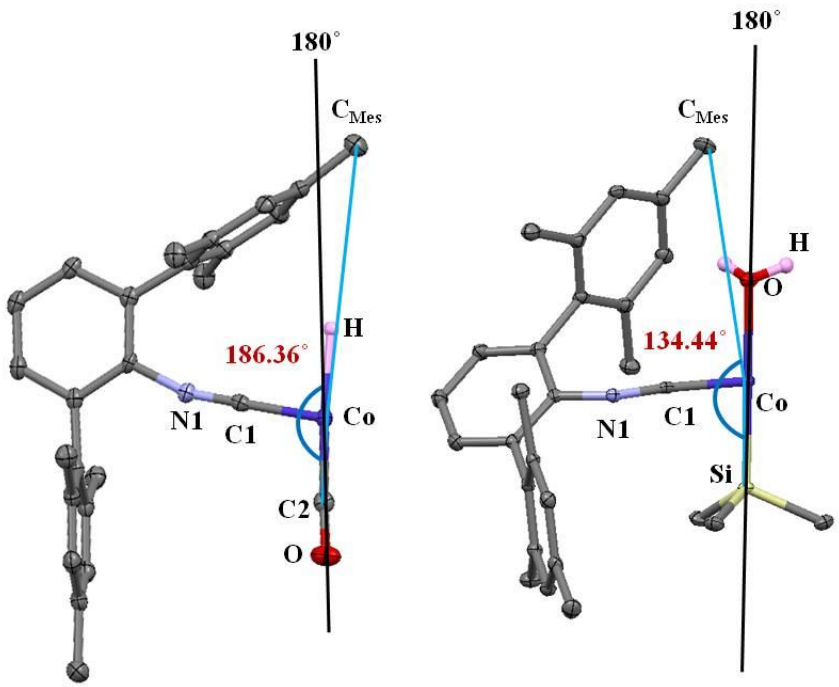

Figure 3. 27. Image portraying how APS (apical position of sterics) angle is measured.

Depending on the substituent bound to cobalt and the space group (due to crystallographically imposed symmetry) it appears that either all three ligands have the same torsion angle or one ligand dominates towards a 0˚ torsion angle while the other two ligands conform to a more relaxed state. The pocket volume formed by the $CNAr^{Mes2}$ mesityl *para*–

methyl groups was calculated by adapting the formula for a tetrahedron, which is essentially an irregular triangular pyramid. The sides are labeled l, m, n, U, V, W (Figure 3.26) and we used the following equations to calculate the volume.[91]

$$l' = m^2 + n^2 + U^2 \quad \textbf{(E3.5)}$$

$$m' = n^2 + l^2 + V^2 \quad \textbf{(E3.6)}$$

$$n' = m^2 + l^2 + W^2 \quad \textbf{(E3.7)}$$

$$Volume = \frac{1}{12} x \sqrt{(4l^2m^2n^2 - l^2l'^2 - m^2m'^2 - n^2n'^2 + l'm'n'} \quad \textbf{(E3.8)}$$

Further studies are needed to elucidate the relationship between the $CNAr^{Mes2}$ ligand framework and the pocket volume formed around different substrates that bind to the vacant coordination site. This flexible pocket likely provides an important network of host–guest interactions that may contribute to the stabilization of complexes (**9**·(*n*–C_6H_{14})·2(C_6H_6)), (**10**·(*n*–C_7H_{16})), and (**12**).

3.13 SC– SC Argon and Xenon Intercalation Experiments with Complex (12)

Inspired by the successful intercalation of dinitrogen to complex (**12**) (section 3.11), we attempted to mirror those experiments with argon gas. We utilized a pressure cell to aid in the single crystal to single crystal (SC–SC) transformation. The pressure cell we built was originally designed by Stanford Synchrotron Radiation Lightsource (SSRL) scientists in collaboration with M. H. B. Stowell (CalTech).[92] This apparatus allows for single crystal samples to be placed under moderate to high pressures of a gas (capable of attaching most any gases) which we modified to incorporate the capability of exposure to vacuum (apparatus shown in Figure 3.28 and setup explained in section 3.19).

Figure 3. 28. Image of the pressure cell used for the SC–SC transformation experiments with argon and xenon gas. Goniometer pin is placed underneath cap labeled (1), further details in Section 3.19.

We refer to single crystal (**16**) in the following study which is essentially the same as single crystal (**12**). The reason for assigning it as complex (**16**) is that it contained slightly higher initial argon occupancy of 4.0 electrons (~ 22% occupancy of argon) as compared to single crystal (**12**) which contained 2.5 electrons (~ 14% occupancy of argon). We speculate that the crystallization process is sensitive to the various pressures of argon inherently used in the synthesis of these complexes. Following an initial data collection (Figure 3.29), single crystal (**16**) was placed into pre–purged pressure cell and exposed to argon gas at 120 psi for 12 hours. An X–ray data collection at 90K resulted in structure (**17**) (Figure 3.30) showing an increased Q-peak size of Q = 5.04 electrons and freely refined occupancy of Ar ~ 38.82%. This is an increase from structure (**16**) which contains a Q-peak size of Q = 4.0 electrons and freely refined occupancy of Ar ~ 24.37%. Single crystal (**17**) was placed back into the pressure cell at 120 psi for an additional 12 hours under an argon atmosphere and a data set was collected at 90K resulting in complex (**18**) (Figure 3.31).

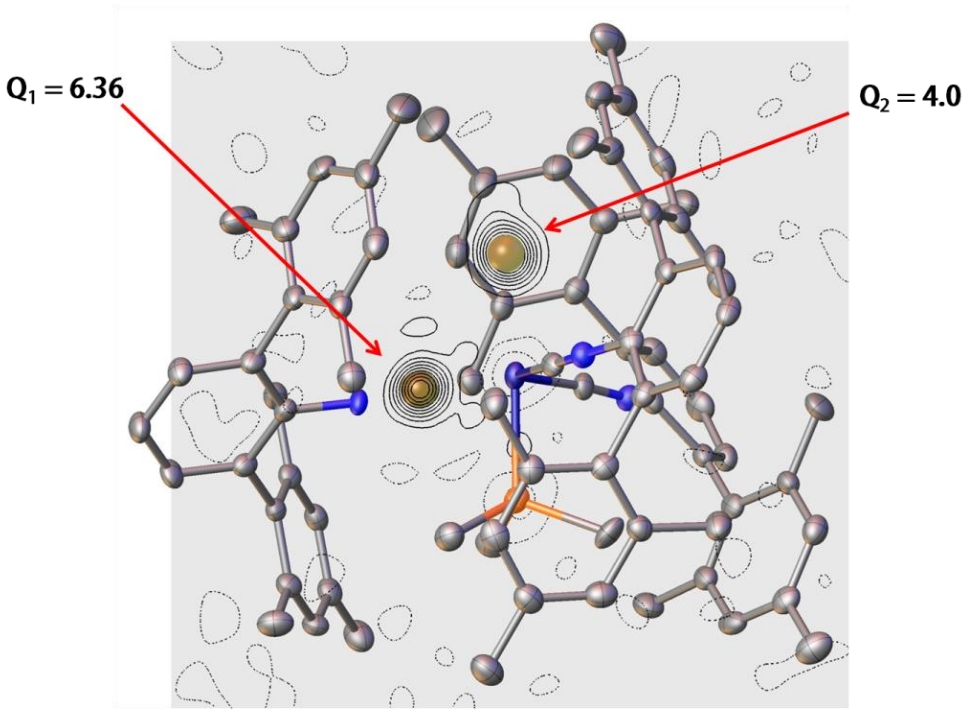

Figure 3. 29. Molecular structure of complex (**16**) showing Q-peaks belonging to the isocyanide carbon and the proposed argon atom. Electron density difference map shown in the plane of the Q-peak1 belonging to the isocyanide carbon and the argon atom Q-peak2.

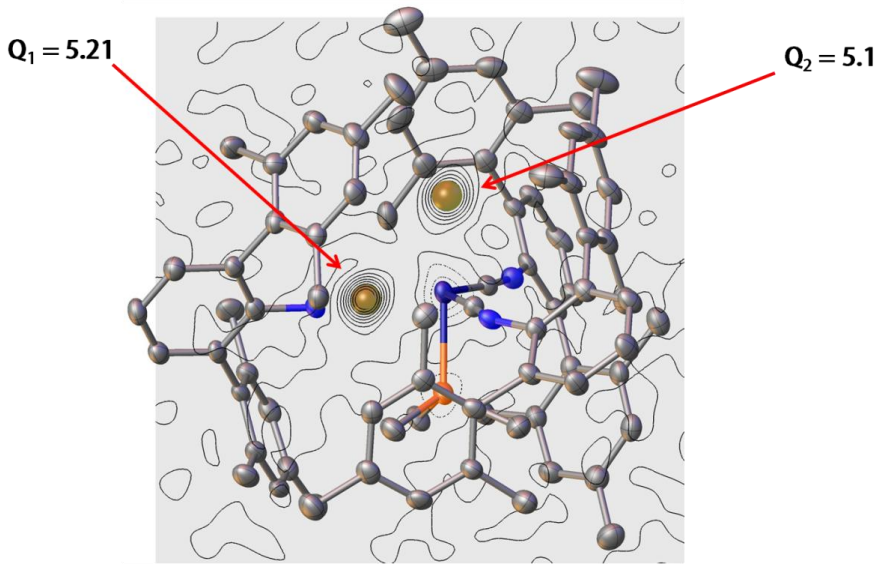

Figure 3. 30. Molecular structure of complex (**17**) after argon gas pressurization of complex (**16**) showing an increase in the size of Q-peak2. Electron density difference map shown in the plane of the Q-peak2 (belonging to the isocyanide carbon) and Q-peak1.

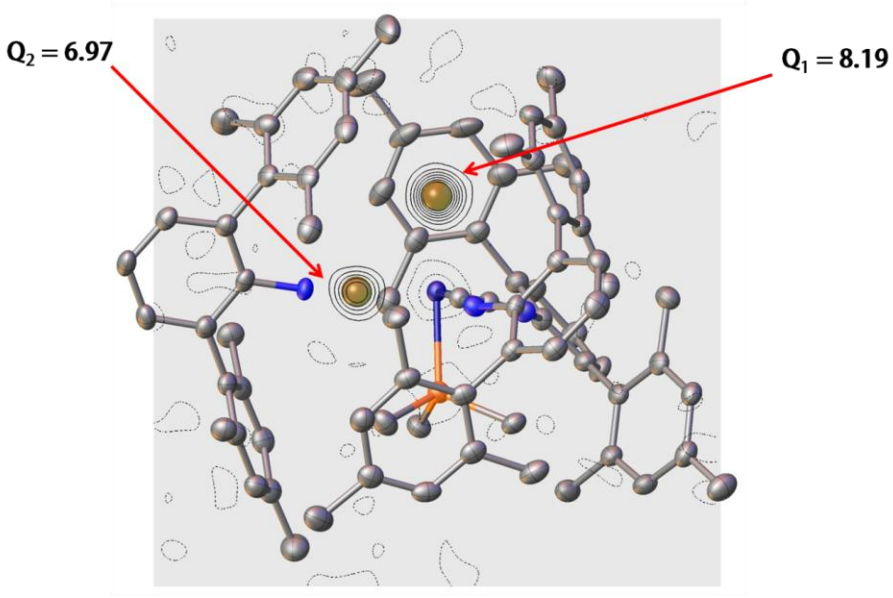

Figure 3. 31. Molecular structure of complex (**18**) after argon gas pressurization of complex (**17**) showing an increase in Q-peak size. Q-peak1 represents the largest electron density Q-peak. Electron density difference map shown in the plane of Q-peak2 (belonging to the isocyanide carbon) and Q-peak1.

Complex (**18**) shows an increase in Q-peak occupancy to Ar ~ 47.52% with Q = 8.06 electrons. Attempts with increased duration of exposure times or higher pressures resulted in a marked decrease of crystal quality and seemingly no variation in Q-peak occupancy from complex (**18**). When argon is added at 120 psi to crystal (**16**) there is an increase in electron density of the Q-peak located in close proximity to cobalt (2.279 Å) (Figure 3.29, Figure 3.30, Figure 3.31). The increase of electron density is standardized to the electron density of a known Q-peak belonging to the carbon atom C1 of the $CNAr^{Mes2}$ ligand. Comparison of the Q-peak to C1 essentially serves as an internal standard throughout the three experiments, as carbon will not increase in electron density. Ongoing efforts to intercalate argon gas are currently underway and future experiments will be geared to pressurization and Kyroflex soaking experiments. We have recently been successful at outfitting a low temperature Bruker Kryoflex device to extrude an argon gas stream. This holds value in future SC–SC transformation attempts, with the goal of mirroring the N_2 soaking experiments but with argon gas intercalation (see section 3.20)

3.14 Polymorph complex (20)

Attempts to reproduce single crystals of complexes (**12**) or (**16**) resulted in the discovery of a new polymorph complex (**20**), which was crystallographically characterized at 90K and refined to 0.83 Å resolution. Complex (**20**) has similar features to complex (**16**) in that a Q-peak = ~ 4 electrons is in close proximity to cobalt (see below for specific features). Complex (**20**) was exposed to dinitrogen gas under similar experimental conditions as complex (**12**) resulting in the intercalation and binding of N_2 to the cobalt metal center. All atoms in the dinitrogen adduct were refined to full occupancy with no reminiscent features belonging to the original Q-peak. Moreover, complex (**20**) crystallizes in space group P–$3C_1$ with 2 independent molecules in the asymmetric unit in addition to a peripherally located nonane solvent molecule that lacks close contacts to the cobalt metal center. These two independent cobalt metal centers lie on special positions and are related by a 3–fold rotation axis with 1/3 of each molecule existing in the asymmetric unit. This crystallographic symmetry makes the determination of the Q-peak in close proximity to the metal center slightly challenging (as it is shared over three positions). In addition to the complication brought about by the crystallographic symmetry, we speculate that there is pseudo–crystallographic symmetry, which relates the two independent Q-peaks.[93] This is shown by manipulating Q1 (in close proximity to Co1) wherein there is a corresponding shift in Q2 (located in close proximity to Co2).

As previously mentioned, we speculate that the $CNAr^{Mes2}$ architectural framework forms a protective pocket around the cobalt metal center which aids in the entrapment of the noble gas argon, strikingly similar to clathrate compounds. Selected metrical parameters from complexes (**12**) and (**20**) are compared in Table 3. 4. The data portrays a relationship between the Co–Ar bond distance and the APS angle (APS angle defined in Figure 3.27). Furthermore,

there appears to be a correlation between the Co–Ar bond distance and the $CNAr^{Mes2}$ pocket volume (Table 3. 4).

Table 3. 4. Metrical parameters relating APS angle, Co–Ar bond distance, and pocket volume for argon complexes (**12**) and (**20**).

	Complex (12)	**Complex (20)** ***A***	**Complex (20)** ***B***
Co–Ar	2.277 Å	2.401 Å	2.578 Å
APS = Co–Ar–C_{Mes1}	152.90˚	131.86˚	126.34˚
APS = Co–Ar–C_{Mes2}	134.84˚	131.86˚	126.34˚
APS = Co–Ar–C_{Mes3}	127.59˚	131.86˚	126.34˚
Avg. APS angle	138.44˚	131.86˚	126.34˚
Volume of pocket	15.4199 $Å^3$	15.9625 $Å^3$	19.8475 $Å^3$

Polymorph (**20**) is sensitive to higher pressures and when SC–SC intercalation experiments were performed over 40 psi the integrity of the single crystal was compromised. Contrastingly, complex (**12**) can be exposed to high pressure (350 psi) for 30 hours with noticeable decrease in crystal quality but still remains amenable to X–ray diffraction methods. The inability of complex (**20**) to maintain its macroscopic integrity is possibly due to solvent incorporation thereby allowing for a detrimental molecular movement upon exposure to a guest molecule. The guest–induced lattice rearrangement in polymorph complex (**20**) mirrors previous studies that reported severe fracturing of single crystals into polycrystalline material.[94,95]

Exposure of polymorph complex (**20**) to xenon gas in the pressure cell apparatus at 14 psi for 24 hours mirrored the results from argon pressure experiments with complex (**12**). The Q-peak increased to 8 electrons which correlates to a xenon occupancy of ~ 14%. This percentage correlates to prior argon pressure experiments with an argon occupancy of ~ 48%. Future investigations are needed to substantiate the intercalation of noble gases into complexes (**12**) and (**20**). It is unclear why the Q-peak occupancy increases to 8 electrons in both xenon and argon pressure experiments and why there is a decrease in bond distance from 2.217 Å to 2.118 Å. This result is in direct opposition of the expected bond lengthening as

exemplified by the structurally characterized tetra–xenono gold(II) cation complex ($AuXe^{2+}(Sb_2F_{11}^-)_2$). [96] The results from argon and xenon gas pressurization experiments for complexes (**12**) and (**20**) may be a result of adventitious water condensing onto the crystal upon exposure to the atmosphere in the few seconds of transfer from the low temperature Bruker Kryoflex (at 90K) to the pressure cell apparatus. Nonetheless, the isolation of polymorph (**20**) has allowed for the comparison of two mutually exclusive complexes. Both of these complexes initially consist of a small percentage of argon (less than 25%) that is readily displaced by the intercalation of N_2 gas.

3.15 Alkane Length vs. σ–complex Stability in the Solid–State

Treatment of complex (**3**) with *n*–hexane and *n*–heptane produces σ–complexes (**9**·(*n*–C_6H_{14})·2(C_6H_6)) and (**10**·(*n*–C_7H_{16})), respectively, but, interestingly, the crystallization of complex (**3**) with nonane produced non alkane–coordinated complex (**12**) and polymorph (**20**). One possibility for the discrepancy between alkane coordination (or lack thereof) could be related to internal motions of the alkane becoming more pronounced as the chain length and degrees of freedom increases.[97-99] Interestingly, when the internal alkane in σ–complexes (**9**·(*n*–C_6H_{14})·2(C_6H_6)) and (**10**·(*n*–C_7H_{16})) are topologically compared, it is noticed that they possess different conformers with (**9**·(*n*–C_6H_{14})·2(C_6H_6)) having the bound *n*–hexane molecule in an eclipsed geometry and complex (**10**·(*n*–C_7H_{16})) containing the bound *n*–heptane molecule in a staggered geometry. Also noteworthy, is the co–facial orientation of the two cobalt complexes in (**9**·(*n*–C_6H_{14})·2(C_6H_6)) containing a Si–Co1–Co2 angle of 172.38˚ and complex (**10**·(*n*–C_7H_{16})) containing a comparable Si–Co1–Co2 angle of 173.67˚ (Figure 3.32). Contrastingly, the disordered end of the internal *n*–heptane molecule in complex (**10**·(*n*–C_7H_{16})) contains a significantly contracted Si–Co2–Co1 angle of 161.52˚. These differences in the co–facial nature between (**9**·(*n*–C_6H_{14})·2(C_6H_6)) and (**10**·(*n*–C_7H_{16})) are likely a result of

increased alkane chain length (this point is highlighted by the canting of the two cobalt faces in the *n*-heptane structure shown on the right side in Figure 3.32).

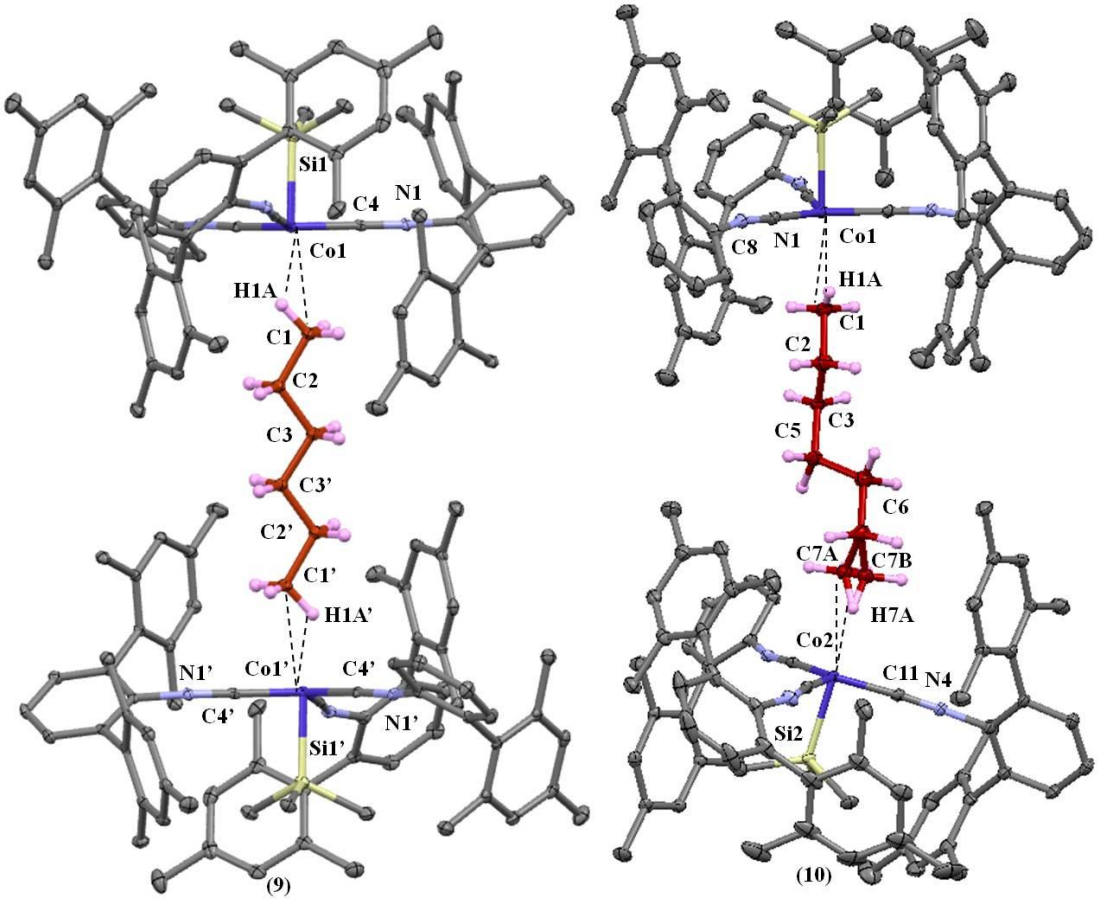

Figure 3. 32. Crystal structures (**9**·(*n*–C_6H_{14})·2(C_6H_6)) and (**10**·(*n*–C_7H_{16})) viewed side by side highlighting the non–cofacial character of complex (**10**·(*n*–C_7H_{16})). Several mesityl groups were removed for clarity. Thermal ellipsoids set at 30% probability.

The relationship between alkane length and degrees of freedom may contribute to the lack of a nonane σ–complex. This is evidenced by the increase in sub–vdW interactions (r_{vdW}(H) = 1.20 Å and r_{vdW}(C) = 1.70 Å)[52] at the disordered end of the bound *n*–heptane molecule in complex (**10**·(*n*–C_7H_{16})) and the lack of formation of an alkane σ–complex with the larger alkane nonane. Further studies are underway to isolate other alkane σ–complexes, which will enable a broader scope for comparison. Efforts in the laboratory are also geared towards determining if dimer formation occurs with *n*–octane (C_8H_{18}) or if the shorter alkanes

like *n*–pentane (C_5H_{12}) will form a monomer from repulsion effects between the $CNAr^{Mes2}$ ligands.

3.16 Conclusions

Herein we report the crystallographic characterization of alkane σ–complexes (**9**·(*n*–C_6H_{14})·2(C_6H_6)) and (**10**·(*n*–C_7H_{16})) which show a distinct η^2-H,C σ–type interaction with *n*–hexane and *n*–heptane, respectively. Attempts to distinguish spectroscopic features of (**9**·(*n*–C_6H_{14})·2(C_6H_6)) and (**10**·(*n*–C_7H_{16})) with low temperature (–80 ˚C) Nuclear Magnetic Resonance spectroscopy were unsuccessful to date. Therefore, the dichotomy continues between alkane σ–complexes that have been identified from X–ray diffraction methods and those examined spectroscopically. When a solvent mixture of nonane is employed with diamagnetic complex (**3**) $Co(SiMe_3)(CNAr^{Mes2})_3$ under an argon atmosphere, single crystals of complex (**12**) are produced containing the formula $Ar_{1/7}Co((SiCH_3)_3)(CNAr^{Mes2})_3$. Single crystals of complex (**12**) were manipulated in SC–SC dinitrogen intercalation experiments resulting in full occupancy and binding of dinitrogen to the cobalt metal center. Pressure cell experiments aimed at intercalating argon and xenon into complex (**12**) and (**20**) resulted in increased Q-peak sizes but decreased bond lengths which are unlikely from intercalation of the noble gases. Based on the dinitrogen exposure experiments, we believe that complexes (**9**·(*n*–C_6H_{14})·2(C_6H_6)), (**10**·(*n*–C_7H_{16})), (**12**), and (**20**) mimic clathrate networks but with the added advantage of containing a highly Lewis acidic cobalt metal center of proper electronic structure to engage in bonding. Further studies are aimed at isolating alkane σ–complexes of *cyclo*–C_5H_{10}, C_8H_{18}, and C_5H_{12} and assigning spectroscopic features for the η^2–C,H, σ–type interaction in complex (**9**·(*n*–C_6H_{14})·2(C_6H_6)).

3.17 Materials and Methods

General Considerations

All manipulations were carried out under an ultra–high purity argon atmosphere of in an MBraun single–station glove box (~1.2 atm). Solvents were dried and deoxygenated according to standard procedures.[100] Reagent grade starting materials were purchased from commercial sources and were used as received or purified by standard procedures.[101] The compounds $CNAr^{Mes2}$,[48] and (η2–PPN)Co($CNAr^{Mes2}$)$_3$ (**1**) were prepared according to literature procedures.[49] Cyclohexane[D_{12}] (Cambridge Isotope Laboratories) was either degassed and stored over 4 Å molecular sieves for 2 d or stirred in a solution of NaK/benzophenone, distilled, degassed, and stored over degassed sieves prior to use. Celite 405 (Fisher Scientific) was dried under vacuum (24 h) at a temperature above 250 ºC and stored in the glovebox prior to use. Solution ^{1}H NMR spectra were recorded on a JEOL ECA–500 spectrometer. ^{1}H NMR chemical shifts are reported in ppm relative to $SiMe_4$ (^{1}H and ^{13}C δ = 0.0 ppm) with reference to residual–protio resonances of 1.43 ppm for cyclohexane[D_{12}]. FTIR spectra were recorded on a Thermo–Nicolet iS10 FTIR spectrometer. Samples were prepared as KBr pellets using a manual hand press. The following abbreviations are used for the intensities and characteristics of important IR absorption bands: vs = very strong, s = strong, m=medium, w = weak, vw = very weak; b = broad, vb = very broad, sh = shoulder.

Synthesis of Co($SiMe_3$)($CNAr^{Mes2}$)$_3$ (3). To a room temperature benzene (C_6H_6) solution (296K) of (η^2–PPN)Co($CNAr^{Mes2}$)$_3$ (**1**, 0.036 g, 0.022 mmol, 2 mL; PPN = $(C_6H_5)_3P{=}N{=}P(C_6H_5)_3$) was added ($Me_3SiCl$ (1.05 g, 9.66 mmol, 440 equiv) quickly with no stirring. A pipette was used to mix the solution and then all volatile materials were removed under reduced pressure. The benzene was allowed to freeze under pressure and sublime to dryness over the course of 45 min. The resulting residue was then washed with thawing *n*–pentane (2 mL) and all volatile materials were then removed again under reduced pressure.

This procedure was repeated two times for a total of three *n*–pentane washes. The remaining brown residue was then extracted with thawing *n*–pentane and filtered through fiber–glass filter paper. The filtrate was then dried again under reduced pressure while being kept cold to provide $Co(SiMe_3)(CNAr^{Mes2})_3$ (**3**) as a brown–yellow solid. Yield: 0.020 g, 0.017 mmol, 77%. ^{1}H NMR (500.1 MHz, 20 °C, cyclohexane[D12]): δ = 7.13 (t, 3H, *J* = 7.0 Hz, *p*–Ar), 6.91 (d, 6H, *J* = 7.0 Hz, *m*–Ar), 6.62 (s, 12H, *m*–Mes), 2.17 (s, 18H, *p*–CH_3, Mes), 1.96 (s, 36H, *o*–CH_3, Mes), –1.11 (s, 9H, Si(CH_3)$_3$) ppm. FTIR (KBr pellet, 20 °C): ν(CN) = 2030 (s), 1943 (vs) cm–1, also 3043 (w), 2999 (w), 2922 (s), 2852 (m), 1613 (m), 1577 (m), 1487 (w), 1459 (m), 1450 (m), 1376 (m), 1231 (w), 1101 (w), 1032 (w), 849 (m), 831 (m), 801 (w) 754 (w) cm–1.The cold work–up of complex **3** is critical to its synthesis, as it is observed to decompose over the course of 2 h to the free ligand, CNArMes2, the tetrakisisocyanide complex Co(SiMe3)(CNArMes2)4 and other unidentified products.[102] The rapid decomposition of complex **3** prevented suitable ^{13}C{^{1}H} NMR and combustion analysis.

Crystallization of (μ^2–(η^2-H,*C*–($CH_3(CH_2)_4CH_3$))[$Co(SiMe_3)(CNAr^{Mes2})_3$]$_2$·(*n*–$C_6H_{14}$)·2($C_6H_6$) (1·(*n*–$C_6H_{14}$)·2($C_6H_6$)). To a freshly prepared sample of solid $Co(SiMe_3)(CN^{ArMes2})_3$ (**3**), was added *n*–hexane (1 mL) containing 50 μL of benzene (C_6H_6;5% v/v). The resulting solution was stored at –35 °C to produce Figure 3.5 dark red single crystals of **9**·(*n*–C_6H_{14})·(C_6H_6) over the course of 60 – 70 h. The crystallization of **9**·(*n*–C_6H_{14})·2(C_6H_6) is reproducible and the unit cells of several crystals (approx. 10) from different batches of $Co(SiMe_3)(CN^{ArMes2})_3$ (**3**) were screened to ensure formulation. Importantly, the successful crystallization of X–ray quality single crystals of **9**·(*n*–C_6H_{14})·2(C_6H_6) can be reproduced starting from different batches of (η^2–PPN)$Co(CNAr^{Mes2})_3$ (**1**) as well.

Crystallization of (μ^2–(η^2-H,*C*–($CH_3(CH_2)_5CH_3$))[$Co(SiMe_3)(CNAr^{Mes2})_3]_2$·(*n*–$C_7H_{16}$) (1·(*n*–$C_7H_{16}$)). To a freshly prepared sample of solid $Co(SiMe_3)(CN^{ArMes2})_3$ (**3**), was added *n*–heptane (1 mL) containing 50 μL of benzene (C_6H_6; 5% v/v). The resulting solution was stored at –35 °C to produce Figure 3.6 dark red single crystals of **10**·(*n*–C_7H_{16}) over the course of 100 h. The crystallization of **10**·(*n*–C_7H_{16}) is reproducible and the unit cells of several crystals (approx. 10) from different batches of $Co(SiMe_3)(CN^{ArMes2})_3$ (**3**) were screened to ensure formulation. Importantly, the successful crystallization of X–ray quality single crystals of **10**·(*n*–C_7H_{16}) can be reproduced starting from different batches of (η^2–PPN)$Co(CNAr^{Mes2})_3$ (**1**) as well.

Synthesis of (DME)$Co(SiMe_3)(CNAr^{Mes2})_3$ (4) To a freshly prepared sample of solid $Co(SiMe_3)(CN^{ArMes2})_3$ (**3**), (0.026 g) was added 1.3 ml of DME at room temperature. The resulting solution was stored at –35 °C to produce red single crystals. Yield: 0.018 g, 0.015 mmol, 64%. ^{1}H NMR (500.1 MHz, 20 °C, C_6D_{14}): δ = 7.17 (t, 3H, *J* = 7.5 Hz, *p*–Ar), 6.96 (d, 6H, *J* = 7.7 Hz, *m*–Ar), 6.70 (s, 12H, *m*–Mes), 3.42 (s, DME–CH_2), 3.28 (s, DME–CH_3) 2.24 (s, 18H, *p*–CH_3, Mes), 2.03 (s, 36H, *o*–CH_3, Mes), –1.07 (bs, 9H, Si(CH_3)$_3$). –1.57 (bs, 1H) ppm. FTIR (KBr pellet, 20 °C): ν(CN) = 2015 (s), 1943 (vs) cm–1, also 2946 (w), 2917 (w), 2729 (s), 1612 (m), 1577 (m), 1488 (w), 1450 (m), 1407 (m), 1375 (m), 1231 (w), 1119 (w), 1031 (w), 848 (m), 831 (m), 801 (w) 752 (w) cm–1.

Synthesis of (OC)$Co(Si(CH_3)_3)(CNAr^{Mes2})_3$ (5). To a C_6H_6 solution of $(N_2)Co(TMS)(CNAr^{Mes2})_3$ (80 mg, 0.0679 mmol, 5 mL) was added 1.0 equiv of CO gas via syringe (1.8 mL, 0.0679 mmol). The reaction mixture was allowed to stir for 25 m with intermittent shaking and changed in color from red to yellow. All volatiles were then removed under reduced pressure and the yellow residue was extracted with Et_2O. Filtration of this solution through Celite, followed by storage at -35 ˚C overnight, produced yellow crystals, which were collected and dried *in vacuo*. Yield: 70 mg, 0.0594 mmol, 87 % ^{1}H NMR (400.1

MHz, C_6D_6, 20 ^oC): δ = 6.94 (t, 3H, *J* = 7 Hz, *p*-Ph), 6.90 (s, 12H, *m*-Mes), 6.86 (d, 6H, *J* = 7 Hz), 2.30 (s, 18H *p*-Mes), 2.14 (s, 36H, *o*-Mes), -0.65 (s, 9H, Si(CH_3)$_3$) ppm. $^{13}C\{^1H\}$ NMR (125.7.6 MHz, C_6D_6, 20 ℃): δ = 209.5 (*C*O), 177.9 (*C*NR), 138.4, 137.1, 135.9, 135.8, 131.1, 129.6, 128.7, 128.6 126.1, 21.4 (*p*-Mes), 21.0 (*o*-Mes) 6.0 (Si(CH_3)$_3$) ppm. FTIR (C_6D_6, KBr windows, 25 ℃): (υ_{CN}) 2026 (s) and 1973 (s) cm^{-1}; (υ_{CO}) 2076 (s) cm^{-1}, also 3031 (m), 3000 (bs), 2967 (m), 2948 (m), 2920 (s), 2859 (s), 1613 (m), 1580 (m), 1480 (w), 1451 (m), 1413 (m), 1376 (m), 1330 (w), 1271 (w), 1233 (m), 1033 (w), 848 (m), 834 (m), 754 (m), 738 (w), 680 (m), 632 (w) 602 (w), 565 (w), 540 (w) cm^{-1}. Anal. Calcd. for $C_{79}H_{84}N_3CoSi$: C, 80.51; H, 7.18; N, 3.57. Found: C, 79.60; H, 7.21; N, 3.39.

Synthesis of $(H_2O)Co(SiMe_3)(CNAr^{Mes2})_3$ (6). To a freshly prepared sample of solid $Co(SiMe_3)(CN^{ArMes2})_3$ (**3**), (0.026 g) was added wet benzene at room temperature. The solvent was removed by exposure to vacuum and stored at –35 °C in a *n*–hexane solution producing red single crystals.

Synthesis of $(C_6H_{12})Co(SiMe_3)(CNAr^{Mes2})_3$ (7). To a freshly prepared sample of solid $Co(SiMe_3)(CN^{ArMes2})_3$ (**3**), (0.026 g) was added 1.3 ml of a 85:15 v/v *n*–hexane: 1–hexene solvent mixture. The resulting solution was stored at –35 °C to produce orange single crystals. Yield: 0.007 g, 0.0057mmol, 25%. ^1H NMR (500.1 MHz, 20 °C, C_6D_{14}): δ = 7.14 (t, 3H, *J* = 7.5 Hz, *p*–Ar), 6.85 (d, 6H, *J* = 8.0 Hz, *m*–Ar), 6.79 (s, 12H, *m*–Mes), 2.25 (s, 18H, *p*–CH_3, Mes), 2.02 (s, 36H, *o*–CH_3, Mes), –1.11 (s, 9H, Si(CH_3)$_3$) ppm.

Synthesis of $(H_2)Co(SiMe_3)(CNAr^{Mes2})_3$ (8). To a freshly prepared sample of solid $Co(SiMe_3)(CN^{ArMes2})_3$ (**3**), (0.026 g) was added 0.7 ml of C_6D_{14} at room temperature. Addition of H_2 gas at –78˚C resulted in the formation of complex (**8**). The resulting solution was stored at –78 °C for 60hrs producing yellow single crystals. Yield: 0.002 g, 0.001 mmol, Yield 8%. ^1H NMR (500.1 MHz, -80 °C, C_6D_{14}): δ = 7.31 (bs, 3H, *p*–Ar), 7.11 (bs, 6H, *m*–Ar), 6.87 (s, 12H, *m*–Mes), 2.41 (s, 18H, *p*–CH_3, Mes), 2.11 (s, 36H, *o*–CH_3, Mes), –0.90 (s, 9H, Si(CH_3)$_3$),

–6.16 (bs, 2, Co–H_2) ppm. The rapid decomposition of complex **8** prevented suitable $^{13}C\{^1H\}$ NMR and combustion analysis.

3.18 Crystallographic Structure Determinations

General. The single crystal X–ray structure determination of **9**·(*n*–C_6H_{14})·2(C_6H_6) and **10**·(*n*–C_7H_{16}) was carried out at 90K on a Bruker Platform Diffractometer equipped with a Bruker APEX II detector. The crystallographic data were integrated using the Bruker SAINT software program and scaled using the SADABS software program. Structure solution by direct methods (SHELXS) produced a complete phasing model consistent with the proposed structure. All non–hydrogen atoms were refined anisotropically by full–matrix least–squares (SHELXL–97).[103] All hydrogen atoms of the bridging *n*–hexane molecule and *n*–heptane were located in the electron–density difference map and their positions and thermal parameters were refined isotropically by full–matrix least–squares (SHELXL–97), except 2–Hydrgoen atoms connected to the terminal disordered C7 which, importantly, are not in close contact to the cobalt metal center. All other hydrogen atoms were placed using a riding model. Their positions were constrained relative to their parent atom using the appropriate HFIX command in SHELXL–97. Crystallographic data–collection and refinement information is listed in Table 3.5. The full crystal structure **9**·(*n*–C_6H_{14})·2(C_6H_6) is shown in Figure 3.6. A full listing of bond lengths (Å) and angles (°) for **9**·(*n*–C_6H_{14})·2(C_6H_6) is found in Table 3.7 The full crystal structure **10**·(*n*–C_7H_{16}) is shown in Figure 3.7. A full listing of bond lengths (Å) and angles (°) for **10**·(*n*–C_7H_{16}) is found in Table 3.9. All anisotropic displacement parameters for the non–hydrogen atoms in **9**·(*n*–C_6H_{14})·2(C_6H_6) are listed in Table 3.8 and for **10**·(*n*–C_7H_{16}) are listed in Table 3.10. A Crystallographic Information File (CIF) for **9**·(*n*–C_6H_{14})·2(C_6H_6) and **10**·(*n*–C_7H_{16}) has been deposited with the Cambridge Crystallographic Data Center under reference code 888006 (www.ccdc.cam.ac.uk).

3.19 Pressure Cell Experiments

The exemplary embodiment shown in Figure 3.28 consists of (1) a stainless steel cap that unscrews and allows for a single crystal mounted on a goniometer pin to be securely placed into a fitted docking station. Once goniometer pin is securely sealed with cap (1) a series of Swagelock valves allow for the exposure to a gas of choice (nitrogen, argon, xenon, etc.) at pressures ranging from 0–580 p.s.i. If Swagelock valve (2), (3) and (4) are opened to incoming gas (connected to valve (2)) and valve (5) is closed, the single crystal can be pressurized under the inert atmosphere. Alternatively, closing Swagelock valves (3), (4) and opening (5) exposes the single crystal to vacuum. All crystals that were placed into the cell were purged for several minutes before pressurization.

3.20 Argon Extrusion from a Bruker Kryoflex

A Bruker Kryoflex was modified to extrude argon gas at 95 K. In order to adapt argon, one large Dewar (60L) and one medium sized Dewar (30L) were utilized. The normal extrusion apparatus for the liquid N_2 was placed into the large Dewar that was filled with liquid argon. The automatic refill program on BIS (Bruker Instrument Service) uses a sensor to detect liquid N_2 levels. This sensor was placed into the bottom of the medium sized Dewar that was filled with liquid nitrogen. We speculate the sensor detects the thermal conductivity of the liquid and is standardized to liquid N_2. Liquefied argon has a lower thermal conductivity than N_2 (N_2 = 0.002583$Wm^{-1}K^{-1}$ and Ar = 0.001772$Wm^{-1}K^{-1}$) and therefore, likely is not detectable by the sensor. The density is also higher (N2 = 0.808 g/mL and Ar = 1.784) and caused several issues with the flow rate which were circumvented by using a stronger pump and placing it next to the argon Dewar (not locating it on the floor 4ft below).

3.21 General Computational Considerations

Density Functional Theory (DFT) calculations on the model complex (η^2-H,*C*–$(CH_3(CH_2)_4CH_3)$)Co($SiMe_3$)$(CNXyl)_3$ (**11**) were carried out using the Gaussian03 program

suite.[104] The input for model complex **11** was derived from the atomic coordinates of (μ^2–(η^2-H,*C*–($CH_3(CH_2)_4CH_3$))[$Co(SiMe_3)(CNAr^{Mes2})_3]_2$ (**9**) as determined by X–ray diffraction. Model complex **11** was subject to full geometry optimization using the 6–31G** basis set for the non–transition metal atoms and the Stuttart/Dresden pseudo relativistic effective core potential (SDD) basis set[105] for cobalt (Co). These basis sets were used in conjunction with the hybrid PBE0 functional for geometry optimization.[106] The PBE0 functional is known to provide reliable computational results for late transition–metal systems and for alkane σ–complexes specifically.[107, 108]

A single–point energy calculation was then performed on the optimized structure of **4** with the 6–311++G(3df,2pd) basis set for the non–transition metal atoms and the SDD basis set for the Co with the PBE0 functional. The results of this single–point energy calculation were used in all subsequent electron density topology calculations. Topological analysis of the electron density in **11** according to the Atoms in Molecules method[64,109] was carried out with the AIMAll program package.[110] Determination of electron density properties at important bond critical points (BCPs) within **11** were derived from the AIMAll output and are listed in below.

Table 3.5. Crystallographic Data Collection and Refinement Information for **9**·(*n*–C_6H_{14})·2(C_6H_6) and **10**·(*n*–C_7H_{16})·(C_7H_{16})

Compound	**9**·(*n*–C_6H_{14}) · 2(C_6H_6)	**10**·(*n*–C_7H_{16})·(C_7H_{16})
Formula	$C_{180}H_{208}Co_2N_6Si_2$	$C_{170}H_{197}Co_2N_6Si_2$
Crystal System	Triclinic	Monoclinic
Space Group	P -1	P 2_1/n
a, Å	14.1272(9)	27.9639(4)
b, Å	15.0585(10)	13.6108(2)
c, Å	19.1631(12)	38.8781(6)
α, deg	103.942(4)	90
β, deg	109.539(4)	97.0230(10)
γ, deg	95.784(4)	90
V, Å^3	3803.5(4)	14686.4(4)
Z	1	4
Radiation (λ, Å)	Mo–Kα, 0.71073	Cu–Kα, 1.54178
ρ (calcd.), g/cm^3	1.148	1.129
μ (Cu Kα), mm^{-1}	0.288	2.32
Temp, K	90(2)	100(2)
θ max, deg	26.46	70.20
data/parameters	15422 / 906	27342/ 1772
R_1	0.0543	0.0570
wR_2	0.1040	0.1451
GOF	1.013	1.038

Table 3.6. Optimized Cartesian Coordinates for (η^2-H,*C*–($CH_3(CH_2)_4CH_3$))Co($SiMe_3$)($CNXyl)_3$ (**11**) at the PBE0/6–31G**/SDD(ECP) Level.

Co	0.28439100	0.01569200	–0.28100300
Si	1.10435900	0.01318100	–2.37129100
N	1.54715800	2.69937600	–0.00333900
N	1.93145800	–2.41937300	0.21101800
N	–2.39845900	–0.25867300	–1.54623700
C	1.02207800	1.63181700	–0.11016200
C	1.28002100	–1.43809300	0.02567500
C	–1.32652400	–0.16897300	–1.02817600
H	–5.16278500	–0.30881100	8.04909600
C	–4.89723400	0.25772700	7.15107200
H	–4.61462000	1.26802700	7.46704400
H	–5.79948700	0.34690800	6.53581800
C	–3.76855200	–0.41234900	6.37751500
H	–2.88918400	–0.51912300	7.02683100
H	–4.06592100	–1.43330100	6.10256300
C	–3.37112800	0.34995100	5.11741400
H	–3.07728000	1.37364500	5.39063400
H	–4.24938700	0.45280600	4.46409200
H	–0.45766800	0.40597700	1.43387800
C	–0.70173800	–0.22344300	2.32121400
H	–0.97625500	–1.22845900	1.99379300
H	0.20744200	–0.29280100	2.92530800
C	–1.83974300	0.45029100	3.07832900
H	–2.71231000	0.54296300	2.41848900
H	–1.54859700	1.47429100	3.34827100
C	–2.23748000	–0.3107520	0 4.33975400
H	–2.53155000	–1.3342760	0 4.06635200
H	–1.35914700	–0.41329100	4.99303700
C	1.73769400	4.06129200	0.00453400
C	3.04220100	4.55743200	0.17957900
C	3.22035800	5.93908300	0.19131000
H	4.22166700	6.33975500	0.32431100

Table 3.6. **Continued** Optimized Cartesian Coordinates for (η^2-H,*C*–($CH_3(CH_2)_4CH_3$))Co($SiMe_3$)($CNXyl)_3$ (**11**) at the PBE0/6–31G**/SDD(ECP) Level

C	2.13961300	6.80147900	0.03794300
C	0.85732100	6.28994400	–0.13231900
H	0.01402800	6.96477200	–0.25268800
C	0.62822600	4.91535700	–0.15418400
C	2.94204100	–3.29390800	0.53154600
C	2.80306800	–4.64672800	0.17221500
C	3.83513700	–5.52087100	0.50669300
H	3.74592300	–6.56934200	0.23557200
C	4.96621400	–5.06853400	1.17835900
C	5.08176800	–3.72669800	1.52682900
H	5.96608100	–3.37548000	2.05175500
C	4.07735400	–2.81304600	1.21305200
C	–3.55147700	–0.78015200	–2.08387200
C	–4.44244600	0.08992900	–2.73803100
C	–5.60820700	–0.45108400	–3.27593500
H	–6.30735100	0.20601100	–3.78605800
C	–5.88327700	–1.81032700	–3.16586200
C	–4.98956500	–2.65283000	–2.51270600
H	–5.20599800	–3.71436100	–2.42741100
C	–3.80889900	–2.15974800	–1.96028900
C	3.00298900	0.05385400	–2.39966100
H	3.42615300	–0.84547700	–1.94062400
H	3.37101700	0.11065800	–3.43147400
H	3.38436000	0.92292500	–1.85453200
C	0.58689300	–1.54077700	–3.33331400
H	–0.49711800	–1.57562500	–3.48076300
H	1.06212500	–1.55703800	–4.32187000
H	0.88447900	–2.44934300	–2.79979400
C	0.51332500	1.50109300	–3.39140200
H	0.87675200	2.44519300	–2.97343900
H	0.87983700	1.42542200	–4.42254800
H	–0.58001800	1.54576200	–3.42337900
C	–0.74538300	4.34637600	–0.33814300

Table 3.6. **Continued** Optimized Cartesian Coordinates for (η^2-H,*C*–($CH_3(CH_2)_4CH_3$))Co($SiMe_3$)($CNXyl)_3$ (**11**) at the PBE0/6–31G**/SDD(ECP) Level

H	–0.78970300	3.68665400	–1.21166600
H	–1.04193900	3.73531000	0.52224000
H	–1.48300400	5.14221600	–0.46530600
C	4.19353700	3.61090200	0.34061200
H	4.02103900	2.91405200	1.16765800
H	4.33342800	3.00153500	–0.55927300
H	5.12221100	4.15382400	0.53211300
C	1.57694600	–5.11207300	–0.55418900
H	0.66715900	–4.86220500	0.00212200
H	1.48939900	–4.62699800	–1.53279700
H	1.60160500	–6.19318000	–0.71006600
C	4.18223800	–1.36478200	1.58108400
H	4.11615900	–0.72257200	0.69604400
H	3.36148900	–1.06248300	2.24158000
H	5.12705800	–1.15938800	2.08961200
C	–2.83551300	–3.05141600	–1.25167000
H	–1.84976600	–3.02477100	–1.72900000
H	–2.68327200	–2.72894100	–0.21520500
H	–3.18935200	–4.08497800	–1.24248600
C	–4.12556300	1.55113900	–2.84726200
H	–3.95279500	1.99381300	–1.86052400
H	–3.21193300	1.71590800	–3.42928800
H	–4.94120400	2.09282600	–3.33221500
H	2.29702600	7.87604600	0.05173900
H	5.76042100	–5.76449000	1.43248300
H	–6.79767600	–2.21459200	–3.59024500

Table 3.7. Bond lengths [Å] and angles [˚] for **9**·(*n*–C_6H_{14})·2(C_6H_6)

C(1)-N(1)	1.187(3)	C(16)-C(17)	1.494(3)
C(1)-Co(1)	1.816(2)	C(17)-C(18)	1.388(3)
C(2)-N(1)	1.395(3)	C(17)-C(23)	1.408(3)
C(2)-C(3)	1.402(3)	C(18)-C(20)	1.398(3)
C(2)-C(16)	1.406(3)	C(18)-C(19)	1.506(3)
C(3)-C(13)	1.391(3)	C(19)-H(19A)	0.9800
C(3)-C(4)	1.498(3)	C(19)-H(19B)	0.9800
C(4)-C(10)	1.396(3)	C(19)-H(19C)	0.9800
C(4)-C(5)	1.407(3)	C(20)-C(21)	1.384(3)
C(5)-C(6)	1.392(3)	C(20)-H(20)	0.9500
C(5)-C(12)	1.505(3)	C(21)-C(22)	1.384(3)
C(6)-C(7)	1.390(3)	C(21)-C(25)	1.507(3)
C(6)-H(6)	0.9500	C(22)-C(23)	1.386(3)
C(7)-C(9)	1.379(3)	C(22)-H(22)	0.9500
C(7)-C(8)	1.511(3)	C(23)-C(24)	1.511(3)
C(8)-H(8A)	0.9800	C(24)-H(24A)	0.9800
C(8)-H(8B)	0.9800	C(24)-H(24B)	0.9800
C(8)-H(8C)	0.9800	C(24)-H(24C)	0.9800
C(9)-C(10)	1.400(3)	C(25)-H(25A)	0.9800
C(9)-H(9)	0.9500	C(25)-H(25B)	0.9800
C(10)-C(11)	1.501(3)	C(25)-H(25C)	0.9800
C(11)-H(11A)	0.9800	C(26)-N(2)	1.188(3)
C(11)-H(11B)	0.9800	C(26)-Co(1)	1.799(2)
C(11)-H(11C)	0.9800	C(27)-C(28)	1.398(3)
C(12)-H(12A)	0.9800	C(27)-N(2)	1.402(3)
C(12)-H(12B)	0.9800	C(27)-C(32)	1.406(3)
C(12)-H(12C)	0.9800	C(28)-C(29)	1.399(3)
C(13)-C(14)	1.387(3)	C(28)-C(42)	1.497(3)
C(13)-H(13)	0.9500	C(29)-C(30)	1.379(3)
C(14)-C(15)	1.383(3)	C(29)-H(29)	0.9500
C(14)-H(14)	0.9500	C(30)-C(31)	1.384(4)
C(15)-C(16)	1.393(3)	C(30)-H(30)	0.9500
C(15)-H(15)	0.9500	C(31)-C(32)	1.390(3)

Table 3.7. Continued Bond lengths [Å] and angles [˚] for **9**·(*n*–C_6H_{14})·2(C_6H_6)

C(31)-H(31)	0.9500	C(46)-C(47)	1.517(4)
C(32)-C(33)	1.491(3)	C(47)-H(47A)	0.9800
C(33)-C(34)	1.392(3)	C(47)-H(47B)	0.9800
C(33)-C(39)	1.404(3)	C(47)-H(47C)	0.9800
C(34)-C(36)	1.393(3)	C(48)-C(49)	1.397(4)
C(34)-C(35)	1.510(3)	C(48)-H(48)	0.9500
C(35)-H(35A)	0.9800	C(49)-C(50)	1.498(4)
C(35)-H(35B)	0.9800	C(50)-H(50A)	0.9800
C(35)-H(35C)	0.9800	C(50)-H(50B)	0.9800
C(36)-C(37)	1.382(4)	C(50)-H(50C)	0.9800
C(36)-H(36)	0.9500	C(51)-Si(1)	1.878(2)
C(37)-C(38)	1.391(3)	C(51)-H(51A)	0.9800
C(37)-C(41)	1.511(3)	C(51)-H(51B)	0.9800
C(38)-C(39)	1.384(3)	C(51)-H(51C)	0.9800
C(38)-H(38)	0.9500	C(52)-Si(1)	1.881(2)
C(39)-C(40)	1.508(4)	C(52)-H(52A)	0.9800
C(40)-H(40A)	0.9800	C(52)-H(52B)	0.9800
C(40)-H(40B)	0.9800	C(52)-H(52C)	0.9800
C(40)-H(40C)	0.9800	C(53)-Si(1)	1.881(2)
C(41)-H(41A)	0.9800	C(53)-H(53A)	0.9800
C(41)-H(41B)	0.9800	C(53)-H(53B)	0.9800
C(41)-H(41C)	0.9800	C(53)-H(53C)	0.9800
C(42)-C(49)	1.400(3)	C(54)-N(3)	1.191(3)
C(42)-C(43)	1.400(3)	C(54)-Co(1)	1.817(2)
C(43)-C(45)	1.397(3)	C(55)-N(3)	1.398(3)
C(43)-C(44)	1.500(4)	C(55)-C(56)	1.402(3)
C(44)-H(44A)	0.9800	C(55)-C(60)	1.404(3)
C(44)-H(44B)	0.9800	C(56)-C(57)	1.390(3)
C(44)-H(44C)	0.9800	C(56)-C(70)	1.497(3)
C(45)-C(46)	1.382(4)	C(57)-C(58)	1.384(3)
C(45)-H(45)	0.9500	C(57)-H(57)	0.9500
C(46)-C(48)	1.383(4)	C(58)-C(59)	1.390(4)

Table 3.7. Continued Bond lengths [Å] and angles [˚] for **9**·(*n*–C_6H_{14})·2(C_6H_6)

C(58)-H(58)	0.9500	C(74)-C(75)	1.378(3)
C(59)-C(60)	1.384(3)	C(74)-C(78)	1.502(3)
C(59)-H(59)	0.9500	C(75)-C(76)	1.389(3)
C(60)-C(61)	1.493(3)	C(75)-H(75)	0.9500
C(61)-C(62)	1.391(3)	C(76)-C(77)	1.509(3)
C(61)-C(67)	1.404(3)	C(77)-H(77A)	0.9800
C(62)-C(63)	1.392(4)	C(77)-H(77B)	0.9800
C(62)-C(69)	1.512(3)	C(77)-H(77C)	0.9800
C(63)-C(64)	1.381(4)	C(78)-H(78A)	0.9800
C(63)-H(63)	0.9500	C(78)-H(78B)	0.9800
C(64)-C(66)	1.389(4)	C(78)-H(78C)	0.9800
C(64)-C(65)	1.504(4)	C(79)-C(80)	1.519(3)
C(65)-H(65A)	0.9800	C(79)-H(79A)	0.9800
C(65)-H(65B)	0.9800	C(79)-H(79B)	0.9800
C(65)-H(65C)	0.9800	C(79)-H(79C)	0.9800
C(66)-C(67)	1.383(3)	C(80)-C(81)	1.500(3)
C(66)-H(66)	0.9500	C(80)-H(80A)	0.9900
C(67)-C(68)	1.513(3)	C(80)-H(80B)	0.9900
C(68)-H(68A)	0.9800	C(81)-C(81)#1	1.518(4)
C(68)-H(68B)	0.9800	C(81)-H(81A)	0.9900
C(68)-H(68C)	0.9800	C(81)-H(81B)	0.9900
C(69)-H(69A)	0.9800	C(82)-C(83)	1.506(6)
C(69)-H(69B)	0.9800	C(82)-H(82A)	0.9800
C(69)-H(69C)	0.9800	C(82)-H(82B)	0.9800
C(70)-C(71)	1.394(3)	C(82)-H(82C)	0.9800
C(70)-C(76)	1.399(3)	C(83)-C(84)	1.472(6)
C(71)-C(73)	1.392(3)	C(83)-H(83A)	0.9900
C(71)-C(72)	1.511(3)	C(83)-H(83B)	0.9900
C(72)-H(72A)	0.9800	C(84)-C(84)#2	1.527(8)
C(72)-H(72B)	0.9800	C(84)-H(84A)	0.9900
C(72)-H(72C)	0.9800	C(84)-H(84B)	0.9900
C(73)-C(74)	1.389(3)	C(85)-C(86)	1.361(5)
C(73)-H(73)	0.9500	C(85)-C(90)	1.364(4)

Table 3.7. Continued Bond lengths [Å] and angles [˚] for **9**·(*n*–C_6H_{14})·2(C_6H_6)

C(85)-H(85)	0.9500	H(8A)-C(8)-H(8B)	109.5
C(86)-C(87)	1.395(4)	C(7)-C(8)-H(8C)	109.5
C(86)-H(86)	0.9500	H(8A)-C(8)-H(8C)	109.5
C(87)-C(88)	1.401(4)	H(8B)-C(8)-H(8C)	109.5
C(87)-H(87)	0.9500	C(7)-C(9)-C(10)	122.3(2)
C(88)-C(89)	1.359(5)	C(7)-C(9)-H(9)	118.9
C(88)-H(88)	0.9500	C(10)-C(9)-H(9)	118.9
C(89)-C(90)	1.355(4)	C(4)-C(10)-C(9)	118.4(2)
C(89)-H(89)	0.9500	C(4)-C(10)-C(11)	121.9(2)
C(90)-H(90)	0.9500	C(9)-C(10)-C(11)	119.6(2)
Si(1)-Co(1)	2.2573(7)	C(10)-C(11)-H(11A)	109.5
Angles		C(10)-C(11)-H(11B)	109.5
N(1)-C(1)-Co(1)	178.2(2)		
N(1)-C(2)-C(3)	120.01(19)		
N(1)-C(2)-C(16)	118.6(2)	H(11A)-C(11)-H(11B)	109.5
C(3)-C(2)-C(16)	121.4(2)	C(10)-C(11)-H(11C)	109.5
C(13)-C(3)-C(2)	117.9(2)	H(11A)-C(11)-H(11C)	109.5
C(13)-C(3)-C(4)	119.4(2)	H(11B)-C(11)-H(11C)	109.5
C(2)-C(3)-C(4)	122.58(19)	C(5)-C(12)-H(12A)	109.5
C(10)-C(4)-C(5)	120.5(2)	C(5)-C(12)-H(12B)	109.5
C(10)-C(4)-C(3)	121.0(2)	H(12A)-C(12)-H(12B)	109.5
C(5)-C(4)-C(3)	118.4(2)	C(5)-C(12)-H(12C)	109.5
C(6)-C(5)-C(4)	118.8(2)	H(12A)-C(12)-H(12C)	109.5
C(6)-C(5)-C(12)	119.8(2)	H(12B)-C(12)-H(12C)	109.5
C(4)-C(5)-C(12)	121.4(2)	C(14)-C(13)-C(3)	121.6(2)
C(7)-C(6)-C(5)	121.7(2)	C(14)-C(13)-H(13)	119.2
C(7)-C(6)-H(6)	119.2	C(3)-C(13)-H(13)	119.2
C(5)-C(6)-H(6)	119.2	C(15)-C(14)-C(13)	119.5(2)
C(9)-C(7)-C(6)	118.3(2)	C(15)-C(14)-H(14)	120.2
C(9)-C(7)-C(8)	120.9(2)	C(13)-C(14)-H(14)	120.2
C(6)-C(7)-C(8)	120.8(2)	C(14)-C(15)-C(16)	121.2(2)
C(7)-C(8)-H(8A)	109.5	C(14)-C(15)-H(15)	119.4
C(7)-C(8)-H(8B)	109.5	C(16)-C(15)-H(15)	119.4

Table 3.7. Continued Bond lengths [Å] and angles [˚] for **9**·(*n*–C_6H_{14})·2(C_6H_6).

C(15)-C(16)-C(2)	118.1(2)	C(21)-C(25)-H(25A)	109.5
C(15)-C(16)-C(17)	120.65(19)	C(21)-C(25)-H(25B)	109.5
C(2)-C(16)-C(17)	121.04(19)	H(25A)-C(25)-H(25B)	109.5
C(18)-C(17)-C(23)	120.0(2)	C(21)-C(25)-H(25C)	109.5
C(18)-C(17)-C(16)	122.4(2)	H(25A)-C(25)-H(25C)	109.5
C(23)-C(17)-C(16)	117.6(2)	H(25B)-C(25)-H(25C)	109.5
C(17)-C(18)-C(20)	119.1(2)	N(2)-C(26)-Co(1)	176.27(19)
C(17)-C(18)-C(19)	121.1(2)	C(28)-C(27)-N(2)	119.31(19)
C(20)-C(18)-C(19)	119.8(2)	C(28)-C(27)-C(32)	121.6(2)
C(18)-C(19)-H(19A)	109.5	N(2)-C(27)-C(32)	119.1(2)
C(18)-C(19)-H(19B)	109.5	C(27)-C(28)-C(29)	118.1(2)
H(19A)-C(19)-H(19B)	109.5	C(27)-C(28)-C(42)	122.3(2)
C(18)-C(19)-H(19C)	109.5	C(29)-C(28)-C(42)	119.4(2)
H(19A)-C(19)-H(19C)	109.5	C(30)-C(29)-C(28)	121.1(2)
H(19B)-C(19)-H(19C)	109.5	C(30)-C(29)-H(29)	119.5
C(21)-C(20)-C(18)	121.9(2)	C(28)-C(29)-H(29)	119.5
C(21)-C(20)-H(20)	119.1	C(29)-C(30)-C(31)	119.8(2)
C(18)-C(20)-H(20)	119.1	C(29)-C(30)-H(30)	120.1
C(22)-C(21)-C(20)	117.9(2)	C(31)-C(30)-H(30)	120.1
C(22)-C(21)-C(25)	120.9(2)	C(30)-C(31)-C(32)	121.5(2)
C(20)-C(21)-C(25)	121.2(2)	C(30)-C(31)-H(31)	119.3
C(21)-C(22)-C(23)	122.2(2)	C(32)-C(31)-H(31)	119.3
C(21)-C(22)-H(22)	118.9	C(31)-C(32)-C(27)	117.9(2)
C(23)-C(22)-H(22)	118.9	C(31)-C(32)-C(33)	119.8(2)
C(22)-C(23)-C(17)	118.8(2)	C(27)-C(32)-C(33)	122.3(2)
C(22)-C(23)-C(24)	120.2(2)	C(34)-C(33)-C(39)	120.3(2)
C(17)-C(23)-C(24)	120.9(2)	C(34)-C(33)-C(32)	120.3(2)
C(23)-C(24)-H(24A)	109.5	C(39)-C(33)-C(32)	119.3(2)
C(23)-C(24)-H(24B)	109.5	C(33)-C(34)-C(36)	119.1(2)
H(24A)-C(24)-H(24B)	109.5	C(33)-C(34)-C(35)	120.9(2)
C(23)-C(24)-H(24C)	109.5	C(36)-C(34)-C(35)	120.0(2)
H(24A)-C(24)-H(24C)	109.5	C(34)-C(35)-H(35A)	109.5
H(24B)-C(24)-H(24C)	109.5	C(34)-C(35)-H(35B)	109.5

Table 3.7. Continued Bond lengths [Å] and angles [˚] for **9**·(*n*–C_6H_{14})·2(C_6H_6).

H(35A)-C(35)-H(35B)	109.5	C(42)-C(43)-C(44)	121.6(2)
C(34)-C(35)-H(35C)	109.5	C(43)-C(44)-H(44A)	109.5
H(35A)-C(35)-H(35C)	109.5	C(43)-C(44)-H(44B)	109.5
H(35B)-C(35)-H(35C)	109.5	H(44A)-C(44)-H(44B)	109.5
C(37)-C(36)-C(34)	121.7(2)	C(43)-C(44)-H(44C)	109.5
C(37)-C(36)-H(36)	119.1	H(44A)-C(44)-H(44C)	109.5
C(34)-C(36)-H(36)	119.1	H(44B)-C(44)-H(44C)	109.5
C(36)-C(37)-C(38)	118.1(2)	C(46)-C(45)-C(43)	121.8(3)
C(36)-C(37)-C(41)	121.3(2)	C(46)-C(45)-H(45)	119.1
C(38)-C(37)-C(41)	120.6(2)	C(43)-C(45)-H(45)	119.1
C(39)-C(38)-C(37)	122.1(2)	C(45)-C(46)-C(48)	118.3(2)
C(39)-C(38)-H(38)	118.9	C(45)-C(46)-C(47)	120.7(3)
C(37)-C(38)-H(38)	118.9	C(48)-C(46)-C(47)	121.1(3)
C(38)-C(39)-C(33)	118.7(2)	C(46)-C(47)-H(47A)	109.5
C(38)-C(39)-C(40)	120.0(2)	C(46)-C(47)-H(47B)	109.5
C(33)-C(39)-C(40)	121.3(2)	H(47A)-C(47)-H(47B)	109.5
C(39)-C(40)-H(40A)	109.5	C(46)-C(47)-H(47C)	109.5
C(39)-C(40)-H(40B)	109.5	H(47A)-C(47)-H(47C)	109.5
H(40A)-C(40)-H(40B)	109.5	H(47B)-C(47)-H(47C)	109.5
C(39)-C(40)-H(40C)	109.5	C(46)-C(48)-C(49)	122.1(2)
H(40A)-C(40)-H(40C)	109.5	C(46)-C(48)-H(48)	118.9
H(40B)-C(40)-H(40C)	109.5	C(49)-C(48)-H(48)	118.9
C(37)-C(41)-H(41A)	109.5	C(48)-C(49)-C(42)	118.6(2)
C(37)-C(41)-H(41B)	109.5	C(48)-C(49)-C(50)	120.6(2)
H(41A)-C(41)-H(41B)	109.5	C(42)-C(49)-C(50)	120.8(2)
C(37)-C(41)-H(41C)	109.5	C(49)-C(50)-H(50A)	109.5
H(41A)-C(41)-H(41C)	109.5	C(49)-C(50)-H(50B)	109.5
H(41B)-C(41)-H(41C)	109.5	H(50A)-C(50)-H(50B)	109.5
C(49)-C(42)-C(43)	120.3(2)	C(49)-C(50)-H(50C)	109.5
C(49)-C(42)-C(28)	118.2(2)	H(50A)-C(50)-H(50C)	109.5
C(43)-C(42)-C(28)	121.4(2)	H(50B)-C(50)-H(50C)	109.5
C(45)-C(43)-C(42)	118.9(2)	Si(1)-C(51)-H(51A)	109.5
C(45)-C(43)-C(44)	119.5(2)	Si(1)-C(51)-H(51B)	109.5

Table 3.7. Continued Bond lengths [Å] and angles [˚] for **9**·(*n*–C_6H_{14})·2(C_6H_6).

H(51A)-C(51)-H(51B)	109.5	C(59)-C(60)-C(61)	119.9(2)
Si(1)-C(51)-H(51C)	109.5	C(55)-C(60)-C(61)	121.6(2)
H(51A)-C(51)-H(51C)	109.5	C(62)-C(61)-C(67)	120.2(2)
H(51B)-C(51)-H(51C)	109.5	C(62)-C(61)-C(60)	120.8(2)
Si(1)-C(52)-H(52A)	109.5	C(67)-C(61)-C(60)	119.0(2)
Si(1)-C(52)-H(52B)	109.5	C(61)-C(62)-C(63)	118.5(2)
H(52A)-C(52)-H(52B)	109.5	C(61)-C(62)-C(69)	120.9(2)
Si(1)-C(52)-H(52C)	109.5	C(63)-C(62)-C(69)	120.6(2)
H(52A)-C(52)-H(52C)	109.5	C(64)-C(63)-C(62)	122.5(2)
H(52B)-C(52)-H(52C)	109.5	C(64)-C(63)-H(63)	118.7
Si(1)-C(53)-H(53A)	109.5	C(62)-C(63)-H(63)	118.7
Si(1)-C(53)-H(53B)	109.5	C(63)-C(64)-C(66)	117.9(2)
H(53A)-C(53)-H(53B)	109.5	C(63)-C(64)-C(65)	121.0(2)
Si(1)-C(53)-H(53C)	109.5	C(66)-C(64)-C(65)	121.1(2)
H(53A)-C(53)-H(53C)	109.5	C(64)-C(65)-H(65A)	109.5
H(53B)-C(53)-H(53C)	109.5	C(64)-C(65)-H(65B)	109.5
N(3)-C(54)-Co(1)	175.40(19)	H(65A)-C(65)-H(65B)	109.5
N(3)-C(55)-C(56)	119.4(2)	C(64)-C(65)-H(65C)	109.5
N(3)-C(55)-C(60)	119.6(2)	H(65A)-C(65)-H(65C)	109.5
C(56)-C(55)-C(60)	121.0(2)	H(65B)-C(65)-H(65C)	109.5
C(57)-C(56)-C(55)	118.6(2)	C(67)-C(66)-C(64)	121.6(2)
C(57)-C(56)-C(70)	119.9(2)	C(67)-C(66)-H(66)	119.2
C(55)-C(56)-C(70)	121.4(2)	C(64)-C(66)-H(66)	119.2
C(58)-C(57)-C(56)	120.9(2)	C(66)-C(67)-C(61)	119.2(2)
C(58)-C(57)-H(57)	119.5	C(66)-C(67)-C(68)	120.2(2)
C(56)-C(57)-H(57)	119.5	C(61)-C(67)-C(68)	120.6(2)
C(57)-C(58)-C(59)	119.7(2)	C(67)-C(68)-H(68A)	109.5
C(57)-C(58)-H(58)	120.2	C(67)-C(68)-H(68B)	109.5
C(59)-C(58)-H(58)	120.2	H(68A)-C(68)-H(68B)	109.5
C(60)-C(59)-C(58)	121.2(2)	C(67)-C(68)-H(68C)	109.5
C(60)-C(59)-H(59)	119.4	H(68A)-C(68)-H(68C)	109.5
C(58)-C(59)-H(59)	119.4	H(68B)-C(68)-H(68C)	109.5
C(59)-C(60)-C(55)	118.5(2)	C(62)-C(69)-H(69A)	109.5

Table 3.7. Continued Bond lengths [Å] and angles [˚] for **9**·(*n*–C_6H_{14})·2(C_6H_6).

C(62)-C(69)-H(69B)	109.5	H(77A)-C(77)-H(77C)	109.5
H(69A)-C(69)-H(69B)	109.5	H(77B)-C(77)-H(77C)	109.5
C(62)-C(69)-H(69C)	109.5	C(74)-C(78)-H(78A)	109.5
H(69A)-C(69)-H(69C)	109.5	C(74)-C(78)-H(78B)	109.5
H(69B)-C(69)-H(69C)	109.5	H(78A)-C(78)-H(78B)	109.5
C(71)-C(70)-C(76)	120.4(2)	C(74)-C(78)-H(78C)	109.5
C(71)-C(70)-C(56)	118.7(2)	H(78A)-C(78)-H(78C)	109.5
C(76)-C(70)-C(56)	120.8(2)	H(78B)-C(78)-H(78C)	109.5
C(73)-C(71)-C(70)	118.9(2)	C(80)-C(79)-H(79A)	109.5
C(73)-C(71)-C(72)	120.6(2)	C(80)-C(79)-H(79B)	109.5
C(70)-C(71)-C(72)	120.6(2)	H(79A)-C(79)-H(79B)	109.5
C(71)-C(72)-H(72A)	109.5	C(80)-C(79)-H(79C)	109.5
C(71)-C(72)-H(72B)	109.5	H(79A)-C(79)-H(79C)	109.5
H(72A)-C(72)-H(72B)	109.5	H(79B)-C(79)-H(79C)	109.5
C(71)-C(72)-H(72C)	109.5	C(81)-C(80)-C(79)	114.0(2)
H(72A)-C(72)-H(72C)	109.5	C(81)-C(80)-H(80A)	108.7
H(72B)-C(72)-H(72C)	109.5	C(79)-C(80)-H(80A)	108.7
C(74)-C(73)-C(71)	121.7(2)	C(81)-C(80)-H(80B)	108.7
C(74)-C(73)-H(73)	119.2	C(79)-C(80)-H(80B)	108.7
C(71)-C(73)-H(73)	119.2	H(80A)-C(80)-H(80B)	107.6
C(75)-C(74)-C(73)	118.2(2)	C(80)-C(81)-C(81)#1	112.9(2)
C(75)-C(74)-C(78)	120.9(2)	C(80)-C(81)-H(81A)	109.0
C(73)-C(74)-C(78)	120.9(2)	C(81)#1-C(81)-H(81A)	109.0
C(74)-C(75)-C(76)	122.2(2)	C(80)-C(81)-H(81B)	109.0
C(74)-C(75)-H(75)	118.9	C(81)#1-C(81)-H(81B)	109.0
C(76)-C(75)-H(75)	118.9	H(81A)-C(81)-H(81B)	107.8
C(75)-C(76)-C(70)	118.7(2)	C(83)-C(82)-H(82A)	109.5
C(75)-C(76)-C(77)	119.4(2)	C(83)-C(82)-H(82B)	109.5
C(70)-C(76)-C(77)	121.9(2)	H(82A)-C(82)-H(82B)	109.5
C(76)-C(77)-H(77A)	109.5	C(83)-C(82)-H(82C)	109.5
C(76)-C(77)-H(77B)	109.5	H(82A)-C(82)-H(82C)	109.5
H(77A)-C(77)-H(77B)	109.5	H(82B)-C(82)-H(82C)	109.5
C(76)-C(77)-H(77C)	109.5	C(84)-C(83)-C(82)	114.4(4)

Table 3.7. Continued Bond lengths [Å] and angles [˚] for **9**·(*n*–C_6H_{14})·2(C_6H_6).

C(84)-C(83)-H(83A)	108.7	C(87)-C(88)-H(88)	120.2
C(82)-C(83)-H(83A)	108.7	C(90)-C(89)-C(88)	121.1(3)
C(84)-C(83)-H(83B)	108.7	C(90)-C(89)-H(89)	119.4
C(82)-C(83)-H(83B)	108.7	C(88)-C(89)-H(89)	119.4
H(83A)-C(83)-H(83B)	107.6	C(89)-C(90)-C(85)	120.3(3)
C(83)-C(84)-C(84)#2	116.6(4)	C(89)-C(90)-H(90)	119.9
C(83)-C(84)-H(84A)	108.1	C(85)-C(90)-H(90)	119.9
C(84)#2-C(84)-H(84A)	108.1	C(1)-N(1)-C(2)	156.2(2)
C(83)-C(84)-H(84B)	108.1	C(26)-N(2)-C(27)	152.3(2)
C(84)#2-C(84)-H(84B)	108.1	C(54)-N(3)-C(55)	154.9(2)
H(84A)-C(84)-H(84B)	107.3	C(51)-Si(1)-C(52)	106.93(12)
C(86)-C(85)-C(90)	120.6(3)	C(51)-Si(1)-C(53)	105.56(12)
C(86)-C(85)-H(85)	119.7	C(52)-Si(1)-C(53)	107.10(11)
C(90)-C(85)-H(85)	119.7	C(51)-Si(1)-Co(1)	113.06(8)
C(85)-C(86)-C(87)	119.9(3)	C(52)-Si(1)-Co(1)	111.19(8)
C(85)-C(86)-H(86)	120.1	C(53)-Si(1)-Co(1)	112.57(9)
C(87)-C(86)-H(86)	120.1	C(26)-Co(1)-C(1)	118.79(10)
C(86)-C(87)-C(88)	118.6(3)	C(26)-Co(1)-C(54)	119.07(9)
C(86)-C(87)-H(87)	120.7	C(1)-Co(1)-C(54)	121.34(9)
C(88)-C(87)-H(87)	120.7	C(26)-Co(1)-Si(1)	85.16(7)
C(89)-C(88)-C(87)	119.5(3)	C(1)-Co(1)-Si(1)	87.31(7)
C(89)-C(88)-H(88)	120.2	C(54)-Co(1)-Si(1)	88.56(7)

Table 3.8 Anisotropic displacement parameters ($Å^2 x\ 10^3$) for **9**·(*n*–C_6H_{14})·2(C_6H_6). The anisotropic displacement factor exponent takes the form: $-2\pi^2[\ h^2\ a^{*2}U^{11} + ...\ + 2\ h\ k\ a^*\ b^*\ U^{12}\ ]$

	U^{11}	U^{22}	U^{33}	U^{23}	U^{13}	U^{12}
C(1)	14(1)	19(1)	18(1)	2(1)	6(1)	0(1)
C(2)	18(1)	19(1)	17(1)	7(1)	10(1)	7(1)
C(3)	17(1)	22(1)	17(1)	6(1)	9(1)	6(1)
C(4)	20(1)	17(1)	19(1)	7(1)	8(1)	2(1)
C(5)	24(1)	18(1)	20(1)	7(1)	10(1)	3(1)

Table 3.8. Continued Anisotropic displacement parameters ($Å^2 x\ 10^3$) for **9**·(*n*–C_6H_{14})·2(C_6H_6). The anisotropic displacement factor exponent takes the form: $-2\pi^2[\ h^2\ a^{*2}U^{11} + ...\ + 2\ h\ k\ a^*\ b^*\ U^{12}\ ]$

C(6)	29(1)	23(1)	19(1)	3(1)	10(1)	6(1)
C(7)	28(1)	29(2)	18(1)	3(1)	2(1)	2(1)
C(8)	40(2)	61(2)	21(1)	-1(1)	0(1)	16(2)
C(9)	21(1)	32(2)	25(1)	8(1)	5(1)	8(1)
C(10)	21(1)	20(1)	19(1)	5(1)	7(1)	3(1)
C(11)	23(1)	32(2)	22(1)	7(1)	9(1)	9(1)
C(12)	26(1)	29(1)	24(1)	7(1)	14(1)	8(1)
C(13)	24(1)	20(1)	22(1)	7(1)	10(1)	1(1)
C(14)	30(1)	26(1)	22(1)	14(1)	11(1)	4(1)
C(15)	24(1)	30(1)	18(1)	12(1)	7(1)	7(1)
C(16)	18(1)	23(1)	16(1)	6(1)	8(1)	6(1)
C(17)	18(1)	24(1)	14(1)	8(1)	5(1)	6(1)
C(18)	20(1)	24(1)	16(1)	6(1)	5(1)	6(1)
C(19)	28(1)	31(2)	28(1)	5(1)	13(1)	8(1)
C(20)	27(1)	22(1)	18(1)	2(1)	5(1)	5(1)
C(21)	21(1)	25(1)	21(1)	7(1)	3(1)	1(1)
C(22)	18(1)	32(2)	23(1)	11(1)	8(1)	8(1)
C(23)	19(1)	23(1)	18(1)	9(1)	5(1)	5(1)
C(24)	31(1)	27(1)	28(1)	8(1)	16(1)	6(1)
C(25)	29(1)	33(2)	33(1)	2(1)	8(1)	-5(1)
C(26)	24(1)	15(1)	14(1)	6(1)	9(1)	4(1)
C(27)	14(1)	15(1)	24(1)	3(1)	5(1)	2(1)
C(28)	16(1)	20(1)	25(1)	3(1)	8(1)	3(1)
C(29)	19(1)	35(2)	34(1)	8(1)	12(1)	9(1)
C(30)	20(1)	44(2)	33(1)	11(1)	8(1)	13(1)
C(31)	24(1)	35(2)	26(1)	9(1)	7(1)	8(1)
C(32)	16(1)	21(1)	22(1)	4(1)	5(1)	1(1)
C(33)	18(1)	23(1)	18(1)	8(1)	4(1)	6(1)
C(34)	22(1)	21(1)	21(1)	8(1)	5(1)	5(1)
C(35)	28(1)	24(1)	30(1)	8(1)	8(1)	1(1)
C(36)	22(1)	26(1)	28(1)	12(1)	8(1)	1(1)
C(37)	25(1)	34(2)	22(1)	14(1)	9(1)	9(1)
C(38)	29(1)	27(1)	20(1)	2(1)	6(1)	4(1)

Table 3.8. Continued Anisotropic displacement parameters ($Å^2 x\ 10^3$) for **9**·(*n*–C_6H_{14})·2(C_6H_6). The anisotropic displacement factor exponent takes the form: $-2\pi^2[\ h^2\ a^{*2}U^{11} + ...\ + 2\ h\ k\ a^*\ b^*\ U^{12}\ ]$

C(39)	19(1)	26(1)	25(1)	4(1)	6(1)	1(1)
C(40)	35(2)	30(2)	45(2)	-5(1)	17(1)	-6(1)
C(41)	38(2)	42(2)	31(1)	15(1)	17(1)	8(1)
C(42)	14(1)	27(1)	30(1)	10(1)	13(1)	7(1)
C(43)	19(1)	31(2)	30(1)	8(1)	14(1)	7(1)
C(44)	36(2)	31(2)	34(2)	3(1)	18(1)	3(1)
C(45)	24(1)	47(2)	31(1)	14(1)	15(1)	12(1)
C(46)	23(1)	53(2)	44(2)	27(2)	21(1)	19(1)
C(47)	37(2)	75(2)	58(2)	45(2)	24(2)	26(2)
C(48)	26(1)	31(2)	59(2)	24(1)	26(1)	14(1)
C(49)	20(1)	27(1)	40(2)	10(1)	17(1)	8(1)
C(50)	34(2)	25(2)	55(2)	8(1)	19(1)	5(1)
C(51)	30(1)	28(2)	24(1)	2(1)	11(1)	10(1)
C(52)	30(1)	28(2)	21(1)	3(1)	6(1)	1(1)
C(53)	30(1)	38(2)	20(1)	7(1)	12(1)	6(1)
C(54)	15(1)	18(1)	14(1)	4(1)	6(1)	8(1)
C(55)	19(1)	17(1)	15(1)	4(1)	8(1)	0(1)
C(56)	21(1)	19(1)	20(1)	6(1)	8(1)	3(1)
C(57)	20(1)	25(1)	32(1)	9(1)	11(1)	3(1)
C(58)	26(1)	24(1)	38(2)	11(1)	15(1)	-2(1)
C(59)	28(1)	19(1)	35(1)	9(1)	12(1)	3(1)
C(60)	25(1)	20(1)	20(1)	7(1)	12(1)	5(1)
C(61)	27(1)	12(1)	28(1)	7(1)	14(1)	3(1)
C(62)	34(1)	17(1)	29(1)	8(1)	16(1)	6(1)
C(63)	41(2)	20(1)	34(1)	6(1)	24(1)	9(1)
C(64)	30(1)	17(1)	48(2)	12(1)	21(1)	8(1)
C(65)	37(2)	34(2)	60(2)	19(2)	26(2)	15(1)
C(66)	29(1)	17(1)	34(1)	11(1)	11(1)	5(1)
C(67)	28(1)	14(1)	26(1)	7(1)	12(1)	2(1)
C(68)	33(1)	29(2)	26(1)	7(1)	12(1)	3(1)
C(69)	48(2)	37(2)	27(1)	9(1)	19(1)	9(1)
C(70)	14(1)	18(1)	24(1)	4(1)	9(1)	2(1)
C(71)	17(1)	23(1)	26(1)	7(1)	7(1)	4(1)

Table 3.8. Continued Anisotropic displacement parameters ($Å^2 x\ 10^3$) for **9**·(*n*–C_6H_{14})·2(C_6H_6). The anisotropic displacement factor exponent takes the form: $-2\pi^2[\ h^2\ a^{*2}U^{11} + ...\ + 2\ h\ k\ a^*\ b^*\ U^{12}\ ]$

C(72)	34(2)	26(1)	24(1)	4(1)	1(1)	6(1)
C(73)	23(1)	24(1)	24(1)	1(1)	7(1)	5(1)
C(74)	26(1)	19(1)	30(1)	7(1)	14(1)	8(1)
C(75)	29(1)	20(1)	24(1)	9(1)	10(1)	7(1)
C(76)	20(1)	22(1)	22(1)	6(1)	9(1)	2(1)
C(77)	42(2)	22(1)	25(1)	6(1)	12(1)	7(1)
C(78)	43(2)	22(1)	36(2)	6(1)	14(1)	11(1)
C(79)	41(2)	31(2)	38(2)	9(1)	26(1)	5(1)
C(80)	26(1)	23(1)	22(1)	5(1)	7(1)	7(1)
C(81)	28(1)	24(1)	24(1)	7(1)	12(1)	6(1)
C(82)	91(3)	97(3)	62(2)	41(2)	22(2)	24(3)
C(83)	104(4)	116(4)	61(3)	20(3)	18(3)	31(3)
C(84)	96(3)	64(3)	51(2)	22(2)	12(2)	30(3)
C(85)	55(2)	35(2)	41(2)	14(1)	1(2)	10(2)
C(86)	32(2)	26(2)	68(2)	16(2)	-4(2)	-1(1)
C(87)	60(2)	24(2)	72(2)	13(2)	34(2)	4(2)
C(88)	60(2)	39(2)	33(2)	15(1)	0(2)	1(2)
C(89)	42(2)	62(2)	55(2)	25(2)	7(2)	22(2)
C(90)	60(2)	58(2)	51(2)	23(2)	18(2)	24(2)
N(1)	17(1)	19(1)	16(1)	6(1)	5(1)	4(1)
N(2)	17(1)	20(1)	18(1)	3(1)	8(1)	3(1)
N(3)	20(1)	16(1)	18(1)	5(1)	10(1)	5(1)
Si(1)	21(1)	24(1)	17(1)	4(1)	7(1)	4(1)
Co(1)	15(1)	17(1)	16(1)	6(1)	6(1)	4(1)

Table 3.9. Bond lengths [Å] and angles [˚] for **10**·(*n*–C_7H_{16})·(C_7H_{16})

Co(1)-C(84)	1.806(3)	Si(1)-C(1E)	1.883(3)
Co(1)-C(85)	1.808(3)	N(1)-C(84)	1.193(3)
Co(1)-C(83)	1.820(3)	N(1)-C(110)	1.389(3)
Co(1)-Si(1)	2.2547(8)	N(2)-C(85)	1.188(3)
Si(1)-C(1D)	1.879(3)	N(2)-C(134)	1.390(3)
Si(1)-C(1C)	1.880(3)	N(3)-C(83)	1.173(3)

Table 3.9. Continued Bond lengths [Å] and angles [˚] for **10**·(*n*–C_7H_{16})·(C_7H_{16})

N(3)-C(86)	1.387(3)	C(98)-H(98B)	0.9800
C(1C)-H(1CA)	0.9800	C(98)-H(98C)	0.9800
C(1C)-H(1CB)	0.9800	C(99)-H(99A)	0.9800
C(1C)-H(1CC)	0.9800	C(99)-H(99B)	0.9800
C(1D)-H(1DA)	0.9800	C(99)-H(99C)	0.9800
C(1D)-H(1DB)	0.9800	C(100)-H(10D)	0.9800
C(1D)-H(1DC)	0.9800	C(100)-H(10E)	0.9800
C(1E)-H(1EA)	0.9800	C(100)-H(10F)	0.9800
C(1E)-H(1EB)	0.9800	C(101)-C(102)	1.395(4)
C(1E)-H(1EC)	0.9800	C(101)-C(106)	1.406(4)
C(86)-C(91)	1.398(4)	C(102)-C(103)	1.394(4)
C(86)-C(87)	1.412(4)	C(102)-C(108)	1.508(4)
C(87)-C(88)	1.394(4)	C(103)-C(104)	1.382(5)
C(87)-C(101)	1.492(4)	C(103)-H(103)	0.9500
C(88)-C(89)	1.371(4)	C(104)-C(105)	1.384(5)
C(88)-H(88)	0.9500	C(104)-C(109)	1.515(5)
C(89)-C(90)	1.395(4)	C(105)-C(106)	1.380(4)
C(89)-H(89)	0.9500	C(105)-H(105)	0.9500
C(90)-C(91)	1.395(4)	C(106)-C(107)	1.507(4)
C(90)-H(90)	0.9500	C(107)-H(10G)	0.9800
C(91)-C(92)	1.493(4)	C(107)-H(10H)	0.9800
C(92)-C(93)	1.397(4)	C(107)-H(10I)	0.9800
C(92)-C(97)	1.401(4)	C(108)-H(10J)	0.9800
C(93)-C(94)	1.391(4)	C(108)-H(10K)	0.9800
C(93)-C(99)	1.514(4)	C(108)-H(10L)	0.9800
C(94)-C(95)	1.394(5)	C(109)-H(10M)	0.9800
C(94)-H(94)	0.9500	C(109)-H(10N)	0.9800
C(95)-C(96)	1.387(5)	C(109)-H(10O)	0.9800
C(95)-C(100)	1.519(4)	C(110)-C(111)	1.398(4)
C(96)-C(97)	1.395(4)	C(110)-C(115)	1.414(4)
C(96)-H(96)	0.9500	C(111)-C(112)	1.392(4)
C(97)-C(98)	1.501(4)	C(111)-C(125)	1.495(4)
C(98)-H(98A)	0.9800	C(112)-C(113)	1.395(5)

Table 3.9. Continued Bond lengths [Å] and angles [˚] for **10**·(*n*–C_7H_{16})·(C_7H_{16})

C(112)-H(112)	0.9500	C(128)-C(133)	1.511(5)
C(113)-C(114)	1.375(5)	C(129)-C(130)	1.404(5)
C(113)-H(113)	0.9500	C(129)-H(129)	0.9500
C(114)-C(115)	1.393(4)	C(130)-C(131)	1.501(5)
C(114)-H(114)	0.9500	C(131)-H(13A)	0.9800
C(115)-C(116)	1.486(4)	C(131)-H(13B)	0.9800
C(116)-C(121)	1.386(4)	C(131)-H(13C)	0.9800
C(116)-C(117)	1.410(4)	C(132)-H(13D)	0.9800
C(117)-C(118)	1.387(5)	C(132)-H(13E)	0.9800
C(117)-C(123)	1.502(5)	C(132)-H(13F)	0.9800
C(118)-C(119)	1.371(6)	C(133)-H(13G)	0.9800
C(118)-H(118)	0.9500	C(133)-H(13H)	0.9800
C(119)-C(120)	1.401(5)	C(133)-H(13I)	0.9800
C(119)-C(124)	1.517(5)	C(134)-C(135)	1.401(4)
C(120)-C(121)	1.394(4)	C(134)-C(139)	1.407(4)
C(120)-H(120)	0.9500	C(135)-C(136)	1.394(4)
C(121)-C(122)	1.509(4)	C(135)-C(149)	1.489(4)
C(122)-H(12A)	0.9800	C(136)-C(137)	1.384(4)
C(122)-H(12B)	0.9800	C(136)-H(136)	0.9500
C(122)-H(12C)	0.9800	C(137)-C(138)	1.386(4)
C(123)-H(12D)	0.9800	C(137)-H(137)	0.9500
C(123)-H(12E)	0.9800	C(138)-C(139)	1.391(4)
C(123)-H(12F)	0.9800	C(138)-H(138)	0.9500
C(124)-H(12G)	0.9800	C(139)-C(140)	1.492(4)
C(124)-H(12H)	0.9800	C(140)-C(141)	1.394(4)
C(124)-H(12I)	0.9800	C(140)-C(145)	1.406(4)
C(125)-C(130)	1.391(5)	C(141)-C(142)	1.388(4)
C(125)-C(126)	1.404(4)	C(141)-C(147)	1.511(4)
C(126)-C(127)	1.401(5)	C(142)-C(143)	1.381(4)
C(126)-C(132)	1.507(5)	C(142)-H(142)	0.9500
C(127)-C(128)	1.384(5)	C(143)-C(144)	1.385(5)
C(127)-H(127)	0.9500	C(143)-C(148)	1.517(4)
C(128)-C(129)	1.378(5)	C(144)-C(145)	1.394(4)

Table 3.9. Continued Bond lengths [Å] and angles [˚] for **10**·(*n*–C_7H_{16})·(C_7H_{16})

C(144)-H(144)	0.9500	Co(2)-Si(2)	2.2684(8)
C(145)-C(146)	1.503(4)	Co(2)-H(2)	1.98(3)
C(146)-H(14A)	0.9800	Si(2)-C(6)	1.877(3)
C(146)-H(14B)	0.9800	Si(2)-C(1)	1.881(3)
C(146)-H(14C)	0.9800	Si(2)-C(10)	1.892(3)
C(147)-H(14D)	0.82(4)	N(4)-C(8)	1.177(3)
C(147)-H(14E)	0.95(4)	N(4)-C(13)	1.397(3)
C(148)-H(14F)	0.9800	N(5)-C(11)	1.197(3)
C(148)-H(14G)	0.9800	N(5)-C(59)	1.388(3)
C(148)-H(14H)	0.9800	N(6)-C(9)	1.181(3)
C(149)-C(150)	1.399(5)	N(6)-C(35)	1.390(3)
C(149)-C(154)	1.403(4)	C(1)-H(1A)	0.9800
C(150)-C(151)	1.400(5)	C(1)-H(1B)	0.9800
C(150)-C(156)	1.503(5)	C(1)-H(1C)	0.9800
C(151)-C(152)	1.393(6)	C(1A)-C(15)	1.363(6)
C(151)-H(151)	0.9500	C(1A)-C(14)	1.378(6)
C(152)-C(153)	1.370(5)	C(1A)-H(1AA)	0.9500
C(152)-C(157)	1.518(5)	C(1B)-C(7A)	1.491(16)
C(153)-C(154)	1.394(4)	C(1B)-C(7B)	1.512(8)
C(153)-H(153)	0.9500	C(1B)-C(5)	1.525(5)
C(154)-C(155)	1.506(5)	C(1B)-H(1BA)	1.11(5)
C(155)-H(15A)	0.9800	C(1B)-H(1BB)	1.16(5)
C(155)-H(15B)	0.9800	C(2)-C(3)	1.501(4)
C(155)-H(15C)	0.9800	C(2)-C(7)	1.511(4)
C(156)-H(15D)	0.9800	C(2)-H(2A)	0.9900
C(156)-H(15E)	0.9800	C(2)-H(2B)	0.9900
C(156)-H(15F)	0.9800	C(3)-C(4)	1.529(4)
C(157)-H(15G)	0.9800	C(3)-H(3A)	0.91(5)
C(157)-H(15H)	0.9800	C(3)-H(3B)	0.95(4)
C(157)-H(15I)	0.9800	C(4)-C(5)	1.516(4)
Co(2)-C(11)	1.811(3)	C(4)-H(4A)	1.15(4)
Co(2)-C(8)	1.813(2)	C(4)-H(4B)	1.05(4)
Co(2)-C(9)	1.814(2)	C(5)-H(5A)	1.12(4)

Table 3.9. Continued Bond lengths [Å] and angles [˚] for **10**·(*n*–C_7H_{16})·(C_7H_{16}).

C(5)-H(5B)	1.21(6)	C(19)-H(19)	0.9500
C(6)-H(6A)	0.9800	C(20)-C(21)	1.385(5)
C(6)-H(6B)	0.9800	C(20)-C(24)	1.517(6)
C(6)-H(6C)	0.9800	C(21)-C(22)	1.382(5)
C(7)-H(7A)	0.91(3)	C(21)-H(21)	0.9500
C(7)-H(7B)	1.02(4)	C(22)-C(23)	1.520(4)
C(7)-H(7C)	1.09(4)	C(23)-H(23A)	0.9800
C(7A)-H(2)	0.96(3)	C(23)-H(23B)	0.9800
C(7A)-H(7AA)	1.029(18)	C(23)-H(23C)	0.9800
C(7A)-H(7AB)	0.992(19)	C(24)-H(24A)	0.9800
C(7A)-H(7BA)	1.52(2)	C(24)-H(24B)	0.9800
C(7A)-H(7BB)	0.90(3)	C(24)-H(24C)	0.9800
C(7B)-H(2)	1.04(2)	C(25)-H(25A)	0.9800
C(7B)-H(7AA)	0.79(3)	C(25)-H(25B)	0.9800
C(7B)-H(7AB)	1.52(2)	C(25)-H(25C)	0.9800
C(7B)-H(7BA)	0.960(18)	C(26)-C(31)	1.402(4)
C(7B)-H(7BB)	1.012(19)	C(26)-C(27)	1.404(4)
C(10)-H(10A)	0.9800	C(27)-C(28)	1.377(5)
C(10)-H(10B)	0.9800	C(27)-C(33)	1.517(4)
C(10)-H(10C)	0.9800	C(28)-C(29)	1.395(5)
C(12)-C(14)	1.399(4)	C(28)-H(28)	0.9500
C(12)-C(13)	1.400(5)	C(29)-C(30)	1.388(4)
C(12)-C(26)	1.485(5)	C(29)-C(34)	1.502(5)
C(13)-C(16)	1.407(4)	C(30)-C(31)	1.385(4)
C(14)-H(14)	0.9500	C(30)-H(30)	0.9500
C(15)-C(16)	1.395(4)	C(31)-C(32)	1.513(4)
C(15)-H(15)	0.9500	C(32)-H(32A)	0.9800
C(16)-C(17)	1.484(5)	C(32)-H(32B)	0.9800
C(17)-C(22)	1.400(4)	C(32)-H(32C)	0.9800
C(17)-C(18)	1.412(5)	C(33)-H(33A)	0.9800
C(18)-C(19)	1.388(6)	C(33)-H(33B)	0.9800
C(18)-C(25)	1.519(5)	C(33)-H(33C)	0.9800
C(19)-C(20)	1.384(5)	C(34)-H(34A)	0.9800

Table 3.9. Continued Bond lengths [Å] and angles [˚] for **10**·(*n*–C_7H_{16})·(C_7H_{16}).

C(34)-H(34B)	0.9800	C(50)-C(55)	1.402(4)
C(34)-H(34C)	0.9800	C(50)-C(51)	1.405(4)
C(35)-C(40)	1.407(3)	C(51)-C(52)	1.388(4)
C(35)-C(36)	1.409(3)	C(51)-C(57)	1.509(4)
C(36)-C(37)	1.393(3)	C(52)-C(53)	1.384(4)
C(36)-C(50)	1.496(3)	C(52)-H(52)	0.9500
C(37)-C(38)	1.388(4)	C(53)-C(54)	1.391(4)
C(37)-H(37)	0.9500	C(53)-C(58)	1.509(4)
C(38)-C(39)	1.382(4)	C(54)-C(55)	1.395(4)
C(38)-H(38)	0.9500	C(54)-H(54)	0.9500
C(39)-C(40)	1.397(3)	C(55)-C(56)	1.510(4)
C(39)-H(39)	0.9500	C(56)-H(56A)	0.9800
C(40)-C(41)	1.498(3)	C(56)-H(56B)	0.9800
C(41)-C(42)	1.392(4)	C(56)-H(56C)	0.9800
C(41)-C(46)	1.404(4)	C(57)-H(57A)	0.9800
C(42)-C(43)	1.390(4)	C(57)-H(57B)	0.9800
C(42)-C(48)	1.504(4)	C(57)-H(57C)	0.9800
C(43)-C(44)	1.387(4)	C(58)-H(58A)	0.9800
C(43)-H(43)	0.9500	C(58)-H(58B)	0.9800
C(44)-C(45)	1.383(4)	C(58)-H(58C)	0.9800
C(44)-C(49)	1.515(4)	C(59)-C(64)	1.402(4)
C(45)-C(46)	1.400(4)	C(59)-C(60)	1.412(4)
C(45)-H(45)	0.9500	C(60)-C(61)	1.393(4)
C(46)-C(47)	1.507(4)	C(60)-C(74)	1.499(4)
C(47)-H(47A)	0.9800	C(61)-C(62)	1.381(4)
C(47)-H(47B)	0.9800	C(61)-H(61)	0.9500
C(47)-H(47C)	0.9800	C(62)-C(63)	1.387(4)
C(48)-H(48A)	0.9800	C(62)-H(62)	0.9500
C(48)-H(48B)	0.9800	C(63)-C(64)	1.394(4)
C(48)-H(48C)	0.9800	C(63)-H(63)	0.9500
C(49)-H(49A)	0.9800	C(64)-C(65)	1.492(3)
C(49)-H(49B)	0.9800	C(65)-C(70)	1.391(4)
C(49)-H(49C)	0.9800	C(65)-C(66)	1.406(4)

Table 3.9. Continued Bond lengths [Å] and angles [˚] for **10**·(*n*–C_7H_{16})·(C_7H_{16}).

C(66)-C(67)	1.396(4)	C(81)-H(81B)	0.9800
C(66)-C(72)	1.505(4)	C(81)-H(81C)	0.9800
C(67)-C(68)	1.371(4)	C(82)-H(82A)	0.9800
C(67)-H(67)	0.9500	C(82)-H(82B)	0.9800
C(68)-C(69)	1.393(4)	C(82)-H(82C)	0.9800
C(68)-C(73)	1.515(4)	C(7SA)-C(6SB)	1.944(15)
C(69)-C(70)	1.392(4)	C(7SA)-H(7SA)	0.9800
C(69)-H(69)	0.9500	C(7SA)-H(7SB)	0.9800
C(70)-C(71)	1.514(4)	C(7SA)-H(7SC)	0.9800
C(71)-H(71A)	0.9800	C(7SB)-C(6SA)	1.586(19)
C(71)-H(71B)	0.9800	C(7SB)-H(7SD)	0.9800
C(71)-H(71C)	0.9800	C(7SB)-H(7SE)	0.9800
C(72)-H(72A)	0.9800	C(7SB)-H(7SF)	0.9800
C(72)-H(72B)	0.9800	C(5SA)-C(6SB)	1.486(12)
C(72)-H(72C)	0.9800	C(5SA)-C(4S)	1.492(9)
C(73)-H(73A)	0.9800	C(5SA)-H(5SA)	0.9900
C(73)-H(73B)	0.9800	C(5SA)-H(5SB)	0.9900
C(73)-H(73C)	0.9800	C(6SB)-H(6SA)	0.9900
C(74)-C(75)	1.397(4)	C(6SB)-H(6SB)	0.9900
C(74)-C(79)	1.407(4)	C(5SB)-C(6SA)	1.511(14)
C(75)-C(76)	1.389(4)	C(5SB)-C(4S)	1.654(11)
C(75)-C(81)	1.521(4)	C(5SB)-H(5SC)	0.9900
C(76)-C(77)	1.399(5)	C(5SB)-H(5SD)	0.9900
C(76)-H(76)	0.9500	C(6SA)-H(6SC)	0.9900
C(77)-C(78)	1.389(5)	C(6SA)-H(6SD)	0.9900
C(77)-C(82)	1.511(5)	C(4S)-C(3S)	1.520(6)
C(78)-C(79)	1.395(4)	C(4S)-H(4S)	1.15(8)
C(78)-H(78)	0.9500	C(4S)-H(4SA)	1.08(10)
C(79)-C(80)	1.507(4)	C(3S)-C(2S)	1.541(6)
C(80)-H(80A)	0.9800	C(3S)-H(3SA)	0.9900
C(80)-H(80B)	0.9800	C(3S)-H(3SB)	0.9900
C(80)-H(80C)	0.9800	C(2S)-C(1S)	1.499(6)
C(81)-H(81A)	0.9800	C(2S)-H(2SA)	0.9900

Table 3.9. Continued Bond lengths [Å] and angles [˚] for **10**·(*n*–C_7H_{16})·(C_7H_{16}).

C(2S)-H(2SB)	0.9900	Si(1)-C(1E)-H(1EB)	109.5
C(1S)-H(1SA)	0.9800	H(1EA)-C(1E)-H(1EB)	109.5
C(1S)-H(1SB)	0.9800	Si(1)-C(1E)-H(1EC)	109.5
C(1S)-H(1SC)	0.9800	H(1EA)-C(1E)-H(1EC)	109.5
Angles		H(1EB)-C(1E)-H(1EC)	109.5
C(84)-Co(1)-C(85)	122.52(11)	N(3)-C(83)-Co(1)	178.3(2)
C(84)-Co(1)-C(83)	119.60(11)	N(1)-C(84)-Co(1)	178.0(2)
C(85)-Co(1)-C(83)	117.07(11)	N(2)-C(85)-Co(1)	177.6(2)
C(84)-Co(1)-Si(1)	87.43(8)	N(3)-C(86)-C(91)	119.1(2)
C(85)-Co(1)-Si(1)	86.42(8)	N(3)-C(86)-C(87)	118.9(2)
C(83)-Co(1)-Si(1)	87.12(8)	C(91)-C(86)-C(87)	122.0(2)
C(1D)-Si(1)-C(1C)	108.10(12)	C(88)-C(87)-C(86)	117.6(3)
C(1D)-Si(1)-C(1E)	106.51(13)	C(88)-C(87)-C(101)	119.4(3)
C(1C)-Si(1)-C(1E)	107.02(13)	C(86)-C(87)-C(101)	122.8(2)
C(1D)-Si(1)-Co(1)	111.10(9)	C(89)-C(88)-C(87)	121.2(3)
C(1C)-Si(1)-Co(1)	112.33(9)	C(89)-C(88)-H(88)	119.4
C(1E)-Si(1)-Co(1)	111.50(9)	C(87)-C(88)-H(88)	119.4
C(84)-N(1)-C(110)	164.5(3)	C(88)-C(89)-C(90)	120.5(3)
C(85)-N(2)-C(134)	159.5(3)	C(88)-C(89)-H(89)	119.7
C(83)-N(3)-C(86)	167.9(3)	C(90)-C(89)-H(89)	119.7
Si(1)-C(1C)-H(1CA)	109.5	C(89)-C(90)-C(91)	120.6(3)
Si(1)-C(1C)-H(1CB)	109.5	C(89)-C(90)-H(90)	119.7
H(1CA)-C(1C)-H(1CB)	109.5	C(91)-C(90)-H(90)	119.7
Si(1)-C(1C)-H(1CC)	109.5	C(90)-C(91)-C(86)	118.0(3)
H(1CA)-C(1C)-H(1CC)	109.5	C(90)-C(91)-C(92)	120.4(3)
H(1CB)-C(1C)-H(1CC)	109.5	C(86)-C(91)-C(92)	121.6(2)
Si(1)-C(1D)-H(1DA)	109.5	C(93)-C(92)-C(97)	120.6(3)
Si(1)-C(1D)-H(1DB)	109.5	C(93)-C(92)-C(91)	120.9(3)
H(1DA)-C(1D)-H(1DB)	109.5	C(97)-C(92)-C(91)	118.5(3)
Si(1)-C(1D)-H(1DC)	109.5	C(94)-C(93)-C(92)	118.9(3)
H(1DA)-C(1D)-H(1DC)	109.5	C(94)-C(93)-C(99)	120.0(3)
H(1DB)-C(1D)-H(1DC)	109.5	C(92)-C(93)-C(99)	121.1(3)
Si(1)-C(1E)-H(1EA)	109.5	C(93)-C(94)-C(95)	121.7(3)

Table 3.9. Continued Bond lengths [Å] and angles [˚] for **10**·(*n*–C_7H_{16})·(C_7H_{16}).

C(93)-C(94)-H(94)	119.2	C(103)-C(102)-C(108)	119.2(3)
C(95)-C(94)-H(94)	119.2	C(101)-C(102)-C(108)	122.0(3)
C(96)-C(95)-C(94)	118.4(3)	C(104)-C(103)-C(102)	122.3(3)
C(96)-C(95)-C(100)	120.7(3)	C(104)-C(103)-H(103)	118.8
C(94)-C(95)-C(100)	120.9(3)	C(102)-C(103)-H(103)	118.8
C(95)-C(96)-C(97)	121.6(3)	C(103)-C(104)-C(105)	117.7(3)
C(95)-C(96)-H(96)	119.2	C(103)-C(104)-C(109)	120.7(3)
C(97)-C(96)-H(96)	119.2	C(105)-C(104)-C(109)	121.6(3)
C(96)-C(97)-C(92)	118.8(3)	C(106)-C(105)-C(104)	122.3(3)
C(96)-C(97)-C(98)	121.2(3)	C(106)-C(105)-H(105)	118.8
C(92)-C(97)-C(98)	120.0(3)	C(104)-C(105)-H(105)	118.8
C(97)-C(98)-H(98A)	109.5	C(105)-C(106)-C(101)	119.1(3)
C(97)-C(98)-H(98B)	109.5	C(105)-C(106)-C(107)	120.6(3)
H(98A)-C(98)-H(98B)	109.5	C(101)-C(106)-C(107)	120.3(3)
C(97)-C(98)-H(98C)	109.5	C(106)-C(107)-H(10G)	109.5
H(98A)-C(98)-H(98C)	109.5	C(106)-C(107)-H(10H)	109.5
H(98B)-C(98)-H(98C)	109.5	H(10G)-C(107)-H(10H)	109.5
C(93)-C(99)-H(99A)	109.5	C(106)-C(107)-H(10I)	109.5
C(93)-C(99)-H(99B)	109.5	H(10G)-C(107)-H(10I)	109.5
H(99A)-C(99)-H(99B)	109.5	H(10H)-C(107)-H(10I)	109.5
C(93)-C(99)-H(99C)	109.5	C(102)-C(108)-H(10J)	109.5
H(99A)-C(99)-H(99C)	109.5	C(102)-C(108)-H(10K)	109.5
H(99B)-C(99)-H(99C)	109.5	H(10J)-C(108)-H(10K)	109.5
C(95)-C(100)-H(10D)	109.5	C(102)-C(108)-H(10L)	109.5
C(95)-C(100)-H(10E)	109.5	H(10J)-C(108)-H(10L)	109.5
H(10D)-C(100)-H(10E)	109.5	H(10K)-C(108)-H(10L)	109.5
C(95)-C(100)-H(10F)	109.5	C(104)-C(109)-H(10M)	109.5
H(10D)-C(100)-H(10F)	109.5	C(104)-C(109)-H(10N)	109.5
H(10E)-C(100)-H(10F)	109.5	H(10M)-C(109)-H(10N)	109.5
C(102)-C(101)-C(106)	119.8(3)	C(104)-C(109)-H(10O)	109.5
C(102)-C(101)-C(87)	119.4(3)	H(10M)-C(109)-H(10O)	109.5
C(106)-C(101)-C(87)	120.6(3)	H(10N)-C(109)-H(10O)	109.5
C(103)-C(102)-C(101)	118.8(3)	N(1)-C(110)-C(111)	119.8(3)

Table 3.9. Continued Bond lengths [Å] and angles [˚] for **10**·(*n*–C_7H_{16})·(C_7H_{16}).

N(1)-C(110)-C(115)	118.8(3)	C(116)-C(121)-C(122)	120.4(3)
C(111)-C(110)-C(115)	121.4(3)	C(120)-C(121)-C(122)	120.1(3)
C(112)-C(111)-C(110)	118.5(3)	C(121)-C(122)-H(12A)	109.5
C(112)-C(111)-C(125)	118.6(3)	C(121)-C(122)-H(12B)	109.5
C(110)-C(111)-C(125)	122.6(2)	H(12A)-C(122)-H(12B)	109.5
C(111)-C(112)-C(113)	120.9(3)	C(121)-C(122)-H(12C)	109.5
C(111)-C(112)-H(112)	119.5	H(12A)-C(122)-H(12C)	109.5
C(113)-C(112)-H(112)	119.5	H(12B)-C(122)-H(12C)	109.5
C(114)-C(113)-C(112)	119.6(3)	C(117)-C(123)-H(12D)	109.5
C(114)-C(113)-H(113)	120.2	C(117)-C(123)-H(12E)	109.5
C(112)-C(113)-H(113)	120.2	H(12D)-C(123)-H(12E)	109.5
C(113)-C(114)-C(115)	121.9(3)	C(117)-C(123)-H(12F)	109.5
C(113)-C(114)-H(114)	119.1	H(12D)-C(123)-H(12F)	109.5
C(115)-C(114)-H(114)	119.1	H(12E)-C(123)-H(12F)	109.5
C(114)-C(115)-C(110)	117.6(3)	C(119)-C(124)-H(12G)	109.5
C(114)-C(115)-C(116)	120.6(3)	C(119)-C(124)-H(12H)	109.5
C(110)-C(115)-C(116)	121.7(3)	H(12G)-C(124)-H(12H)	109.5
C(121)-C(116)-C(117)	120.6(3)	C(119)-C(124)-H(12I)	109.5
C(121)-C(116)-C(115)	119.7(3)	H(12G)-C(124)-H(12I)	109.5
C(117)-C(116)-C(115)	119.6(3)	H(12H)-C(124)-H(12I)	109.5
C(118)-C(117)-C(116)	118.0(3)	C(130)-C(125)-C(126)	120.3(3)
C(118)-C(117)-C(123)	120.0(3)	C(130)-C(125)-C(111)	121.1(3)
C(116)-C(117)-C(123)	122.0(3)	C(126)-C(125)-C(111)	118.4(3)
C(119)-C(118)-C(117)	122.7(3)	C(127)-C(126)-C(125)	118.8(3)
C(119)-C(118)-H(118)	118.7	C(127)-C(126)-C(132)	119.9(3)
C(117)-C(118)-H(118)	118.7	C(125)-C(126)-C(132)	121.3(3)
C(118)-C(119)-C(120)	118.6(3)	C(128)-C(127)-C(126)	121.9(3)
C(118)-C(119)-C(124)	120.9(4)	C(128)-C(127)-H(127)	119.1
C(120)-C(119)-C(124)	120.5(4)	C(126)-C(127)-H(127)	119.1
C(121)-C(120)-C(119)	120.6(3)	C(129)-C(128)-C(127)	117.9(3)
C(121)-C(120)-H(120)	119.7	C(129)-C(128)-C(133)	122.2(4)
C(119)-C(120)-H(120)	119.7	C(127)-C(128)-C(133)	119.9(4)
C(116)-C(121)-C(120)	119.5(3)	C(128)-C(129)-C(130)	122.5(4)

Table 3.9. Continued Bond lengths [Å] and angles [˚] for **10**·(*n*–C_7H_{16})·(C_7H_{16}).

C(128)-C(129)-H(129)	118.7	C(136)-C(137)-H(137)	120.0
C(130)-C(129)-H(129)	118.7	C(138)-C(137)-H(137)	120.0
C(125)-C(130)-C(129)	118.4(3)	C(137)-C(138)-C(139)	121.0(3)
C(125)-C(130)-C(131)	120.6(3)	C(137)-C(138)-H(138)	119.5
C(129)-C(130)-C(131)	120.9(3)	C(139)-C(138)-H(138)	119.5
C(130)-C(131)-H(13A)	109.5	C(138)-C(139)-C(134)	118.1(3)
C(130)-C(131)-H(13B)	109.5	C(138)-C(139)-C(140)	120.6(3)
H(13A)-C(131)-H(13B)	109.5	C(134)-C(139)-C(140)	121.3(2)
C(130)-C(131)-H(13C)	109.5	C(141)-C(140)-C(145)	119.8(3)
H(13A)-C(131)-H(13C)	109.5	C(141)-C(140)-C(139)	120.8(3)
H(13B)-C(131)-H(13C)	109.5	C(145)-C(140)-C(139)	119.3(3)
C(126)-C(132)-H(13D)	109.5	C(142)-C(141)-C(140)	119.5(3)
C(126)-C(132)-H(13E)	109.5	C(142)-C(141)-C(147)	118.6(3)
H(13D)-C(132)-H(13E)	109.5	C(140)-C(141)-C(147)	121.9(3)
C(126)-C(132)-H(13F)	109.5	C(143)-C(142)-C(141)	121.8(3)
H(13D)-C(132)-H(13F)	109.5	C(143)-C(142)-H(142)	119.1
H(13E)-C(132)-H(13F)	109.5	C(141)-C(142)-H(142)	119.1
C(128)-C(133)-H(13G)	109.5	C(142)-C(143)-C(144)	118.2(3)
C(128)-C(133)-H(13H)	109.5	C(142)-C(143)-C(148)	120.8(3)
H(13G)-C(133)-H(13H)	109.5	C(144)-C(143)-C(148)	121.0(3)
C(128)-C(133)-H(13I)	109.5	C(143)-C(144)-C(145)	122.0(3)
H(13G)-C(133)-H(13I)	109.5	C(143)-C(144)-H(144)	119.0
H(13H)-C(133)-H(13I)	109.5	C(145)-C(144)-H(144)	119.0
N(2)-C(134)-C(135)	119.1(2)	C(144)-C(145)-C(140)	118.6(3)
N(2)-C(134)-C(139)	119.4(2)	C(144)-C(145)-C(146)	120.2(3)
C(135)-C(134)-C(139)	121.5(2)	C(140)-C(145)-C(146)	121.2(3)
C(136)-C(135)-C(134)	118.2(3)	C(145)-C(146)-H(14A)	109.5
C(136)-C(135)-C(149)	121.6(3)	C(145)-C(146)-H(14B)	109.5
C(134)-C(135)-C(149)	120.1(2)	H(14A)-C(146)-H(14B)	109.5
C(137)-C(136)-C(135)	121.0(3)	C(145)-C(146)-H(14C)	109.5
C(137)-C(136)-H(136)	119.5	H(14A)-C(146)-H(14C)	109.5
C(135)-C(136)-H(136)	119.5	H(14B)-C(146)-H(14C)	109.5
C(136)-C(137)-C(138)	120.0(3)	C(141)-C(147)-H(14D)	118(3)

Table 3.9. Continued Bond lengths [Å] and angles [˚] for **10**·(*n*–C_7H_{16})·(C_7H_{16}).

C(141)-C(147)-H(14E)	109(2)	C(150)-C(156)-H(15E)	109.5
H(14D)-C(147)-H(14E)	114(4)	H(15D)-C(156)-H(15E)	109.5
C(143)-C(148)-H(14F)	109.5	C(150)-C(156)-H(15F)	109.5
C(143)-C(148)-H(14G)	109.5	H(15D)-C(156)-H(15F)	109.5
H(14F)-C(148)-H(14G)	109.5	H(15E)-C(156)-H(15F)	109.5
C(143)-C(148)-H(14H)	109.5	C(152)-C(157)-H(15G)	109.5
H(14F)-C(148)-H(14H)	109.5	C(152)-C(157)-H(15H)	109.5
H(14G)-C(148)-H(14H)	109.5	H(15G)-C(157)-H(15H)	109.5
C(150)-C(149)-C(154)	120.6(3)	C(152)-C(157)-H(15I)	109.5
C(150)-C(149)-C(135)	118.6(3)	H(15G)-C(157)-H(15I)	109.5
C(154)-C(149)-C(135)	120.9(3)	H(15H)-C(157)-H(15I)	109.5
C(149)-C(150)-C(151)	118.3(3)	C(11)-Co(2)-C(8)	118.93(11)
C(149)-C(150)-C(156)	121.3(3)	C(11)-Co(2)-C(9)	117.53(11)
C(151)-C(150)-C(156)	120.5(3)	C(8)-Co(2)-C(9)	121.99(11)
C(152)-C(151)-C(150)	121.4(4)	C(11)-Co(2)-Si(2)	89.74(8)
C(152)-C(151)-H(151)	119.3	C(8)-Co(2)-Si(2)	82.83(8)
C(150)-C(151)-H(151)	119.3	C(9)-Co(2)-Si(2)	85.20(8)
C(153)-C(152)-C(151)	119.3(3)	C(11)-Co(2)-H(2)	92.8(7)
C(153)-C(152)-C(157)	121.1(4)	C(8)-Co(2)-H(2)	87.0(6)
C(151)-C(152)-C(157)	119.6(4)	C(9)-Co(2)-H(2)	102.6(6)
C(152)-C(153)-C(154)	121.2(4)	Si(2)-Co(2)-H(2)	169.4(6)
C(152)-C(153)-H(153)	119.4	C(6)-Si(2)-C(1)	107.31(13)
C(154)-C(153)-H(153)	119.4	C(6)-Si(2)-C(10)	108.30(13)
C(153)-C(154)-C(149)	119.1(3)	C(1)-Si(2)-C(10)	106.57(14)
C(153)-C(154)-C(155)	118.7(3)	C(6)-Si(2)-Co(2)	109.80(10)
C(149)-C(154)-C(155)	122.2(3)	C(1)-Si(2)-Co(2)	112.66(10)
C(154)-C(155)-H(15A)	109.5	C(10)-Si(2)-Co(2)	111.98(10)
C(154)-C(155)-H(15B)	109.5	C(8)-N(4)-C(13)	161.8(3)
H(15A)-C(155)-H(15B)	109.5	C(11)-N(5)-C(59)	162.7(2)
C(154)-C(155)-H(15C)	109.5	C(9)-N(6)-C(35)	164.6(2)
H(15A)-C(155)-H(15C)	109.5	Si(2)-C(1)-H(1A)	109.5
H(15B)-C(155)-H(15C)	109.5	Si(2)-C(1)-H(1B)	109.5
C(150)-C(156)-H(15D)	109.5	H(1A)-C(1)-H(1B)	109.5

Table 3.9. Continued Bond lengths [Å] and angles [˚] for **10**·(*n*–C_7H_{16})·(C_7H_{16}).

Si(2)-C(1)-H(1C)	109.5	H(4A)-C(4)-H(4B)	112(3)
H(1A)-C(1)-H(1C)	109.5	C(4)-C(5)-C(1B)	115.2(3)
H(1B)-C(1)-H(1C)	109.5	C(4)-C(5)-H(5A)	106(2)
C(15)-C(1A)-C(14)	120.3(3)	C(1B)-C(5)-H(5A)	107(2)
C(15)-C(1A)-H(1AA)	119.8	C(4)-C(5)-H(5B)	112(3)
C(14)-C(1A)-H(1AA)	119.8	C(1B)-C(5)-H(5B)	101(3)
C(7A)-C(1B)-C(7B)	21.6(4)	H(5A)-C(5)-H(5B)	116(4)
C(7A)-C(1B)-C(5)	117.6(6)	Si(2)-C(6)-H(6A)	109.5
C(7B)-C(1B)-C(5)	113.3(4)	Si(2)-C(6)-H(6B)	109.5
C(7A)-C(1B)-H(1BA)	94(3)	H(6A)-C(6)-H(6B)	109.5
C(7B)-C(1B)-H(1BA)	114(3)	Si(2)-C(6)-H(6C)	109.5
C(5)-C(1B)-H(1BA)	109(3)	H(6A)-C(6)-H(6C)	109.5
C(7A)-C(1B)-H(1BB)	117(3)	H(6B)-C(6)-H(6C)	109.5
C(7B)-C(1B)-H(1BB)	104(3)	C(2)-C(7)-H(7A)	97.7(19)
C(5)-C(1B)-H(1BB)	112(3)	C(2)-C(7)-H(7B)	105(2)
H(1BA)-C(1B)-H(1BB)	104(3)	H(7A)-C(7)-H(7B)	123(3)
C(3)-C(2)-C(7)	114.4(3)	C(2)-C(7)-H(7C)	110(2)
C(3)-C(2)-H(2A)	108.7	H(7A)-C(7)-H(7C)	118(3)
C(7)-C(2)-H(2A)	108.7	H(7B)-C(7)-H(7C)	102(3)
C(3)-C(2)-H(2B)	108.7	C(1B)-C(7A)-H(2)	114.0(19)
C(7)-C(2)-H(2B)	108.7	C(1B)-C(7A)-H(7AA)	110(2)
H(2A)-C(2)-H(2B)	107.6	H(2)-C(7A)-H(7AA)	105(3)
C(2)-C(3)-C(4)	114.8(3)	C(1B)-C(7A)-H(7AB)	111(4)
C(2)-C(3)-H(3A)	101(3)	H(2)-C(7A)-H(7AB)	110(3)
C(4)-C(3)-H(3A)	116(3)	H(7AA)-C(7A)-H(7AB)	105(2)
C(2)-C(3)-H(3B)	108(2)	C(1B)-C(7A)-H(7BA)	84(2)
C(4)-C(3)-H(3B)	114(2)	H(2)-C(7A)-H(7BA)	80.7(16)
H(3A)-C(3)-H(3B)	102(3)	H(7AA)-C(7A)-H(7BA)	48(3)
C(5)-C(4)-C(3)	115.2(3)	H(7AB)-C(7A)-H(7BA)	153(4)
C(5)-C(4)-H(4A)	104(2)	C(1B)-C(7A)-H(7BB)	124(3)
C(3)-C(4)-H(4A)	112(2)	H(2)-C(7A)-H(7BB)	117(3)
C(5)-C(4)-H(4B)	107(2)	H(7AA)-C(7A)-H(7BB)	34(4)
C(3)-C(4)-H(4B)	107(2)	H(7AB)-C(7A)-H(7BB)	71(4)

Table 3.9. Continued Bond lengths [Å] and angles [˚] for **10**·(*n*–C_7H_{16})·(C_7H_{16}).

H(7BA)-C(7A)-H(7BB)	83(3)	C(12)-C(14)-H(14)	119.3
C(1B)-C(7B)-H(2)	107.4(15)	C(1A)-C(15)-C(16)	121.4(4)
C(1B)-C(7B)-H(7AA)	126(3)	C(1A)-C(15)-H(15)	119.3
H(2)-C(7B)-H(7AA)	119(3)	C(16)-C(15)-H(15)	119.3
C(1B)-C(7B)-H(7AB)	86(3)	C(15)-C(16)-C(13)	117.5(4)
H(2)-C(7B)-H(7AB)	74.8(16)	C(15)-C(16)-C(17)	120.3(3)
H(7AA)-C(7B)-H(7AB)	81(2)	C(13)-C(16)-C(17)	122.1(3)
C(1B)-C(7B)-H(7BA)	107(3)	C(22)-C(17)-C(18)	119.4(4)
H(2)-C(7B)-H(7BA)	112(2)	C(22)-C(17)-C(16)	120.1(3)
H(7AA)-C(7B)-H(7BA)	80(4)	C(18)-C(17)-C(16)	120.6(3)
H(7AB)-C(7B)-H(7BA)	161(4)	C(19)-C(18)-C(17)	118.7(3)
C(1B)-C(7B)-H(7BB)	113(3)	C(19)-C(18)-C(25)	121.3(4)
H(2)-C(7B)-H(7BB)	101(2)	C(17)-C(18)-C(25)	120.0(4)
H(7AA)-C(7B)-H(7BB)	35(4)	C(20)-C(19)-C(18)	122.6(4)
H(7AB)-C(7B)-H(7BB)	46(3)	C(20)-C(19)-H(19)	118.7
H(7BA)-C(7B)-H(7BB)	115(4)	C(18)-C(19)-H(19)	118.7
N(4)-C(8)-Co(2)	174.8(2)	C(19)-C(20)-C(21)	117.4(4)
N(6)-C(9)-Co(2)	176.4(2)	C(19)-C(20)-C(24)	121.5(4)
Si(2)-C(10)-H(10A)	109.5	C(21)-C(20)-C(24)	121.1(4)
Si(2)-C(10)-H(10B)	109.5	C(22)-C(21)-C(20)	122.5(3)
H(10A)-C(10)-H(10B)	109.5	C(22)-C(21)-H(21)	118.8
Si(2)-C(10)-H(10C)	109.5	C(20)-C(21)-H(21)	118.8
H(10A)-C(10)-H(10C)	109.5	C(21)-C(22)-C(17)	119.3(3)
H(10B)-C(10)-H(10C)	109.5	C(21)-C(22)-C(23)	120.4(3)
N(5)-C(11)-Co(2)	177.0(2)	C(17)-C(22)-C(23)	120.4(3)
C(14)-C(12)-C(13)	117.1(3)	C(22)-C(23)-H(23A)	109.5
C(14)-C(12)-C(26)	120.8(3)	C(22)-C(23)-H(23B)	109.5
C(13)-C(12)-C(26)	122.0(2)	H(23A)-C(23)-H(23B)	109.5
N(4)-C(13)-C(12)	119.3(3)	C(22)-C(23)-H(23C)	109.5
N(4)-C(13)-C(16)	118.6(3)	H(23A)-C(23)-H(23C)	109.5
C(12)-C(13)-C(16)	122.1(3)	H(23B)-C(23)-H(23C)	109.5
C(1A)-C(14)-C(12)	121.5(4)	C(20)-C(24)-H(24A)	109.5
C(1A)-C(14)-H(14)	119.3	C(20)-C(24)-H(24B)	109.5

Table 3.9. Continued Bond lengths [Å] and angles [˚] for **10**·(*n*–C_7H_{16})·(C_7H_{16}).

H(24A)-C(24)-H(24B)	109.5	H(32B)-C(32)-H(32C)	109.5
C(20)-C(24)-H(24C)	109.5	C(27)-C(33)-H(33A)	109.5
H(24A)-C(24)-H(24C)	109.5	C(27)-C(33)-H(33B)	109.5
H(24B)-C(24)-H(24C)	109.5	H(33A)-C(33)-H(33B)	109.5
C(18)-C(25)-H(25A)	109.5	C(27)-C(33)-H(33C)	109.5
C(18)-C(25)-H(25B)	109.5	H(33A)-C(33)-H(33C)	109.5
H(25A)-C(25)-H(25B)	109.5	H(33B)-C(33)-H(33C)	109.5
C(18)-C(25)-H(25C)	109.5	C(29)-C(34)-H(34A)	109.5
H(25A)-C(25)-H(25C)	109.5	C(29)-C(34)-H(34B)	109.5
H(25B)-C(25)-H(25C)	109.5	H(34A)-C(34)-H(34B)	109.5
C(31)-C(26)-C(27)	119.6(3)	C(29)-C(34)-H(34C)	109.5
C(31)-C(26)-C(12)	120.3(3)	H(34A)-C(34)-H(34C)	109.5
C(27)-C(26)-C(12)	120.1(3)	H(34B)-C(34)-H(34C)	109.5
C(28)-C(27)-C(26)	118.9(3)	N(6)-C(35)-C(40)	119.7(2)
C(28)-C(27)-C(33)	119.8(3)	N(6)-C(35)-C(36)	119.2(2)
C(26)-C(27)-C(33)	121.3(3)	C(40)-C(35)-C(36)	121.1(2)
C(27)-C(28)-C(29)	122.4(3)	C(37)-C(36)-C(35)	118.1(2)
C(27)-C(28)-H(28)	118.8	C(37)-C(36)-C(50)	120.1(2)
C(29)-C(28)-H(28)	118.8	C(35)-C(36)-C(50)	121.6(2)
C(30)-C(29)-C(28)	117.8(3)	C(38)-C(37)-C(36)	121.2(2)
C(30)-C(29)-C(34)	120.3(3)	C(38)-C(37)-H(37)	119.4
C(28)-C(29)-C(34)	121.7(3)	C(36)-C(37)-H(37)	119.4
C(31)-C(30)-C(29)	121.4(3)	C(39)-C(38)-C(37)	120.1(2)
C(31)-C(30)-H(30)	119.3	C(39)-C(38)-H(38)	120.0
C(29)-C(30)-H(30)	119.3	C(37)-C(38)-H(38)	120.0
C(30)-C(31)-C(26)	119.8(3)	C(38)-C(39)-C(40)	120.9(2)
C(30)-C(31)-C(32)	119.1(3)	C(38)-C(39)-H(39)	119.5
C(26)-C(31)-C(32)	121.1(3)	C(40)-C(39)-H(39)	119.5
C(31)-C(32)-H(32A)	109.5	C(39)-C(40)-C(35)	118.4(2)
C(31)-C(32)-H(32B)	109.5	C(39)-C(40)-C(41)	119.3(2)
H(32A)-C(32)-H(32B)	109.5	C(35)-C(40)-C(41)	122.2(2)
C(31)-C(32)-H(32C)	109.5	C(42)-C(41)-C(46)	119.8(2)
H(32A)-C(32)-H(32C)	109.5	C(42)-C(41)-C(40)	121.8(2)

Table 3.9. Continued Bond lengths [Å] and angles [˚] for **10**·(*n*–C_7H_{16})·(C_7H_{16}).

C(46)-C(41)-C(40)	118.4(2)	H(49B)-C(49)-H(49C)	109.5
C(43)-C(42)-C(41)	119.5(2)	C(55)-C(50)-C(51)	120.0(2)
C(43)-C(42)-C(48)	119.9(2)	C(55)-C(50)-C(36)	120.2(2)
C(41)-C(42)-C(48)	120.6(2)	C(51)-C(50)-C(36)	119.7(2)
C(44)-C(43)-C(42)	121.9(2)	C(52)-C(51)-C(50)	119.1(3)
C(44)-C(43)-H(43)	119.0	C(52)-C(51)-C(57)	118.8(3)
C(42)-C(43)-H(43)	119.0	C(50)-C(51)-C(57)	122.1(2)
C(45)-C(44)-C(43)	118.0(2)	C(53)-C(52)-C(51)	121.9(3)
C(45)-C(44)-C(49)	121.6(3)	C(53)-C(52)-H(52)	119.0
C(43)-C(44)-C(49)	120.4(3)	C(51)-C(52)-H(52)	119.0
C(44)-C(45)-C(46)	121.9(3)	C(52)-C(53)-C(54)	118.3(2)
C(44)-C(45)-H(45)	119.0	C(52)-C(53)-C(58)	120.6(3)
C(46)-C(45)-H(45)	119.0	C(54)-C(53)-C(58)	121.1(3)
C(45)-C(46)-C(41)	118.8(2)	C(53)-C(54)-C(55)	121.8(3)
C(45)-C(46)-C(47)	119.6(2)	C(53)-C(54)-H(54)	119.1
C(41)-C(46)-C(47)	121.6(2)	C(55)-C(54)-H(54)	119.1
C(46)-C(47)-H(47A)	109.5	C(54)-C(55)-C(50)	118.8(2)
C(46)-C(47)-H(47B)	109.5	C(54)-C(55)-C(56)	119.6(2)
H(47A)-C(47)-H(47B)	109.5	C(50)-C(55)-C(56)	121.6(2)
C(46)-C(47)-H(47C)	109.5	C(55)-C(56)-H(56A)	109.5
H(47A)-C(47)-H(47C)	109.5	C(55)-C(56)-H(56B)	109.5
H(47B)-C(47)-H(47C)	109.5	H(56A)-C(56)-H(56B)	109.5
C(42)-C(48)-H(48A)	109.5	C(55)-C(56)-H(56C)	109.5
C(42)-C(48)-H(48B)	109.5	H(56A)-C(56)-H(56C)	109.5
H(48A)-C(48)-H(48B)	109.5	H(56B)-C(56)-H(56C)	109.5
C(42)-C(48)-H(48C)	109.5	C(51)-C(57)-H(57A)	109.5
H(48A)-C(48)-H(48C)	109.5	C(51)-C(57)-H(57B)	109.5
H(48B)-C(48)-H(48C)	109.5	H(57A)-C(57)-H(57B)	109.5
C(44)-C(49)-H(49A)	109.5	C(51)-C(57)-H(57C)	109.5
C(44)-C(49)-H(49B)	109.5	H(57A)-C(57)-H(57C)	109.5
H(49A)-C(49)-H(49B)	109.5	H(57B)-C(57)-H(57C)	109.5
C(44)-C(49)-H(49C)	109.5	C(53)-C(58)-H(58A)	109.5
H(49A)-C(49)-H(49C)	109.5	C(53)-C(58)-H(58B)	109.5

Table 3.9. Continued Bond lengths [Å] and angles [˚] for **10**·(*n*–C_7H_{16})·(C_7H_{16}).

H(58A)-C(58)-H(58B)	109.5	C(69)-C(68)-C(73)	120.7(3)
C(53)-C(58)-H(58C)	109.5	C(70)-C(69)-C(68)	121.5(3)
H(58A)-C(58)-H(58C)	109.5	C(70)-C(69)-H(69)	119.2
H(58B)-C(58)-H(58C)	109.5	C(68)-C(69)-H(69)	119.2
N(5)-C(59)-C(64)	119.6(2)	C(65)-C(70)-C(69)	119.2(3)
N(5)-C(59)-C(60)	119.4(2)	C(65)-C(70)-C(71)	121.5(3)
C(64)-C(59)-C(60)	121.1(2)	C(69)-C(70)-C(71)	119.3(3)
C(61)-C(60)-C(59)	118.0(3)	C(70)-C(71)-H(71A)	109.5
C(61)-C(60)-C(74)	120.3(2)	C(70)-C(71)-H(71B)	109.5
C(59)-C(60)-C(74)	121.7(2)	H(71A)-C(71)-H(71B)	109.5
C(62)-C(61)-C(60)	121.5(3)	C(70)-C(71)-H(71C)	109.5
C(62)-C(61)-H(61)	119.2	H(71A)-C(71)-H(71C)	109.5
C(60)-C(61)-H(61)	119.2	H(71B)-C(71)-H(71C)	109.5
C(61)-C(62)-C(63)	119.6(3)	C(66)-C(72)-H(72A)	109.5
C(61)-C(62)-H(62)	120.2	C(66)-C(72)-H(72B)	109.5
C(63)-C(62)-H(62)	120.2	H(72A)-C(72)-H(72B)	109.5
C(62)-C(63)-C(64)	121.2(3)	C(66)-C(72)-H(72C)	109.5
C(62)-C(63)-H(63)	119.4	H(72A)-C(72)-H(72C)	109.5
C(64)-C(63)-H(63)	119.4	H(72B)-C(72)-H(72C)	109.5
C(63)-C(64)-C(59)	118.5(2)	C(68)-C(73)-H(73A)	109.5
C(63)-C(64)-C(65)	118.8(2)	C(68)-C(73)-H(73B)	109.5
C(59)-C(64)-C(65)	122.7(2)	H(73A)-C(73)-H(73B)	109.5
C(70)-C(65)-C(66)	120.2(2)	C(68)-C(73)-H(73C)	109.5
C(70)-C(65)-C(64)	120.7(2)	H(73A)-C(73)-H(73C)	109.5
C(66)-C(65)-C(64)	119.0(2)	H(73B)-C(73)-H(73C)	109.5
C(67)-C(66)-C(65)	118.4(3)	C(75)-C(74)-C(79)	120.5(3)
C(67)-C(66)-C(72)	120.4(3)	C(75)-C(74)-C(60)	119.2(3)
C(65)-C(66)-C(72)	121.2(3)	C(79)-C(74)-C(60)	120.3(3)
C(68)-C(67)-C(66)	122.3(3)	C(76)-C(75)-C(74)	119.4(3)
C(68)-C(67)-H(67)	118.9	C(76)-C(75)-C(81)	120.1(3)
C(66)-C(67)-H(67)	118.9	C(74)-C(75)-C(81)	120.5(3)
C(67)-C(68)-C(69)	118.3(3)	C(75)-C(76)-C(77)	121.5(3)
C(67)-C(68)-C(73)	120.9(3)	C(75)-C(76)-H(76)	119.2

Table 3.9. Continued Bond lengths [Å] and angles [˚] for **10**·(*n*–C_7H_{16})·(C_7H_{16}).

C(77)-C(76)-H(76)	119.2	H(7SE)-C(7SB)-H(7SF)	109.5
C(78)-C(77)-C(76)	117.8(3)	C(6SB)-C(5SA)-C(4S)	112.2(6)
C(78)-C(77)-C(82)	121.1(3)	C(6SB)-C(5SA)-H(5SA)	109.2
C(76)-C(77)-C(82)	121.1(3)	C(4S)-C(5SA)-H(5SA)	109.2
C(77)-C(78)-C(79)	122.5(3)	C(6SB)-C(5SA)-H(5SB)	109.2
C(77)-C(78)-H(78)	118.7	C(4S)-C(5SA)-H(5SB)	109.2
C(79)-C(78)-H(78)	118.7	H(5SA)-C(5SA)-H(5SB)	107.9
C(78)-C(79)-C(74)	118.1(3)	C(5SA)-C(6SB)-C(7SA)	94.6(7)
C(78)-C(79)-C(80)	119.6(3)	C(5SA)-C(6SB)-H(6SA)	112.8
C(74)-C(79)-C(80)	122.3(3)	C(7SA)-C(6SB)-H(6SA)	112.8
C(79)-C(80)-H(80A)	109.5	C(5SA)-C(6SB)-H(6SB)	112.8
C(79)-C(80)-H(80B)	109.5	C(7SA)-C(6SB)-H(6SB)	112.8
H(80A)-C(80)-H(80B)	109.5	H(6SA)-C(6SB)-H(6SB)	110.3
C(79)-C(80)-H(80C)	109.5	C(6SA)-C(5SB)-C(4S)	112.6(8)
H(80A)-C(80)-H(80C)	109.5	C(6SA)-C(5SB)-H(5SC)	109.1
H(80B)-C(80)-H(80C)	109.5	C(4S)-C(5SB)-H(5SC)	109.1
C(75)-C(81)-H(81A)	109.5	C(6SA)-C(5SB)-H(5SD)	109.1
C(75)-C(81)-H(81B)	109.5	C(4S)-C(5SB)-H(5SD)	109.1
H(81A)-C(81)-H(81B)	109.5	H(5SC)-C(5SB)-H(5SD)	107.8
C(75)-C(81)-H(81C)	109.5	C(5SB)-C(6SA)-C(7SB)	100.0(9)
H(81A)-C(81)-H(81C)	109.5	C(5SB)-C(6SA)-H(6SC)	111.8
H(81B)-C(81)-H(81C)	109.5	C(7SB)-C(6SA)-H(6SC)	111.8
C(77)-C(82)-H(82A)	109.5	C(5SB)-C(6SA)-H(6SD)	111.8
C(77)-C(82)-H(82B)	109.5	C(7SB)-C(6SA)-H(6SD)	111.8
H(82A)-C(82)-H(82B)	109.5	H(6SC)-C(6SA)-H(6SD)	109.5
C(77)-C(82)-H(82C)	109.5	C(5SA)-C(4S)-C(3S)	108.6(5)
H(82A)-C(82)-H(82C)	109.5	C(5SA)-C(4S)-C(5SB)	29.1(4)
H(82B)-C(82)-H(82C)	109.5	C(3S)-C(4S)-C(5SB)	118.7(5)
C(6SA)-C(7SB)-H(7SD)	109.5	C(5SA)-C(4S)-H(4S)	96(4)
C(6SA)-C(7SB)-H(7SE)	109.5	C(3S)-C(4S)-H(4S)	111(4)
H(7SD)-C(7SB)-H(7SE)	109.5	C(5SB)-C(4S)-H(4S)	113(4)
C(6SA)-C(7SB)-H(7SF)	109.5	C(5SA)-C(4S)-H(4SA)	127(5)
H(7SD)-C(7SB)-H(7SF)	109.5	C(3S)-C(4S)-H(4SA)	109(5)

Table 3.9. Continued Bond lengths [Å] and angles [˚] for **10**·(*n*–C_7H_{16})·(C_7H_{16}).

C(5SB)-C(4S)-H(4SA)	99(5)	C(3S)-C(2S)-H(2SA)	109.4
H(4S)-C(4S)-H(4SA)	103(6)	C(1S)-C(2S)-H(2SB)	109.4
C(4S)-C(3S)-C(2S)	113.7(3)	C(3S)-C(2S)-H(2SB)	109.4
C(4S)-C(3S)-H(3SA)	108.8	H(2SA)-C(2S)-H(2SB)	108.0
C(2S)-C(3S)-H(3SA)	108.8	C(2S)-C(1S)-H(1SA)	109.5
C(4S)-C(3S)-H(3SB)	108.8	C(2S)-C(1S)-H(1SB)	109.5
C(2S)-C(3S)-H(3SB)	108.8	H(1SA)-C(1S)-H(1SB)	109.5
H(3SA)-C(3S)-H(3SB)	107.7	C(2S)-C(1S)-H(1SC)	109.5
C(1S)-C(2S)-C(3S)	111.4(3)	H(1SA)-C(1S)-H(1SC)	109.5
C(1S)-C(2S)-H(2SA)	109.4	H(1SB)-C(1S)-H(1SC)	109.5

Table 3.10. Anisotropic displacement parameters ($Å^2$x 10^3)for **10**·(*n*–C_7H_{16})·(C_7H_{16}). The anisotropic displacement factor exponent takes the form: $-2\pi^2[h^2a^{*2}U^{11} + ... + 2 h k a^* b^* U^{12}]$

	U^{11}	U^{22}	U^{33}	U^{23}	U^{13}	U^{12}
Co(1)	26(1)	22(1)	15(1)	0(1)	2(1)	2(1)
Si(1)	28(1)	25(1)	17(1)	0(1)	1(1)	-2(1)
N(1)	33(1)	25(1)	27(1)	-2(1)	0(1)	5(1)
N(2)	30(1)	28(1)	19(1)	-3(1)	5(1)	-2(1)
N(3)	34(1)	28(1)	19(1)	3(1)	1(1)	-1(1)
C(1C)	38(1)	31(1)	17(1)	2(1)	-3(1)	-7(1)
C(1D)	41(2)	22(1)	26(1)	-3(1)	2(1)	-3(1)
C(1E)	28(1)	32(1)	27(1)	0(1)	2(1)	-5(1)
C(83)	27(1)	25(1)	16(1)	-2(1)	4(1)	2(1)
C(84)	30(1)	27(1)	16(1)	1(1)	2(1)	0(1)
C(85)	27(1)	20(1)	17(1)	0(1)	-2(1)	0(1)
C(86)	37(1)	26(1)	19(1)	0(1)	5(1)	4(1)
C(87)	35(1)	30(1)	23(1)	4(1)	4(1)	5(1)
C(88)	37(2)	43(2)	32(2)	13(1)	2(1)	7(1)
C(89)	44(2)	48(2)	46(2)	26(2)	6(1)	3(2)
C(90)	36(2)	41(2)	47(2)	18(2)	10(1)	-1(1)

Table 3.10. Continued Anisotropic displacement parameters ($Å^2$x 10^3)for **10**·(*n*–C_7H_{16})·(C_7H_{16}). The anisotropic displacement factor exponent takes the form: $-2\pi^2[h^2a^{*2}U^{11} + ... + 2 h k a^* b^* U^{12}]$

C(91)	35(1)	30(1)	27(1)	5(1)	8(1)	4(1)
C(92)	33(1)	29(1)	30(2)	7(1)	7(1)	-6(1)
C(93)	41(2)	29(1)	34(2)	6(1)	9(1)	-7(1)
C(94)	47(2)	43(2)	37(2)	5(1)	1(1)	-15(2)
C(95)	31(2)	45(2)	48(2)	16(2)	-1(1)	-9(1)
C(96)	30(1)	40(2)	44(2)	8(1)	10(1)	-2(1)
C(97)	35(2)	30(1)	34(2)	8(1)	9(1)	-5(1)
C(98)	43(2)	35(2)	41(2)	2(1)	12(1)	4(1)
C(99)	63(2)	36(2)	37(2)	1(1)	13(2)	3(2)
C(100)	39(2)	71(3)	66(3)	18(2)	-10(2)	-11(2)
C(101)	36(1)	29(1)	24(1)	7(1)	-1(1)	6(1)
C(102)	40(2)	37(2)	28(2)	-2(1)	6(1)	0(1)
C(103)	47(2)	45(2)	35(2)	-2(1)	14(1)	-3(2)
C(104)	41(2)	40(2)	43(2)	1(2)	5(1)	-3(1)
C(105)	46(2)	33(2)	41(2)	-2(1)	-3(1)	-4(1)
C(106)	43(2)	31(1)	25(2)	1(1)	1(1)	5(1)
C(107)	53(2)	46(2)	37(2)	-9(2)	6(2)	1(2)
C(108)	47(2)	61(2)	35(2)	-18(2)	11(1)	-8(2)
C(109)	50(2)	69(3)	67(3)	-7(2)	12(2)	-17(2)
C(110)	30(1)	25(1)	35(2)	2(1)	5(1)	5(1)
C(111)	40(2)	26(1)	36(2)	1(1)	8(1)	5(1)
C(112)	52(2)	39(2)	45(2)	-2(2)	16(2)	11(2)
C(113)	50(2)	43(2)	63(2)	3(2)	15(2)	24(2)
C(114)	43(2)	42(2)	54(2)	6(2)	1(2)	16(2)
C(115)	33(1)	29(1)	42(2)	6(1)	0(1)	6(1)
C(116)	32(1)	29(1)	38(2)	3(1)	-12(1)	9(1)
C(117)	38(2)	32(2)	60(2)	-2(2)	-13(2)	5(1)
C(118)	49(2)	36(2)	65(2)	-2(2)	-29(2)	0(2)
C(119)	70(2)	33(2)	41(2)	-2(2)	-31(2)	8(2)
C(120)	60(2)	33(2)	31(2)	4(1)	-11(1)	4(2)
C(121)	46(2)	25(1)	29(2)	3(1)	-14(1)	7(1)
C(122)	48(2)	32(1)	32(2)	0(1)	-4(1)	-1(1)

Table 3.10. Continued Anisotropic displacement parameters ($Å^2 x\ 10^3$)for **10**·(*n*–C_7H_{16})·(C_7H_{16}). The anisotropic displacement factor exponent takes the form: $-2\pi^2[\ h^2a^{*2}U^{11} + ... + 2\ h\ k\ a^*\ b^*\ U^{12}\ ]$

C(123)	34(2)	47(2)	103(3)	0(2)	-4(2)	3(2)
C(124)	110(4)	58(2)	44(2)	-11(2)	-30(2)	5(2)
C(125)	49(2)	34(1)	30(2)	-1(1)	11(1)	14(1)
C(126)	55(2)	36(2)	29(2)	-1(1)	11(1)	7(2)
C(127)	68(2)	41(2)	31(2)	3(1)	16(2)	15(2)
C(128)	54(2)	55(2)	34(2)	-2(2)	10(2)	26(2)
C(129)	46(2)	56(2)	37(2)	-8(2)	4(1)	17(2)
C(130)	40(2)	40(2)	48(2)	-5(2)	10(1)	12(1)
C(131)	49(2)	54(2)	73(3)	1(2)	7(2)	2(2)
C(132)	79(3)	39(2)	41(2)	1(2)	10(2)	-11(2)
C(133)	70(3)	79(3)	36(2)	1(2)	3(2)	38(2)
C(134)	30(1)	33(1)	19(1)	-1(1)	4(1)	-2(1)
C(135)	33(1)	34(1)	24(1)	-5(1)	7(1)	-4(1)
C(136)	44(2)	43(2)	26(2)	-8(1)	13(1)	-2(1)
C(137)	42(2)	51(2)	30(2)	1(1)	15(1)	-8(2)
C(138)	37(2)	38(2)	32(2)	2(1)	6(1)	-9(1)
C(139)	29(1)	31(1)	26(1)	-2(1)	1(1)	-3(1)
C(140)	35(1)	28(1)	24(1)	-1(1)	3(1)	-6(1)
C(141)	37(2)	27(1)	29(2)	0(1)	1(1)	-5(1)
C(142)	44(2)	28(1)	41(2)	-3(1)	3(1)	-1(1)
C(143)	54(2)	34(2)	35(2)	-7(1)	6(1)	-10(1)
C(144)	45(2)	47(2)	27(2)	-3(1)	-4(1)	-12(2)
C(145)	36(2)	40(2)	26(2)	2(1)	-2(1)	-3(1)
C(146)	43(2)	65(2)	43(2)	-1(2)	-9(2)	6(2)
C(147)	37(2)	38(2)	42(2)	-8(1)	-6(1)	2(1)
C(148)	74(3)	50(2)	47(2)	-18(2)	10(2)	-12(2)
C(149)	46(2)	30(1)	26(2)	-8(1)	14(1)	-1(1)
C(150)	67(2)	33(2)	31(2)	-7(1)	17(2)	2(2)
C(151)	93(3)	33(2)	35(2)	-3(1)	27(2)	6(2)
C(152)	82(3)	29(2)	50(2)	-14(2)	41(2)	-9(2)
C(153)	60(2)	36(2)	51(2)	-16(2)	27(2)	-11(2)
C(154)	49(2)	35(2)	37(2)	-14(1)	16(1)	-6(1)

Table 3.10. Continued Anisotropic displacement parameters ($Å^2 x\ 10^3$)for **10**·(*n*–C_7H_{16})·(C_7H_{16}). The anisotropic displacement factor exponent takes the form: $-2\pi^2[\ h^2a^{*2}U^{11} + ... + 2\ h\ k\ a^*\ b^*\ U^{12}\ ]$

C(155)	54(2)	49(2)	54(2)	-11(2)	-4(2)	-7(2)
C(156)	79(3)	49(2)	46(2)	2(2)	-7(2)	9(2)
C(157)	128(4)	38(2)	93(4)	-11(2)	65(3)	-20(2)
Co(2)	24(1)	21(1)	13(1)	0(1)	6(1)	2(1)
Si(2)	29(1)	30(1)	17(1)	-3(1)	4(1)	-2(1)
N(4)	30(1)	25(1)	35(1)	-7(1)	12(1)	0(1)
N(5)	31(1)	24(1)	20(1)	1(1)	1(1)	1(1)
N(6)	26(1)	22(1)	16(1)	-4(1)	7(1)	-3(1)
C(1)	28(1)	50(2)	24(1)	-5(1)	2(1)	-5(1)
C(1A)	85(3)	29(2)	110(4)	7(2)	70(3)	20(2)
C(1B)	47(2)	51(2)	29(2)	3(2)	4(1)	-10(2)
C(2)	39(2)	43(2)	37(2)	-7(2)	1(1)	4(1)
C(3)	32(2)	29(2)	22(2)	-4(1)	2(1)	-4(1)
C(4)	48(2)	35(2)	27(2)	-3(1)	-2(1)	1(1)
C(5)	50(2)	48(2)	36(2)	1(2)	0(1)	-10(2)
C(6)	44(2)	40(2)	18(1)	-5(1)	3(1)	0(1)
C(7)	41(2)	42(2)	28(2)	-4(1)	-1(1)	1(1)
C(7A)	43(2)	31(4)	30(4)	-3(3)	2(3)	6(3)
C(7B)	43(2)	31(4)	30(4)	-3(3)	2(3)	6(3)
C(8)	28(1)	24(1)	15(1)	0(1)	8(1)	-2(1)
C(9)	28(1)	19(1)	16(1)	-4(1)	4(1)	2(1)
C(10)	41(2)	30(1)	29(2)	-2(1)	5(1)	-7(1)
C(11)	26(1)	27(1)	16(1)	-4(1)	5(1)	-1(1)
C(12)	35(2)	22(1)	67(2)	4(1)	26(2)	1(1)
C(13)	33(1)	21(1)	53(2)	-4(1)	23(1)	-1(1)
C(14)	61(2)	31(2)	90(3)	17(2)	43(2)	15(2)
C(15)	82(3)	29(2)	85(3)	-8(2)	60(2)	3(2)
C(16)	47(2)	27(1)	65(2)	-14(2)	36(2)	-5(1)
C(17)	49(2)	38(2)	46(2)	-20(2)	31(2)	-6(1)
C(18)	69(2)	59(2)	54(2)	-35(2)	43(2)	-28(2)
C(19)	67(2)	94(3)	32(2)	-37(2)	27(2)	-30(2)
C(20)	58(2)	71(2)	35(2)	-24(2)	23(2)	-15(2)

Table 3.10. Continued Anisotropic displacement parameters ($Å^2 x\ 10^3$)for **10**·(*n*–C_7H_{16})·(C_7H_{16}). The anisotropic displacement factor exponent takes the form: $-2\pi^2[\ h^2a^{*2}U^{11} + ... + 2\ h\ k\ a^*\ b^*\ U^{12}\ ]$

C(21)	47(2)	49(2)	38(2)	-16(2)	19(1)	-3(2)
C(22)	40(2)	38(2)	45(2)	-16(2)	22(1)	-3(1)
C(23)	35(2)	33(2)	67(2)	1(2)	8(2)	-1(1)
C(24)	79(3)	121(4)	29(2)	-22(2)	6(2)	-23(3)
C(25)	105(4)	79(3)	64(3)	-41(2)	50(3)	-55(3)
C(26)	28(1)	23(1)	54(2)	4(1)	7(1)	5(1)
C(27)	31(2)	27(1)	56(2)	7(1)	2(1)	1(1)
C(28)	46(2)	25(1)	55(2)	3(1)	-10(2)	-1(1)
C(29)	45(2)	32(2)	39(2)	-1(1)	-8(1)	4(1)
C(30)	30(1)	31(1)	40(2)	1(1)	-2(1)	0(1)
C(31)	27(1)	25(1)	41(2)	1(1)	3(1)	1(1)
C(32)	43(2)	31(1)	43(2)	-3(1)	11(1)	-8(1)
C(33)	44(2)	36(2)	84(3)	8(2)	13(2)	-7(2)
C(34)	92(3)	45(2)	43(2)	-5(2)	-4(2)	-9(2)
C(35)	24(1)	26(1)	14(1)	-2(1)	6(1)	0(1)
C(36)	27(1)	24(1)	19(1)	-3(1)	6(1)	-2(1)
C(37)	36(1)	29(1)	25(1)	-10(1)	15(1)	-5(1)
C(38)	38(2)	35(1)	27(2)	-8(1)	20(1)	-7(1)
C(39)	33(1)	27(1)	26(1)	-3(1)	12(1)	-7(1)
C(40)	26(1)	23(1)	18(1)	-4(1)	7(1)	-1(1)
C(41)	28(1)	19(1)	17(1)	-1(1)	8(1)	-3(1)
C(42)	27(1)	28(1)	20(1)	1(1)	7(1)	-2(1)
C(43)	31(1)	24(1)	23(1)	1(1)	12(1)	4(1)
C(44)	40(2)	25(1)	19(1)	-3(1)	12(1)	-3(1)
C(45)	35(1)	29(1)	21(1)	-2(1)	1(1)	-5(1)
C(46)	28(1)	23(1)	23(1)	0(1)	5(1)	0(1)
C(47)	32(2)	33(1)	46(2)	-5(1)	-3(1)	6(1)
C(48)	36(2)	45(2)	45(2)	-12(2)	-7(1)	9(1)
C(49)	56(2)	31(1)	31(2)	-13(1)	9(1)	-2(1)
C(50)	27(1)	22(1)	20(1)	-5(1)	9(1)	0(1)
C(51)	28(1)	29(1)	24(1)	-4(1)	6(1)	3(1)
C(52)	33(1)	28(1)	27(1)	2(1)	8(1)	6(1)

Table 3.10. Continued Anisotropic displacement parameters ($Å^2$x 10^3)for **10**·(*n*–C_7H_{16})·(C_7H_{16}). The anisotropic displacement factor exponent takes the form: $-2\pi^2[h^2a^{*2}U^{11} + ... + 2 h k a^* b^* U^{12}]$

C(53)	31(1)	20(1)	37(2)	-1(1)	10(1)	0(1)
C(54)	28(1)	25(1)	29(1)	-4(1)	6(1)	-1(1)
C(55)	29(1)	23(1)	24(1)	-2(1)	8(1)	1(1)
C(56)	37(2)	33(1)	25(1)	2(1)	3(1)	-4(1)
C(57)	34(2)	37(2)	31(2)	-2(1)	-3(1)	2(1)
C(58)	40(2)	26(1)	54(2)	11(1)	5(1)	-4(1)
C(59)	34(1)	22(1)	18(1)	2(1)	1(1)	5(1)
C(60)	34(1)	28(1)	23(1)	0(1)	-3(1)	2(1)
C(61)	43(2)	39(2)	27(2)	6(1)	-13(1)	2(1)
C(62)	56(2)	37(2)	27(2)	12(1)	-9(1)	0(2)
C(63)	47(2)	29(1)	25(2)	7(1)	0(1)	-2(1)
C(64)	34(1)	24(1)	17(1)	1(1)	0(1)	4(1)
C(65)	32(1)	23(1)	18(1)	3(1)	1(1)	-2(1)
C(66)	41(2)	24(1)	22(1)	2(1)	3(1)	0(1)
C(67)	49(2)	30(1)	24(1)	-3(1)	1(1)	-7(1)
C(68)	41(2)	38(2)	23(1)	6(1)	-6(1)	-10(1)
C(69)	33(1)	37(2)	30(2)	2(1)	-2(1)	5(1)
C(70)	36(1)	29(1)	23(1)	-3(1)	1(1)	0(1)
C(71)	42(2)	42(2)	43(2)	-16(2)	0(1)	11(1)
C(72)	52(2)	34(2)	43(2)	-11(1)	3(2)	7(2)
C(73)	52(2)	51(2)	31(2)	7(2)	-14(1)	-12(2)
C(74)	29(1)	32(1)	31(2)	2(1)	-9(1)	3(1)
C(75)	32(1)	37(2)	33(2)	3(1)	-5(1)	7(1)
C(76)	30(2)	51(2)	45(2)	10(2)	2(1)	7(1)
C(77)	31(2)	46(2)	55(2)	5(2)	-7(1)	-6(1)
C(78)	37(2)	43(2)	48(2)	-4(2)	-10(1)	-5(1)
C(79)	36(2)	37(2)	33(2)	-2(1)	-8(1)	1(1)
C(80)	52(2)	44(2)	32(2)	-4(1)	-5(1)	1(2)
C(81)	45(2)	41(2)	37(2)	-2(1)	5(1)	10(1)
C(82)	40(2)	65(2)	95(3)	6(2)	6(2)	-17(2)
C(7SA)	106(9)	100(9)	43(5)	19(8)	1(5)	22(9)
C(7SB)	67(7)	65(7)	63(9)	30(8)	-5(5)	-5(7)

Table 3.10. Continued Anisotropic displacement parameters ($Å^2 x\ 10^3$)for **10**·(*n*–C_7H_{16})·(C_7H_{16}). The anisotropic displacement factor exponent takes the form: $-2\pi^2[\ h^2 a^{*2} U^{11} + ... + 2\ h\ k\ a^*\ b^*\ U^{12}\ ]$

C(5SA)	60(5)	53(4)	55(5)	-8(4)	10(4)	10(4)
C(6SB)	65(5)	76(6)	55(5)	-1(4)	-7(4)	4(4)
C(5SB)	52(6)	56(5)	53(6)	-3(5)	7(4)	6(4)
C(6SA)	55(5)	71(6)	55(6)	20(5)	21(4)	21(5)
C(4S)	59(2)	61(2)	55(2)	-7(2)	-6(2)	3(2)
C(3S)	56(2)	68(3)	64(3)	-17(2)	-17(2)	8(2)
C(2S)	56(2)	71(2)	46(2)	-13(2)	-3(2)	9(2)
C(1S)	83(3)	112(4)	54(3)	-3(3)	-2(2)	-3(3)

3.22 References

1. Bergman, R. G. *Science* **1984,** *223,* 902-908.

2. True, R. W. *Oil and Gas Journal* **2012,** *110* (7).

3. Lange, J.-P. Economics of Alkane Conversion. In *Sustainable Strategies for the Upgrading of Natural Gas Fundamentals, Challenges and Opportunities;* Springer, 2005; pp 3-24.

4. Stahl, S. S.; Labinger, J. A.; Bercaw, J. E. *Angew. Chem. Int. Ed.* **1998,** *37,* 2180-2192
.
5. Green, J. C.; Green, M. L. H.; Parkin, G. *Chem. Commun.* **2012,** *48,* 11481-11503.

6. Labinger, J. A.; Bercaw, J. E. *Nature* **2002,** *417,* 507-514.

7. Crabtree, R. H. *Journal of Organometallic Chemistry* **2004,** *689,* 4083-4091.

8. rcov(Co) = 1.25 Å: Pauling, L. The Nature of the Chemical Bond. Cornell University Press, Cornell, 1960; Vol. 3rd ed., pp Chap. 11, P. 402.

9. Kubas, G. J. *Metal-dihydrogen and Sigma-bond Complexes;* Kluwer Academic: New York, 2001.

10. Crabtree, R. H. *Angew. Chem., Int. Ed.* **1993,** *32,* 789.

11. Trofimenko, S. *J. Am. Chem. Soc.* **1968,** *90,* 4754.

12. Cotton, F. A.; Stanislowski, A. G. *J. Am. Chem. Soc.* **1974,** *96,* 5074.

13. Brookhart, M.; Green, M. L. H.; Parkin, G. *Proc. Natl. Acad. Sci. U.S.A.* **2007,** *104*, 6908.

14. Parkin, G. *Acc. Chem. Res.* **2009,** *42*, 315.

15. Brookhart, M.; Green, M. L. H. *J. Organomet. Chem.* **1983,** *250,* 395.

16. Cobar, E. A.; Khaliullin, R. Z.; Bergman, R. G.; Head-Gordon, M. *PNAS* **2007,** *104*, 6963-6968.

17. For a more complete history of the activation of alkanes see Hall, C.; Perutz, R. N. *Chem. Rev.* **1996,** *96,* 3125.

18. Perutz, R. N. T. J. J. *Inorg. Chem.* **1975,** *97,* 4791.

19. Perutz, R. N.; Turner, J. J. *J. Am. Chem. Soc.* **1975,** *97,* 4791.

20. Kelly, J. M.; Hermann, H.; Von Gustorf, E. K. *J. Chem. Soc. Chem. Commun.* **1973,** 105.

21. Shilov, A. E. *Activation of Saturated Hydrocarbons by Transition Metal Complexes;* Reidel: Dordrecht, 1984.

22. Breckenridge, H. W.; Sinai, N. *J. Phys. Chem.* **1981,** *85,* 3557.

23. Breckenridge, W. H.; Sterward, G. M. *J. Am. Chem. Soc.* **1986,** *108,* 364.

24. Hoyano, J. K.; Graham, W. A. G. *J. Am. Chem. Soc* **1982,** *104,* 3723-3725.

25. Janowicz, A. H.; Bergman, R. G. *J. Am. Chem. Soc* **1982,** *104,* 352-354.

26. Bengali, A. A.; Schultz, R. H.; Moore, C. B.; Bergman, R. G. *J. Am. Chem. Soc.* **1994,** *116,* 9585-9589.

27. Schultz, R. H.; Bengali, A. A.; Tauber, M. J.; Weiller, B. H.; Wasserman, E. P.; Kyle, K. R.; Moore, C. B.; Bergman, R. G. *J. Am. Chem. Soc.* **1994,** *116,* 7369-7377.

28. Yeston, J. S. P. Flash Kinetics in Liquefied Noble Gases: Studies of Alkane Activation and Ligand Dynamics at Rhodium Carbonyl Centers, and a Search for Xenon-Carbene Adducts. In *Dissertation;* UC Berkeley, 2001.

29. Geftakis, S.; Ball, G. E. *J. Am. Chem. Soc* **1998,** *120,* 9953.

30. Lawes, D. J.; Geftakis, S.; Ball, G. E. *J. Am. Chem. Soc.* **2005,** *127,* 4134.

31. Lawes, D. J.; Darwish, T. A.; Clark, T.; Harper, J. B.; Ball, G. E. *Angew. Chem. Int. Ed.* **2006,** *45,* 4486.

32. Ball, G. E.; Brookes, C. M.; Cowan, A. J.; Darwish, T. A.; George, M. W.; Kawanami, H. J.; Portius, P.; Rourke, J. *Proc. Natl. Acad. Sci. U. S. A.* **2007,** *104,* 6927.

33. Young, R. D.; Hill, A. F.; Hillier, W.; Ball, G. E. *J. Am. Chem. Soc* **2011,** *133,* 13806.

34. Young, R. D.; Lawes, D. J.; Hill, A. F.; Ball, G. E. *J. Am. Chem. Soc.* **2012,** *134,* 8294.

35. Duckett, S. B.; George, M. W.; Jina, O. S.; Matthews, S. L.; Perutz, N. R.; Sun, X. Z.; Vuong, K. Q. *Chem. Commun.* **2009,** 1401.

36. Calladine, J. A.; Duckett, S. B.; George, M. W.; Matthews, S. L.; Perutz, R. N.; Torres, O.; Vuong, K. Q. *J. Am. Chem. Soc.* **2011,** *133,* 2303.

37. Bernskoetter, W. H.; Schauer, C. K.; Goldberg, K. I.; Brookhart, M. *Science* **2009,** *326,* 553.

38. Evans, D. R.; Drovetskaya, T.; Bau, R.; Reed, C. A.; Boyd, P. D. W.; Reed, C. A. *J. Am. Chem. Soc.* **1997,** *119,* 3633.

39. Castro–Rodriguez, I.; Nakai, H.; Gantzel, P.; Zakharov, L. N.; Rheingold, A. L.; Meyer, K. *J. Am. Chem. Soc.* **2003,** *125,* 1573.

40. D., P. S.; Thompson, A. L.; Algarra, A. G.; Apperley, D. C.; Macgregor, S. A.; Weller, A. S. *Science* **2013,** (In Press).

41. Elian, M.; Hoffmann, R. *Inorg. Chem.* **1975,** *14,* 1058-1076.

42. Margulieux, G. W.; Weidemann, N.; Lacy, D. C.; Moore, C. E.; Rheingold, A. L.; Figueroa, J. S. *J. Am. Chem. Soc.* **2012,** *132,* 5033-5035.

43. Labios, L. A.; Millard, M. D.; Rheingold, A. L.; Figueroa, J. S. *J. Am. Chem. Soc.* **2009,** *131,* 11318-11319.

44. Emerich, B. M.; Moore, C. E.; Fox, B. J.; Rheingold, A. L.; Figueroa, J. S. *Organometallics* **2011,** *30,* 2598-2608.

45. Cotton, F. A. *J. Am. Chem. Soc.* **1961,** *83,* 351-355.

46. Malatesta, L.; Bonati, F. *Isocyanide Complexes of Transition Metals;* Wiley: New York, 1969.

47. Bonati, F.; Minghetti, G. *Inorg. Chim. Acta.* **1974,** *9,* 95-112.

48. Fox, B. J.; Sun, Q. Y.; DiPasquale, A. G.; Fox, A. R.; Rheingold, A. L.; Figueroa, J. S. *Inorg. Chem.* **2008,** *47,* 9010.

49. Carpenter, A. E.; Margulieux, G. W.; Millard, M. D.; Moore, C. E.; Weidemann, N.; Rheingold, A. L.; Figueroa, J. S. *Angew. Chem. Int. Ed* **2012,** *51,* 9412-9416.

50. Margulieux, G.; Carpenter, A. E.; Millard, M. D.; Figueroa, J. S. dihydrogen, pyridine, and ammonia coordinated crystal structures are unpuplished results.

51. McNamara, B. K.; Yeston, J. S.; Bergman, R. G.; Moore, C. B. *J. Am. Chem. Soc* **1999,** *121,* 6473-6443.

52. Bondi, A. *J. Phys. Chem* **1964,** *68*, 441.

53. Zaric, S.; Hall, M. B. *J. Phys. Chem. Soc.* **1997,** *101*, 4646.

54. Chatt, J.; Duncanson, L. A. *J. Chem. Soc.* **1953,** 2939.

55. Masa, W. *Crystal Structure Determination*, 2nd ed.; Springer-Verlag, 2004; pp 161-162.

56. Heiberg, H.; Gropen, L. A.; Swang, O. *Int. J. Quant. Chem.* **2003,** *92*, 391.

57. Da Silva, J. C. S.; De ALmeida, W. B.; Rocha, W. R. *Chem. Phys.* **2009,** *365*, 85.

58. Crabtree, R. H.; Holt, E. M.; Lavin, M.; Morehouse, S. M. *Inorg. Chem.* **1985,** *24*, 1986.

59. rcov(Co) = 1.11 Å: Pyykko, P.; Atsumi, M. *Chem. Eur. J.* **2009,** *15*, 186.

60. rcov(Co) = 1.15 Å: Batsanov, S. S. *Russ. Chem. Bull.* **1995,** *44*, 2245.

61. rcov(Co) = 1.26 Å: Cordero, B.; Gomez, V.; Platero-Prats, A. E.; Reves, J.; Echeverria, J.; Cremades, E.; Barragan, F.; Alvarez, S. *Dalton Trans* **2008,** 2832.

62. rcov(Co) = 1.38 Å: Palacios, A. A.; Aullon, G.; Alemany, P.; Alvarez, S. *Inorg. Chem.* **2000 ,** *39*, 3166.

63. Dawoodi, Z.; Green, M. L. H.; Mtetwa, B. S. V.; Prout, K. *J. Chem. Soc., Chem. Commun.* **1982,** 802.

64. Bader, R. F. W. *Chem. Rev.* **1991,** *893*.

65. Da Silva, J. C. S.; De Almeida, W. B.; Rocha, W. R. *Chem. Phys.* **2009,** *365*, 85.

66. Popelier, P. L. A.; Logothetis, G. *J. Organomet. Chem.* **1998,** *555*, 101.

67. Thakur, T. S.; Desiraju, G. R. *Chem. Commun.* **2006,** 552.

68. Maudsley, A. A. *Journal of Magnetic Resonance* **1988,** *76*, 287-305.

69. Millard, M. D.; Carpenter, A. E.; Figueroa, J. S. u. r.

70. Bryant, R. G. The NMR Time Scale. *Journal of Chemical Education* **1983,** *60*, 933-935.

71. Sceats, E. L.; Figueroa, J. S.; Cummins, C. C.; Loening, N. M.; Van der Wel, P.; Griffin, R. G. *Polyhedron* **2004,** *23,* 2751-2768.

72. Hwang, T.; Shaka, A. J. *Journal of Magnetic Resonance, Series A* **1995,** *112,* 275-279.

73. Tott, K.; Stonehouse, J.; Keeler, J.; Hwang, T.; Shaka, A. J. *J. Am. Chem. Soc.* **1995,** *117,* 4199-4200.

74. Tannus, A.; Garwood, M. *NMR in Biomedicine* **1997,** *10,* 423-434.

75. Silver, M. S.; Joseph, R. I.; Hoult, D. I. *Journal of Magnetic Resonance* **1984,** *59,* 347-351.

76. Schreckenbach, G.; Ziegler, T. *J. Phys. Chem.* **1995,** *99,* 606-611.

77. Sceats, E. L.; Figueroa, J. S.; Cummins, C. C.; Loening, N. M.; Van der Wel, P.; Griffin, R. G. *Polyhedron* **2004,** *23,* 2751-2278.

78. Berger, S.; Braun, S. *200 and More NMR Experiments;* Wiley-VCH: New York, 2004.

79. Rossi, A. R.; Hoffmann, R. *Inorg. Chem.* **1975,** *14,* 365.

80. Sacconi, L. *Pure and Applied Chemistry* **1968,** *27,* 95-127.

81. Huheey, J. E.; Keiter, E. A.; Keiter, R. L. *Inorganic Chemistry: Principles of Structure and Reactivity,* 4th ed.; HarperCollins Colllege, 1993.

82. Greenwood, N. N.; Earnshaw, A. *Chemistry of the Elements*, 2nd ed.; Reed Educational, 1997; p 893.

83. Dyadin, Y. A.; Larionov, E. G.; Manakov, A. Y.; Zhurko, F. V.; Aladko, E. Y.; Mikina, T. V.; Komarov, V. Y. *Mendeleev Commun.* **1999,** *9(5),* 209-210.

84. Dyadin, Y. A.; Terekhova, I. S.; Rodionova, T. V.; Soldatov, D. V. *Journal of Structural Chemistry* **1999,** *40,* 645-653.

85. Ehlers, A. W.; Frenking, G.; Baerends, E. J. *Organometallics* **1997,** *16,* 4896-4902.

86. Weiller, B. H. *J. Am. Chem. Soc.* **1992,** *114,* 10910-10915.

87. Ball, G. E.; Darwish, T. A.; Geftakis, S.; George, M. W.; Lawes, D. J.; Portius, P.; Rourke, J. P. *PNAS* **2005,** *102,* 1853-1858.

88. Calladine, J. A.; Vuong, K. Q.; Sun, X. Z.; George, M. W. *Pure Appl. Chem.* **2009,** *81*, 1667-1675.

89. Childs, G. I.; Grills, D. C.; Sun, X. Z.; George, M. W. *Pure Appl. Chem.* **2001,** *73*, 443-447.

90. Mugridge, J. S.; Szigethy, G.; Bergman, R. G.; Raymond, K. N. *J. Am. Chem. Soc.* **2010,** *132*, 16256-16264.

91. Uspensky, J. V. *Theory of Equations;* McGraw–Hill Book Co.: New York, 1948.

92. Soltis, S. M.; Stowell, M. H. B.; Wiener, M. C.; N., P. J. G.; Rees, D. C. *J. Appl. Cryst.* **1997,** *30*, 190-194.

93. Zwart, P. H.; Grosse-kunstleve, R. W.; Lebdev, A. A.; Murshudov, G. N.; Adams, P. D. *Acta Cryst.* **2008,** *D64*, 99-107.

94. Atwood, J. L.; Barbour, L. J.; Agoston, J.; Schottel, B. L. *Science* **2002,** *298*, 1000.

95. Lennartson, A.; Hakansson, M.; Jagner, S. *New J. Chem.* **2007,** *31*, 344.

96. Seidel, S.; Seppelt, K. *Science* **2000,** *290*, 117.

97. Nairn, J. A.; Braun, C. L. *Chem. Phys. Lett.* **1977,** *52* (2), 385-387.

98. Brown, M. S.; Grant, D. M.; Horton, W. J.; Mayne, C. L.; Evans, G. T. *J. Am. Chem. Soc.* **1985,** *107*, 6698-6707.

99. Nakaoki, T.; Nagano, H.; Yanagida, T. *Journal of Molecular Structure* **2004,** *699*, 1-7.

100. Pangborn, A. B.; Giardello, M. A.; Grubbs, R. H.; Rosen, R. K.; Timmers, F. J. *Organometallics* **1996,** *15*, 1518.

101. Arnarego, W. L. F.; Chai, C. L. L. *Purification of Laboratory Chemicals* , 5th ed.; Elsevier, 2003.

102. Millard, M. D.; Carpenter, A. E.; Margulieux, G. W.; Rheingold, A. L.; Figueroa, J. S. *Unpublished Results*.

103. Sheldrick, G. M. *Acta Cryst.* **2008,** *A64*, 112.

104. Frisch, M. J.; Trucks, G. W.; Schlegel, H. B.; Scuseria, G. E. Robb, M. A.; Cheeseman, J. R.; Montgomery, J. A.; Vreven, Jr., T.; Kudin, K. N.; Burant, J. C.; Millam, J. M.;
Iyengar, S. S.; Tomasi, J.; Barone, V.; Mennucci, B.; Cossi, M.; Scalmani, G.;
Rega, N.; Petersson, G. A.; Nakatsuji, H.; Hada, M.; Ehara, M.; Toyota, K.;
Fukuda, R. ; Hasegawa, J.; Ishida, M.; Nakajima, T.; Honda, Y.; Kitao, O.; Nakai, H.; Klene, M.; Li, X.; Knox, J. E.; Hratchian, H. P.; Cross, J. B.; Bakken, V.; Adamo, C.; Jaramillo, J.; Gomperts, R.; Stratmann, R. E.; Yazyev, O.; Austin, A. J.; Cammi, R.; Pomelli, C.; Ochterski, J. W.; Ayala, P. Y.; Morokuma, K.; Voth, G. A.; Salvador, P.; Dannenberg, J. J.; Zakrzewski, V. G.; Dapprich, S.; Daniels, A. D.; Strain, M. C.; Farkas, O.; Malick, D. K.; Rabuck, A. D.; Raghavachari, K.; Foresman, J. B.; Ortiz, J. V.; Cui, Q.; Baboul, A. G.; Clifford, S.; Cioslowski, J.; Stefanov, B. B.; Liu, G.; Liashenko, A.; Piskorz, P.; Komaromi, I.; Martin, R. L.; Fox, D. J.; Keith, T.; Al–Laham, M. A.; Peng, C. Y.; Nanayakkara, A.; Challacombe, M.; Gill, P. M. W.; Johnson, B.; Chen, W.; Wong, M. W.; Gonzalez, C.; Pople, J. A. Gaussian 03, Revision D.01, Gaussian, Inc., Wallingford CT, 2004.

105. Andrae, D.; HauBermann, U.; Dolg, M.; Stoll, H.; Preuss, H. *Theor. Chim. Acta.* **1990,** *77*, 123.

106. Perdew, J. P.; Burke, K.; Ernzerhof, M. *Phys. Rev. Lett.* **1990,** *77*, 3865.

107. Walter, M. D.; White, P. S.; Schauer, C. K.; Brookhart, M. *Jew J. Chem.* **2011,** *35*, 2884.

108. Quintal, M. M.; Karton, A.; Iron, M. A.; Boese, M. A.; Boese, A. D.; Martin, J. M. L. *J. Phys. Chem. A* **2006,** *110*, 709.

109. Bader, R. F. W. *Atoms in Molecules: A Quantum Theory;* Clarendon Press:Oxford: New York, 1990.

110. AIMALL (Version 12.06.03), T. A. K. T. G. S. O. P. K. U. (., 2012.

Chapter 3: Much of the material for this chapter comes directly from a manuscript entitled "Crystallographic Characterization of a Cobalt sigma-Alkane Complex Formed in Solution" by Matthew D. Millard, Alex E. Carpenter, Stephen P. George, Arnold L. Rheingold, and Joshua S. Figueroa, which has been submitted to *Science*, **2013-** in review